

NASA/TP-2003-212051

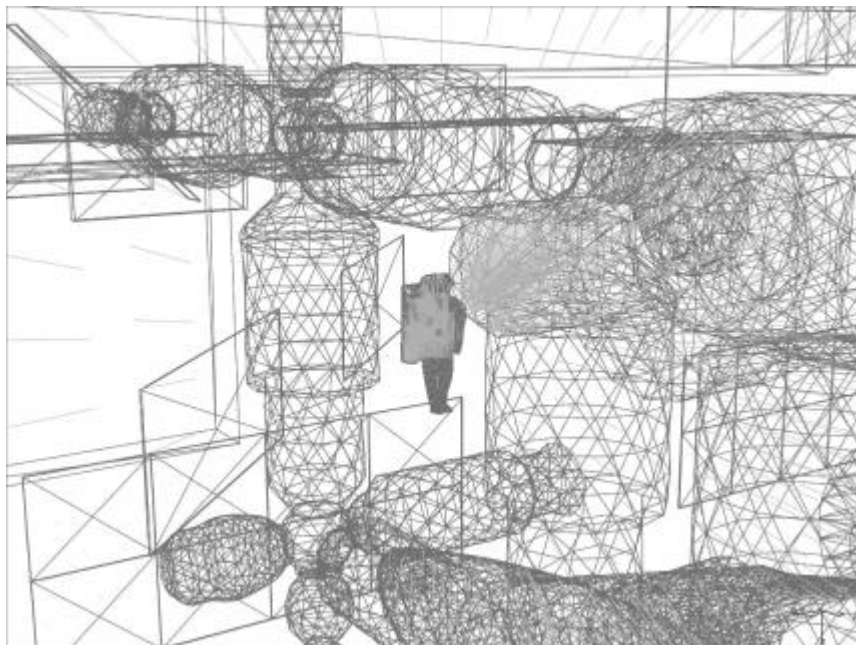


# Radiation Protection Studies of International Space Station Extravehicular Activity Space Suits

*Francis A. Cucinotta, Mark R. Shavers, Editors*  
*Lyndon B. Johnson Space Center*  
*Houston, Texas*

*Premkumar B. Saganti, Editor*  
*Prairie View A&M University*  
*Prairie View, Texas*

*Jack Miller, Editor*  
*Lawrence Berkeley National Laboratory*  
*Berkeley, California*



---

December 2003

## The NASA STI Program Office . . . in Profile

Since its founding, NASA has been dedicated to the advancement of aeronautics and space science. The NASA Scientific and Technical Information (STI) Program Office plays a key part in helping NASA maintain this important role.

The NASA STI Program Office is operated by Langley Research Center, the lead center for NASA's scientific and technical information. The NASA STI Program Office provides access to the NASA STI Database, the largest collection of aeronautical and space science STI in the world. The Program Office is also NASA's institutional mechanism for disseminating the results of its research and development activities. These results are published by NASA in the NASA STI Report Series, which includes the following report types:

- **TECHNICAL PUBLICATION.** Reports of completed research or a major significant phase of research that present the results of NASA programs and include extensive data or theoretical analysis. Includes compilations of significant scientific and technical data and information deemed to be of continuing reference value. NASA's counterpart of peer-reviewed formal professional papers but has less stringent limitations on manuscript length and extent of graphic presentations.
- **TECHNICAL MEMORANDUM.** Scientific and technical findings that are preliminary or of specialized interest, e.g., quick release reports, working papers, and bibliographies that contain minimal annotation. Does not contain extensive analysis.
- **CONTRACTOR REPORT.** Scientific and technical findings by NASA-sponsored contractors and grantees.

- **CONFERENCE PUBLICATION.** Collected papers from scientific and technical conferences, symposia, seminars, or other meetings sponsored or cosponsored by NASA.
- **SPECIAL PUBLICATION.** Scientific, technical, or historical information from NASA programs, projects, and mission, often concerned with subjects having substantial public interest.
- **TECHNICAL TRANSLATION.** English-language translations of foreign scientific and technical material pertinent to NASA's mission.

Specialized services that complement the STI Program Office's diverse offerings include creating custom thesauri, building customized databases, organizing and publishing research results . . . even providing videos.

For more information about the NASA STI Program Office, see the following:

- Access the NASA STI Program Home Page at <http://www.sti.nasa.gov>
- E-mail your question via the Internet to [help@sti.nasa.gov](mailto:help@sti.nasa.gov)
- Fax your question to the NASA Access Help Desk at (301) 621-0134
- Telephone the NASA Access Help Desk at (301) 621-0390
- Write to:  
NASA Access Help Desk  
NASA Center for AeroSpace Information  
7121 Standard  
Hanover, MD 21076-1320

NASA/TP-2003-212051



# Radiation Protection Studies of International Space Station Extravehicular Activity Space Suits

*Francis A. Cucinotta, Mark R. Shavers, Editors*  
*Lyndon B. Johnson Space Center*  
*Houston, Texas*

*Premkumar B. Saganti, Editor*  
*Prairie View A&M University*  
*Prairie View, Texas*

*Jack Miller, Editor*  
*Lawrence Berkeley National Laboratory*  
*Berkeley, California*

National Aeronautics and  
Space Administration  
Johnson Space Center  
Houston, Texas 77058-3696

---

December 2003

Available from:

NASA Center for AeroSpace Information  
7121 Standard  
Hanover, MD 21076-1320

National Technical Information Service  
5285 Port Royal Road  
Springfield, VA 22161

This report is also available in electronic form at <http://techreports.larc.nasa.gov/cgi-bin/NTRS>

# CONTENTS

	<b>Page</b>
Acronyms .....	vii
Preface .....	ix
Chapter 1, Introduction to Radiation Issues for International Space Station Extravehicular Activities	1
1.1 Ionizing Radiation Environment and Exposures in Low Earth Orbit .....	2
1.2 Dosimetric Quantities and Regulatory Dose Limits for Stochastic Radiation Effects .....	8
1.2.1 Deterministic Effects .....	10
1.2.2 Environmental Monitoring, Crew Dosimetry and Alerts .....	11
1.2.3 Radiation Dose Reduction .....	11
1.2.4 The EMU Space Suit .....	12
1.2.5 EMU Hard Upper Torso (HUT) .....	13
1.2.6 EMU Helmet .....	14
1.2.7 EMU Personal Life Support System .....	14
1.2.8 Liquid Cooling Ventilation Garment .....	14
1.2.9 Orlan-M Space Suit .....	15
1.2.10 Human Phantom .....	16
1.3 References .....	17
Chapter 2, Proton and Electron Threshold Energy Measurements for Extravehicular Activity Space Suits .....	19
Abstract .....	20
2.1 Introduction .....	20
2.2 Methods and Materials .....	21
2.2.1 Suit Configurations .....	21
2.2.2 Phantom .....	23
2.2.3 CT-Based Measurements .....	24
2.2.4 Electron and Proton Measurements .....	24
2.3 Results and Discussion .....	26
2.4 Summary .....	31
2.5 Acknowledgments .....	33
References .....	33
Chapter 3, Radiation Tests of the Extravehicular Mobility Unit Space Suit for the International Space Station Using Energetic Protons .....	35
Abstract .....	36
3.1 Introduction .....	36
3.2 Experimental Configurations .....	38
3.2.1 Detectors and Electronics .....	38
3.2.2 Calibration .....	39
3.2.3 Relation of $\Delta E$ in Silicon to LET .....	40
3.3 Analysis of Bare-Beam Data .....	40
3.3.1 Beam Quality .....	40
3.3.2 $\Delta E$ Spectra: Events Lost by Scattering .....	41
3.3.3 Event Pile-Up in the $\Delta E$ Spectra .....	42

# CONTENTS

(continued)

	<b>Page</b>
3.3.4 High- $\Delta E$ Tails, Pile-Up Removal Methods .....	43
3.3.5 Interpretation of the High- $\Delta E$ Tails .....	45
3.3.6 Beam Energies, Calibration Adjustment .....	46
3.3.7 Landau Distribution Calculations.....	47
3.3.8 Nuclear Interactions and High- $\Delta E$ Tails.....	48
3.3.9 Quantitative Effects of the High- $\Delta E$ Tails .....	49
3.4 Results With the EMU Space Suit and Phantom.....	50
3.4.1 General Considerations .....	50
3.4.2 Brain Location: 223-MeV Beam.....	51
3.4.3 Brain Location: 136-MeV Beam.....	55
3.4.4 Slice 8: 223-MeV Beam .....	55
3.4.5 Slice 8: 136 MeV Beam .....	61
3.4.6 Slice 9: 223 MeV Beam .....	62
3.4.7 Slice 9: 136 MeV Beam .....	62
3.4.8 Alternative Explanation of Slow Protons .....	65
3.4.9 Summary of Results With Detectors in the Phantom .....	65
3.5 Conclusions .....	67
3.6 Acknowledgments .....	67
3.7 References .....	68
Appendix A – Nuclear Interactions in Silicon .....	69
Chapter 4, Characterization of the Radiation Shielding Properties of U.S. and Russian Extravehicular Activity Suits .....	71
Abstract.....	72
4.1 Introduction .....	72
4.2 Experiment .....	74
4.2.1 Detectors.....	74
4.2.2 Irradiations to 6 MeV Electrons and 60 MeV Protons.....	76
4.2.3 Irradiations to 232 MeV Protons.....	77
4.3 Results and Discussion.....	82
4.3.1 Doses From 6 MeV Electron Irradiations.....	82
4.3.2 60 MeV Proton Irradiations .....	82
4.3.3 Results From 232 MeV Proton Irradiations .....	83
4.4 Conclusions .....	94
4.5 References .....	96
Chapter 5, A Comparison of Model Calculation and Measurement of Absorbed Dose for Proton Irradiation .....	97
Abstract.....	98
5.1 Introduction .....	98
5.2 Methods.....	98

# CONTENTS

(continued)

	<b>Page</b>
5.3 Results.....	101
5.4 Conclusions .....	103
5.5 References .....	103
Chapter 6, In Vitro Studies on Space Radiation-Induced Delayed Genetic Responses: Shielding Effects .....	105
Abstract.....	106
6.1 Introduction .....	107
6.2 Materials & Methods .....	107
6.2.1 Source of Proton Radiation .....	107
6.2.2 Setup of Phantom Head and EMU Helmet .....	107
6.2.3 Source of Haemopoietic Bone Marrow Stem Cells/In Vitro Culture Conditions.....	108
6.2.4 Cytogenetic Analysis .....	109
6.2.5 Apoptosis-DNA Damage .....	109
6.2.6 Analysis for Cytokines.....	110
6.3 Results.....	110
6.3.1 Cytogenetic Analysis .....	110
6.3.2 Apoptosis-DNA Damage .....	111
6.3.3 Cytokine Production/Release in Irradiated and Control Culture Supernatants .....	111
6.4 Discussion .....	112
6.5 Acknowledgments .....	113
6.6 References .....	113
Chapter 7, Radiation Dose From Reentrant Electrons.....	121
Abstract.....	122
Introduction.....	122
Results .....	122
Conclusions .....	123
Acknowledgement.....	124
References .....	126
Chapter 8, Shuttle Space Suit: Fabric/LCVG Model Validation.....	127
Abstract.....	128
Introduction.....	128
Computational Model .....	128
Space Suit Fabric Model.....	130
Results and Implications .....	132
Future Activity .....	133
Conclusion .....	133
References .....	134
Contact .....	134
Chapter 9, Preliminary Shuttle Space Suit Shielding Model .....	135
9.1 Introduction .....	136
9.2 Space Suit Description .....	136

# CONTENTS

(continued)

	<b>Page</b>
9.3 Space Suit Model .....	139
9.4 Human Geometry Model.....	142
9.5 Environmental Models .....	142
9.6 Computational Procedures .....	145
9.7 Results.....	148
9.8 Conclusion.....	152
9.9 References .....	153
Contact .....	154
Chapter 10, Radiation Exposure Analysis for ISS: The Female Astronaut in EVA.....	155
Abstract.....	156
Introduction.....	156
Scenario and Model-Derived Environment.....	156
Orbital Tracks and Fluxes.....	156
Flux Directionality .....	158
Configuration CAD Solid Models .....	160
ISS 8-A Configuration.....	160
Human Geometry Model .....	164
Transport of Energetic Trapped Particles .....	165
Results .....	166
Summary and Conclusions.....	169
References.....	169
Chapter 11, Risk of Skin Cancer From Space Radiation .....	171
Abstract.....	172
Introduction.....	172
Biological Factors in Skin Carcinogenesis.....	172
Radiation Epidemiology of Skin Cancers .....	173
Estimates of Skin Cancer Risk for Space Missions.....	174
References.....	176
Chapter 12, Summary and Recommendations for Future Work .....	177
References.....	181

## ACRONYMS

ACR	anomalous cosmic rays
BCC	basal cell carcinoma
BRYNTRN	baryon transport model
CAF	computerized anatomical female
CAM	computerized anatomical male
CT	computerized tomography
EMU	extravehicular mobility unit
ERI	Eril Research, Inc.
ERR	excess relative risk
EVA	extravehicular activity
EVVA	extravehicular visor assembly
GCR	galactic cosmic ray
HUT	hard upper torso
ISS	International Space Station
IVA	intravehicular activities
JSC	Johnson Space Center
LCVG	liquid cooling and ventilation garment
LEO	low Earth orbit
LET	linear energy transfer
LLU	Loma Linda University
LLUMC	Loma Linda University Medical Center
LLUPTF	Loma Linda University Proton Treatment Facility
LTA	lower torso assembly
MWC	multiple water connector
NCRP	National Council on Radiation Protection and Measurements
PI	propidium iodide
PLSS	primary life support subsystem
PNTD	plastic nuclear track detector
RBE	relative biological effectiveness
RMS	root mean square
SCC	squamous cell carcinoma
SPE	solar particle event
TLD	thermoluminescence dosimeter
TPS	treatment planning system



# RADIATION MEASUREMENTS AND ANALYSIS OF THE INTERNATIONAL SPACE STATION EXTRAVEHICULAR ACTIVITY SPACE SUITS

## PREFACE

This publication presents the results of recent investigations that evaluate the radiation shielding characteristics of two space suits—NASA’s Extravehicular Mobility Unit (EMU) and the Russian Space Agency’s Orlan-M—currently worn during extravehicular activity (EVA) involving construction and maintenance of the International Space Station (ISS). The experiments and analysis were supported by the EVA Project Office and the Space Radiation Health Project Office at NASA Johnson Space Center, and by the Loma Linda University (LLU) Proton Treatment Center. NASA Langley Research Center supported the studies by allowing their Radiation Design Team to perform a large analysis task by including the development of computerized model of the EMU. The majority of experiments were carried out at LLU, however additional measurements were made at Brookhaven National Laboratory (BNL) and at the Lawrence Berkeley National Laboratory (LBNL).

For context, the first chapter provides background information about the dynamic radiation environment experienced at the ISS and includes a brief summary of dosimetric quantities and space radiation health and protection requirements for activities in low Earth orbit. The Introduction also superficially describes the space suits and presents goals of the several experiments performed with them in January 2000, at the Loma Linda University Proton Treatment Facility. Supporting studies report the development and application of a computer model of the EMU space suit and the difficulty of shielding EVA crewmembers from high-energy reentrant electrons, a previously unevaluated component of the space radiation environment.

Chapters 2 through 6 of this publication report the results of experiments that evaluate the radiation shielding characteristics of the space suits. Chapter 2 presents the first experimental measurements of the water-equivalent thickness of the space suit fabric layup, helmet, torso, limbs, and boots using proton, electron, and photon irradiation techniques. The threshold energies required for penetration of the space suits by electrons and protons were experimentally determined and reported. Chapters 3 and 4 report proton doses measured at organ locations in a human phantom placed inside each space suit. Doses were measured using detectors worn by astronauts and by passive dosimeters that also measure the radiation environment in spacecraft. In addition, procedures were devised and data were collected using solid-state detectors that have a rich legacy from experiments of heavy-ion measurements at particle accelerators. Together, the current experiments emphasize the detection of incident particles and deleterious secondary ions produced by accelerated (250 MeV) protons inside the space suits and human phantom. Space suit shielding information from the analysis in Chapter 2 is used as input to the proton transport model BRYNTRN to simulate absorbed dose measurements in the abdomen and the results are compared in Chapter 5. Three radiobiology studies were performed of biological endpoints that are used to evaluate the response of cells to radiation insult: cytogenetic aberrations measure chromosomal instability; early and late apoptosis (“programmed cell death”) quantify delayed cell killing due to gene mutation or via epigenetic damage; and, TGF- $\beta_1$  cytokine production/release as measure of a specific cell-to-cell growth communication signal. Marrow cell cultures from two strains of mice were

placed inside the human phantom head with and without the EMU helmet in place and irradiated with high-energy protons at various low-dose levels. Chapter 6 reports the results of those quantitative studies.

Chapter 7 describes a study of the potential radiological health impact on EVA crewmembers of two virtually unexamined environmental sources of high-energy electrons—reentrant trapped electrons and atmospheric albedo or “splash” electrons. The radiological consequences of those sources have not been evaluated previously and, under closer scrutiny, may prove to be non-negligible for ISS EVA during either quiet or stormy space weather conditions. A detailed computational model of the shielding distribution provided by the fabric, helmet, rigid torso, and other components of the NASA astronauts’ EMU is being developed for exposure evaluation studies. The model is introduced in Chapters 8 and 9 and used in Chapter 10 to investigate how trapped particle anisotropy impacts female organ doses during EVA. Chapter 11 presents a mini-review of issues related to estimating skin cancer risk from space radiation. The final chapter contains conclusions about the protective qualities of the suit brought to light from these studies, as well as recommendations for future operational radiation protection investigations and practices.

The recent programmatic focus on radiation protection for EVA exposures is only one component of the NASA Space Radiation Health Project Office’s proactive management of radiation protection for human activities in space. Ionizing radiation exposures to long-term ISS crewmembers are increased by a factor of ~10 or more above typical Space Shuttle experiences, and it is quite possible that some individuals will receive doses that will restrict their time allowed on EVA or on orbit. Anticipation of these events prompted programmatic reviews and development of improved technologies and new procedures for the radiation mission support team, including near-real-time space weather monitoring, information analysis, integration, and reporting to flight surgeons and mission controllers. New research and dosimetry technologies and skills acquired by the NASA Space Radiation Health Project Office and its supporting research programs include improved spacecraft environmental and personnel dosimetry, improved ground-based physics and radiation transport models, leading-edge radiobiology studies of the deleterious effects of space-like ionizing radiation fields, and broadening and deepening investigations of risk analysis.

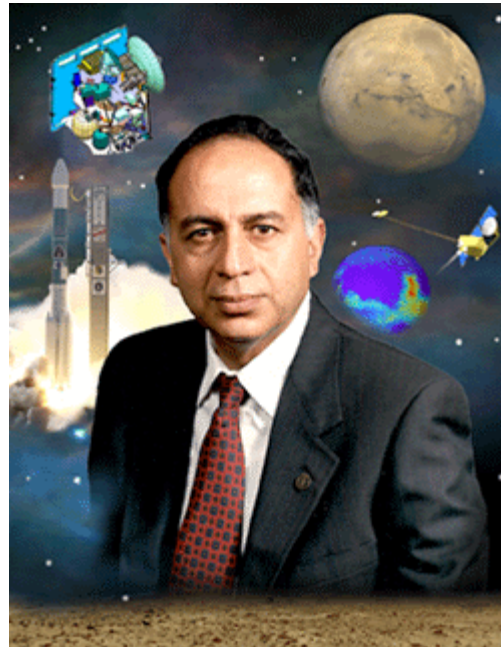
The editors wish to thank Gregory Harbaugh, Steve Poulos, and Joseph Kosmo of the EVA Project Office, and Greg Nelson, Michael Moyers, and Steve Rightnar of Loma Linda University for their assistance with the experiments, and also John Wilson and the Radiation Design Team at NASA Langley Research Center for their analysis support. We also wish to acknowledge Hamilton Sundstrand for their assistance with the EMU and Orlan-M space suits. We wish to thank Garry Qualls of LaRC for providing the cover illustration.

M. R. Shavers, P. Saganti, F. A. Cucinotta  
Space Radiation Health Project, NASA Johnson Space Center  
Houston, Texas

J. Miller  
Lawrence Berkeley National Laboratory  
Berkeley, California

## Dedication

This publication is dedicated to a colleague for whom we share many fond and respectful memories, Dr. Gautam D. Badhwar.



Dr. Gautam D. Badhwar (1940–2001)



# **CHAPTER 1**

## **INTRODUCTION TO RADIATION ISSUES FOR INTERNATIONAL SPACE STATION EXTRAVEHICULAR ACTIVITIES**

M. R. Shavers, P. B. Saganti, J. Miller, F. A. Cucinotta  
Space Radiation Health Project  
NASA Johnson Space Center  
Houston, Texas

# **INTRODUCTION TO RADIATION ISSUES FOR INTERNATIONAL SPACE STATION EXTRAVEHICULAR ACTIVITIES**

The International Space Station (ISS) provides significant challenges for radiation protection of the crew due to a combination of circumstances including: the extended duration of missions for many crewmembers, the exceptionally dynamic nature of the radiation environment in ISS orbit, and the necessity for numerous planned extravehicular activities (EVA) for station construction and maintenance. Radiation protection requires accurate radiation dose measurements and precise risk modeling of the transmission of high fluxes of energetic electrons and protons through the relatively thin shielding provided by the space suits worn during EVA. Experiments and analyses have been performed due to the necessity to assure complete radiation safety for the EVA crew and thereby ensure mission success. The detailed characterization described of the material and topological properties of the ISS space suits can be used as a basis for design of space suits used in future exploration missions.

In radiation protection practices, risk from exposure to ionizing radiation is determined analytically by the level of exposure, the detrimental quality of the radiation field, the inherent radiosensitivity of the tissues or organs irradiated, and the age and gender of the person at the time of exposure. During low Earth orbit (LEO) EVA, the relatively high fluxes of low-energy electrons and protons lead to large variations in exposure of the skin, lens of the eye, and tissues in other shallow anatomical locations. The technical papers in this publication describe a number of ground-based experiments that precisely measure the thickness of the NASA extravehicular mobility unit (EMU) and Russian Zvezda Orlan-M suits using medical computerized tomography (CT) X-ray analysis, and particle accelerator experiments that measure the minimum kinetic energy required by electrons and photons to penetrate major components of the suits. These studies provide information necessary for improving the understanding of the current ISS space suits and provide insights into improved approaches for the design of future suits. This chapter begins with a summary of the dynamic ionizing radiation environment in LEO space and introduces the concepts and quantities used to quantify exposure to space radiation in LEO. The space suits used for EVA and the experimental partial human phantom are described. Subsequent chapters report results from measured charged particle fields before and after incident protons and secondary particles are transported through the space suits and into organs and tissues.

## **1.1 IONIZING RADIATION ENVIRONMENT AND EXPOSURES IN LOW EARTH ORBIT**

The most notable difference between most occupational radiation exposures that occur on Earth and those in space is that astronauts experience a persistent low background field of radiations of mixed biological effectiveness, including energetic electrons, the high-energy heavy-ion component of galactic cosmic rays (GCR), secondary neutrons, and densely ionizing low-energy secondary ions and energy-degraded primary ions. In general, the significant sources of radiation exposure in LEO are relatively well known, and measured crew doses aboard the Space Shuttle are usually characterized in advance of the missions to within  $\pm 25\%$  by computer simulations of the

transport of the GCR and trapped electron and proton environment and shielding models. Relative to exposures during intravehicular activities (IVA), exposures that occur during EVA have always been lower because of the shorter duration and deliberate timing of EVAs to minimize dose. Also, GCR exposures in LEO are not well attenuated by shielding and differences between IVA and EVA GCR doses are small. Trapped radiation exposures that occur during EVA are more difficult to predict and assess due to limitations in the accessibility of the radiation dosimetry and due to other circumstances that are apparent from the discussion, below.

Past Space Shuttle missions lasted no more than 18 days, whereas ISS crewmembers may be on orbit for 6 months or longer at the higher orbits preferred by mission planners to reduce atmospheric drag on spacecraft. ISS orbits at  $51.6^\circ$  with an altitude profile of 360-460 km (**Figure 1-1**). The dose rate experienced by inhabitants of ISS at the highest altitudes shown in **Figure 1-1** is approximately twice that at the lowest altitude. Albeit brief compared with the 11-year-long period of the solar activity cycle, the radiation environment experienced by a crew can change appreciably within a few minutes due to passage through the trapped particle belts or due to the dynamics associated with geomagnetospheric response to transient solar activity. Energetic GCR ions are present, are very penetrating, and dominate the cumulative exposure aboard ISS. However, in the radiation belts, high doses of protons or electrons occur behind minimal shielding.

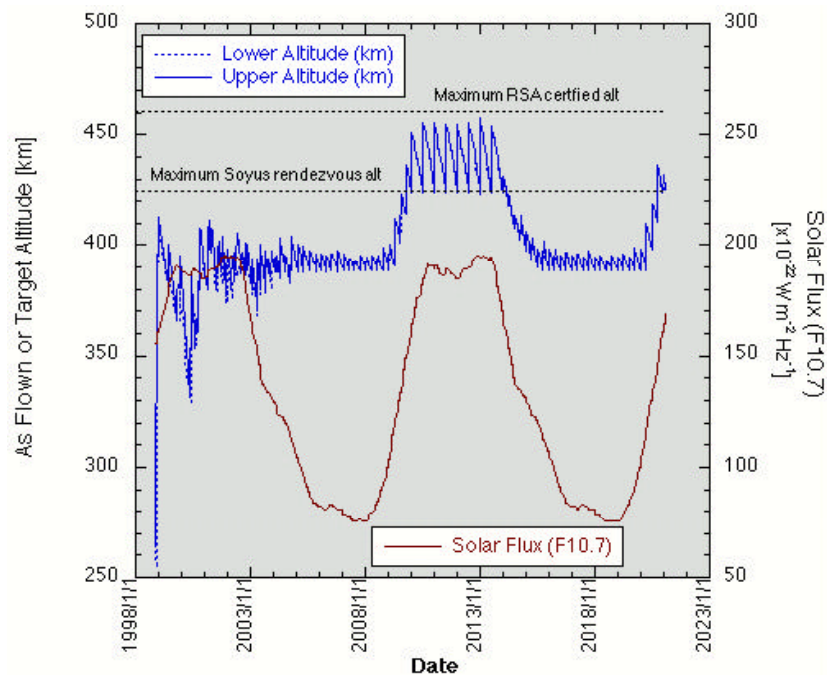


**Figure 1-1.** ISS altitude profile for the period 17 November 1998 through 5 May 2001. The Russian ISS segment hardware is limited to 460 km. The maximum docking altitude for the Soyuz vehicles is ~425 km.

Typical trapped proton energy spectra at ISS orbit during conditions of high and low solar activity vary in intensity by a factor of ~2, as shown in **Figure 1-2**. The intensity of the trapped proton flux is highest when solar radiation activity is lowest. The non-alignment of the Earth’s magnetic poles with the geophysical poles accounts for the well-known “anomalous” proton region above South America/Atlantic Ocean, through which several transits of trapped protons occur daily. In this region, the flux is highly anisotropic due to the azimuthal drift of the protons. The low-altitude atmosphere is denser, driving the east-west effect, and the protons are near their mirror points and

thus near 90° equatorial pitch angle. The directional difference in proton flux could be a factor of 2 to several times higher in the leading edge of the spacecraft compared to the trailing edge (Heckman and Nakano, 1965).

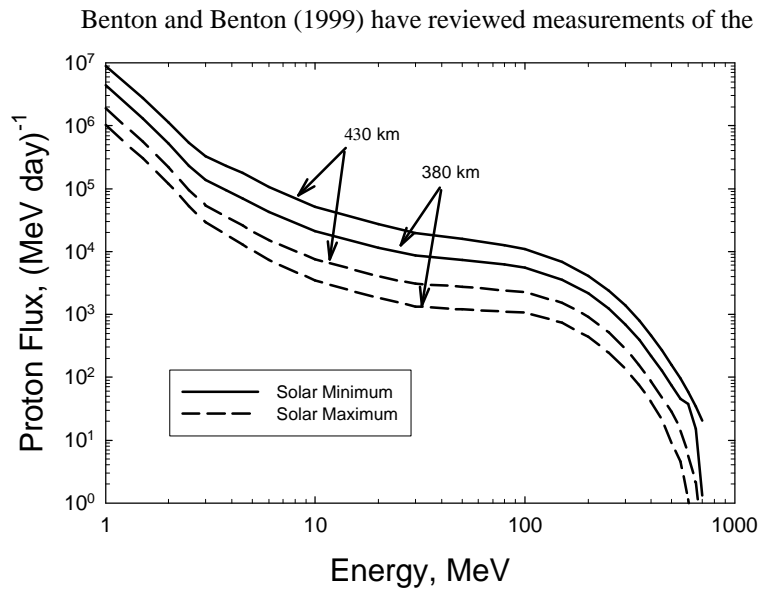


**Figure 1-2.** Representative trapped proton spectra for conditions typical of maximum and minimum solar activity on ISS.

include the radiation exposure accumulated during the entire mission. On a high-altitude mission, STS-61 (28.5° × 595 km), thermoluminescence radiation dosimeters (TLDs) were placed at various locations of the EVA crewmembers' bodies. The levels of uncertainties of the dosimeter measurements were too high to reveal an

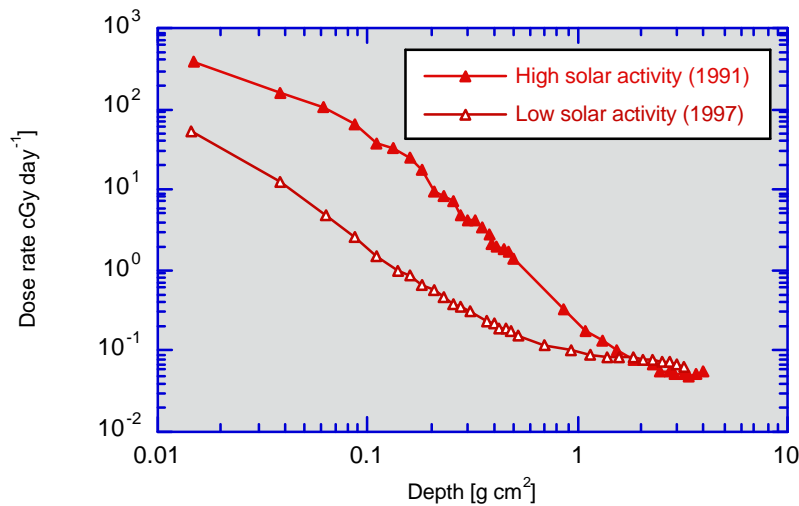


**Figure 1-3.** Dose rate measured by TLDs outside the *Mir* Space Station (51.65° inclination orbit × ~400 km altitude) during periods of low solar activity (1991) and high solar activity (1997).

Their data (**Figure 1-3**) indicate the absorbed dose falls off as much as 3 orders of magnitude over the first cm of penetration through the *Mir* space station. EVA dose measurements have been performed on all Space Shuttle and ISS missions. Golightly et al. (1995) compared measured doses for mission crewmembers who performed EVA and crewmembers who did not and found no statistically significant differences in absorbed dose between the paired groups. Unfortunately, those data were collected with dosimeters placed in a highly shielded location (inside the EMU and on the upper thorax under the right arm) and

include the radiation exposure accumulated during the entire mission. On a high-altitude mission, STS-61 (28.5° × 595 km), thermoluminescence radiation dosimeters (TLDs) were placed at various locations of the EVA crewmembers' bodies. The levels of uncertainties of the dosimeter measurements were too high to reveal an increased dose associated with EVAs beyond the background exposure recorded from the IVA segments of the mission. A single set of data exists that records doses received to an astronaut and a cosmonaut exclusively during EVA (Deme et al., 1999). During low solar activity (29 April, 1997), the Hungarian Pille TLDs were worn in a pocket on the outside of the Orlan-M space suits. Measured EVA absorbed dose rates were between 60 and 80  $\mu\text{Gy hr}^{-1}$ , approximately 3 to 4 times higher than the contemporaneous dose measured inside the station.

Spacecraft shielding and EVAs in low-inclination orbits have protected space inhabitants in LEO from substantial exposure to energetic electrons. With the Space Station at an orbital inclination of 51.6°, EVAs are now

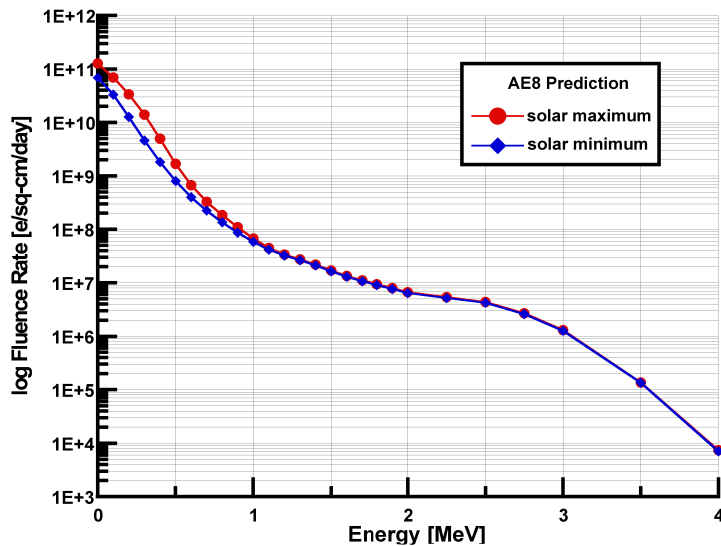


**Figure 1-4.** Typical trapped electron spectra for conditions of maximum and minimum solar activity. Note the increased flux during maximum solar activity. In contrast, the trapped proton flux is lower during maximum solar activity due to proton losses within the expanded atmosphere.

exposed on most orbits to “outer electron belts.” Energetic electrons will intercept ISS at high latitudes, about 20% of each orbit. A review of the CRESS satellite data indicates trapped electrons with kinetic energy as high as 30 MeV (Gussenhoven, 1996), although models generally consider only <5 MeV (inner zone) or <7 MeV (outer zone) electron populations. Typical trapped electron energy spectra at ISS orbit during conditions of high and low solar activity are shown in **Figure 1-4**.

While crewmembers inside spacecraft are well protected from the external electrons, the same is not true for those performing EVA. Unlike the more stable inner belt, the flux of trapped particles in the outer zone may change over 6 orders of magnitude in a matter of minutes (Barth 1996). High fluxes of electrons

penetrate the thin areas of the space suit and irradiate shallow tissues, such as the skin and lens of the eyes. The electron dose gradient near the surface of the body is extremely steep, decreasing by as much as three orders of magnitude within the first cm of depth, as indicated in **Figure 1-5**. For both electrons and protons, the protection an inhomogeneous space suit provides to tissues near body surfaces is difficult to determine analytically. The steep dose gradient, the inhomogeneous shielding provided by the space suit and surrounding tissues in the body, the simultaneous protracted and fractioned exposure to a changing field of mixed radiation quality, and, directionality of the ionizing field components all contribute to the problem.

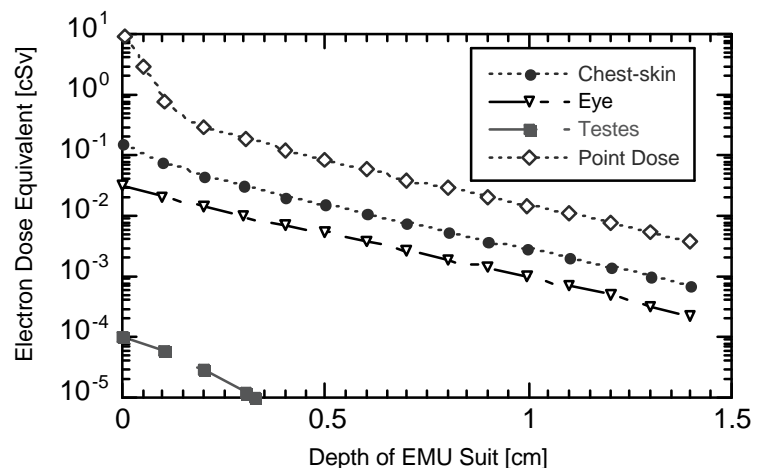


**Figure 1-5.** Trapped electron dose equivalent for a 6-hour-long EVA at ISS orbit estimated as a function of EMU suit thickness for an isotropic field in the worst-case orbit alignment during solar minimum activity conditions and calm geomagnetic storm conditions.

Occasional exposures take place on ISS during events associated with transient solar activity. Such events added significant radiation exposure to

crewmembers aboard *Mir*. Severe solar particle events (SPEs) associated with solar flares directed toward Earth and that last for a period of hours or days can increase the proton dose aboard ISS with rapid onset to levels that require crewmembers to seek refuge in well-shielded locations. An example is shown in **Figure 1-6**, a plot of the proton flux above various energy thresholds measured by GOES-8 satellite during a moderate event in July 2000.

For this event, the low-energy channel is especially relevant for EVA since the threshold for proton penetration through a space suit (~10 MeV) is much lower than for spacecraft (~30 MeV). The flux of particles

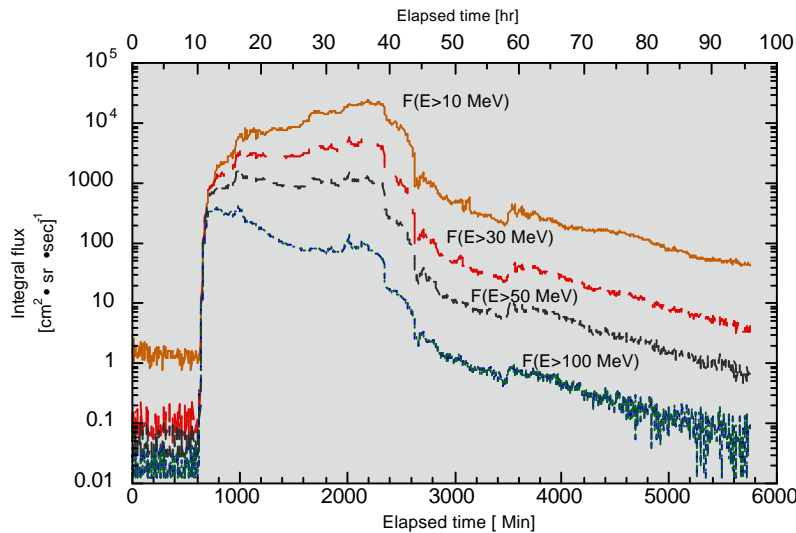


**Figure 1-6.** Integral proton flux spectra of the 14-17 July 2000 solar flare as measured in geosynchronous Earth orbit by the GOES-8 satellite.

below 30 MeV also continues to rise by a factor of 3 or more before peaking, while the integral flux above 30 MeV increases by about a factor of 2. High-energy protons can arrive at Earth within 10 to 90 minutes after observable manifestations appear in the solar corona at visible or X-ray wavelengths. Time-integrated energy spectra from major events observed in the past are shown in **Figure 1-7**.

Geomagnetic storms, a worldwide disturbance of the Earth's magnetic field that is distinct from regular diurnal variations, have some impact on low-altitude, low-

inclination missions. Energetic particle flux associated with the shock wave driven by a coronal mass ejection can increase suddenly by two orders of magnitude at ISS.

Such events can occur every month or even several times during a single month, and last for many days at a time. Geomagnetic disturbances (caused by coronal mass ejections of charged particles from the Sun targeted at Earth) and a severe SPE share a common cause and, occurring in coincidence, could provide a harmful dose to crewmembers. During geomagnetic storms, the protective magnetic field is compressed and higher fluxes of protons and electrons reach lower latitudes as the

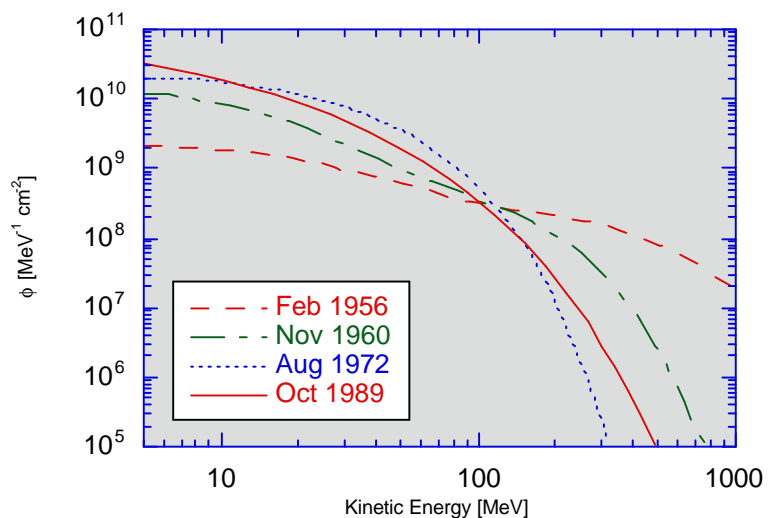


**Figure 1-7.** Proton energy spectra in free space for several major solar proton events.

polar-cap boundary expands. Charged particles penetrate closed field lines and can spiral along newly opened field lines to directly intercept as much as 40% of the ISS orbit. During the last two solar cycles, the probability of that occurring during a significant SPE was ~24% and was even higher during the most intense SPEs (Turner and Baker, 1998; NRC, 2000). Radiation doses to shallow (*e.g.*, skin, eye) and deep (*e.g.*, haematopoietic) tissues may significantly increase during such events, especially if commencement of an undetected storm coincides with EVA. EVA conditions aboard ISS are dangerous when the angular widths of the polar SPE zones are greater than 35° and directional proton flux is above 400 particles cm<sup>-2</sup>s<sup>-1</sup>steradian<sup>-1</sup> (NRC, 2000). The angular width of the widened SPE zone currently is estimated using  $K_p$  as a proxy, where  $K_p$  is a 3-hr average planetary geomagnetic storm index used by space physicists. The value of  $K_p$  is determined from ground-based magnetometers in many locations throughout North America. The index value of 1 to 9 indicates current strength and geomagnetic field compression. The window of opportunity for safe EVAs is much shorter during strong magnetic storms, as indicated by the analysis of the October 1989 SPE, shown in **Figure 1-8** as estimated using the model of Wilson et al. (1991). However, additional considerations for electron belt enhancements need to be considered during times of high solar activity. Because electrons are less penetrating than solar protons, it should be possible to design space suits to minimize any impacts from trapped electrons.

The total absorbed dose from EVA results from trapped protons and electrons, GCR, and perhaps some of the “anomalous” components of galactic cosmic ions (ACR), including low-energy alpha particles and heavy ions that are completely absorbed by spacecraft, but not by EVA space suits. When interacting in matter, each of these incident

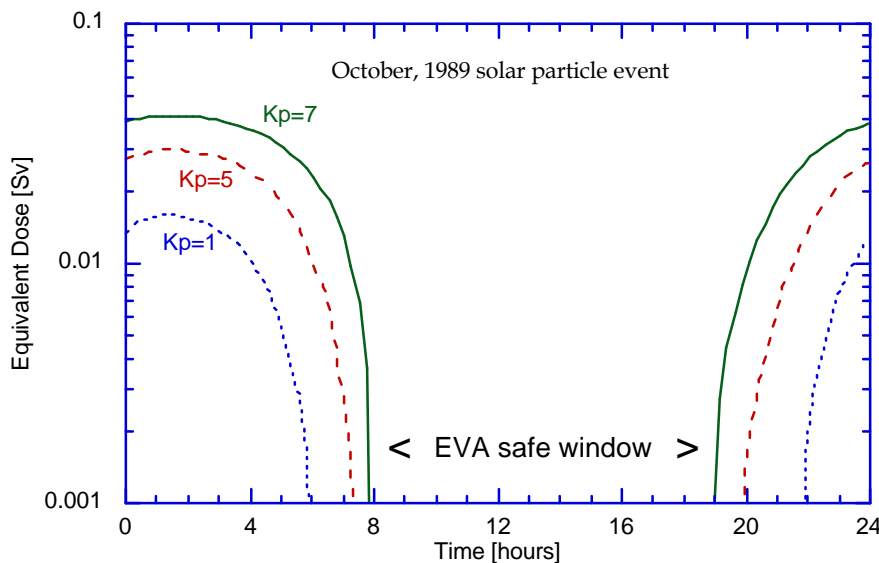


**Figure 1-8.** Time period when EVAs could have been safely performed on ISS during October 1989 solar particle event.

particles generates secondary radiation, including photons and secondary electrons, pions, neutrons, protons and other ions. The secondary particles can be either less or more penetrating than the incident particle, and may originate inside or outside the human body. The ACR component comprises largely singly charged photo-ionized ions of He, C, O, Ne, and Ar that have low energy and low penetrability through spacecraft. Being singly charged, they have high rigidity (thus able to penetrate

the magnetosphere to the ISS orbit) and some will penetrate a space suit. Although they are known to form trapped radiation belts, the ACR comprise less than 5% of the GCR flux of >10 MeV/A ions, and are not expected to pose a significant biological risk to astronauts (Badhwar, 2000).

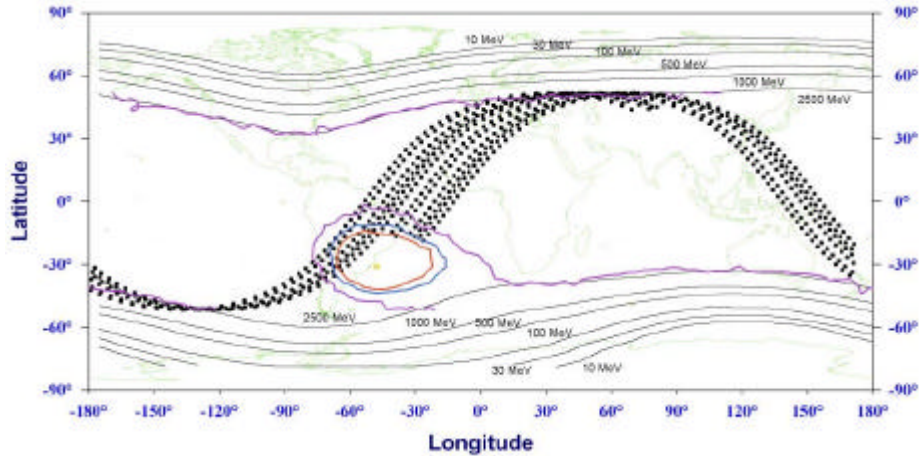


**Figure 1-9.** Start locations (each dot) for orbits that maintain low dose equivalent to the skin (<math><0.3\text{ mSv}</math>) for ISS EVAs of 6-hr duration. Low-energy thresholds for solar protons are shown as labeled contours.

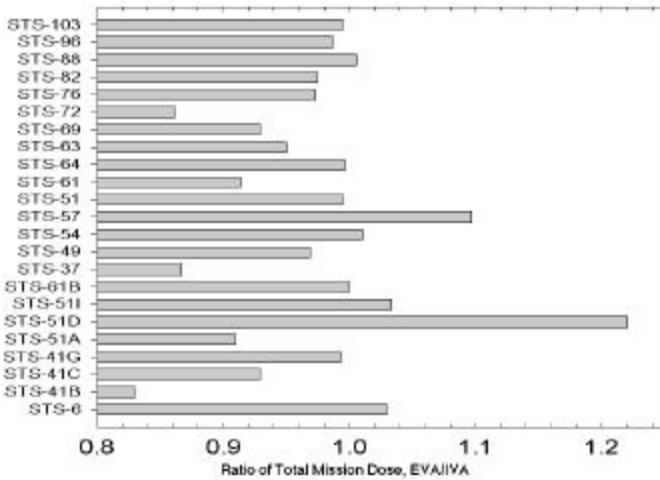


**Figure 1-10.** Absorbed dose ratio, EVA/IVA, for Space Shuttle astronauts. “IVA” refers to the average absorbed dose to crewmembers who remained inside the Space Shuttle during EVAs.

dosimeter outside ISS is recommended by a recent National Research Council report on radiation risks to ISS crews and is a high priority (NRC 2000).

The effectiveness of EVA timing to minimize radiation exposure is reflected in **Figure 1-10**, however limitations in EVA dosimetry need to be considered in such comparisons.

## 1.2 DOSIMETRIC QUANTITIES AND REGULATORY DOSE LIMITS FOR STOCHASTIC RADIATION EFFECTS

Stochastic quantities for external irradiations are expressed as equivalent dose,  $H_T$ , with units of Sv. The equivalent dose is derived by multiplying organ-absorbed dose from the radiation incident on the body,  $D_T$  [ $\text{J kg}^{-1}$ , or Gy], by the appropriate radiation weighting factor,  $w_R$ . Radiation weighting factors, given (ICRP 1991), are not

dependent on the rate of linear energy transfer (LET). In current practice, when spectral information is available for a radiation field, LET-dependent radiation quality factors,  $Q(L)$ , are used in place of  $w_R$ , where

$$Q(L[\text{keV} / \text{mm}]) = \begin{cases} 1 & L < 10 \\ 0.32L - 2.2 & 10 \leq L < 100 \\ 3000 / L & L \geq 100 \end{cases}, \quad (1)$$

as shown graphically in **Figure 1-11**. Neither  $w_R$  nor  $Q(L)$  is organ-dependent; that is, the *relative* harm of the various types of radiation is considered to be the same for stochastic or deterministic biological effects (discussed below) in all organs and tissues.

The measure of detriment due to stochastic effects from non-uniform exposures is effective dose,  $E$ . Effective dose is calculated as the sum of tissue weighted  $H_T$  for all irradiated tissues or organs,

$$E = \sum_T w_T H_T, \quad (2)$$

where the tissue weighting factor  $w_T$  represents the proportionate detriment (stochastic) of tissue  $T$  when the whole body is uniformly irradiated. Effective dose incorporates stochastic risks such as nonfatal cancer, genetic risks, and relative length of life lost into the determination of  $w_T$ . Conceptually, effective dose to a tissue carries the same risk associated with a uniform whole-body exposure of the same equivalent dose. For activities in space, the National Council on Radiation Protection and Measurements (NCRP) (2000) recommends that equivalent dose should be approximated as organ dose equivalents (ICRU, 1993):

$$H_T \approx \int dV_T \int Q(L) D(L) dL, \quad (3)$$

where  $V_T$  is a volume element in tissue  $T$  and the  $Q(L)$  relationship is used in place of  $w_R$ . Eqn (3) allows a more precise calculation of equivalent dose and is considered to provide an acceptable approximation for calculating effective dose,  $E$ . Large uncertainties are present in the above model of cancer risk from space radiation (Cucinotta et al., 2001a).

Career limits that are related to age at time of exposure and sex were recommended by the NCRP (2000) in Report No. 132 for space activities are given in **Table 1-1**. Although the career limits are age- and gender-specific, the ICRP (1991) determined that other factors (*e.g.*, the model used to translate risks from one population of people to another, as well as special characteristics of national populations) could be more important determinants of the relative contributions of cancer in various organs to the total cancer risk.

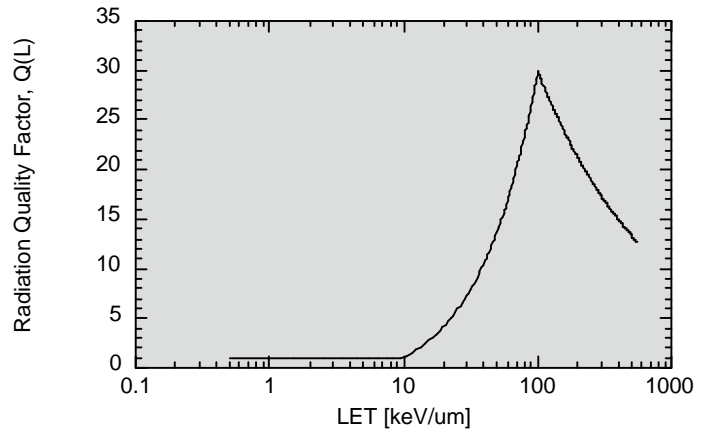


**Figure 1-11.** The radiation quality factor for ionizing radiation used by NASA for all space activities. Defined in Publication 60 of the ICRP (ICRP 1991).

**Table 1-1.** Effective Dose Limits for a Ten-Year Career Based on 3% Excess Lifetime Risk of Fatal Cancer<sup>a</sup>

Age at Exposure	Female <i>E</i> (Sv)	Male <i>E</i> (Sv)
25	0.4	0.7
35	0.6	1.0
45	0.9	1.5
55	1.7	3.0

<sup>a</sup>Additional components of radiation detriment associated are discussed in text

### 1.2.1 Deterministic Effects

The non-stochastic or *deterministic* biological effects are those that occur with severity (not probability) that is proportionate to dose and have a presumed dose threshold for clinically significant presentation. Proposed exposure limits on non-stochastic effects are on the same order of magnitude as career doses for acute, short-term exposures. These quantities are currently under review, and are measured in terms of gray equivalents. The dosimetric quantity *gray equivalent* is calculated by multiplying the organ or tissue dose by a factor that describes the relative biological effectiveness (RBE) of a particular type of radiation. The recently proposed radiation dose limits for bone marrow, eye, and skin exposures during activities in space, shown in **Table 1-2**, are based on response thresholds for fractionated exposures. Stochastic limits on career exposure of the bone marrow are sufficiently low to prevent deterministic effects. The deterministic exposure limits values prevent deleterious responses from exposures over a single one-year period, but these limits should not be approached year after year. Recommended RBE values for deterministic effects in these tissues are independent of tissue type, and are presented in **Table 1-3**. The RBE of electrons is taken as 1.

**Table 1-2.** Recommended Organ Dose Limits for Deterministic Effects in People of All Ages (NCRP 2000)

	Bone Marrow (Gy-Eq)	Eye (Gy-Eq)	Skin (Gy-Eq)
Career	–	4.0	6.0
1 y	0.50	2.0	3.0
30 d	0.25	1.0	1.5

The radiation dose limits for space activities allow exposures that are higher than regulatory limits for terrestrial workers in the United States. For example, the skin limit for ground-based workers is 0.5 Sv per year, averaged over the highest exposed 1 cm<sup>2</sup> area of skin, and 0.15 Sv for the lenses of the eyes (CFR 2000). The recently proposed dose limits are based on a very limited amount of data that is relevant to exposures in space (NCRP 2000). Only EVAs that occur during extreme conditions have the potential to exceed the thresholds for these effects. The time-course of exposure is an important determinant of statistical observations of biological harm. In general, protracted and fractionated exposures to low doses of low-LET radiations (electrons and high-energy protons) are less deleterious than an acute exposure at the same dose level. This temporal effect is recognized and was included in the derivation of deterministic and stochastic dose limits for space activities.

**Table 1-3.** RBE Values for Determining Deterministic Dose (Gray Equivalents) From Absorbed Dose (NCRP 2000)

Radiation type	Recommended RBE	Range
Neutrons, 1 to 5 MeV	6.0	(4–8)
Neutrons, 5 to 50 MeV	3.5	(2–5)
Heavy ions (He, C, Ne, Ar)	2.5	(1–4)
Protons > 2 MeV	1.5	–

## 1.2.2 Environmental Monitoring, Crew Dosimetry and Alerts

Constellations of satellites (*e.g.*, SOHO, ACE, GOES, POES) monitor diagnostic solar surface conditions, the strength of the geomagnetic field, and proton and electron fluxes in geosynchronous Earth orbit and in other locations in high-Earth orbits. A system of radiation safety alert levels and response procedures are in place so that a flight director can initiate evasive actions, such as postponing EVAs and locating crew to shelter in well-shielded locations.

Radiation detectors aboard ISS include instruments that monitor the interior ionizing radiation environment and telemeter that information at regular intervals. Solid-state detectors measure the dose levels, and information about the directionality and quality of the radiation environment is collected by charged particle spectrometers. The crew passive dosimeter each crewmember wears measures that crewmember’s radiation dose of record. Detectors and computer models are used to characterize the ambient radiation environment inside ISS and to report the dose equivalent to dose-limiting body organs. Each astronaut on EVA wears the same dosimeter during the entire mission and the results are read after return to Earth.

## 1.2.3 Radiation Dose Reduction

As previously mentioned, substantial dose reduction can be achieved by carefully scheduling EVAs to avoid trapped proton belts and the electron “horns” at high latitudes. Real-time space weather monitoring and implementation of existing flight rules greatly reduce the likelihood of dangerous radiation exposure from scheduled EVAs during SPE and/or storm conditions. Further dose reduction can be attained aboard ISS with specially designed radiation shields and the advantageous placement of onboard supplies or equipment that can contribute ancillary shielding. The directionality of penetrating trapped protons impinging on ISS can be exploited for dose reduction by shielding. The JSC Space Radiation Health Project Office’s recent assessment of shielding materials with simulated space radiation environments at ground-based accelerators initiated the placement of polyethylene shielding around an ISS crew sleeping area. Future shielding enhancements, if deployed around crew quarters and pre- and post-sleep activity areas, will substantially reduce radiation doses.

For EVA, due to the low penetrability of low-energy electrons and protons, radiation dose to tissues near the body surface is determined by the minimum thickness of a space suit, and even thin amounts of additional shielding could significantly attenuate these exposures. The most effective dose-reduction strategies for EVA are scheduling EVA during benign environmental conditions, monitoring and responding to environmental conditions in real-time, and limiting total time outside.

Near-real-time evaluations of the radiation dose levels are available to crews. Pille TLD personal dosimeters can be deployed during a transient event or during EVA activities with the Orlan-M space suits outside ISS and then analyzed on orbit immediately to monitor exposures as they accumulate. New technologies are being developed to model the ambient radiation environment at any location inside or surrounding ISS and to provide the capability for a crewmember to visualize the regions of higher and lower exposure as the background radiation environment changes and spacecraft components and shielding materials are repositioned. Future crews in LEO will play an important role in monitoring and reducing their own exposure level during transient events.

### 1.2.4 The EMU Space Suit

The complexity of the EMU is apparent from **Figures 1-12 to 1-15**. On Earth, an EMU weighs approximately 127.3 kg (280 lb). Modular components include 11 space suit assembly items and 7 major life support system components that sustain life in a hostile environment that includes a near vacuum with rapid and severe ambient temperature gradients, intense ultraviolet radiation exposure, and the possibility of a micrometeoroid or orbital debris strike.

Anderson et al., in Chapter 9, provide the material composition and thickness of major subsystems of the EMU. Most individual layers of fabric material are homogenous, if not uniformly thick, and some have moving parts. Requirements for flexibility limit the mass and internal pressure (4.3 psid or 29.6 kPa) of the suit, yet substantial quantities of aluminum and heavier metal (poor space radiation shields) are present (Anon, 1999; 2000).

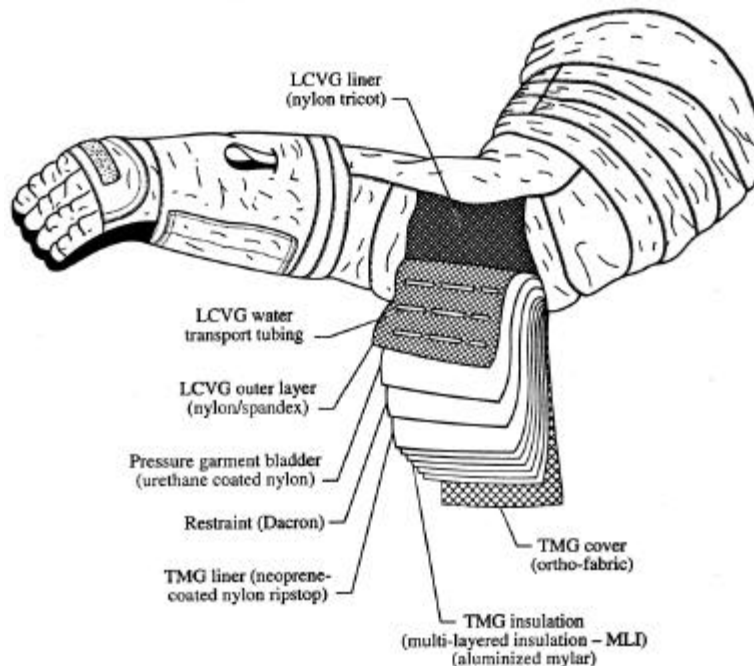


**Figure 1-12.** Fabric material layout used for the arms and legs of the EMU. The inner liquid-cooling and ventilation garment, also shown, is a non-homogenous fabric covering the torso and limbs that supports small water-transport tubes for regulating body temperature. (Reproduced with permission from Hamilton Sundstrand.)

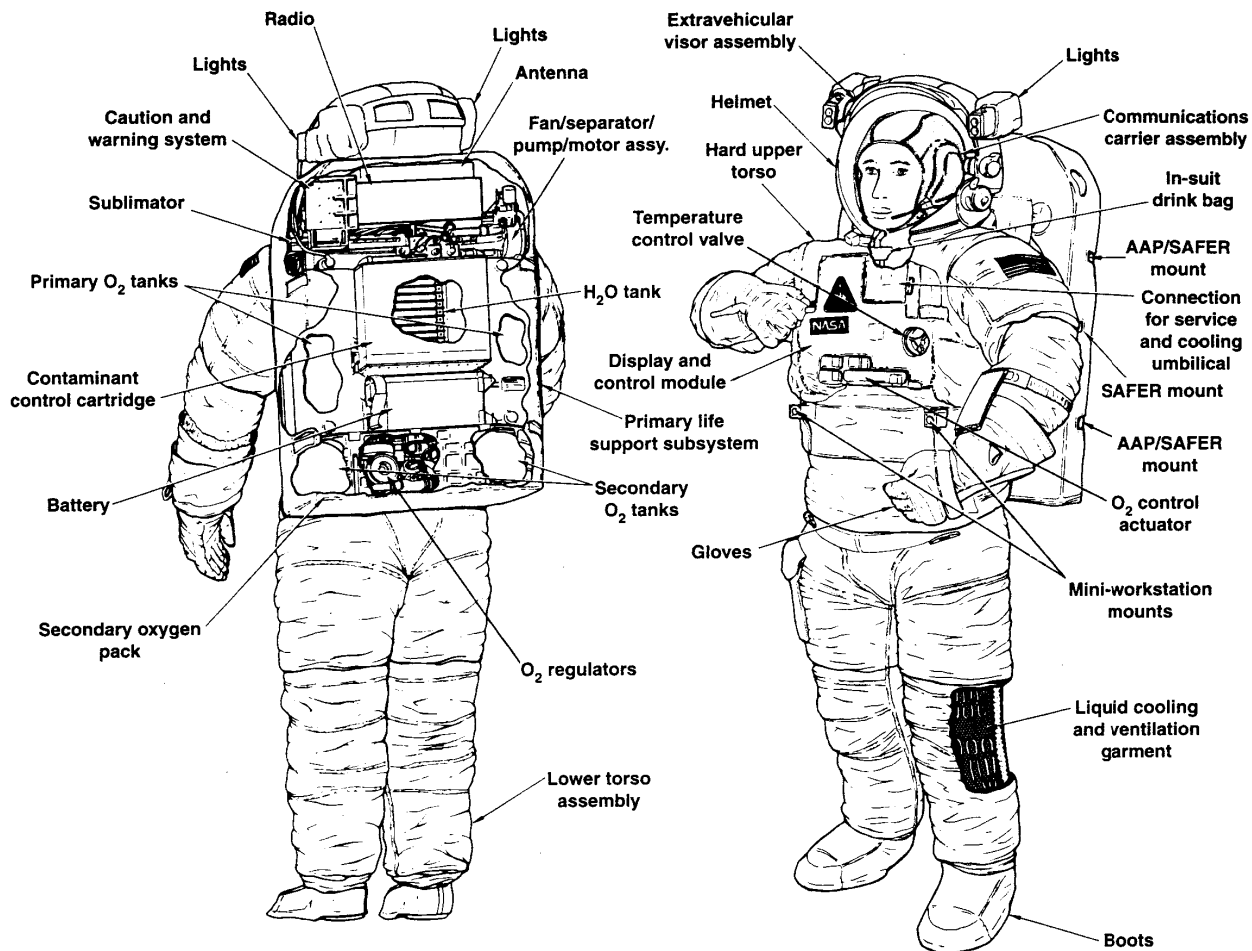
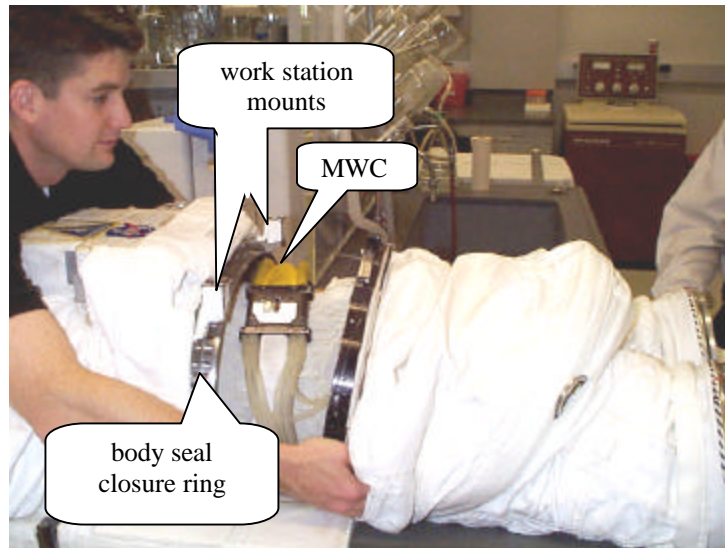


Figure 1-13. Major components of the EMU space suit assembly and life support system. (Reproduced with permission from Hamilton Sundstrand.)

### 1.2.5 EMU Hard Upper Torso (HUT)

The HUT provides the structural mounting interface for the primary life support subsystem backpack (PLSS), the display and controls module mounted on the chest, the helmet, arms, lower torso assembly and the EMU electrical harness. The rigid fiberglass hard torso shell is the main component of the fabric-covered HUT. Many metallic components are present, as well, and their presence influences the radiation field transported through the suit and complicates experimental analysis and modeling. The helmet attaches to the HUT shell with the metallic neck ring and the lower torso assembly is mounted to the HUT shell with the metallic body seal closure. Additional metal hardware provides for fluid passages from the PLSS to the DCM and to the liquid cooling and ventilation garment (LCVG). Of particular significance is the metallic LCVG side of the multiple water connector (MWC), which mates cooling water line and body gas vent tubes. The metal body seal closure mounts provide the HUT with external interfaces to the mini-work station and the modified mini-work station outside the chest of the suit. The MWC and other metallic components are visible in **Figure 1-14**.



**Figure 1-14.** Mating of the EMU hard upper torso (left) with the lower torso assembly (right). The metallic LCVG coupling of the multiple water connector (MWC) “buckle” is visible between the torso sections, and the metal workstation mounts are visible on the metallic Body Seal Closure ring of the HUT.

### 1.2.6 EMU Helmet

The EMU helmet and extravehicular visor assembly (EVVA) (**Figure 1-15**) protects the lenses of the eyes from photochemical damage caused by ambient ultraviolet photons (320 to 400 nm UV-A), and protects the cornea from shorter wavelength UV-B and UV-C. The retina and cornea are also protected from potential damage from intense visible, infrared, radio frequency, and microwave exposures. The EVVA is important for reducing cataract risk (Cucinotta et al., 2001b).

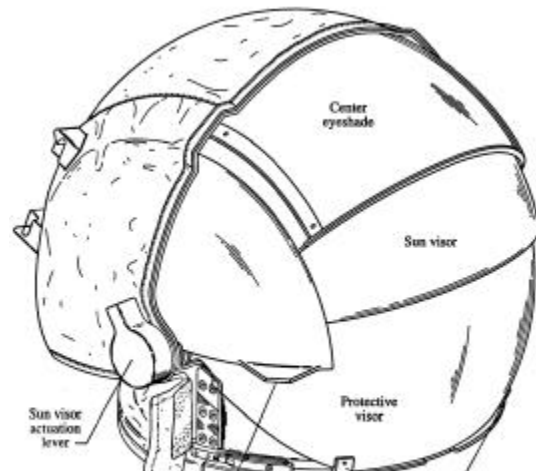


**Figure 1-15.** Illustration of the extravehicular visor assembly of the EMU showing protective visors and eyeshades. (Reproduced with permission from Hamilton Sundstrand.)

### 1.2.7 EMU Personal Life Support System

Due to its contents’ bulk, the PLSS (backpack) provides significant directional radiation shielding and scattering. It contains the primary water tanks, the silver-zinc EMU electricity battery, fans, pumps, a radio, and other equipment, including a metal oxide CO<sub>2</sub> sorbent canister that alone weighs 14.5 kg. To minimize corrosion, the ventilation subsystem and other components in the PLSS are composed of stainless steel (Fe, Cr, Ni) rather than aluminum.

### 1.2.8 Liquid Cooling Ventilation Garment

The LCVG covers the torso, arms, and legs to provide temperature regulation of the body. On Earth, it weighs ~3.5 kg dry, and holds 0.23 to 0.34 kg of water. The ethyl vinyl acetate cooling inlet/outlet tubes attached to

the MWC are approximately 8 mm, and the transport tubes sewn inside the garment are approximately 4 mm outer diameter, and 84 m in length. The areal density of the Spandex/Nylon fabric is 0.034 g cm<sup>2</sup>, and the transport tubes (see **Figure 1-12**) filled with water are 0.078 g cm<sup>2</sup> maximum. The nonuniformity of the LCVG shielding “shadow” at the skin is a topic of ongoing research (Anderson et al., 2001).

### 1.2.9 Orlan-M Space Suit

The Orlan-M (**Figures 1-16 and 1-17**) is one of many space suits designed and manufactured by Zvezda (“Star”) for the Russian space program since the mid-1960s. The “M” model was first tested and used to perform EVA aboard the *Mir* Space Station on 29 April, 1997; it was the 154th EVA, the 78th Russian/Soviet, and the 77<sup>th</sup> EVA for the United States (Portree and Treviño 1997). Within a year, the suit had been worn during a dozen EVAs.

The space suit body consists of an aluminum alloy torso and helmet of ~1.2 mm thickness and the arm and legs are

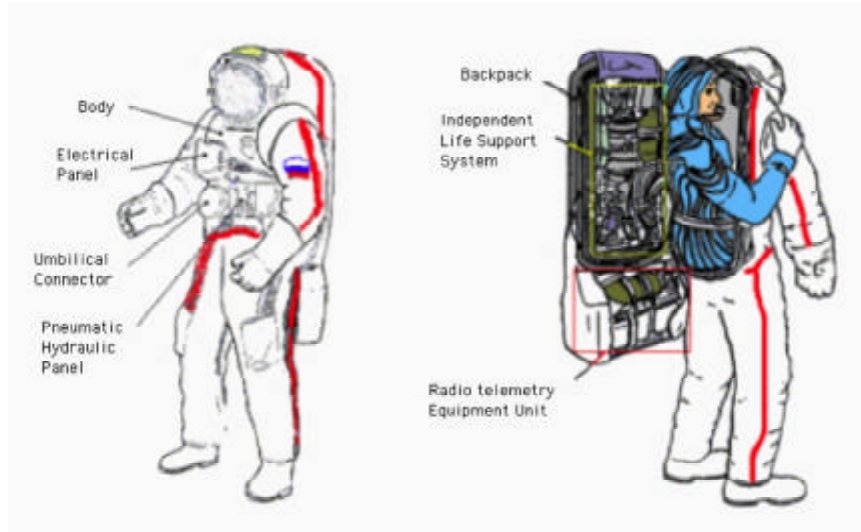


**Figure 1-16.** Illustration of the Orlan-M space suit (Anon., 1997).



**Figure 1-17.** Orlan-M EVA space suit used in experiments at Loma Linda University Medical Center.

soft shell. Unlike the EMU, both the helmet and life support backpack of the Orlan-M are integrated components of the suit. The wearer enters the suit from the rear through a hatch between the life-support backpack and the rigid body. The fabric layup is described in **Table 1-4**. The Orlan-M accommodates persons with chest circumference of 94-110 cm and standing height of 165-182 cm. The suit mass is no greater than 100 kg, and requires an external support structure for handling on Earth. (Unfortunately, the structure prevented some experimental procedures that were performed on the EMU.) The operating pressure is 40.7 kPascal (5.9 psi). Noticeable upgrades to the space suit from the earlier Orlan-DMA model include a second visor on top of the helmet and a functionally improved glove design. The underwear-coveralls are made of a cotton-knitted fabric. The cooling garment consists of ~60 m of water-filled tubes. The cooling garment completely filled with cooling liquid, together with the coverall, weighs less than 3 kg. However, these components were not available for testing.

**Table 1-4.** Orlan-M Suit Fabric Layup

Layer	Material	Comments
Protective garment	Phenilon	Nomex type
Radio-fabric	Capron & silver	Mesh type
PETF film	Polyethylene	Porous type
PETF film	Polyethylene	Reinforced porous
PETF film	Polyethylene	Porous type
PETF film	Polyethylene	Reinforced porous
PETF film	Polyethylene	Thick layer
Radio-fabric	Capron & silver	Mesh type
Lining	Capron	Nylon type
Restraint layer	LAVSAN (Polyethylene), Dacron	Thick cloth type
Primary bladder	Natural latex type	Rubber stretch type
Redundant bladder	Rubber-coated Capron	Metallic rubber
Lining	Capron	Nylon type
Liquid cooling garment	Spandex & Capron tricot	Porous stretch fabric
Inner garment		

### 1.2.10 Human Phantom

The Phantom Laboratory of Salem, New York, manufactured the anthropomorphic phantom used to simulate the astronaut body for the Loma Linda University (LLU) radiobiology program. The incomplete phantom, shown in **Figure 1-18**, is sized to the 50th percentile U.S. male anthropometry (Alderson 1962). The phantom is constructed with a human skeleton cast inside material with the mass density ( $1.002 \text{ g cm}^3$ ) and radiological equivalence (electron density) of soft tissue. Molded lungs fit the contours of human lungs in a median respiratory state within the natural human rib cage and are composed of low-density ( $0.305 \text{ g cm}^3$ ) polymeric foam. Phantoms are sliced into 2.5-cm-thick axial cross-sectional slices. In the space suit experiments performed at LLU reported herein, TLDs, solid-state silicon detectors, CR-39 plastic nuclear track detectors (PNTDs), and cell samples are placed outside the left eye and deep in the head and upper and lower abdomen.



**Figure 1-18.** Photograph of partial human phantom of tissue-equivalent material. Detectors and biological samples were irradiated at various positions inside the phantom. Large removable plugs are visible in the abdomen and right thigh.

## 1.3 REFERENCES

- Alderson, S. W., Lanzl, L. H., Rollins, M., Spira, J., 1962. An instrumented phantom system for analog computation of treatment plans. *The American J. of Roentgenology, Radium Therapy, and Nuclear Medicine*, Vol. 87(1), p185.
- Anderson, B. M.; Nealy, J. E.; Qualls, G. D., Staritz, P. J.; Wilson, J. W.; Kim, M.-H. Y., Cucinotta, F. A., Atwell, W., DeAngelis, G., Ware, J., Persans, A. E., 2001. Shuttle space suit (radiation) model development. Soc. Auto. Eng., Inc. SAE Paper 01ICES-2363.
- Anon., 1997. Orlan-M Extra-vehicular Activity Spacesuit Training Manual. Yu. A. Gagarin Cosmonaut Training Center. Publication 01.09.05.05(0)T0002, (English translation: SS1653/TTI/DG/GL/08/19/98).
- Anon, 1999. EMU system training workbook. NASA-Johnson Space Center publication JSC-19450, 2-49-2-55.
- Anon, 2000. NASA EMU LSS/SSA data book, Rev. F. Hamilton Standard, 451.
- Badhwar, G., 2000. Free space radiation environment. In: Fujitake, K.; Majima, H.; Ando, K.; Yasuda, H.; Suzuki, M. Risk evaluation of cosmic-ray exposure in long-term manned space mission. Proceedings of the International workshop on Responses to heavy particle radiation, Chiba, July 9-10, 1998. Kodansha Scientific, Ltd., Tokyo.
- Barth, J., 1996. Modeling space radiation environments. IEEE Short Course: Applying computer simulation tools to radiation effects problems. IEEE Publications Services, Piscataway, NJ.
- Benton, E. R., Benton, E. V., 1999. A survey of radiation measurements made aboard Russian spacecraft in low-earth orbit, NASA Contractor's Report-1999-209256, National Technical Information Service, Springfield, VA 22161.
- CFR, 2000. Code of Federal Regulations. Part 20—Standards for protection against radiation. Washington, DC: Office of the Federal Registrar, National Archives and Records Administration.
- Cucinotta, F. A., Schimmerling, W., Wilson, J. W., Peterson, L. E., Badhwar, G. D., Saganti, P., and Dicello, J. F. 2001a. Space radiation cancer risks and uncertainties for Mars missions. *Radiat. Res.* **156**: 682-688.
- Cucinotta, F. A., Manuel, F., Jones, J., Izsard, G., Murray, J., Djojonegoro, B., and Wear, M. 2001b. Space radiation and cataracts in astronauts. *Radiat. Res.* **156**: 460-466.
- Deme, S., Apathy, I., Hejja, I., Lang, E., Feher, I., 1999. Extra dose due to extravehicular activity during the NASA-4 mission measured by an on-board TLD system. *Rad. Prot. Dos.* 85(1-4):121-124.
- Gussenhoven, M. S. Mullen, E. G., Brautigam, D. H., 1996. Improved understanding of the Earth's radiation belts from the CRRES satellite. *IEEE Trans. on Nucl. Science* 43(2): 353-368.
- Golightly, M. J., Weyland, M. D.; Hardy, A. C., 1995. Radiation exposure to astronauts during EVAs. Soc. Auto. Eng. Warrendale, PA, SAE technical paper series 951593.
- Heckman, H. H. and Nakano G. H., 1965. Direct observation of mirroring protons in the South Atlantic anomaly. *Space Res.* 5:329.
- ICRP, 1991. International Commission on Radiological Protection. 1990 Recommendations of the International Commission on Radiological Protection, ICRP Publication 60. Oxford: Pergamon Press; Ann. ICRP 21(1-3).

- ICRU, 1993. International Commission on Radiation Units and Measurements. Quantities and units in radiation protection dosimetry, ICRU Report 51. Bethesda, MD: ICRU.
- NCRP, 1993. National Council on Radiation Protection and Measurements. Limitation of exposure to ionizing radiation. NCRP Report No. 116. Bethesda, MD: NCRP.
- NCRP, 2000. National Council on Radiation Protection and Measurements. Radiation protection guidance for activities in low-earth orbit. NCRP Report No. 132. Bethesda, MD: NCRP.
- NRC, 2000. National Research Council. Radiation and the International Space Station: Recommendations to reduce risk. National Academy Press: Washington, D.C.
- Portree, D. S. F., and Treviño, R. C. Walking to Olympus: An EVA Chronology. NASA History Office, Code Z, NASA Headquarters, Washington, DC 20546, Monographs in Aerospace History Series #7, Oct. 1997.
- Reitz, G., Bucker, H., Facius, R., Beaujean, R., Enge, W., 1990. Dosimetry results of Cosmos 1887. Nucl. Tracks & Rad. Meas. 17(2)99–104.
- Rudd, M. E., 1997. HZE interactions in biological materials. In: Wilson, J. W., Miller, J., Konradi, A., Cucinotta, F. A. (Eds.) Shielding strategies for human space exploration. NASA Conference Publication 3360, National Technical Information Service, Springfield, VA 22161.
- Turner, R. E., Baker, J. E. 1998. Solar particle events and International Space Station. Acta Astronautica 42, 107–114.
- Wilson, J. W., Townsend, L. W., Schimmerling, W., Khandelwal, G. S., Kahn, F., Nealy, J. E., Cucinotta, F. A., Simonsen, L. C., Shinn, J. L., Norbury, J. W. Transport Methods and Interactions for Space Radiations. NASA Reference Publication, RP-1257, 1991.

**CHAPTER 2**

**PROTON AND ELECTRON THRESHOLD**

**ENERGY MEASUREMENTS**

**FOR EXTRAVEHICULAR ACTIVITY**

**SPACE SUITS**

M. F. Moyers, G. D. Nelson  
Dept. of Radiation Medicine  
Loma Linda University  
Loma Linda, California

P. B. Saganti  
Space Radiation Health Project  
NASA Johnson Space Center  
Houston, Texas

# PROTON AND ELECTRON THRESHOLD ENERGY MEASUREMENTS FOR EXTRAVEHICULAR ACTIVITY SPACE SUITS

## ABSTRACT

Construction of ISS will require more than 1000 hours of EVA. Outside of ISS during EVA, astronauts and cosmonauts are likely to be exposed to a large fluence of electrons and protons. Development of radiation protection guidelines requires the determination of the minimum energy of electrons and protons that penetrate the suits at various locations. Measurements of the water-equivalent thickness of both U.S. and Russian EVA suits were obtained by performing CT scans. Specific regions of interest of the suits were further evaluated using a differential range shift technique. This technique involved measuring thickness ionization curves for 6-MeV electron and 155-MeV proton beams with ionization chambers using a constant source-to-detector distance. The thicknesses were obtained by stacking polystyrene slabs immediately upstream of the detector. The thicknesses of the 50% ionizations relative to the maximum ionizations were determined. The detectors were then placed within the suit and the stack thickness adjusted until the 50% ionization was reestablished. The difference in thickness between the 50% thicknesses was then used with standard range-energy tables to determine the threshold energy for penetration. This report provides a detailed description of the experimental arrangement and results.

## 2.1 INTRODUCTION

Construction of ISS will require more than 1000 hours of EVA. Outside of ISS during EVA, astronauts and cosmonauts are likely to be exposed to a significant fluence of electrons and protons. **Figures 2-1 and 2-2** contain typical energy spectra of electrons and protons anticipated at the orbit of ISS. When the current-generation EVA suits were designed, the architects had not envisioned the multitude of extensive-duration EVAs required for ISS construction, and radiation shielding was not of paramount importance. Radiation protection guidelines are therefore required before construction of ISS may commence in earnest. These guidelines will be based on calculational models that require validation. Achieving direct measurements of the minimum energy of electrons and protons that

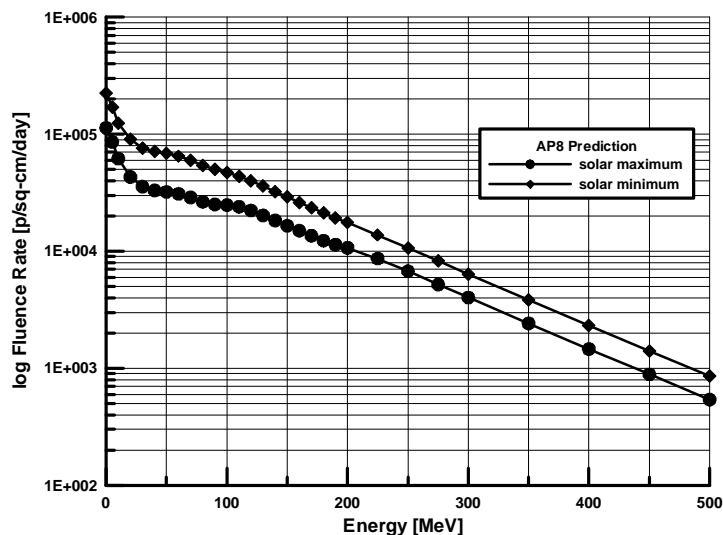


**Figure 2-1.** Typical electron spectra at the orbit of ISS predicted using the AE8 simulation. The circles represent the fluence rate at solar maximum while the diamonds represent the fluence rate at solar minimum. (Data courtesy of Ed Semones, NASA Johnson Space Center.)

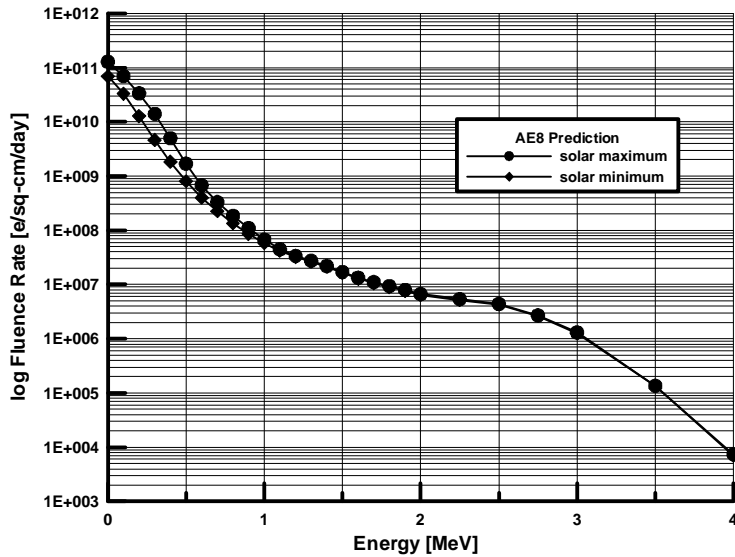


**Figure 2-2.** Typical proton spectra at ISS orbit predicted using the AP8 simulation. The circles represent the fluence rate at solar maximum while the diamonds represent the fluence rate at solar minimum. (Data courtesy of Ed Semones, NASA Johnson Space Center.)

can penetrate the suits at various locations is one of the validation steps. Additionally, these measurements may influence the designs of future space suits.

CT scans provided maps of the water equivalent thickness of both U.S. and Russian EVA suits. The minimum energy of electrons and protons that can penetrate these thicknesses were interpolated from standard range-energy tables. Specific regions of interest of the suits were evaluated directly with electron and proton beams, using a differential range shift technique.

## 2.2 METHODS AND MATERIALS

### 2.2.1 Suit Configurations

We studied both U.S. and Russian EVA suits. The U.S. suit is referred to as the EMU, the Russian suit as the Orlan-M. The EMU consists of many interchangeable parts that are combined to fit individual astronauts. **Tables 2-1 and 2-2** give the published composition and thicknesses of various components of the EMU helmet and extremities, respectively.

The helmet and EVVA, seen in **Figure 2-3**, consists of several layers, including an inner polycarbonate pressure bubble, a protective visor, a gold-plated sun visor, and an eyeshade.

The majority of the suit covering the extremities, seen in **Figure 2-4**, consists of twelve layers, including a urethane-coated

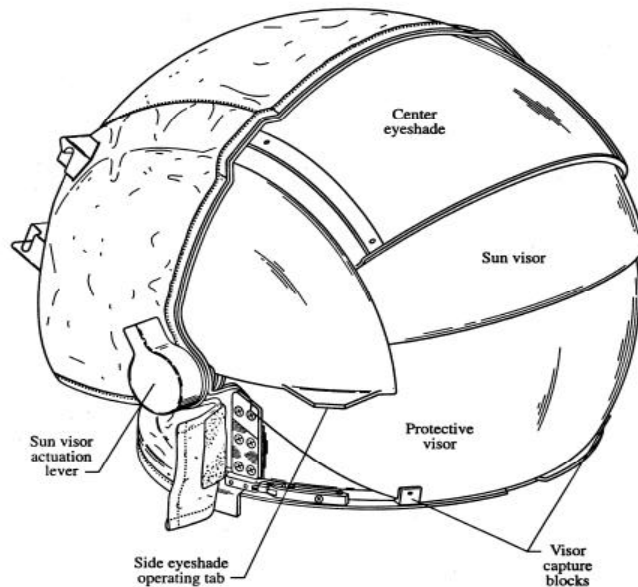


**Figure 2-3.** U.S. helmet and extravehicular visor assembly showing placement of visors and sunshades.

nylon to hold pressure, aluminum for thermal insulation, Kevlar for micrometeoroid protection, and water-filled tubing for cooling. The suit material covering the upper torso is the same as over the extremities except that a hard fiberglass shell having a thickness between 0.075" to 0.125" (0.10" avg.) is substituted for the pressure bladder and pressure-restraint layers.

The Orlan-M is a single-piece unit that comes in only one size but which, with cinch straps, can accommodate a limited range of different-size cosmonauts. The chest and abdomen of the Orlan contains a hard aluminum shell with entry provided via a door at the rear. The EMU provided for this experiment consisted of a mixture of training and flight-qualified parts. Sham backpacks were attached to each suit. Both suits were loaded with cooling liquid throughout the measurements, but were not pressurized.

**Table 2-1.** Configuration for Helmet/Extravehicular Visor Assembly of Extravehicular Mobility Unit  
*Data taken from Kosmo (1989). Materials listed from inside to outside.*

Item	Material	Thickness [in]	Density Thickness [g/cm <sup>2</sup> ]
protective bubble	polycarbonate	0.06	0.182
ventilation pad	not available	not available	not available
protective visor	polycarbonate	0.06	0.182
sun visor	polysulfone with gold coating	0.06	0.190
sun shade	polycarbonate	0.06	0.182
back shell	polycarbonate	0.125	0.381
back thermal meteoroid garment	Teflon liner	0.01	0.028
	5 plies non-woven Dacron	0.03	0.011
	5 plies aluminized Mylar	0.02	0.004
	Teflon/Nomex/Kevlar	0.02	0.049

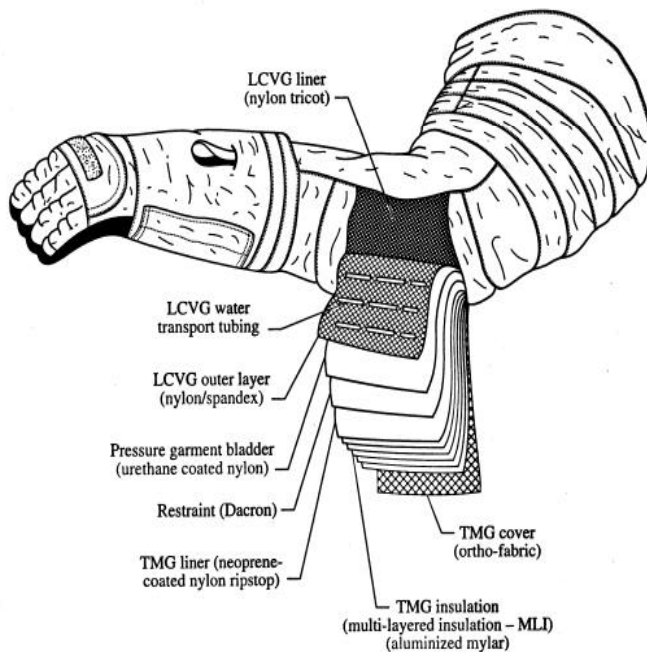


**Figure 2-4.** U.S. EMU soft suit components showing multilayer fabrication.

Cross section of material layup used for fabric for the arms and legs of the spacesuit.

**Table 2-2.** Configuration for Arms and Lower Torso of Extravehicular Mobility Unit  
(Data taken from Kosmo (1989)). *Materials listed from inside to outside.*

Item	Material	Thickness [in]	Density Thickness [g/cm <sup>2</sup> ]
undergarment	Capilare	not available	not available
liquid coolant vent garment	Nylon chiffon Nylon Spandex 1/16" ethylvinyl acetate tubing for H <sub>2</sub> O	0.02	0.154
pressure bladder layer	Urethane-coated Nylon ripstop	0.011	0.014
pressure restraint layer	Dacron polyester	0.011	0.021
thermal meteoroid garment	Neoprene coated Nylon ripstop 5 plies aluminized Mylar Teflon/Nomex/Kevlar	0.009 0.025 0.02	0.028 0.014 0.049

## 2.2.2 Phantom

An anthropomorphic phantom was installed inside each suit during CT scanning and most threshold



**Figure 2-5.** Anthropomorphic phantom used to simulate astronauts and cosmonauts inside EVA suits.

measurements in order to maintain the shape of the suit similar to its condition during an EVA. The Phantom Laboratory (Salem, New York) specially made the phantom for LLU with several cavities and inserts to accommodate various detectors and biological samples. As seen in **Figure 2-5**, the phantom spanned the top of the head to just above the knees and was cut transversely to provide 12 slices. The phantom also had two arms, removable at the shoulders, which were inflexible and stopped at the wrists. Most of the phantom consisted of a tissue-equivalent plastic with a composition by weight, as stated by the manufacturer, of 9.18% hydrogen, 67.78% carbon, 2.50% nitrogen, 20.31% oxygen, and 0.22% antimony.



**Figure 2-6.** Anthropomorphic phantom in Orlan-M space suit as seen from back through entry door. Phantom is wearing the liquid-cooled ventilation garment.

LLU measurements of rectangular blocks of this material manufactured at the same time as the phantom



**Figure 2-7.** Feet first entry of EMU suit with sham backpack into the CT scanner. The arms are raised over the head to facilitate chest entry into the scanner aperture. Additional scans were performed to accommodate the helmet and gloves.

we performed all scans using the highest available photon energy, 140 kVp. Other scanning parameters were: a tube current of 140 mA, slice thickness of 3 mm, and 10-mm distance between slice centers. We transferred the image data to a radiotherapy treatment planning system (TPS) to determine the water equivalent thickness at multiple locations.

After entry into the TPS, image segmentation was performed by manual contouring. We simulated energy deposition distributions with 155-MeV proton beams from a variety of directions, using a TPS tool to interrogate the integral water equivalent path length across sample locations, and then using standard range-energy tables (ICRU, 1984; Janni, 1982) to determine the threshold energy for penetration.

## 2.2.4 Electron and Proton Measurements

The source of electrons for determining the threshold energy was a Siemens KD-2 electron accelerator (Siemens Medical Systems, Concord, California). The source of protons was the Loma Linda University Proton Treatment Facility (LLUPTF) (Moyers, 1999). We first measured the thickness ionization curves for nominal energy 6-MeV electron and 155-MeV proton beams without the suits with a 0.07-cm<sup>3</sup> thimble ionization chamber (Capintec, Nashville, Tennessee) using a constant source-to-detector distance and a stack of polystyrene slabs. The slope of the ionization versus thickness curve at the distal edge was then calculated. Next, we determined the thickness of the polystyrene stack, or range shifter, in terms of water equivalence (Moyers, 1992), needed to obtain an ionization nearly 50% of the maximum ionization. This thickness is called the "reference thickness" or  $T_R$ . We

yielded a density of 1.002 g/cm<sup>3</sup>. Molded within the phantom were a human skeleton, various air cavities, and low-density polymeric foam to simulate lung tissue. The measured density of the lung material was 0.305 g/cm<sup>3</sup>. **Figure 2-6** shows the phantom inside the Orlan suit with the liquid-cooled ventilation garment installed.

## 2.2.3 CT-Based Measurements

We performed CT scans with a General Electric 9800 scanner. **Figure 2-7** shows the EMU being scanned feet first. **Figure 2-8** shows the Orlan being scanned headfirst. The image reconstruction area was 480 mm in diameter with a transit bore of 690 mm. The reconstructed images consisted of 512 by 512 pixels per slice. Due to the presence of metal within the suits,



**Figure 2-8.** Headfirst entry of Orlan-M suit with sham backpack into the CT scanner. A second scan was performed headfirst to accommodate the lower torso.

then placed the detectors within the suit at the same distance from the source and adjusted the stack thickness until the 50% ionization was reestablished to within 1 mm of thickness. The water equivalent thickness is called the "sample thickness" or  $T_S$ . The thickness of the suit material was calculated using Equation 1.

$$\text{Suit Thickness} = (T_R - T_S) + \frac{(RI_R - RI_S)}{\text{Gradient}} \quad (\text{Eq. 1})$$

where:  $RI_R \equiv$  relative ionization at reference thickness

$RI_S \equiv$  relative ionization at sample thickness

and Gradient  $\equiv$  slope on the distal edge of the ionization versus thickness curve.

The water equivalent thickness of the suit was thus the difference in relative ionizations divided by the gradient added to the difference in block thicknesses. This thickness was then used with standard range-energy tables (ICRU, 1984; Janni, 1982) to determine the threshold energy for penetration. Standard range-energy tables (ICRU, 1984; Janni, 1982) were used to determine the threshold energy for penetration from the measured suit thickness. In order for these measurements to be performed at any suit and gantry position, special extension cones were constructed to position the polystyrene slabs within the beam. These cones allowed for the stacking of polystyrene slabs within 20 mm of the suit surface.



**Figure 2-9.** Orlan-M suit in position with Siemens KD-2 linear electron accelerator for determining the threshold energy of electrons needed to penetrate the helmet. The beam is entering from the lower left through the cone containing the polystyrene rangeshifter plates.



**Figure 2-10.** EMU suit in position in LLUPTF gantry #1 for determining the threshold energy of protons needed to penetrate the neck region where the hard upper torso connects to the helmet assembly. The beam enters from the upper right through the cone containing the polystyrene rangeshifter plates. The cable entering the large hole at the bottom of the torso is attached to the ionization chamber. On the lower left is an electronic digital imaging device used for aligning patients during proton therapy.

**Figure 2-9** shows the setup with the KD-2 electron accelerator for determining the threshold energy of electrons for penetrating the Orlan helmet. **Figure 2-10** shows the setup with gantry #1 of the LLUPTF for determining the threshold energy of protons penetrating the neck region of the EMU.

Alignment of the ionization chamber with the beam was usually performed visually using the treatment unit's internal light field or alignment lasers. Certain locations within the suit occasionally prevented the use of these methods. In these cases, radiographs were made to localize the chamber.

**Figure 2-11** shows a radiograph of the thimble ionization chamber inside a finger of a glove.

## 2.3 RESULTS AND DISCUSSION

The CT planning resulted in 36 measurements. **Table 2-3** is a listing of the locations where useful water equivalent thickness measurements could be determined from the CT scans. The "swatch" refers to a flat sample of soft laminated suit material used to cover the extremities and abdomen. Glove thickness measurements were made from the dorsal direction only, as the astronaut will normally be carrying a tool or gripping a handhold that offers protection to the ventral side.

**Figure 2-12** is a slice through the abdomen of the phantom where the HUT connects to the lower half of the suit using a metal ring.

**Figure 2-13** is an example plan showing a 155-MeV, 60-mm modulated proton beam entering the helmet from the superior/anterior direction. **Figure 2-14** shows a plan of a 155 MeV proton beam entering the U.S. suit from the posterior direction. The suit piece being measured in this case was the HUT that is formed out of fiberglass. **Table 2-3** also gives the results of the CT water equivalent measurements and the calculated electron and proton threshold energies.

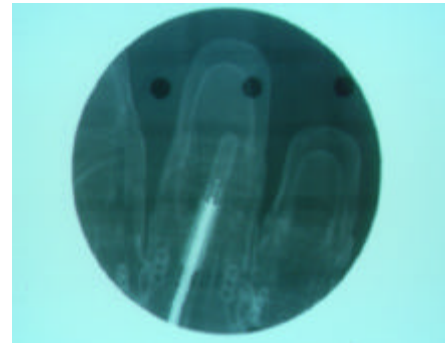


**Figure 2-11.** Radiographic image of the small thimble ionization chamber within a finger of a glove. The image shows that the detecting volume is at the middle phalanx of the ring finger.



**Figure 2-12.** XCT image of the abdominal region of the phantom within the EMU. The cone-shaped lines from the middle to anterior aspect of the phantom are formed by a removable cylinder inserted into a hole in the phantom. The bright dots around the circumference are ball bearings at the joint of the hard upper torso and the lower suit allowing rotation of the suit just above the hips. The bright object above the phantom is the metal connecting buckle for the liquid carrying tubes flowing from the back pack to the liquid-cooling ventilation garment.

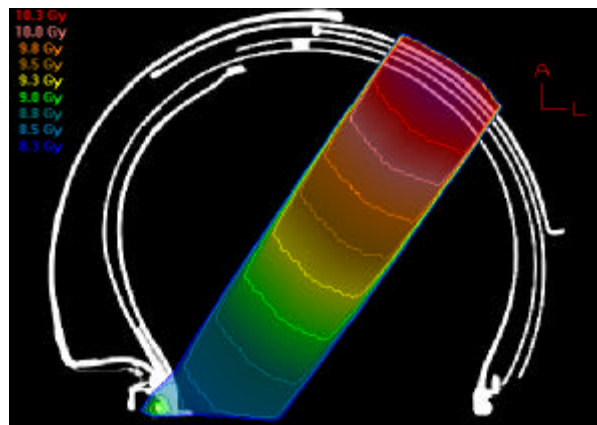


**Figure 2-13.** A sagittal XCT scan and plan of the U.S. helmet and extravehicular visor assembly. The astronaut's face would be to the right of the image and the back of the head to the left. A simulated 155-MeV proton beam enters from the anterior/superior direction passing through the eye shade, sun visor, protective visor, and bubble. At 155 MeV, very little protection is afforded by the thin plastic layers.

**Table 2-3.** Electron and Proton Threshold Energies Derived From CT Water-Equivalent Measurements

Sample Location Code	Location Description	Thickness [mm H <sub>2</sub> O]	Electron Energy [MeV]	Proton Energy [MeV]
C1.	EMU swatch	1.8 min.	0.51	12.3
C2.	Orlan swatch	2.4 min.	0.62	14.4
C3.	EMU helmet, anterior / superior entrance			
a.	sun shade	3.0	0.74	16.3
b.	sun visor	2.0	0.55	13.0
c.	protective visor	1.3	0.40	10.2
d.	bubble	1.7	0.48	11.9
C4.	EMU helmet, posterior entrance			
a.	back shell	3.6	0.86	18.1
b.	bubble	1.9	0.53	12.6
c.	ventilation pad	4.5	1.02	20.5
C5.	EMU glove, dorsal entrance	2.2	0.59	13.7
C6.	Orlan glove, dorsal entrance	1.1	0.36	9.3
C7.	EMU HUT, left posterior entrance	3.3	0.80	17.2
C8.	EMU HUT, right posterior entrance	4.4	1.01	20.2
C9.	Orlan helmet, right lateral entrance			
a.	outer	2.8	0.70	15.7
b.	middle	2.7	0.68	15.4
c.	inner	4.0	0.93	19.1
C10.	Orlan helmet, left lateral entrance			
a.	outer	2.4	0.63	14.4
b.	middle	2.8	0.70	15.7
c.	inner	4.3	0.99	20.0
C11.	EMU helmet, posterior entrance			
a.	back shell	5.0	1.12	21.7
b.	sun shade	2.5	0.65	14.7
c.	sun visor	2.4	0.63	14.4
d.	bubble	3.5	0.84	17.8
e.	ventilation pad	4.0	0.93	19.1
C12.	EMU helmet, right lateral entrance, bubble	2.0	0.55	13.0
C13.	EMU helmet, posterior entrance			
a.	back shell	3.6	0.86	18.1
b.	bubble	3.6	0.86	18.1
c.	ventilation pad	4.3	0.99	20.0
C14.	EMU, posterior hip entrance	2.1	0.57	13.3

Two issues need to be discussed with respect to the CT planning. The first concerns the large amount of steel in the suits and associated equipment. For the photon energies used by the CT scanner, steel completely absorbs some photons via the photoelectric effect and scatters other photons at large angles via Compton scattering. Both processes result in the production of artifacts during image reconstruction, increasing the uncertainty of the thickness measurements. The second issue is the presence of the sham backpacks. The initial experiment design did not include these. As seen in **Figures 2-12 and 2-14**, their presence forced some suit components to extend beyond the reconstruction circle. Some components also intruded into the space reserved for calibrating the CT detectors, resulting in additional artifacts and uncertainties.

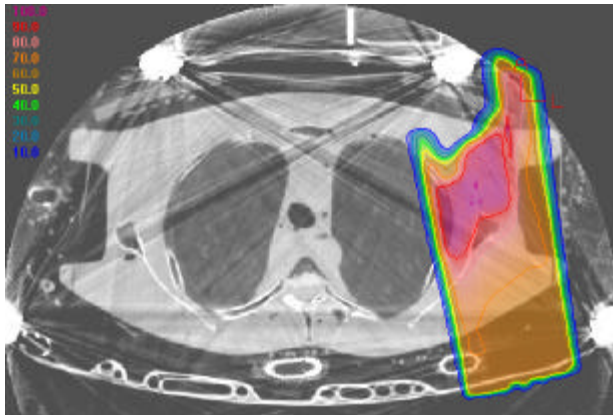


**Figure 2-14.** An axial XCT scan and plan of the U.S. hard upper torso through the phantom's chest. The lungs, ribcage, and spinal vertebrae may be seen. The arms were not attached to the phantom for this scan. Artifacts from the metal components of the suit are easily seen. A simulated 155-MeV proton beam enters the phantom's back shoulder passing through the hard upper torso.

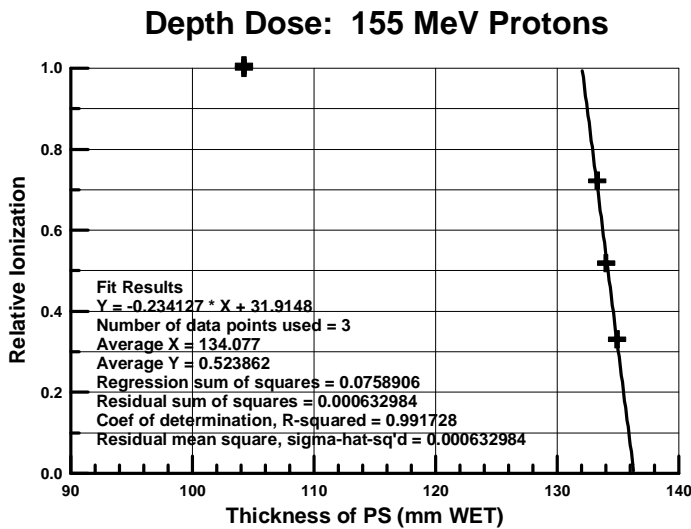


**Figure 2-16.** Ionization versus range shifter thickness for the 155-MeV proton beam. The thickness is given in terms of water equivalent thickness. Plotted crosses represent the measured ionization. The solid line is a fit through the 3 points on the distal edge. Results of the linear fitting are also given.

Figures 2-15 and 2-16 show, respectively, the electron and proton range ionization curves for the electron and proton beams using the range shifter blocks and a constant source-to-detector distance. The solid

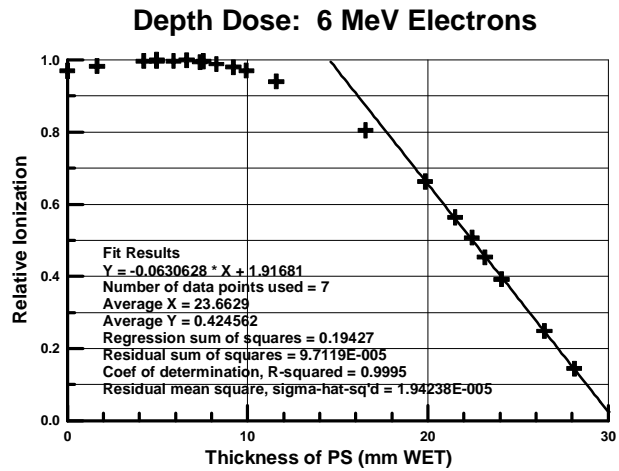


**Figure 2-15.** Ionization versus range shifter thickness for the 6 MeV electron beam. The thickness is given in terms of water equivalent thickness. Plotted crosses represent the measured ionization. The solid line is a fit through the 7 points on the distal edge. Results of the linear fitting are also given.

lines are linear fits along the distal edges. The ionization gradient at the distal edge is 6.3% per mm for the electron beam and 23.4% per mm for the proton beam.

There were 33 thickness measurements at 20 locations with the electron beam (Table 2-4). The derived energies are given in Table 2-5. Sample locations listed as "a" and "b" represent different reference or sample depths for the measurement but the same suit location.

**Table 2-4.** Coding for Electron Measurement Locations

Code	Description
E1.	U.S. glove, right hand, ring finger, middle phalanx, dorsal entrance
E2.	U.S. glove, right hand, ring finger, proximal phalanx, dorsal entrance
E3.	U.S. glove, right hand, index finger, middle phalanx, dorsal entrance
E4.	Russian glove, right hand, ring finger, middle phalanx, dorsal entrance
E5.	Russian glove, right hand, ring finger, proximal phalanx, dorsal entrance
E6.	Russian glove, right hand, index finger, middle phalanx, dorsal entrance
E7.	U.S. helmet, bubble+protective visor, anterior entrance
E8.	U.S. helmet, bubble+ventilation pad+retracted sun visor+retracted sun shade, posterior entrance
E9.	U.S. helmet, bubble+ventilation pad (sun visor and sun shade forward), posterior entrance
E10.	U.S. helmet/upper torso ring, left anterior entrance
E11.	U.S. upper left arm
E12.	U.S. HUT, right lateral entrance
E13.	U.S. swatch
E14.	Russian swatch
E15.	Russian helmet, bubble, anterior entrance
E16.	Russian helmet, bubble+ sun visor, anterior entrance
E17.	Russian hard torso (chest), anterior entrance
E18.	Russian left elbow patch, dorsal entrance
E19.	U.S. boot, middle phalanx, inferior entrance
E20.	U.S. boot, middle phalanx, superior entrance

Although the U.S. and Russian gloves appear very thin, they are at the limit of this measurement technique for electrons. The thin finger covering was deemed necessary during the glove design for dexterity so that the astronauts could grab handholds placed on the outside of the station and manipulate various tools and station components. When incident upon flat surfaces, the resolving power of the electron beam is about 0.4 mm or 0.08 MeV.

When measuring surfaces having curves and folds, thickness averaging occurs as a result of range straggling and the uncertainty increases. Another source of uncertainty is due to an unknown source-to-detector distance when the detector is installed within the suit. This effect should be less than 4% however, which would translate to a maximum error in thickness of 0.7 mm or 0.14 MeV.

There were 33 thickness measurements at 19 locations with the proton beam (**Table2-6**). The derived energies are given in **Table 2-7**. The glove measurements appear thicker in the proton beam than the electron and provide a closer match to the CT results. The resolving power of the proton beam is about 0.1 mm when incident upon flat surfaces. Because the protons are heavier than electrons, they do not scatter as much, resulting in less thickness averaging due to range straggling. One source of error, although small, is that the water equivalence of the blocks was measured at energies higher than found near the distal edge where the suit was placed. This should result in at most a 2% error in the thickness.

**Table 2-5. Electron Threshold Measurements**  
*The sample thickness is reported in terms of water equivalent thickness.*

Sample Location	Ref Depth [mm]	Sample Depth [mm]	R-S Depth [mm]	Ref Depth Dose	Sample Depth Dose	R-S Depth Dose	Grad Reduc [mm]	Sample Thickness [mm]	Electron Energy [MeV]
E1a	22.99	22.99	+0.00	0.5076	0.4705	+0.0371	+0.59	0.59	0.23
E1b	22.99	22.09	+0.90	0.5076	0.5490	-0.0414	-0.66	0.24	0.13
E2	22.99	22.09	+0.90	0.5076	0.4989	+0.0087	+0.14	1.04	0.34
E3a	22.99	22.09	+0.90	0.5076	0.4939	+0.0137	+0.22	1.12	0.36
E3b	22.99	21.18	+1.81	0.5076	0.5702	-0.0626	-0.99	0.82	0.29
E4a	22.99	23.85	-0.86	0.5308	0.4767	+0.0541	+0.86	0.00	N/A
E4b	22.99	22.09	+0.90	0.5308	0.6433	-0.1125	-1.79	-0.89	N/A
E5a	22.99	23.85	-0.86	0.5308	0.4325	+0.0983	+1.56	0.70	0.26
E5b	22.99	22.99	+0.00	0.5308	0.5079	+0.0229	+0.36	0.36	0.17
E6a	22.99	23.85	-0.86	0.5308	0.4694	0.0614	+0.97	0.11	0.09
E6b	22.99	22.99	+0.00	0.5308	0.5461	-0.0153	-0.24	-0.24	N/A
E7a	21.18	18.82	+2.36	0.4930	0.4548	+0.0382	+0.61	2.97	0.73
E7b	21.18	17.91	+3.27	0.4930	0.5057	-0.0127	-0.20	3.07	0.76
E8	21.18	8.65	+12.53	0.4930	0.4882	+0.0048	+0.08	12.61	2.53
E9	21.18	12.22	+8.96	0.4930	0.5216	-0.0286	-0.45	8.51	1.76
E10	21.18	0.0	+21.18	0.4930	0.2050	+0.2880	+4.73	25.75	5.05
E11a	21.18	15.25	+5.93	0.4930	0.4489	+0.0441	+0.70	6.63	1.42
E11b	21.18	14.34	+6.84	0.4930	0.5347	-0.0417	-0.66	6.18	1.33
E12a	21.18	18.82	+2.36	0.4930	0.4816	+0.0114	+0.18	2.54	0.65
E12b	21.18	17.91	+3.27	0.4930	0.5432	-0.0502	-0.80	2.47	0.64
E13a	22.99	22.99	+0.00	0.5083	0.4453	+0.0630	+1.00	1.00	0.34
E13b	22.99	22.09	+0.90	0.5083	0.5105	-0.0022	-0.03	0.87	0.31
E14a	22.99	22.99	+0.00	0.5083	0.4009	+0.1074	+1.70	1.70	0.49
E14b	22.99	21.18	+1.81	0.5083	0.5358	-0.0275	-0.44	1.37	0.42
E15	22.99	19.72	+3.27	0.5083	0.5092	-0.0009	-0.01	3.26	0.79
E16	22.99	16.15	+6.84	0.5083	0.5017	+0.0066	+0.11	6.95	1.48
E17	22.99	4.47	+18.52	0.5083	0.5017	+0.0066	+0.10	18.62	3.67
E18a	22.99	15.25	+7.74	0.5083	0.4952	+0.0131	+0.21	7.95	1.66
E18b	22.99	14.34	+8.65	0.5083	0.5294	-0.0211	-0.33	8.32	1.73
E19a	22.99	5.38	+17.61	0.5083	0.4915	+0.0168	+0.27	17.88	3.52
E19b	22.99	4.47	+18.52	0.5083	0.5580	-0.0497	-0.79	17.73	3.49
E20a	22.99	20.28	+2.71	0.5083	0.4937	+0.0146	+0.23	2.94	0.73
E20b	22.99	19.72	+3.27	0.5083	0.5296	-0.0213	-0.33	2.94	0.73

Energy: 6 MeV

Electron Depth Dose Gradient at 50% = 0.063/mm

**Table 2-6.** Coding for Proton Measurement Locations

Code	Description
P1.	U.S. swatch
P2.	Russian swatch
P3.	U.S. helmet, bubble+protective visor (sun visor and sun shade retracted), anterior entrance
P4.	U.S. helmet, bubble+protective visor+sun visor (sun shade retracted), anterior entrance
P5.	U.S. helmet, bubble+ventilation pad+retracted sun visor+retracted sun shade, posterior entrance
P6.	U.S. glove, right hand, ring finger, middle phalanx, dorsal entrance
P7.	U.S. glove, right hand, ring finger, proximal phalanx, dorsal entrance
P8.	U.S. glove, right hand, index finger, middle phalanx, dorsal entrance
P9.	Russian glove, right hand, ring finger, distal phalanx, dorsal entrance
P10.	Russian glove, right hand, ring finger, middle phalanx, dorsal entrance
P11.	U.S. boot, middle phalanx, superior entrance
P12.	U.S. boot, middle phalanx, inferior entrance
P13.	U.S. helmet/upper torso ring, left anterior entrance
P14.	U.S. HUT, right lateral entrance
P15.	U.S. arm
P16.	Russian helmet, bubble, anterior entrance
P17.	Russian helmet, bubble+ sun visor, anterior entrance
P18.	Russian left elbow patch, dorsal entrance
P19.	Russian hard torso (chest), anterior entrance

Another possible advantage of the proton measurement technique compared to that using the electron beam is that the proton snout containing the range shifter blocks could be retracted away from the suit to better guarantee a constant source-to-detector distance. This may reduce the uncertainty due to detector positioning. The last column of **Table 2-7** is the threshold energy for electrons calculated using the sample thicknesses that were determined using the proton beams.

## 2.4 SUMMARY

The thickness of U.S. and Russian EVA suits were determined at various locations using a CT scanner, electron beam, and proton beam. From those measurements, the threshold energies for penetration by electron and proton beams were calculated. The results were provided to NASA so that they may perform validation of transport code calculations and risk estimations. The better resolving power, reduced scatter, and variable distance snout led to the conclusion that the proton thickness measurements should be used to calculate the electron threshold energies as well as the proton threshold energies. If the CT measurements were to be repeated to obtain a full map of the suit, a high-energy, large-bore scanner should be used to reduce the artifacts and cover all components. Lastly, one should consider adding a thin layer of material to the dorsal side of the gloves; this might result in a substantial reduction of dose to the fingers from low-energy electrons.

**Table 2-7. Proton Threshold Measurements**  
*The sample thickness is reported in terms of water equivalent thickness.*

Sample Location	Ref Depth [mm]	Sample Depth [mm]	R-S Depth [mm]	Ref Depth Dose	Sample Depth Dose	R-S Depth Dose	Grad Reduc [mm]	Sample Thickness [mm]	Proton Energy [MeV]	Electron Energy [MeV]
P1	134.94	133.28	+1.66	0.5115	0.5155	-0.0040	-0.02	1.64	16.7	0.47
P2	134.94	132.35	+2.59	0.5115	0.5460	-0.0345	-0.15	2.44	17.7	0.63
P3a	134.35	130.61	+3.74	0.5190	0.4454	+0.0736	+0.31	4.05	19.3	0.94
P3b	134.35	129.71	+4.64	0.5190	0.6646	-0.1456	-0.62	4.02	19.2	0.93
P4a	134.35	128.85	+5.50	0.5190	0.4342	+0.0848	+0.36	5.86	23.7	1.28
P4b	134.35	127.95	+6.40	0.5190	0.6311	-0.1121	-0.48	5.92	23.8	1.29
P5a	134.35	121.11	+13.24	0.5190	0.4125	+0.1065	+0.46	13.70	37.9	2.73
P5b	134.35	120.20	+14.15	0.5190	0.6075	-0.0885	-0.38	13.77	38.0	2.74
P6	134.35	132.54	+1.81	0.5190	0.5015	+0.0175	+0.07	1.88	12.6	0.52
P7a	134.35	132.42	+1.93	0.5190	0.4361	+0.0829	+0.35	2.28	14.0	0.60
P7b	134.35	131.52	+2.83	0.5190	0.6033	-0.0843	-0.35	2.48	14.7	0.64
P8	134.35	132.54	+1.81	0.5190	0.5516	-0.0326	-0.14	1.67	11.7	0.48
P9a	134.35	132.42	+1.93	0.5190	0.4565	+0.0625	+0.27	2.20	13.7	0.59
P9b	134.35	131.52	+2.83	0.5190	0.6604	-0.1414	-0.60	2.23	13.8	0.59
P10a	134.35	132.54	+1.81	0.5190	0.5181	+0.009	+0.00	1.81	12.3	0.51
P10b	134.35	132.43	+1.93	0.5190	0.5842	-0.0652	-0.28	1.65	11.7	0.48
P11a	134.35	130.61	+3.74	0.5190	0.4659	+0.0531	+0.23	3.97	19.1	0.93
P11b	134.35	129.71	+4.64	0.5190	0.6446	-0.1256	-0.54	4.10	19.4	0.95
P12a	134.35	118.08	+16.27	0.5190	0.3823	+0.1367	+0.58	16.85	42.5	3.33
P12b	134.35	117.17	+17.18	0.5190	0.5781	-0.0591	-0.25	16.93	42.6	3.34
P13a	134.35	90.92	+43.43	0.5261	0.4271	+0.0990	+0.42	43.85	72.4	8.75
P13b	134.35	90.02	+44.33	0.5261	0.4772	+0.0489	+0.21	44.54	73.1	8.90
P14a	134.35	130.61	+3.74	0.5261	0.4860	+0.0401	+0.17	3.91	18.9	0.91
P14b	134.35	129.71	+4.64	0.5261	0.6826	-0.1565	-0.67	3.97	19.1	0.93
P15a	134.35	133.44	+0.91	0.4377	0.3340	0.1037	+0.44	1.35	10.4	0.41
P15b	134.35	132.54	+1.81	0.4377	0.5087	-0.0710	-0.30	1.51	11.1	0.45
P16a	134.35	129.71	+4.64	0.4377	0.3382	+0.0995	+0.43	5.07	21.9	1.13
P16b	134.35	128.85	+5.50	0.4377	0.5230	-0.0853	-0.36	5.14	22.0	1.14
P17a	134.35	127.95	+6.40	0.4377	0.3399	+0.0978	+0.42	6.82	25.8	1.45
P17b	134.35	127.04	+7.31	0.4377	0.5318	-0.0941	-0.40	6.91	26.0	1.47
P18a	134.35	128.85	+5.50	0.4377	0.4982	-0.0605	-0.26	5.24	22.3	1.16
P18b	134.35	127.95	+6.40	0.4377	0.6250	-0.1873	-0.80	5.60	23.1	1.23
P19	134.35	125.58	+8.77	0.4377	0.4407	-0.0030	-0.01	8.76	29.6	1.81

Energy: 155 MeV

Proton Depth Dose Gradient = 0.234/mm

## 2.5 ACKNOWLEDGMENTS

This work was partially funded by NASA Cooperative Agreement #NCC9-79. These experiments were made possible by the contribution of many people. Steven Rightnar of LLU assisted with the performance and coordination of the experiments at LLU. Jack Miller of the Lawrence Berkeley Laboratories organized the experiments. Francis Cucinotta of the Johnson Space Center (JSC) sponsored the experiments. Robert Jones of Inland Technical Services, Inc. was responsible for fabricating the extension cone range shifter slab holders. The Phantom Laboratory constructed the special phantom and inserts to the specifications required for the experiments. Jason Poffenberger and Bill Welch of ILC Dover manipulated the phantoms and suits and assisted with the installation of the various detectors. Brett Geisel of Loma Linda University Medical Center (LLUMC) performed the CT scans. Ed Semones of JSC provided the electron and proton spectral data. The accelerator operators at LLU provided beam tuning during the various experiments. Mark Shavers of JSC assisted with editing the manuscript.

## REFERENCES

- International Commission on Radiation Units and Measurements (1984) "Radiation dosimetry: electron beams with energies between 1 and 50 MeV", ICRU Report **35** (International Commission on Radiation Units and Measurements, Bethesda, MD).
- Janni J. F. (1982) Proton range-energy tables, 1 keV - 10 GeV. *Atomic Data and Nuclear Data Tables* **27(2/3)**: 147-339.
- Kosmo J. J., Nachtwey D. S., Hardy A. (1989) Candidate space station EVA space suit - radiation analysis final report. CTSD-SS-241.
- Moyers, M. F. "Proton Therapy" The Modern Technology of Radiation Oncology: A Compendium for Medical Physicists and Radiation Oncologists ed. vanDyk, J. (Wisconsin: Medical Physics Publishing, 1999) p. 823-869.
- Moyers M. F., Miller D. W., Siebers J. V., Galindo R., Sun S., Sardesai M., Chan L. (1992) Water equivalence of various materials for 155 to 250 MeV protons. Medical Physics **19(3)** (1992) p. 829. Abstract.



**CHAPTER 3**

**RADIATION TESTS OF THE**

**EXTRAVEHICULAR MOBILITY UNIT**

**SPACE SUIT FOR THE**

**INTERNATIONAL SPACE STATION**

**USING ENERGETIC PROTONS**

C. Zeitlin, L. Heilbronn, J. Miller  
Lawrence Berkeley National Laboratory  
Berkeley, California

M. Shavers  
Johnson Space Center  
Houston, Texas

# RADIATION TESTS OF THE EXTRAVEHICULAR MOBILITY UNIT SPACE SUIT FOR THE INTERNATIONAL SPACE STATION USING ENERGETIC PROTONS

## ABSTRACT

Measurements using silicon detectors to characterize the radiation transmitted through the EMU space suit and a human phantom have been performed using 155 and 250 MeV proton beams at LLUMC. The beams simulate radiation encountered in space, where trapped protons having kinetic energies on the order of 100 MeV are copious. Protons with 100-MeV kinetic energy and above can penetrate many centimeters of water or other light materials, so that astronauts exposed to such energetic particles will receive doses to their internal organs. This dose can be enhanced or reduced by shielding—either from the space suit or the self-shielding of the body—but minimization of the risk depends on details of the incident particle flux (in particular the energy spectrum) and on the dose responses of the various critical organs. Data were taken to characterize the beams and to calibrate the detectors using the beam in a treatment room at LLUPTF, in preparation for an experiment with the same beams incident on detectors placed in a human phantom within the EMU suit. Nuclear interactions of high-energy protons in various materials produce a small flux of highly ionizing, low-energy secondary radiation. Secondaries are of interest for their biological effects, since they cause doses and especially dose-equivalents to increase relative to the values expected simply from ionization energy loss along the Bragg curve. Because many secondaries have very short ranges, they are best measured in passive track detectors such as CR-39. The silicon detector data presented here are intended to supplement the CR-39 data in regions where silicon has greater sensitivity, in particular the portion of the LET spectrum below 5 keV/ $\mu\text{m}$ . The results obtained in this study suggest that optimizing the radiation shielding properties of space suits is a formidable task. The naïve assumption that adding mass can reduce risk is not supported by the data, which show that reducing the dose delivered at or near the skin by low-energy particles may increase the dose delivered by energetic particles to points deeper in the body.

## 3.1 INTRODUCTION

To accurately estimate doses and dose-equivalents received during extravehicular activities outside ISS, one must take into account the shielding properties of the space suits worn by the astronauts and the self-shielding of the human body with respect to critical areas such as the blood-forming organs and central nervous system. In ISS orbit, there are large fluxes of both protons and electrons with sufficient kinetic energy to penetrate several millimeters of light materials such as fabric or tissue; these fluxes are largest in the trapped particle belts [1]. Although the proton spectrum falls off rapidly with increasing energy, there is a significant flux above 100 MeV, where ranges exceed 10 cm of water and increase rapidly with energy. Proton beams with energies from 60 to 250 MeV, produced at the LLUMC cancer treatment facility [2], were used in the measurements reported here.

Because the EMU space suit is complex and highly inhomogeneous, measurements are needed to definitively determine threshold energies for suit penetration and dose vs. depth relationships for various regions, including the skin and points well inside the body when enclosed by the space suit. Many parts of the suit have areal densities of only

0.2 g cm<sup>-2</sup>, but even the thinnest parts will stop the large fluxes of very low-energy protons ( $E < 12$  MeV) and electrons ( $E < 0.5$  MeV) encountered in the trapped belts. Energy thresholds for suit penetration of electrons and protons were measured at the LLUMC with ionization chambers [3]; the data have been used as input to a computer model of the suit [4]. The threshold energies, while vitally important for understanding the shielding properties of various parts of the EMU suit against low-energy particles, are only part of the required data. It is also necessary to determine the effects of the space suit—and the tissue inside it—on the charged particles with sufficient energy to penetrate the suit and, at the higher energies, many centimeters of tissue.

When highly penetrating radiation (e.g., an energetic proton) traverses a significant depth of shielding and/or tissue, secondary particles produced in nuclear interactions are of concern. Highly ionizing secondaries can be produced in grazing interactions in which a target nucleus recoils, or in more central collisions where the target nucleus breaks apart, sometimes with additional emission of low-velocity charged particles from the decay of excited nuclear states in the abrasion-ablation process [5]. When one integrates fluence over the LET<sup>1</sup> spectrum to obtain dose equivalent, secondary particles with high LET—though not numerous—get a large weight from the quality factor [6], resulting in a significant contribution to dose equivalent [7].

Measurements of the short-ranged, high-LET secondaries produced by an incident beam can be made with CR-39 PNTDs, in combination with TLDs to measure the total dose in a particular exposure [8]. Low-energy particles from target recoils or fragmentation have short ranges, on the order of hundreds of microns or less in water or tissue; for instance, a <sup>12</sup>C nucleus with kinetic energy of 4 MeV/nucleon (about half the maximum possible recoil energy from a 250-MeV proton) has a range of about 85 μm in water, with an initial LET of about 340 keV/μm. Measuring the fluence and LET of such tracks presents many technical challenges; CR-39 is well-suited for this purpose but can only detect particles with LET above about 5 keV/μm, approximately an order of magnitude greater than the LET of the LLUMC 250 MeV proton beam. Thus, in the present experiment, CR-39 misses the primary beam particles and any secondaries with LET below 5 keV/μm. Tracks with ranges shorter than about 10 μm in CR-39 are also missed; these include the tracks from very low-energy target fragments and recoil nuclei. These very short tracks are removed in the etching process [9]; they can have very high LET, and consequently contribute significantly to dose and dose equivalent.

The silicon detector system described here has more typically been used in the measurement of high-energy heavy ion beams and their nuclear fragmentation products [10-14]. Silicon detectors have some advantages compared to CR-39 in this experimental setting, particularly their ability to measure energy deposition events over a dynamic range large enough to include the primary protons and a broad spectrum of secondaries. However, the detectors used here have significant disadvantages in the measurement of short-ranged secondaries: (1) they have “dead layers” (typically about 2% of the detector depth), and (2) they collect charge in a huge volume (compared to CR-39), so that—as explained in more detail below—the direct measurement of the LET of short-ranged secondaries is impossible. However, since the high end of the LET spectrum can be reliably measured in CR-39, we focus on the lower end, and we attempt to find areas of overlap where the two measurement methods can be cross-checked for consistency.

---

<sup>1</sup> Throughout, we use “LET” as shorthand meaning LET<sub>∞</sub> in water.

## 3.2 EXPERIMENTAL CONFIGURATIONS

### 3.2.1 Detectors and Electronics

The accelerator at the LLUMC provided proton beams at energies similar to those encountered in the trapped particle belts through which ISS will pass. Beams with kinetic energies of 250 MeV and 155 MeV at extraction from the synchrotron were made available for the present study and for the measurements of the EMU suit penetration energies. We also used the 155-MeV beam to produce beams with energies of about 60 and 40 MeV by passing the protons through blocks of plastic with the appropriate depths. We took the measurements described here in January 2000 in Gantry 1, a room designed for patient treatment. Data were taken both with and without the EMU suit. To simulate a human body inside the EMU suit, the experiments used a phantom [15] consisting of large portions of a human skeleton and water-equivalent plastic. A frontal view of the phantom is shown in **Figure 3-1**. Drilled holes allowed experimenters to put detectors, encased in tissue-equivalent plastic, in various locations inside the phantom. The phantom is modular; pieces were taken as needed and placed inside the appropriate part of the EMU suit. Gantry 1 was a convenient location for these runs, as it has a motor-driven table that can be moved into the beam, and the beam line itself can be rotated around the table to accommodate a variety of entrance port requirements for treatment.

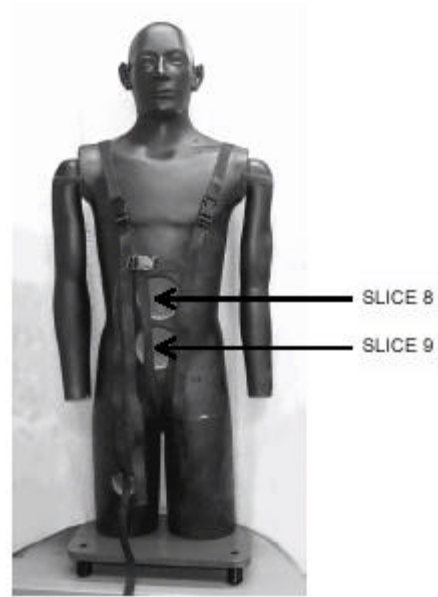


**Figure 3-1.** The human phantom used in conjunction with the EMU space suit. Two of the pre-drilled holes to accommodate detectors are shown. The phantom is modular and can be separated into “slices.”

The first set of measurements used only the bare beam at the four energies mentioned above; these data allow us to calibrate our silicon detector system and to characterize both the beam and the response of the detectors to it. We took a second set of measurements with the same detectors placed inside the phantom at three locations: brain, upper abdomen, and lower abdomen, placing the phantom inside the appropriate piece of the EMU suit for each location.

In all runs, we used a stack of three lithium-drifted silicon detectors. The detectors are right-circular cylinders, with radii of 1.2 cm and depths from 3.06 to 3.08 mm. They measure the deposited energy ( $\Delta E$ ) from the ionization energy losses of charged particles traversing their sensitive volumes. In the measurements with the bare beams in Gantry 1, detectors were placed in a housing typically used on an optical bench at an accelerator. Here, the housing was placed flat on the treatment table with the beam incident vertically from above, as shown schematically in **Figure 3-2(a)**. We refer to the detectors as d3mm1, d3mm2, and d3mm3, with d3mm1 being closest to the nozzle (the end of the beam transport vacuum line). A sketch of the arrangement of detectors and water-equivalent plastic plugs used in the space suit/phantom runs is shown in **Figure 3-2(b)**.

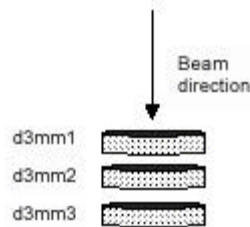


**Figure 3-2(a).** Sketch of the detector configuration for the bare-beam runs. The air gaps between detectors were approximately 1 cm.

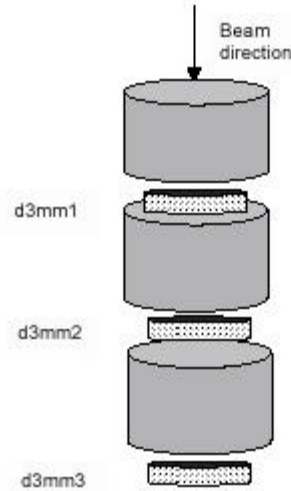


**Figure 3-2(b).** Sketch of the detector configuration for the runs with the detectors placed in the phantom, enclosed by the corresponding piece of the EMU space suit. The plug in front of d3mm1 was 27 mm deep, the others 22 mm. The pieces shown were encased in a larger cylinder (not shown) of water-equivalent plastic (hollow along its central axis to hold the detectors and plugs), and placed in the phantom.

The detectors were biased to full depletion. The charge liberated in each detector was integrated and amplified by a charge-sensitive preamplifier and shaping amplifier combination, the Amptek A225 [16], chosen for its very low noise and compactness (a major issue given the limited space in Gantry 1). Each A225 has two outputs, a fast signal used for timing and triggering, and a slow shaped signal (rise time  $\sim 2 \mu\text{sec}$ ) for precise determination of pulse height. The shaped outputs were further amplified by Tennelec Model 222 biased amplifiers; those outputs were connected to 50-ft BNC cables, which ran from the gantry to the hallway just outside, where NIM logic modules and a CAMAC crate were located; the signals were digitized in a 12-bit, peak-sensing CAMAC ADC.

The fast signal from d3mm1 was used as input to a constant-fraction discriminator, the output of which was used to trigger the readout. If a second fast signal arrived during the 30- $\mu\text{sec}$  readout time of the previous event, the second trigger was vetoed. The ADC was gated on for 5  $\mu\text{sec}$  by a signal derived from the constant-fraction discriminator output; a second event arriving within this window can, in some cases, distort the pulses and cause spuriously large ADC readings, as discussed in more detail below. The ADC results were read out by a Vax computer and the events stored on disk in an event-by-event format.

### 3.2.2 Calibration

In silicon, one electron/hole pair is created for each 3.6 eV of energy deposited; the observed pulse heights were converted to deposited energy ( $\Delta E$ ) using the following procedure to calibrate each channel from preamplifier through ADC. An EG&G Ortec 447 Research Pulser supplied a series of voltage pulses with accurately known

amplitude to a reference capacitor, yielding a charge that was injected directly into the preamp on the same path as the charge coming from the detector. We acquired calibration data and stored them on disk in the same way as beam data; off-line, we analyzed the data to determine the slope and pedestal for each channel. As is typical for these amplifiers and ADCs, excellent linearity is seen over the relevant range of  $\Delta E$ .

### 3.2.3 Relation of DE in Silicon to LET

Energy loss in silicon detectors can be related to energy loss in water. Calculations using the Bethe-Bloch equation [17] show that, for the range of energies encountered in these experiments, it is reasonable to relate measured deposited energy  $\Delta E$  in silicon to LET using a single conversion constant. To a good approximation,  $LET = 0.53 (\Delta E/\Delta x)$  where  $\Delta x$  is the sensitive depth of the silicon. However, when we discuss target fragmentation or target recoil events, it is important to bear in mind that the detectors record the total energy deposited, regardless of the length of a track in the detector. Converting  $\Delta E$  to LET as per the preceding equation is, by definition, averaging over the entire depth of the detector; this can be orders of magnitude greater than the range of a high-LET track. In such cases, the conversion of  $\Delta E$  to LET is not meaningful. Only for particles that pass entirely through a detector, parallel or nearly parallel to the nominal beam axis, can one accurately relate  $\Delta E$  to LET. For stopping particles, estimates of LET obtained from  $\Delta E/\Delta x$  are lower limits.

Preliminary model calculations<sup>2</sup> indicate that the LET spectrum of target fragments produced in proton-silicon interactions is quite complex, and contains a non-negligible fluence of events out to several thousand keV/ $\mu\text{m}$ . Most of the details of this spectrum are impossible to measure in the present experimental configuration. Even in CR-39, significant details of the target fragment spectrum may be lost, since the ranges of the target fragments and recoiling target nuclei are extremely short—above 500 keV/ $\mu\text{m}$ , most tracks have ranges in water of less than 5  $\mu\text{m}$ .

## 3.3 ANALYSIS OF BARE-BEAM DATA

The first runs in Gantry 1 used the proton beam at two values of extracted energy, 250 and 155 MeV, and two additional values of nozzle energy (the energy of the beam as it enters the air gap between the end of the beam line and the detectors). The two lower energies—nominally 60 and 40 MeV—were obtained by passing the 155-MeV beam through thick (> 10 cm water-equivalent) plastic range shifter blocks placed at the end of the vacuum line. Neither the EMU suit nor the phantom was used in these runs.

### 3.3.1 Beam Quality

The Gantry 1 facility is primarily used for patient treatment, with typical intensities of  $10^8$  protons  $\text{s}^{-1} \text{cm}^{-2}$  and higher; our experiment requires a beam intensity of  $10^3$  protons  $\text{s}^{-1} \text{cm}^{-2}$  or lower. This disparity presented a number of difficulties to the accelerator operator, whose feedback and monitoring devices did not register such small

---

<sup>2</sup> A model of proton-silicon interactions is under development, as we wish to study the physical processes that underlie the measured  $\Delta E$  distributions. It will be extended to proton-carbon and proton-proton interactions, with the goal of modeling target fragment production in tissue.

beam currents. As a result, currents were slightly higher than optimal, and some event pile-up (described below) occurred. Because beam intensity varied from run to run, so did the fraction of pile-up events. The treatment of these events is the leading source of systematic error in the data analysis.

The beam spot at the treatment table was considerably larger than the 1.2-cm radius of the detectors. The beams have considerable divergence, caused by two factors: (1) the beam transport optics, which focus the beam at a point upstream of the nozzle, and (2) scattering foils also placed far upstream of the nozzle. Focusing with quadrupole magnets produces a small, divergent beam spot that is enlarged and made more uniform by the scattering foils. Because Coulomb multiple scattering increases with decreasing energy, a set of thinner scattering foils is required to produce the desired spot size with the 155-MeV beam than with the 250-MeV beam. As we will show, the divergence of the beam has noticeable effects on the spectra seen in the silicon detectors.

### 3.3.2 DE Spectra: Events Lost by Scattering

The  $\Delta E$  spectra for the 250-MeV bare-beam run are shown in the histograms in **Figures 3-3(a)**, **(b)**, and **(c)**, for detectors d3mm1, 2, and 3 respectively. The only cut applied in these three histograms is the requirement<sup>3</sup> that  $\Delta E$  in d3mm1 was above 1.4 MeV. Peaks appear near the expected  $\Delta E$  values, with tails of events to higher  $\Delta E$ . A small peak of events in each plot appears in the highest  $\Delta E$  bin; these are events where a relatively large signal saturated the readout electronics. In all three of the histograms in **Figures 3-3(a)-(c)**, about 0.28% of events appear in this “overflow” bin. Also, d3mm2 (about 2%) and d3mm3 (about 5%) have considerable numbers of events with  $\Delta E$  near 0; these are likely events in which the incident proton hit near the edge of d3mm1 and had a trajectory with a sufficiently large

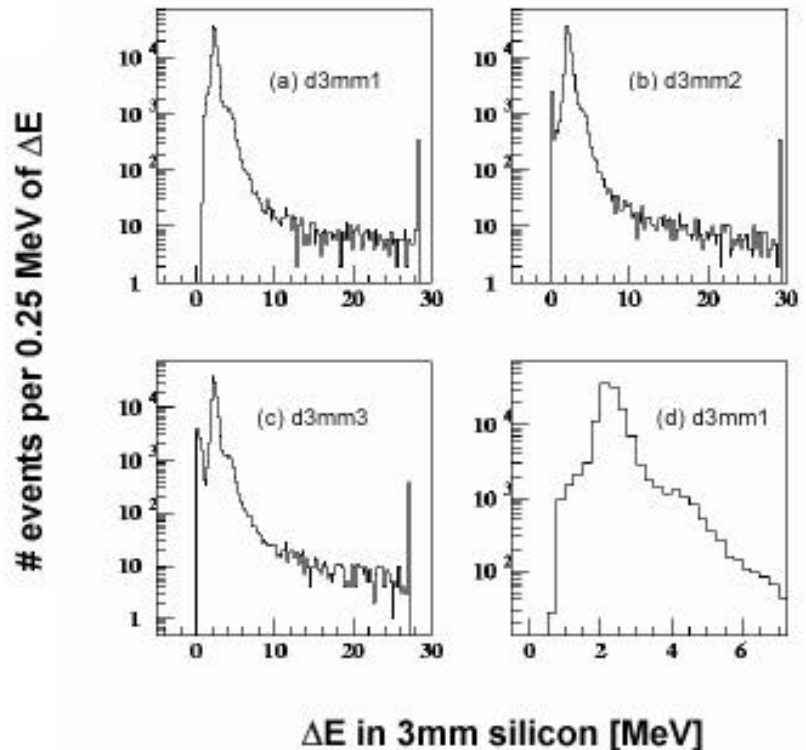


**Figure 3-3.** Histograms of  $\Delta E$  in the three detectors for the bare-beam run with an extracted beam energy of 250 MeV. In (d) we focus on the proton peak region of d3mm1, to clearly show the pile-up peak near 4 MeV.

<sup>3</sup> This value of  $\Delta E$  was obtained from a Gaussian fit to the central bins of the proton peak on the d3mm1 spectrum. A  $\Delta E$  of 1.4 MeV is 3 standard deviations ( $3\sigma$ ) below the mean of the peak found by the fit.

angle with respect to the beam axis that it missed the active area of d3mm2 and/or d3mm3. Our beam line simulation model [14] reproduces these fractions with reasonable accuracy, predicting 1.8% losses in d3mm2 and 7.5% losses in d3mm3. The model shows that Coulomb scattering in the beam-spreading foils is the primary cause of events in which protons hit d3mm1 but miss d3mm2 and/or d3mm3.

### 3.3.3 Event Pile-Up in the DE Spectra

In the d3mm1 spectrum, **Figure 3-3(a)**, a peak is visible just above 4 MeV, close to double the  $\Delta E$  of the main peak. This second peak, which sits on top of the high-end tail of the single-proton distribution, is due to pile-up events with two protons. These can also be identified in scatter plots of  $\Delta E$  in any pair of detectors; **Figure 3-4(a)** shows an example, with  $\Delta E$  in d3mm2 plotted against  $\Delta E$  in d3mm1 for the same event sample as in **Figure 3-3(a)-(c)**. Events in which both detectors were hit by the same particle or particles give well-correlated values of  $\Delta E$ , and these heavily populate the region along a line drawn from the origin at 45°. Bands of events with relatively large  $\Delta E$  in one detector or the other (but not both) are visible. If we take a projection of the entire sample onto either axis, the number of events above the nominal proton  $\Delta E$  will be greatly enhanced by the events along the 45° line with  $\Delta E$  above about 4 MeV in each detector.

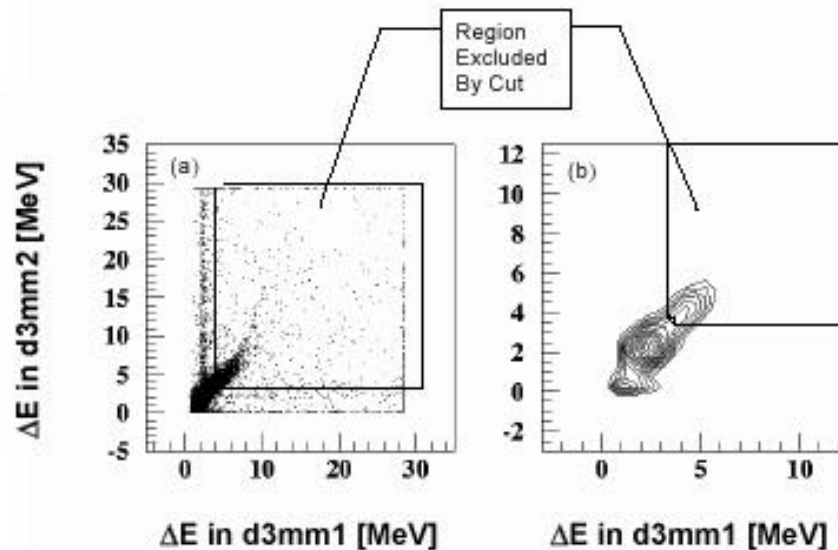


**Figure 3-4.** Scatter plots of d3mm2 vs. d3mm1 for the same event sample as in Figure 3-3, where the only requirement is a hit well above threshold in d3mm1. Figure 3-4(a) shows a concentration of events along the 45° line, indicating both detectors were hit by the same particle or particles. The rectangle superimposed on the data indicates the region excluded by a graphical cut. Figure 3-4(b) shows the same events in the region below 12 MeV in each detector, plotted as contours on a logarithmic-sensitivity scale. Denser contours represent higher concentrations of events.

In **Figure 3-4(b)**, we show the same events, restricted to the region below about 12 MeV, as a contour plot with logarithmic sensitivity. The contours indicate a strong concentration of events with hits corresponding to one proton in both d3mm1 and d3mm2. The other contours contain events where d3mm2 was missed ( $\Delta E$  near 0), as well as pile-up events and possible good events (with only one incident proton) in which both detectors legitimately record a large  $\Delta E$  due to relatively high-energy secondaries with sufficient range to register a signal in each. There

is, in this plot, an unmistakable concentration of events in which both detectors record  $\Delta E$  about twice that of a single proton; these are dominated by pile-up.

In the subsequent analysis, we use four methods to deal with pile-up events:

1. A graphical cut to exclude events in regions likely to be dominated by pile-up, as illustrated by the cut contour shown in **Figure 3-4(a)** and more clearly in **4(b)**
2. A cut to require that the  $\Delta E$  in d3mm1 was within a narrow range centered on the proton peak, and then examine the spectra of events passing the cut in d3mm2 and d3mm3
3. A cut to require that  $\Delta E$  in d3mm2 is in the proton peak, and examine the spectra of events passing the cut in d3mm1 and d3mm3
4. No cut, and look only at the  $\Delta E$  range well above any likely pile-up events

For example, given a proton peak at 2.5 MeV, we might choose to examine the spectrum above 7.5 or 10 MeV, corresponding to  $\Delta E$  greater than three or four times that of a single proton. This is the least biased of the methods, since no cuts are made. As long as there is not a large contamination of pile-up events in a sample, this should yield the most reliable results, although it biases against legitimate high- $\Delta E$  events with  $\Delta E$  below the cutoff.

A cut requiring  $\Delta E$  greater than four times the value of single protons allows us to include any He fragments that are likely to be produced. If it were possible to produce  $^4\text{He}$  at the beam velocity, any such fragments would have an initial  $dE/dx$  four times greater than that of a proton. Naively, we do not expect any He fragments to have the full beam velocity, based simply on invoking momentum conservation in the “brick wall” approximation. If, for example, a 223-MeV proton transfers twice its momentum (the maximum possible in this picture) to a  $^4\text{He}$  fragment—and none to the other nucleons in the target nucleus—then the fragment would have a velocity only slightly more than half that of the incident proton.<sup>4</sup> It would accordingly have an initial  $dE/dx$  about twelve times that of the proton, far above the cut.

### 3.3.4 High-DE Tails, Pile-Up Removal Methods

In the following, we use the 250-MeV and 155-MeV data sets. The spectra obtained with the lower-energy protons are strongly affected by the range-shifting blocks placed on the beam line; energy-loss straggling in the blocks leads to very broad distributions of the proton energy at the exit from the beam transport line. We are interested here in the high- $\Delta E$  tails of the distributions in the detectors, and the broad incident energy distributions render these data unsuitable for this purpose. The main use for the low-energy data is in fine-tuning the pulse-height-to-energy-loss calibration (see subsection 3.3.6 below).

**Figure 3-5** shows a histogram of events in d3mm1 after a pile-up rejection cut of type (1) is applied. A small peak persists around 4 MeV, but it is greatly reduced compared to the pile-up peak in **Figure 3-3(a)**. Because we have presumably removed the vast majority of pile-up events, we can make a somewhat loose operational definition of high- $\Delta E$  events as being those with  $\Delta E > 2\Delta E_{\text{peak}}$ , where  $\Delta E_{\text{peak}}$  is defined as the mean obtained from fitting a

---

<sup>4</sup> This simple calculation does not account for possible increases in fragment velocities due to Fermi motion of the target nucleons.

Gaussian to the central bins of the single-proton peak (the fitted curve is shown in the figure). In **Figure 3-5**, about 0.5% of the events meet this definition, which in this case means  $\Delta E > 4.54$  MeV; in contrast, in the distribution in **Figure 3-3(a)**, with no pile-up rejection cuts, the fraction of events with  $\Delta E > 4.54$  MeV is 2.9%. This clearly shows that most high- $\Delta E$  events are removed by the type (1) cut, but we cannot tell from this simple analysis whether (or how many) valid target-fragmentation or target-recoil events have also been removed.

Applying pile-up rejection method (1) to the  $\Delta E$  histograms for d3mm2 and d3mm3, we find 0.7% and 1.1% of events with  $\Delta E > 2\Delta E_{\text{peak}}$ . These fractions are consistent with the hypothesis that some of the target fragments that are formed upstream (e.g., in d3mm1) have enough energy to reach at least one of the subsequent detectors. This effect leads to a build-up of fragments as one looks deeper in the detector stack. Since the physical processes in other materials are analogous, we expect a similar buildup effect in tissue, bone, etc. When we apply method (2), the tight cut requiring a single proton in d3mm1, and again examine the spectra with  $\Delta E > 2\Delta E_{\text{peak}}$ , we find almost precisely the same fractions of high- $\Delta E$  events (0.7% and 1.1%) in d3mm2 and d3mm3.

Method (3) invokes a tight cut on  $\Delta E$  in d3mm2 to require a single proton there; we make this cut and then examine the d3mm1 and d3mm3 spectra. We find that this removes even more events in the high-end tail of the d3mm1 distribution than did method (1): only 0.3% of events among those passing the cut are found to have  $\Delta E > 2\Delta E_{\text{peak}}$ . In contrast, the effect on the d3mm3 distribution is much less severe—0.9% of events are found in the high-end tail of that spectrum, roughly consistent with the fraction as determined by previous methods. These results suggest two interpretations: first, that many of the target fragments are produced with considerable momentum along the beam direction, so that they penetrate into at least one additional detector downstream from the one in which they originated; second, it may be that many of the protons that interact in d3mm1 are sufficiently perturbed that they do not meet the selection criterion in d3mm2, either because they are slowed down (so that their  $\Delta E$  in d3mm2 is larger than nominal) or because they scatter at large angles and miss d3mm2 entirely. Whatever the mechanism, it is clear that by requiring a single proton in d3mm2, we are systematically biasing against high- $\Delta E$  events in d3mm1.

Turning now to method (4) and examining the d3mm1 spectrum, if we sum events in **Figure 3-3(a)** with  $\Delta E$  above 10 MeV, we find about 0.7% of the events of the sample. This is also true of the sample shown in **Figure 3-5**. This is because the pile-up events almost all yield  $\Delta E$  below 10 MeV. Since the fraction of events defined as high- $\Delta E$  by this method (0.7%) is larger than the 0.5% found using method (1), we tentatively conclude that method

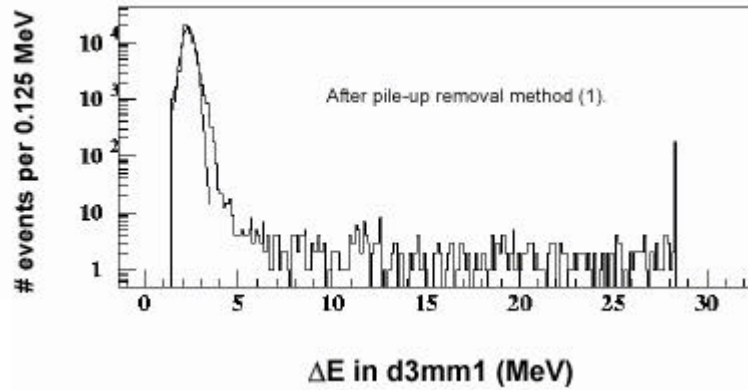


**Figure 3-5.** Histogram of  $\Delta E$  in d3mm1 after application of a pile-up rejection cut based on the scatter plot method described in the text. The curve shown is the best-fitting Gaussian in the central bins of the main proton peak. Data are from the run with a beam energy of 250 MeV at extraction.

(1) does, as hypothesized, remove a significant portion of the valid target fragments from the sample. Applying method (4) to the d3mm2 and d3mm3 spectra shows that, for both, the fraction of events above 10 MeV is about 0.8%, roughly consistent with the fractions obtained by other methods.

Similar analysis of events in the high- $\Delta E$  tails has been performed on the 155 MeV beam data. In all cases, the results obtained with the lower-energy beam are quite close to those obtained at higher energy. This fits well with our expectation (explained below) that nuclear interactions are responsible for the high- $\Delta E$  tails, and the reaction cross sections are not very sensitive to beam energy variations in this range. The results presented in this section are summarized in **Table 3-1**.

**Table 3-1.** Fractions of Events Found in the High- $\Delta E$  Tails of the Distributions in the Three Detectors for the Two Highest-Energy Beams

Method	% of events in high- $\Delta E$ tail 223 MeV beam			% of events in high- $\Delta E$ tail 145 MeV beam		
	d3mm1	d3mm2	d3mm3	d3mm1	d3mm2	d3mm3
1	0.5	0.7	1.1	0.5	0.8	1.1
2	—	0.7	1.1	—	0.8	1.1
3	0.3	—	0.9	0.2	—	0.8
4	0.7	0.8	0.8	0.6	0.8	0.8

NOTE: The fractions depend on the pile-up rejection method and the corresponding definition of the tail. A detailed explanation is in the text. The statistical errors associated with these results are in all cases in the range from 2% to 6% of the values shown in the table.

### 3.3.5 Interpretation of the High-DE Tails

It is notable that, regardless of the method chosen to remove pile-up events and to define the high- $\Delta E$  tails, all the estimates of the fractions of high- $\Delta E$  events are in the range 0.5% to 1.1% (aside from the 0.2 – 0.3% obtained when we introduce a systematic bias against high- $\Delta E$  events, in the case of method (3) applied to d3mm1). As we will show, the high- $\Delta E$  events that remain in each spectrum after pile-up removal can be entirely ascribed to the elastic and inelastic scattering cross sections for protons on silicon. One of the more important conclusions we can draw from this is that there were no high-LET particles coming from the accelerator. High-LET particles could conceivably be produced in the beam transport line by the beam scraping against various apertures. The absence of such particles suggests the beam's trajectory is usually well-controlled through the transport line.

We note that the maximum recoil energy of a silicon nucleus being hit by a 250 MeV proton is about 40 MeV, or about 1.5 MeV/nucleon, corresponding to a range of just under 5  $\mu\text{m}$  in silicon. The saturation point of the electronics in this experiment was around 30 MeV for most detectors, but the presence of counts in the overflow bin suggests that some events do in fact give this maximum energy deposition.

### 3.3.6 Beam Energies, Calibration Adjustment

We momentarily digress to discuss the peaks of the distributions, rather than the tails. The peak locations can, with the aid of careful energy-loss calculations, yield accurate measurements of the incident beam energies and help us to refine the calibration of the detectors.

The 250 and 155 MeV beams are expected to have nozzle energies of about 223 and 136 MeV, respectively [18]. The differences between extracted and nozzle energies are due to ionization energy losses in traversing the scattering foils and beam monitoring hardware, which included ionization chambers and a secondary emission monitor, located near the end of the vacuum line. In the following, we rely on calculations performed using a careful numerical integration of the Bethe-Bloch equation to determine energy loss in various beam line elements. The greater depth of scattering foils needed to spread the 250-MeV beam accounts for the 27-MeV energy loss of that beam after extraction, compared to the 19 MeV lost by the lower-energy beam.

For each silicon detector, the average  $\Delta E$  on events with a single proton is determined by fitting a Gaussian distribution to the central bins of the peak, as illustrated in **Figure 3-5**. These values are shown for each detector in **Table 3-2**, which also shows the results of calculations that assume a dead layer thickness of 2% of detector depth. In the data obtained with 250 MeV extracted beam, all reported  $\Delta E$  values are lower than the calculation predicts, with the ratios of calculated to measured  $\Delta E$  equal to 1.06, 1.10, and 1.08 for d3mm1, d3mm2, and d3mm3 respectively. Setting aside the question of what causes the discrepancies, we make use of the information by taking the ratios of calculated-to-measured  $\Delta E$  in the 223-MeV beam data as correction factors, and applying them to the measured  $\Delta E$ s in the other bare-beam data sets (and to subsequent analysis of this run). The corrected values are as shown in **Table 3-2** for all runs other than the one at 250 MeV.

**Table 3-2.** Deposited Energy in MeV for d3mm1, 2, and 3 With the Bare Beam (left-most columns), Compared to Calculations With Beam Energies as Shown Assuming Dead Layers Were 2% of Detector Thickness

Det. #	$\Delta E$ peak (MeV)	Calc 223 MeV	$\Delta E$ peak (MeV)	Calc 145 MeV	$\Delta E$ peak (MeV)	Calc 60 MeV	$\Delta E$ peak (MeV)	Calc 41 MeV
1	2.27	2.40	3.19	3.19	6.34	6.33	9.1	9.0
2	2.18	2.40	3.15	3.23	6.84	6.96	11.5	11.8
3	2.25	2.43	3.30	3.30	8.10	7.96	16.5	19.4

NOTE: Quoted beam energies are the nozzle energies, determined by iterating the calculation until agreement with data was obtained. The result for d3mm3 with the 41 MeV is an exceptional case, as explained in the text. The ratios between calculated and measured  $\Delta E$ s in the 223 MeV run were used as correction factors for the data values in the other runs.

For the 155-MeV beam with no range-shifting blocks on the beam line, we varied the nozzle energy in the calculation until the predicted  $\Delta E$ s were in good agreement with the corrected data; best agreement was obtained with 145 MeV for the nozzle energy, rather than the expected value of 136 MeV. A detailed calculation shows that this is highly consistent with the absence of one of the two scattering foils usually used for this beam. Further evidence for this comes from looking at the fractions of events with no hit in d3mm2 and/or d3mm3; these are found to be 1.0% and 3.8%, respectively. This is significantly less than would be expected if both foils were present, which would give a scattering distribution similar to that in the 250 MeV data, where the fractions of lost events were 2% and 5% for d3mm2 and d3mm3, respectively.

For the two lower energies that used the 155 MeV extracted beam, the calculation was performed assuming that both scattering foils were in place; we varied the amount of water-equivalent material on the beam line until we again obtained good agreement with the data. Nozzle energies were found to be 60 and 41 MeV with 10.2 and 11.75 cm of water-equivalent material, consistent with the expected values of 60 and 40 MeV, respectively. The LETs in water corresponding to the four nozzle energies of the beams are about 0.42, 0.58, 1.07, and 1.49 keV/ $\mu\text{m}$ , respectively.

In the 41-MeV data, a large disparity exists between the calculated and measured values of  $\Delta E$  in d3mm3. A calculation for a 41-MeV proton predicts a range in silicon of 8.5 mm (8.1 mm for a 40-MeV proton). These facts

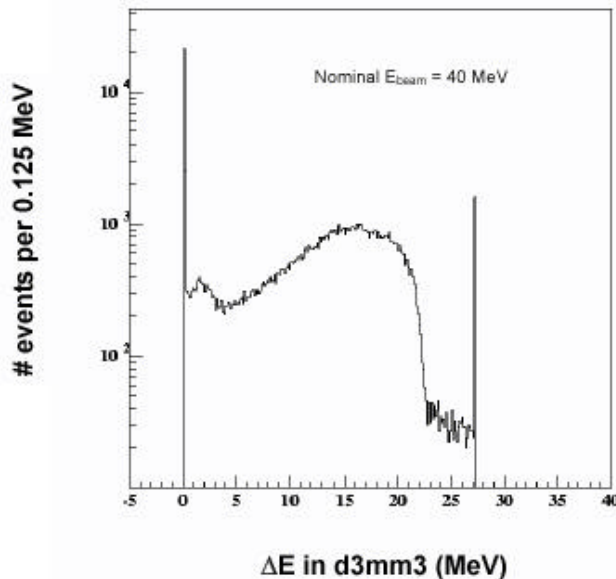


**Figure 3-6.** Deposited energy in d3mm3 in the 40 MeV run. Comparison of measured and calculated  $\Delta E$ 's indicates the actual energy may have been 41 MeV. The broad distribution seen here is due to straggling.

are related: the observed disparity arises because beam particles were stopping in d3mm3, and straggling effects produce a very broad distribution of  $\Delta E$ , as shown in **Figure 3-6**. The calculation that predicts a 19.4-MeV energy loss for protons in d3mm3 is overly simple in its treatment of stopping particles, in that it is assumed that the full energy of the particle at the entrance to d3mm3 will be recorded in the detector. The reality—as shown by **Figure 3-6**—is more complex. Atomic physics effects, including charge screening and charge pickup, reduce the amount of ionization energy deposited in the medium.<sup>5</sup> In this context, the calculated value of 19.4 MeV should be regarded as an approximate upper limit to  $\Delta E$  in d3mm3. The data distribution bears this out: despite a FWHM of about 10 MeV, it drops steeply above 20 MeV.

To test the consistency of the agreement between the data and the calculations (excluding d3mm3 in the 41-MeV data), we performed for each detector a linear regression between the measured and calculated  $\Delta E$ s. The fits give correlation coefficients greater than 0.9998, with most residuals less than 1% of the calculated values. The regression coefficients are used to further correct the  $\Delta E$ s (compounded with the factors obtained from the 250-MeV run) in the analysis of the data sets with the detectors in the space suit/phantom.

### 3.3.7 Landau Distribution Calculations

**Figures 3-7(a)** and **7(b)** show the same data as in **Figure 3-5**, but here we focus on the central bins of the single-proton peak. Even when we restrict the fit to the six peak bins, as in **Figure 3-7(a)**, it is obvious that the data do not obey a Gaussian statistical distribution. From **Figure 3-5**, it is also obvious that the data distribution just

<sup>5</sup> These effects cause the  $dE/dx$  vs. momentum curve to turn over below  $\beta\gamma \approx 0.05$  [17], rather than continuing to increase as  $1/\beta^2$ . The simple calculation used here assumes the curve continues upward indefinitely.

above the single-proton peak contains many more events than the fit distribution can account for. For the detectors used here, the Landau distribution [19] is expected to describe the spectra more accurately. We therefore generated several simulated Landau distributions of  $\Delta E$  for 223-MeV protons in a 3-mm-thick silicon detector, using a Monte Carlo method; the nominal parameters as per Ref. 19 predict a distribution broader than that seen in the data, an effect previously seen in other measurements [20]. This can be seen in **Figure 3-7(b)**, where the Landau distribution with nominal parameters is superimposed on the data (which are shown as a shaded histogram). Reducing the smearing term by 25% yields a distribution that agrees well with the d3mm1 data in the tail region between 3 and 4 MeV; this simulated distribution has a negligible fraction of events (0.02%) with  $\Delta E$  above 4 MeV. This is evidence that the high- $\Delta E$  events seen in the data (after pile-up removal) are due to nuclear interactions. Even the distribution shown in **Figure 3-7(b)**, which is overly broad and shifted to slightly higher  $\Delta E$  than the data, has a negligible fraction of events with  $\Delta E$  greater than twice that of the peak.

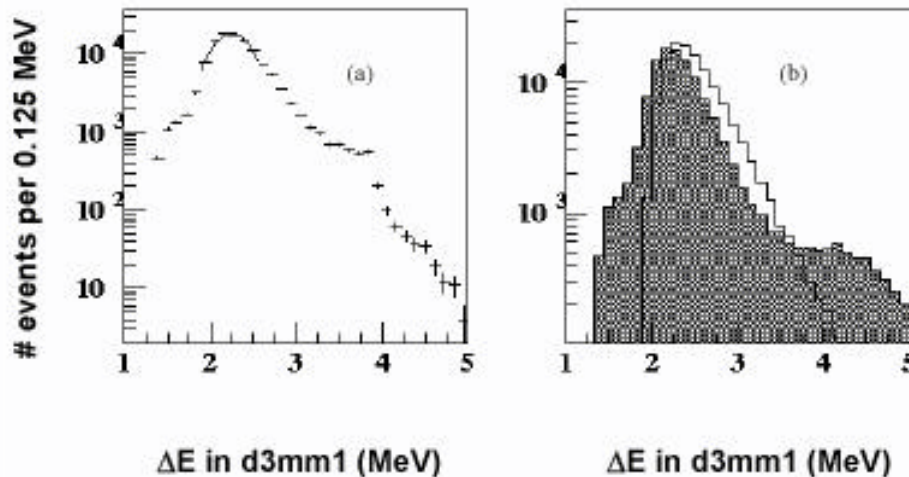


**Figure 3-7.** Histograms of the peak region in d3mm1. In 3-7(a), a Gaussian distribution fit to the center of the peak is shown as a curve, and the data are shown as points with error bars (in the center of the peak, the error bars are too small to be visible on this scale). In 3-7(b), the data are shown as a shaded histogram, and a histogram corresponding to a Landau distribution is superimposed.

### 3.3.8 Nuclear Interactions and High- $\Delta E$ Tails

The bare-beam data provide us with needed information about the detector response, not just in single-proton events, but also in events during which an interaction between an incident proton and a silicon nucleus produces a large  $\Delta E$  in one or more detectors. Proton-silicon (p-Si) nuclear interactions are qualitatively similar to, e.g., p-C interactions in tissue or p-Ca interactions in bone, so we may gain insight into those biologically-interesting reactions by examining p-Si interactions. Further, when considering the high- $\Delta E$  events due to interactions of beam protons in the space suit and tissue-equivalent materials, the high- $\Delta E$  events due to interactions occurring within the detectors must be taken into account as a source of background. For these reasons, it is necessary to understand the high- $\Delta E$  tails observed in the bare-beam data.

As discussed in detail in the Appendix, we estimate the total cross section for proton-silicon reactions at these energies to be about 634 mb (374 mb inelastic, 260 mb elastic). We therefore expect 0.96% of protons to interact in a 3-mm-thick silicon detector, consistent with the fractions of events seen in the high-end tails of the  $\Delta E$  distributions in the bare-beam data. Actually, most of the estimates that were shown in **Table 3-1** are smaller than 1%, but a difference in this direction is not surprising, since we systematically under-count the high- $\Delta E$  events in the data. (The extent to which this is true depends on how the pile-up events are handled.) There are at least two ways in which we under-count events in which there were interactions. First, some reactions will result in  $\Delta E$ s above the proton peak but not far enough above to meet any of our ad hoc definitions of the high- $\Delta E$  tail; second, some events with interactions may be removed by pile-up rejection cuts, particularly when we employ the graphical-cut technique, method (1), or the d3mm2 cut, method (3). Both of these pile-up rejection methods are prone to removing events with relatively light target fragments, such as a knock-out H or He nucleus. As previously described, an energetic, forward-going fragment produced in one detector can register a signal in the next detector. Similarly, when material is placed in close proximity to the detectors, target fragments produced there may penetrate into two or perhaps all three detectors. These events would not pass the graphical cut illustrated in **Figure 3-4**, nor would they pass a tight cut requiring a single proton in d3mm2.

### 3.3.9 Quantitative Effects of the High-DE Tails

**Table 3-3** shows the mean and root mean square (RMS) values of the  $\Delta E$  distributions obtained in the 250- and 155-MeV runs using the four pile-up rejection methods. In the table, we define the quantity  $\delta\Delta E$ , the difference (in percent) between the average  $\Delta E$  of a distribution and the  $\Delta E$  of the single-proton peak in the same distribution. It is apparent that the average  $\Delta E$ s shift to higher values as a result of nuclear interactions in the detectors; the effect is particularly evident in the 250-MeV data. In view of the relatively small probability of nuclear interactions (about 1% per detector), the shifts are large, ranging from 6% to 9%, depending on which method of pile-up rejection is used in a particular data set.

The values of  $\delta\Delta E$  in the 155-MeV data are not as large as those at the higher energy, suggesting that (1) there could be a decrease in the reaction cross sections (this is not expected, as per the previous discussion), or (2), the reduced energy available to either cause fragmentation or recoil of the target nucleus results in smaller energy depositions and hence fewer detectable high- $\Delta E$  events. A combination of the two factors may be responsible for the observed effect.

The changes in average  $\Delta E$  are a measure of the dose (in silicon) arising from p-Si nuclear interactions. We again emphasize the point that the present data do not allow for direct measurements of LET of the secondaries. Also, the volume of the silicon detectors does not correspond to any particular biological target of interest (as would, for instance, a TEPC at the appropriate gas pressure), nor do the density and composition of the detectors correspond to tissue. Nonetheless, because dose is by definition a measure of energy deposition per unit volume, and because the physical processes in tissue are expected to be analogous, we can interpret the  $\Delta E$ s measured in silicon detectors as roughly representing dose to tissue. This is a more accurate statement in the analysis of the space suit/phantom data, where the high-end tails of the  $\Delta E$  distributions are dominated by target fragments, recoils, and other slow particles created in the space suit, tissue-equivalent material, and bones in the phantom.

Because we do not measure the target fragment LET distributions, we cannot estimate quality factors or dose equivalents. Fortunately, those estimates have been reliably made in the same space suit/phantom locations (and a few others) using CR-39 [7]. The silicon detector data can be used as a cross-check on the estimated dose increases attributed to target fragments in the CR-39 data.

**Table 3-3.** Average  $\Delta E$  Values for the Three Detectors and Four Methods of Pile-Up Rejection, for the 223 and 145 MeV (nozzle energies) Bare-Beam Runs

	PUR method	223 MeV beam			145 MeV beam		
		$\Delta E$ Avg (MeV)	$\delta\Delta E$ (%)	RMS (MeV)	$\Delta E$ Avg (MeV)	$\delta\Delta E$ (%)	RMS (MeV)
d3mm1	1	2.54	6	1.55	3.32	4	1.41
	3	2.49	2	1.08	3.25	2	0.86
	4	2.73	14	1.97	3.58	12	1.94
	p peak	2.40	—	0.26	3.19	—	0.33
d3mm2	1	2.58	8	1.76	3.32	5	1.79
	2	2.59	9	1.77	3.30	5	1.78
	4	2.68	13	1.42	3.57	13	2.19
	p peak	2.38	—	0.29	3.15	—	0.43
d3mm3	1	2.66	9	1.85	3.54	7	1.84
	2	2.66	9	1.85	3.54	7	1.80
	3	2.62	7	1.71	3.48	5	1.69
	4	2.81	15	2.03	3.76	14	2.11
	p peak	2.44	—	0.28	3.30	—	0.34

Also shown are the percent increases in the averages compared to the proton peak  $\Delta E$ s ( $\delta\Delta E$ ) and RMSs of the distributions.

## 3.4 RESULTS WITH THE EMU SPACE SUIT AND PHANTOM

The second set of runs made use of the EMU suit, phantom, and water-equivalent plugs of material (this is the same material as in the phantom). A housing for the silicon detectors was made of the water-equivalent material ( $\rho = 1.0 \text{ g cm}^{-3}$ ), with 27 mm of it upstream of d3mm1, 22 mm between d3mm1 and 2, and an additional 22 mm between d3mm2 and 3. The housing was placed in three hole locations (skull, upper abdomen, and lower abdomen) within the phantom, which were encased in the appropriate portion of the EMU suit. At all locations, data were taken with the 250 MeV and 155 MeV nominal beam energies. The ranges of the lower-energy beams were not sufficient to penetrate the material in front of d3mm1, hence there was little reason to run with them. In the following, we present results from each of the three locations.

### 3.4.1 General Considerations

Ionization energy loss in materials interposed between the nozzle and the detectors slows the protons, shifting the locations of the proton peaks to higher  $\Delta E$ . For a given beam energy, the differences in spectra between

bare-beam data and data taken with various pieces of the EMU/phantom combination<sup>6</sup> are due to the site-specific EMU material and the water-equivalent plastic that comprised the detector holder, including the plugs between detectors. Target fragments produced in interactions of protons with nuclei in the suit or plastic may deposit energy in the detectors; to determine the fraction of events with fragments originating outside the detectors, we must subtract the fraction of high- $\Delta E$  events due to interactions in the detectors.

Given the proximity of the water-equivalent material plugs to the detectors, it is reasonable to ask whether relatively high-energy delta electrons produced in the plastic can cause large energy depositions in the detectors. The maximum electron kinetic energy is given, to a good approximation, by  $T_{\max} = 2 m_e \beta^2 \gamma^2 c^2 = 0.54 \text{ MeV}$  for the 223 MeV beam and 0.32 MeV for the 136 MeV beam (where we use the nominal beam energies at the nozzle). The practical ranges for these electrons are about 2 mm and just under 1 mm of water, respectively [21]. High- $\Delta E$  events as we have defined them are always above 4 MeV, so that at least 10 maximum-energy deltas, all produced very near the detectors, would be required to explain a high- $\Delta E$  event. Numerical integration of equation (23.7) of Ref. [17] shows that, with a 223-MeV beam, the rate of production of delta electrons is less than 1 per centimeter in water with a low-end cut of 100 keV electron energy. We therefore expect little or no contamination of the high- $\Delta E$  event samples from this source.

There are important differences between the configuration here and the bare-beam runs considered in the preceding. First, we have shown that the bare-beam spectra in d3mm2 and d3mm3 were influenced by target fragments formed in the detector(s) upstream. But in the arrangement considered here, there was a substantial amount of material in between each pair of detectors, so that slow particles produced far upstream, either in a preceding detector or in the plastic, might not reach a particular detector. This restricts the number of events with correlated high- $\Delta E$  in two detectors to those in which a relatively high-energy target fragment was created. Second, target fragments/recoils may be formed in the plastic in front of a particular detector and would have no influence on the  $\Delta E$  recorded in the previous detector. Third, the additional materials—even though they are low- $Z$ —result in increased Coulomb multiple scattering and losses of particles in the downstream detectors (d3mm2 and d3mm3).<sup>7</sup> Overall, therefore, we expect less correlation of  $\Delta E$  between detectors in these data than in the bare-beam data.

### 3.4.2 Brain Location: 223-MeV Beam

In the first of the runs with the space suit and phantom, the detectors, plugs, and their holder (also made of water-equivalent plastic) were placed in the phantom's head. The arrangement of detectors and plugs is sketched in **Figure 3-2(b)**. The top-most piece of the phantom was temporarily removed to allow access to the hole that had been made in a location corresponding approximately to the middle of the brain. After the detectors were placed in the hole, the top piece of the skull was replaced. The phantom's head was then placed on the Gantry 1 treatment table and the EMU helmet placed over the head. The beam was again incident vertically from above.

**Figures 3-8(a)-8(c)** show histograms of energy deposited in d3mm1, 2, and 3 for the run with the 250-MeV proton beam in this configuration. For each histogram, a single cut has been applied to the data, requiring  $\Delta E >$

---

<sup>6</sup> In these data, we cannot separate the observable effects due to the space suit from those due to the phantom and the water-equivalent plastic.

<sup>7</sup> By definition, there is no loss of particles in d3mm1, since its discriminated signal was used as the trigger.

1.4 MeV in that particular detector, in order to eliminate events where the detector was missed or was hit at its edge, where the charge collection efficiency is much less than 100%. There is little evidence of pile-up in these histograms; in particular, d3mm1 shows no sign of a peak at double the nominal proton  $\Delta E$ . Detector d3mm2 shows a possible shoulder at about twice the proton  $\Delta E$ , and d3mm3 shows a small peak there; fitting a Gaussian to the d3mm3 peak suggests that the number of pile-up events is less than 1% of the total.

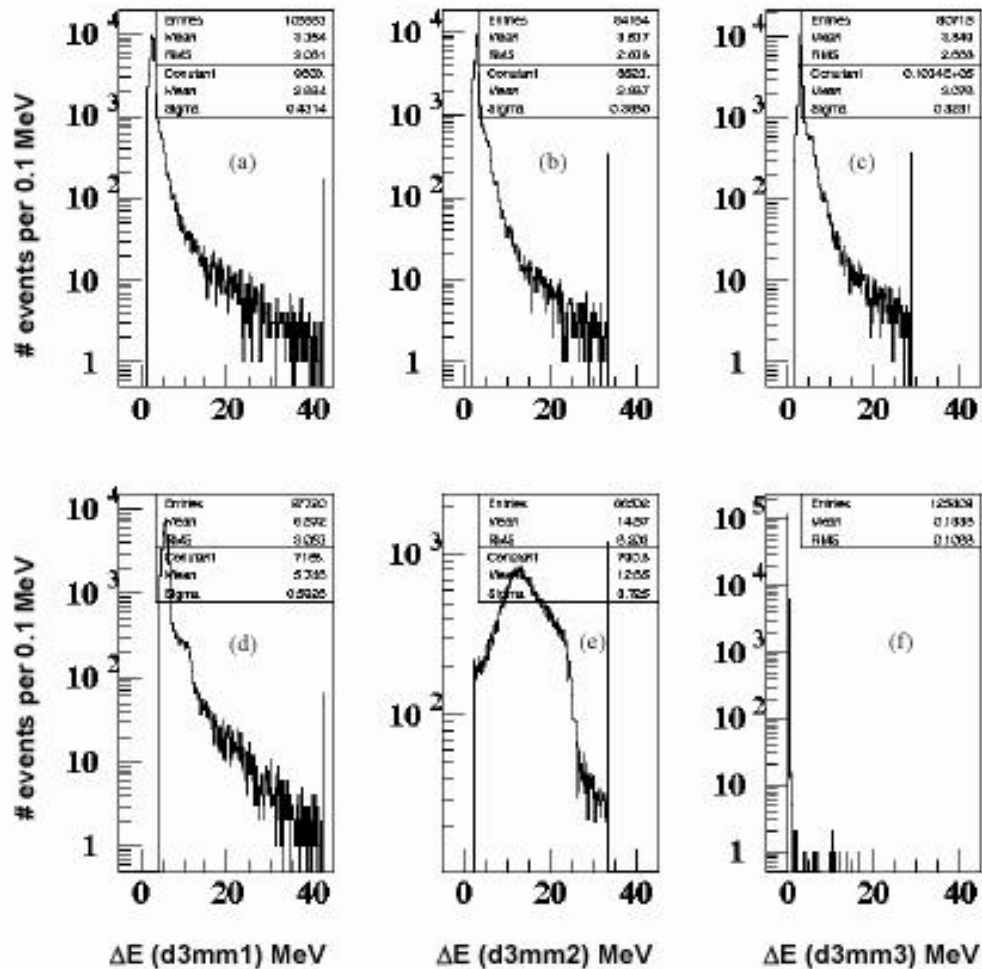


**Figure 3-8.** The top row, 8(a)-(c), shows histograms of  $\Delta E$  in (from left to right) d3mm1, 2, and 3 for the 250 MeV extracted beam incident on the EMU helmet with detectors placed in the position corresponding to the brain. In each histogram,  $\Delta E$  in that detector was required to be above 1.4 MeV to guarantee that the detector was hit by a beam proton and/or a secondary. Text boxes show the numbers of entries, means and RMSs of the entire distribution, and the parameters (constant, mean, and standard deviation) found by Gaussian fits to the central bins of the proton peaks. Bottom row, 3-8(d)-(f): Corresponding histograms with the 155 MeV extracted beam.

Compared to the bare-beam spectra, all detectors show substantial increases in the fractions of events with high  $\Delta E$ , as can be seen by examining the fractions obtained by the four methods previously defined. The results are shown in **Table 3-4**; the fractions are directly comparable to those in **Table 3-1** for the bare-beam runs at the same

extracted beam energies. We include the results from method (3), even though that method is overly restrictive with respect to the high- $\Delta E$  tail in d3mm1.

The fractions in **Table 3-4** show a few interesting trends: Excluding the method (3) results, we see that d3mm1 registers more high- $\Delta E$  events than the other detectors. Given the uneven distribution of materials (the helmet and 27 mm of plastic directly in front of d3mm1, compared to 22 mm of plastic directly in front of d3mm2 or d3mm3), this suggests the formation of many high-LET particles with sufficient energy to reach, and perhaps traverse, d3mm1, but which stopped in d3mm1 or in the plastic between d3mm1 and d3mm2. The fact that d3mm2 and d3mm3 show hints of pile-up, while d3mm1 does not, supports this interpretation: the expected  $\approx 1\%$  of pile-up events with  $\Delta E$  near twice  $\Delta E_{\text{peak}}$  do not show up as a distinct peak because they are swamped by events with target fragments (that fail to reach d3mm2 and d3mm3) that deposit similar amounts of energy.

**Table 3-4.** Fractions of Events Found in the High- $\Delta E$  Tails of the Distributions in the Three Detectors for the Runs Using the EMU Helmet and the Phantom's Head

Method	223 MeV beam % of events in high- $\Delta E$ tail			136 MeV beam % of events in high- $\Delta E$ tail		
	d3mm1	d3mm2	d3mm3	d3mm1	d3mm2	d3mm3
1	4.6	3.0	3.7	3.2	0.6	—
2	—	2.6	3.2	—	0.5	—
3	1.3	—	2.3	0.4	—	—
4 ( $4\Delta E_p$ )	2.0	1.7	1.4	0.8	<1.4	—
4' ( $3\Delta E_p$ )	2.6	2.6	2.3	1.7	<1.4	—

The 136 MeV beam stopped in the water-equivalent plastic between d3mm2 and d3mm3, hence there are no data for d3mm3.

It is clear from **Table 3-4** that method (4) yields significantly lower estimates of events in the tails than are found by the other methods. Because of this, and because these data show little evidence of pile-up, we have implemented a modified version of method (4), which we call method (4'), where we relax the definition of the high-end tail to be those events with  $\Delta E > 3 \Delta E_{\text{peak}}$ . The fractions obtained with this looser definition are in somewhat better agreement with the other methods.

The single-proton peaks in **Figures 3-8(a)-(c)** are shifted to higher  $\Delta E$ s than in the bare-beam run due to the materials in between the nozzle and the detectors; the amount of the shift is an indirect measurement of the total mass of those materials. Using our beam line energy-loss code, we find that the  $\Delta E_{\text{peak}}$  values found in these data are highly consistent with a proton energy of 181 MeV incident on d3mm1, implying energy losses totaling about 42 MeV in the helmet, phantom skull, and first water-equivalent plug. A calculation of energy lost by a 223-MeV beam in water shows that the materials in front of d3mm1 were equivalent to approximately 9.5 cm of water.

Taking the ratio of average  $\Delta E$  over the entire spectrum to  $\Delta E$  of the single-proton peak shows (roughly speaking) the effect of high-LET particles on dose. Using the ratio effectively divides out the increases due to energy loss that shift the spectra to higher  $\Delta E$ . For all three detectors, the increase in the average using method (4) is 22%-25%. In the bare-beam runs, the comparable increases were 13%-15% due to interactions of protons in silicon.

If we divide out<sup>8</sup> the increases found in the bare-beam runs (e.g., for d3mm1, we take 1.24/1.14), we find net increases of 9%, 8%, and 9% for d3mm1, 2, and 3, respectively, in remarkably good agreement with the 7.6% dose increase obtained with CR-39 for the same beam and detector placement [7]. This slightly higher dose increase observed with the silicon detectors may be related to the fact that CR-39 misses target fragments with LET below 5 keV/μm, which appear to be numerous, judging by the number of events in which two or three silicon detectors simultaneously record relatively large ΔE.

Repeating the preceding calculations using method (1), we find increases of 11%-20%, compared to 6%-9% in the bare-beam run. Again dividing out the bare-beam results, we find net increases of 13%, 3%, and 8% for the three detectors. The d3mm2 increase seems anomalously small; this may have to do with the details of the cut contour (which is somewhat subjective) used in this method. The other methods also show increases in average ΔEs in this data set compared to the bare-beam run. Method (2), which employs a tight cut on d3mm1, yields net increases of 2% and 6% for d3mm2 and d3mm3, respectively (note that d3mm2 again shows a very small increase); and method (3) (tight cut on d3mm2) yields net increases of 4% and 7% for d3mm1 and d3mm3, respectively. Recall that method (3) biases against high-ΔE in d3mm1. For d3mm3, the increases found by all methods are remarkably consistent, in all cases between 7% and 9%. The d3mm1 net increases are comparable, 9% and 13% using the least biased methods. The d3mm2 results do not agree particularly well with those from the other detectors except using method (4). The average ΔEs obtained by the various methods are summarized in **Table 3-5**.

In summary, we find a significant increase in the number of high-LET particles in this run compared to the bare-beam run at the same extracted energy. This increase correlates with increased average ΔE in the detectors, typically around 8%-9% after accounting for p-Si interactions. This is quite similar to the 7.6% dose increase attributed to target fragments in the corresponding measurement using CR-39.

**Table 3-5.** Average ΔEs in the Three Detectors Using the Four Methods of Pile-Up Rejection for the Runs Using the EMU Helmet and the Phantom's Head

PUR Method	223 MeV						136 MeV					
	d3mm2		d3mm2		d3mm3		d3mm1		d3mm2		d3mm3	
	Avg ΔE (MeV)	δΔE (%)										
1	3.22	20	3.22	11	3.62	18	6.26	9	13.9	10	—	—
2	—	—	3.19	10	3.55	15	—	—	14.6	15	—	—
3	2.84	6	—	—	3.51	14	6.04	5	—	—	—	—
4	3.35	24	3.54	22	3.85	25	6.57	14	14.6	15	—	—
p peak	2.69	—	2.89	—	3.08	—	5.75	—	12.7	—	—	—

The influence of the high-ΔE tails on the distributions is estimated by δΔE, the percentage increase in the average ΔE over the ΔE of the single-proton peak (shown in the bottom row) in the same spectrum.

<sup>8</sup> This is an *ad hoc* attempt to account for the part of the dose increase (relative to the proton peak) that is due to the nuclear interactions that are known to occur in the detector, as per the preceding section.

### 3.4.3 Brain Location: 136-MeV Beam

With the beam line configuration kept constant, the energy of the proton beam in the accelerator was changed to 155 MeV (extracted) and data taking resumed. The spectra obtained in this run are shown in **Figures 3-8(d)-(f)**. The materials along the beam's path slowed the protons so that they stopped in the plastic between d3mm2 and d3mm3; this is why the d3mm3 spectrum has very nearly 100% of its entries at 0, and also explains the very broad distribution in d3mm2 (due to straggling near the end of the range).

We have applied the usual methods to obtain the fractions of events in the high-end tails for d3mm1 and d3mm2; the results are shown in the right half of **Table 3-4**. Relative to the 155 MeV bare-beam run, an increase in high- $\Delta E$  events in d3mm1 is seen, though it is not as large as in the higher-energy run at the same location (e.g., 3.2% in the tail using method (1) at this energy compared to 4.6% at the higher energy). It is obvious from **Figure 3-8(e)** that we have little information about d3mm2 in regard to the high- $\Delta E$  tail, and we quote only upper limits for methods (4) and (4'). For the other methods, we find fewer high-end events in d3mm2 than in the comparable bare-beam data (right side of **Table 3-1**), likely due to the extremely low energy of the protons as they enter the plug in front of d3mm2 (at about 30 MeV) and as they exit the plug and enter d3mm2 (at about 17 MeV). There is simply not sufficient energy to produce (in the plug) many forward-going fragments with enough range to reach d3mm2; nor is there much energy available for p-Si interactions when the protons reach the detector. The decrease (relative to the 223 MeV beam) seen in the fraction of high- $\Delta E$  events in d3mm1 is qualitatively consistent with this picture (lower energy  $\rightarrow$  fewer target fragments).

The  $\Delta E_{\text{peak}}$  values found in this run are found to be most consistent with calculations where the proton energy incident on d3mm1 is 66 to 67 MeV. In the previous section, we estimated from the 223-MeV beam data that the material in front of d3mm1 in this location represented about 9.5 cm of water; using a nozzle energy of 136 MeV, we predict an incident energy on d3mm1 of 68 MeV, in good agreement with the numbers obtained from the data. The agreement is slightly better with 9.6 cm of water-equivalent material in front of d3mm1 in the calculation.

Net dose increases as estimated (as in the preceding section) by dividing  $\delta\Delta E$  in situ by the corresponding  $\delta\Delta E$  in the bare-beam runs yields the following: method (1), 5% increases in both d3mm1 and 2; method (2), a 10% increase in d3mm2; method (3), a 3% increase in d3mm1 (recall that this method is biased and yields very low estimates for d3mm1); and method (4), 2% increases in both d3mm1 and 2. Although there is some spread in these results, they are with one exception in the range 2% – 5%, and smaller than the corresponding net dose increases found in the same location with the 223-MeV beam.

### 3.4.4 Slice 8: 223-MeV Beam

We removed the detectors from the phantom's skull and placed them inside the hole in slice 8 of the phantom, in the upper abdominal area, as indicated in **Figure 3-1**. We placed the phantom's torso inside the EMU suit's upper section and set it on the treatment table with the detectors centered in the beam. The two parts of the buckle for the LCVG (liquid-cooled ventilation garment) inside the space suit were mated. We noted that the buckle shadowed some of the detector area. We do not know the chemical composition and density of the buckle at present, but it is metallic and not more than 3 cm thick. We also noted that the suit's "swivel bearing," another

metallic piece that rings the suit, was not directly between the nozzle and the detectors, but was not far from the beam, which has a diameter of 15–20 cm.

Figures 3-9(a)–9(c) are the  $\Delta E$  histograms in d3mm1-3 obtained in this configuration with the 223-MeV beam. All three histograms show pronounced increases in the fractions of events above the proton peaks. Table 3-6 shows the results obtained with the different pile-up rejection methods; they are typically in the 10%-20% range, far larger fractions than were seen in the brain data. The average  $\Delta E$ s (see Table 3-7) are shifted to values that are more than double those of the proton peaks, a radical departure from the previous data sets. This is far in excess of any plausible increase from nuclear interactions; there is some other physical effect related to this placement of detectors that was not present in the data sets previously discussed.

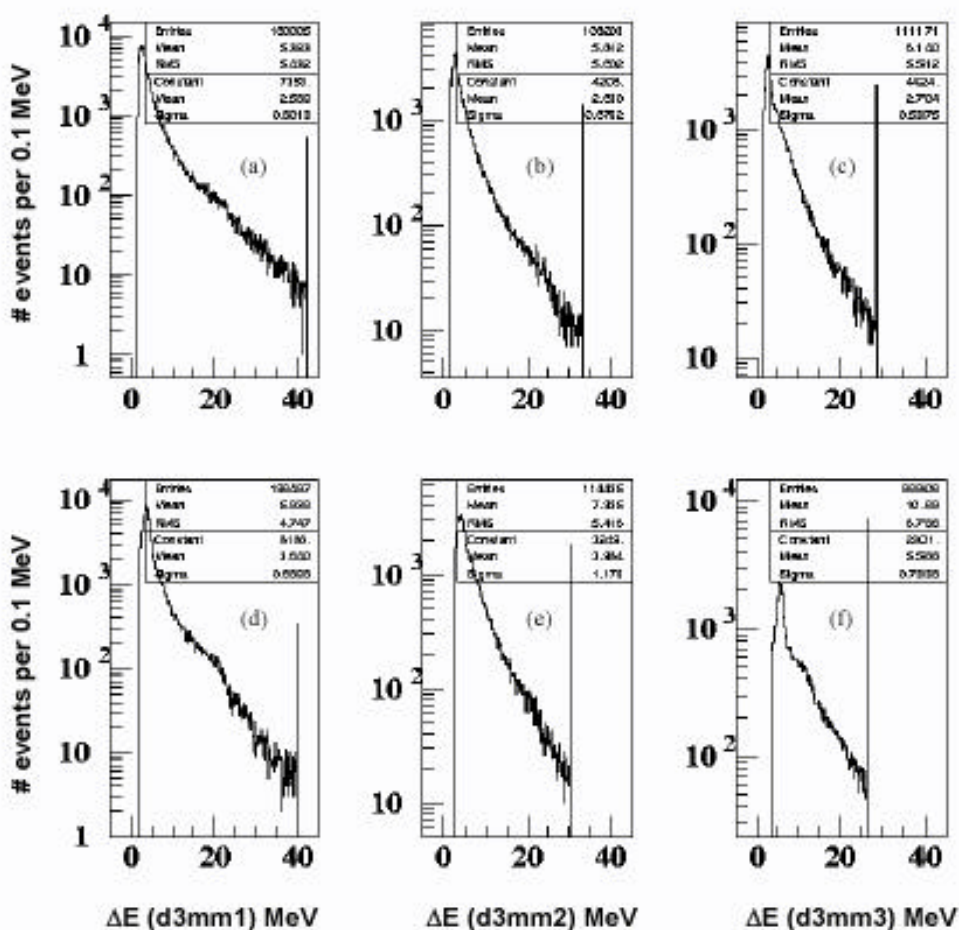


Figure 3-9. Top row: Histograms of  $\Delta E$  in d3mm1, 2, and 3 for the 250 MeV extracted beam incident with detectors placed in the phantom’s upper abdomen (slice 8). Bottom row: Corresponding histograms for the run with the 155 MeV extracted beam. In each case,  $\Delta E$  averaged over the entire distribution is far larger than that of the single-proton peak.

The proton peak locations are most consistent with calculations where the proton energy incident on d3mm1 was about 205 MeV, with an estimated uncertainty of  $\pm 5$  MeV; this is higher than the 181 MeV found with the same beam in the phantom’s brain, meaning that there is—for the most part—less material between the nozzle and d3mm1 in this configuration. A separate calculation shows that the observed 18-MeV energy loss of the beam

between the nozzle and d3mm1 would be produced by about 4.5 cm of water, 2.7 cm of which is accounted for by the first water-equivalent plug. The total of 4.5 cm is less than half of the 9.5 cm found to have been present upstream of d3mm1 in the measurement in the brain. It would therefore seem highly unlikely that the drastic increases in the fractions of events in the high- $\Delta E$  tails can be due to target fragments or recoils, given that there is less material for the protons to interact with.

**Table 3-6.** Fractions of Events Found in the High- $\Delta E$  Tails of the Distributions in the Three Detectors for the Runs in Slice 8 of the Phantom, the Upper Abdomen  
*Pile-up rejection method (1) was not applicable to these data.*

Method	223 MeV beam % of events in high- $\Delta E$ tail			136 MeV beam % of events in high- $\Delta E$ tail		
	d3mm1	d3mm2	d3mm3	d3mm1	d3mm2	d3mm3
2	—	17.5	27.1	—	21.6	31.9
3	9.7	—	20.1	8.0	—	21.6
4 ( $4\Delta E_p$ )	10.6	11.9	12.6	5.8	7.6	12.2
4' ( $3\Delta E_p$ )	16.1	18.5	20.3	10.4	13.6	18.1

We can gain additional insight into the nature of the high- $\Delta E$  tails by examining the scatter plot of d3mm2 vs. d3mm1, shown in **Figure 3-10(a)**. The same data are shown as contours in **Figure 3-10(b)**. There is a high concentration of events with a single proton in the main peak of both detectors, visible as the small contours centered on about 2.5 MeV  $\Delta E$  in each detector. Contours going toward higher  $\Delta E$  in both detectors, but especially in d3mm2, can be seen. The same data points make a nearly vertical dark band of events in **Figure 3-10(a)**. (The band is closer to vertical in 3-10a because of the greater range of  $\Delta E$  in d3mm1 covered in this plot compared to 3-10(b).) This upward-turned band is due to protons that were slowed considerably from beam velocity before reaching d3mm1. Their

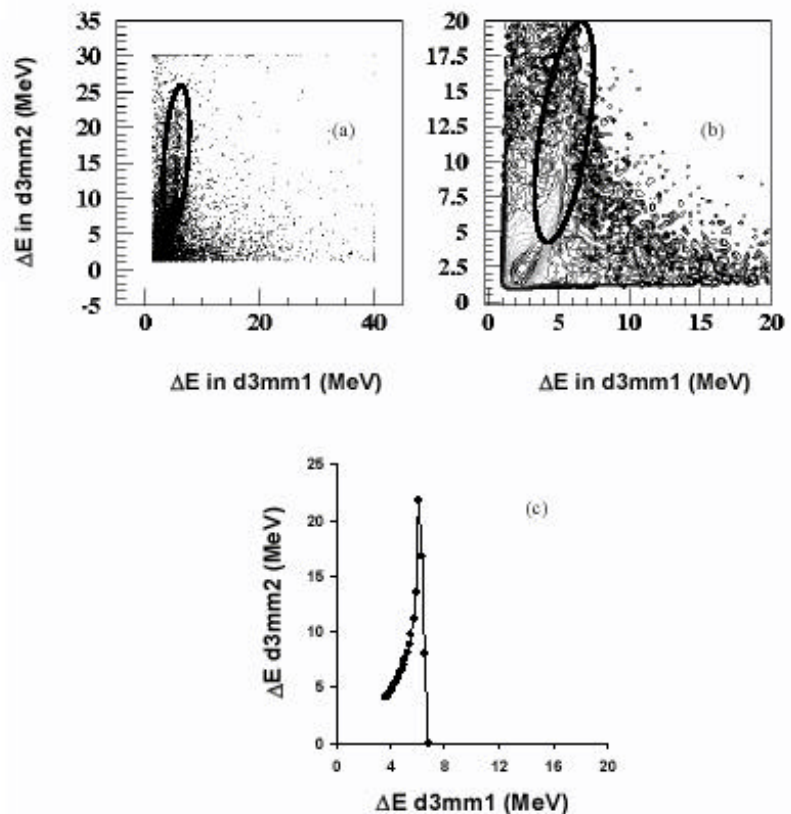


**Figure 3-10.** Left: 3.10(a), scatter plot of  $\Delta E$  in d3mm2 vs.  $\Delta E$  in d3mm1 for the run with the detectors in slice 8 of the phantom (upper abdomen). Right: 3.10(b), same data in the 0-20 MeV range of  $\Delta E$ , shown as a contour plot. In 3.10(a) and 3.10(b), ovals indicate the region populated by slow protons. Bottom: 3.10(c), calculated  $\Delta E$  relation accounting only for ionization energy loss.

velocities—already low before d3mm1—are further reduced by the additional material between d3mm1 and d3mm2. Many of these protons will stop after d3mm2 and leave no signal in d3mm3. This is confirmed by noticing that, in the d3mm3 histogram shown in **Figure 3-9(c)**, there are only 60% as many events with a hit above zero in d3mm3 as there are in **Figure 3-9(a)**, the corresponding histogram for d3mm1.

Our beam line energy loss calculation shows that protons with energies below about 84 MeV will leave this type of  $\Delta E$  pattern. We have calculated the correlation between  $\Delta E$  in d3mm2 and  $\Delta E$  in d3mm1 for slow protons, with incident energies on d3mm1 in the range from 55 to 120 MeV (corresponding to 80 – 135 MeV incident on the water-equivalent  $\Delta$  plug directly in front of d3mm1). The results of the calculation are shown in **Figure 3-10(c)**: the sharply rising, nearly vertical band seen in the data is accurately reproduced.<sup>9</sup> We conclude that these data contain many protons that have energies below 100 MeV when they reach d3mm1. To decrease a proton’s energy from the 223-MeV nozzle energy to 100 MeV requires 24–40 g cm<sup>-2</sup> of material;<sup>10</sup> the first water-equivalent plug accounts for 2.7 g cm<sup>-2</sup>, a small fraction of the total.

It is important to note that the scatter plots show no enhancement in the number of events that would correspond to two protons in each detector. We would expect some hint of this, particularly in the contours of **Figure 3-10(b)**, in the vicinity of  $\Delta E = 5$  MeV in each detector, if there were significant pile-up in this data set. However, no enhancement is seen, consistent with the observation from the  $\Delta E$  histograms that there appears to be very little pile-up in this run, or at least that the pile-up events are far outnumbered by the slow protons.

One conceivable explanation for the large number of high- $\Delta E$  events is that the LCVG buckle is responsible. It is possible that the slow protons seen in the detectors (especially in d3mm1) have scattered in from the buckle, and that they are slow because of ionization energy losses there. However, as we will show, if this is so, the buckle must have very high density in order to produce the observed proton energies. An alternative explanation is that some part of the beam was scraping an aperture in the transport line (see subsection H below).

CT scans of the space suit/phantom, as shown in **Figure 3-11**, show that only a small portion of the detector area was occluded by the buckle. It can also be seen that the buckle’s long axis was not at 90° with respect to the beam direction; that is, protons passing through the buckle had to traverse a pathlength  $L$ , given by  $L = d / \cos(\theta)$  where  $d$  is the depth of material and  $\theta$  is the buckle’s angle of inclination with respect to the normal to the beam axis. Using the MRI images, we estimate  $\theta \approx 22^\circ$ . The outline of the plug that held the detectors is faintly visible as an outline, due to small air gaps around the edges; using this as a landmark to set the approximate scale of the image, we estimate that the buckle is 2.55 cm deep. Given its tilt with respect to the beam axis, this yields a pathlength of about 2.75 cm for particles going entirely through it. To facilitate visualizing the relative positions, in **Figure 3-11c** we overlay a sketch of the detectors, along with a solid gray rectangle representing the detector holder. (The contrast of the buckle has been enhanced.) The sizes and positions of the detectors are roughly to scale. The full three-dimensional geometry is much more complicated than this single slice can represent; still, it is clear that most protons incident on d3mm1 missed the buckle entirely, and many others traversed only the corner of the buckle

---

<sup>9</sup> This is a highly abnormal correlation plot compared to that usually seen for two adjacent detectors; we emphasize that the presence of the 22-mm-thick plug between the detectors is the cause.

<sup>10</sup> The areal density required is strongly dependent on the material’s electron density. This amount of energy loss occurs in 24 g cm<sup>-2</sup> of H<sub>2</sub>O, 30 g cm<sup>-2</sup> of Al, 34 g cm<sup>-2</sup> of stainless steel, or 47 g cm<sup>-2</sup> of Pb.

and therefore not the full depth. Few if any straight-line trajectories traverse the full depth of the buckle and hit the silicon detectors.

Assuming for the moment that the buckle is the source of the low-energy protons, we can get a rough estimate of its density. We hypothesize that the buckle is made of stainless steel, which has a density of  $7.93 \text{ g cm}^{-2}$ . Combined with the 2.55 cm depth estimate and the tilt angle, this yields an areal density of  $21.8 \text{ g cm}^{-2}$ , somewhat

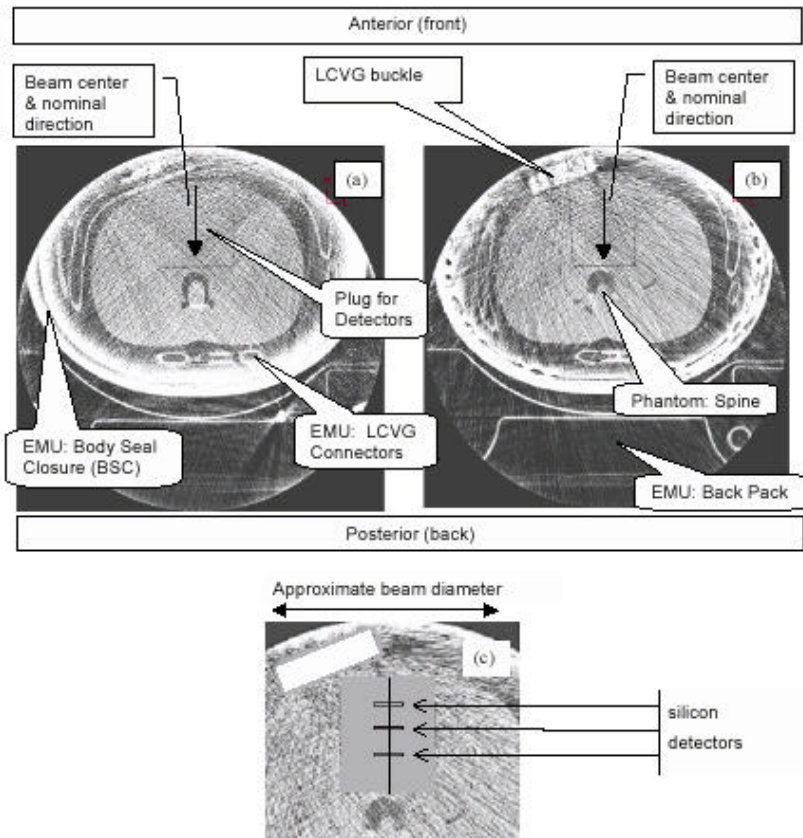


**Figure 3-11.** CT images of the space suit and phantom, the outline of the Body Seal Closure metal joint is shown in 3-11(a) (upper left). Due to limitations of the CT machine bore and image reconstruction size, only the lower portion of the closure is visible from these CT images. In 3-11(b) (upper right), the LCVG buckle can be seen clearly. Figure 3-11(c) is centered on the area containing the buckle, detector holder, and detectors.

lower than the estimates above based on the proton energies seen in the data. Previously, we calculated that the maximum-energy protons (those missing the buckle) that hit d3mm1 had traversed about 4.5 cm of water-equivalent material, 2.7 cm of which is accounted for by the first plastic plug. This leaves about  $1.8 \text{ g cm}^{-2}$  for the other materials between the nozzle and the first plug, assuming those materials have electron densities similar to  $\text{H}_2\text{O}$ . A 223 MeV proton passing through this material and a 2.75 cm long path through the buckle would have an energy of 142 MeV at the first plug, and 122 MeV at d3mm1. There are certainly protons of this energy, and lower, incident on d3mm1 in the data. The presence of the lower-energy protons suggests that the actual density of the buckle is higher than that of stainless steel. If in fact the buckle is a

comparatively low-density material, such as aluminum, then it cannot possibly be the source of the slow protons. In that case, it would have to have been that there was some other thick, dense piece of the space suit in the path of the beam during this run.

If the buckle has such high density, this would be consistent with the hypothesis that many slow protons in d3mm1 have initial trajectories several cm away from the beam centerline that undergo large deflections in the buckle from Coulomb multiple scattering. In this process, the RMS scattering angle is proportional to the charge  $Z$

of the material being traversed, and inversely proportional to the momentum of the incident particle. Thus a thick piece of dense, high-Z material will cause both significant energy loss and scattering, and the effects enhance one another—more scattering as momentum decreases leads to longer paths through the material, which in turn leads to still more scattering. For the case described just above, the average energy in the buckle (assumed to be stainless steel) is about 180 MeV; the calculated RMS scattering angle in steel is about  $4.5^\circ$  at this energy. Assuming a Gaussian<sup>11</sup> scattering distribution, this means that about 5% of the protons hitting the buckle have scattering angles of  $9^\circ$  or larger. A denser and higher-Z material than stainless steel would produce an even broader distribution, both because of increased scattering and increased energy loss; conversely, a less dense, lower-Z material such as aluminum would cause much less scattering—less than  $2^\circ$  RMS for 200 MeV protons in a 2.75 cm ( $7.4 \text{ g cm}^{-2}$ ) piece.

If the beam spot was large enough to entirely cover the buckle, then given that the area of the buckle is large ( $\sim 100 \text{ cm}^2$ ) compared to that of d3mm1 ( $4.5 \text{ cm}^2$ ), it seems plausible that the relatively infrequent large-angle scatters are enough to account for the 10-20% of the detected event samples that are attributable to slow protons. That is, a very large number of protons hit the buckle compared to the number hitting d3mm1 directly, and a small percentage of those in the buckle undergo scattering sufficient to deflect them into d3mm1. Their energy is reduced by ionization energy loss in the buckle and an increased pathlength through the first plug.

An essential feature of the experiment is that any hit above threshold in d3mm1 triggered the readout, so that any slow particles that hit d3mm1 but missed the other detectors (because of stopping or scattering) were recorded. On the other hand, slow particles that missed d3mm1 but entered d3mm2 or d3mm3 (presumably at large angles with respect to the nominal beam axis), would not be recorded. This accounts for the significant reduction in the numbers of entries in the d3mm2 and d3mm3 histograms—**Figure 3-9(b)** and **3-9(c)**—compared to the number in d3mm1 in **Figure 3-9(a)**.

Because the silicon detector spectra were swamped by low-energy protons, it is difficult to make any estimates of the contributions of recoils or target fragments in this location—the methods devised for the previous runs do not apply well to this data set. However, we note that in **Figure 3-10**, it is clear that the tail of the slow protons in d3mm2 extends up to  $\Delta E$  of about 23 MeV. If we assume all events with  $\Delta E > 23 \text{ MeV}$  in d3mm2 are due to target fragments or recoils, we can get lower bounds on their prevalence and contribution to dose. We find 2.75% of the events with hits above zero in d3mm2 satisfy this criterion; fully half of those are in the overflow bin, so we can say only that they had  $\Delta E > 33 \text{ MeV}$ . The events below 23 MeV have an average  $\Delta E$  of 5.10 MeV, the distribution as a whole, 5.81 MeV, so the events above 23 MeV pull the average  $\Delta E$  up by about 14%. It is necessary to correct this for p-Si interactions in the detector, so we have applied the same method to the bare-beam data at 223 MeV beam energy, and find that the events with  $\Delta E > 23 \text{ MeV}$  in that sample pull the average up by 4.5%. Taking this into account, the estimated net increase in dose is 9%. If, as expected, the high-LET particles are mostly produced in the water-equivalent plugs surrounding the detectors—which were the same in all runs—then we would expect to see only small changes in their contribution to dose in going from one location in the phantom to another; hence it is not surprising that the estimated 9% dose increase found here is quite consistent with the 8% net increase estimated for d3mm2 in the phantom's brain (using method (4)).

---

<sup>11</sup> The actual distributions are non-Gaussian – there are more high-angle scatters than predicted by this approximation.

Even at an energy as low as 55 MeV, a proton’s LET is about 1.2 keV/μm, well below the 5-keV/μm threshold of CR-39. If the slow protons were present in the combined TLD/CR-39 exposure, their contributions to dose were integrated in the TLD dose but did not contribute to the estimate of dose ascribed to target fragments (3.4% of the total). The dramatic increases seen in the average ΔE/peak ΔE in our detectors reflect an increase in dose (by factors of about 2) compared to the dose that would be expected were there no source of scattered low-energy protons. In the normalization of the high-LET spectrum in CR-39, the LET of incident beam-energy protons is used to calculate the number of incident protons for a given dose; if present, the slow protons would increase the average LET of the incident particles and consequently affect the normalization.

### 3.4.5 Slice 8: 136 MeV Beam

**Figures 3-9(d)-(f)** show the histograms obtained with the 136 MeV beam in the same upper abdominal location. The spectra are qualitatively similar to those in **Figures 3-9(a)-(c)**, in that they contain many particles with large ΔE. The fractions of events found in the high-ΔE tails are shown in **Table 3-6**, and the average ΔEs in **Table 3-7**. The increase in average ΔE/peak ΔE is large, but not quite as large as in the run with the 223 MeV beam. Probably much of this is due to saturation of the electronics; as can be seen in the **Figure 3-9** histograms, considerably more events in the 136 MeV run appear in the overflow bins than in the 223 MeV run. This is simply because the entire spectrum of particles—including those passing through the LCVG buckle or other scattering source—is shifted to higher ΔE when the beam energy decreases. Therefore, while the saturation of the electronics artificially reduces the values of average ΔE in all data sets, it is a particularly significant effect in this one.

**Table 3-7.** Average ΔEs in the Three Detectors Using Three of the Four Methods of Pile-Up Rejection for the Runs in Phantom Slice 8

PUR Method	223 MeV						136 MeV					
	d3mm2		d3mm2		d3mm3		d3mm1		d3mm2		d3mm3	
	Avg ΔE (MeV)	δΔE (%)										
2	—	—	4.47	70	5.26	94	—	—	6.76	70	10.5	74
3	3.65	36	—	—	4.67	73	4.56	25	—	—	9.02	50
4	5.39	108	5.81	121	6.14	127	5.84	60	7.34	84	11.6	92
p peak	2.59	—	2.63	—	2.70	—	3.64	—	3.98	—	6.03	—

Overall, the lower-energy data are quite consistent with the higher-energy data in the same location. Again, the large flux of low-energy protons scattering into the detectors makes our usual methods of determining the contributions of high-LET particles unusable. We have repeated the analysis described in the preceding section, using d3mm2 and looking at events with ΔE > 23 MeV since this is the largest possible energy deposition from a slow proton that also went through d3mm1. (We note that scatter plots for this data set analogous to those shown in **Figure 3-10** show the same upward-turning band of events due to slow protons.) We find that the events above 23 MeV in d3mm2 pull the average ΔE of the whole distribution up by 14.3%, compared to 4.0% in the bare-beam run at the same extracted beam energy. This leads to an estimated net dose increase of 10%.

### 3.4.6 Slice 9: 223 MeV Beam

Careful examination of the data obtained in this location shows that the detectors recorded only events with  $\Delta E$  corresponding to two protons, or higher, in d3mm1; the problem was an erroneously high setting for the trigger threshold in d3mm1. In a scatter plot of  $\Delta E$  in d3mm3 vs.  $\Delta E$  in d3mm2, one can select the events with one proton in each detector; these turn out to represent about 7% of the sample. When we examine the d3mm1 spectrum on those events, we find only events with  $\Delta E$  corresponding to two protons (or higher  $\Delta E$ ). No events were recorded where only a single proton was incident on d3mm1; therefore, these data cannot be salvaged, except to determine the locations of the single-proton peaks in d3mm2 and d3mm3. These are found to be 2.22 MeV and 2.58 MeV for d3mm2 and d3mm3 respectively. The result for d3mm2 is anomalously low in view of the 2.40 MeV expected in d3mm2 in the bare-beam run with the same extracted beam energy; any materials on the beam line—as were surely present in this run—will cause the peak  $\Delta E$  to increase, not decrease. Calculations show that the d3mm3 result is most consistent with a beam energy of  $223 \pm 10$  MeV incident on d3mm1. However, 223 MeV is the nominal energy of the beam at the nozzle, assuming the upstream scattering foils were in place. If there were no additional materials in between the nozzle and the first plug, the energy at d3mm1 would be about 212 MeV, just slightly below the lower limit of the estimated uncertainty. Given that there was at least some thin material present (the suit fabric and the LCVG fabric), the energy at d3mm1 must in reality be lower than 212 MeV. Thus the d3mm3 peak  $\Delta E$  is also anomalously low, though not as obviously so as for the d3mm2 peak.

There is another (unlikely) possibility: If the scattering foils were absent, the nozzle energy would be about 247 MeV, and a beam energy of 223 MeV (or even 233 MeV, at the high end of the uncertainty) would be possible even with a significant depth of material in between the nozzle and the first plug.

### 3.4.7 Slice 9: 136 MeV Beam

Good data were obtained in this location with the lower beam energy. The histograms in the top row of **Figure 3-12** show the spectra in d3mm1-3 with no cuts against pile-up. Significant pile-up peaks are seen, particularly in d3mm2 and d3mm3. The remaining histograms in **Figure 3-12** are: (second row) d3mm1-3 after pile-up rejection method (1) is applied (third row, from left to right); d3mm1 after method (3) is applied, then d3mm2 and d3mm3 histograms after method (2) is applied. It is clear that the cuts remove most of the pile-up events. **Table 3-8** shows the results using the four methods to obtain the fractions of events found in the high- $\Delta E$  tails, and **Table 3-9** shows the results for average and peak  $\Delta E$ s. The fractions and the values of  $\delta\Delta E$  appear to represent an intermediate case between the results obtained in the brain and those obtained in slice 8 of the phantom. Because there was significant event pile-up in this run, the average  $\Delta E$  and  $\delta\Delta E$  values obtained using method (4) will be pulled up significantly. However, the estimates for fractions of events in the tails using methods (4) and (4') should still be valid, provided (as seems likely) that events with 4 or more protons in coincidence were rare.

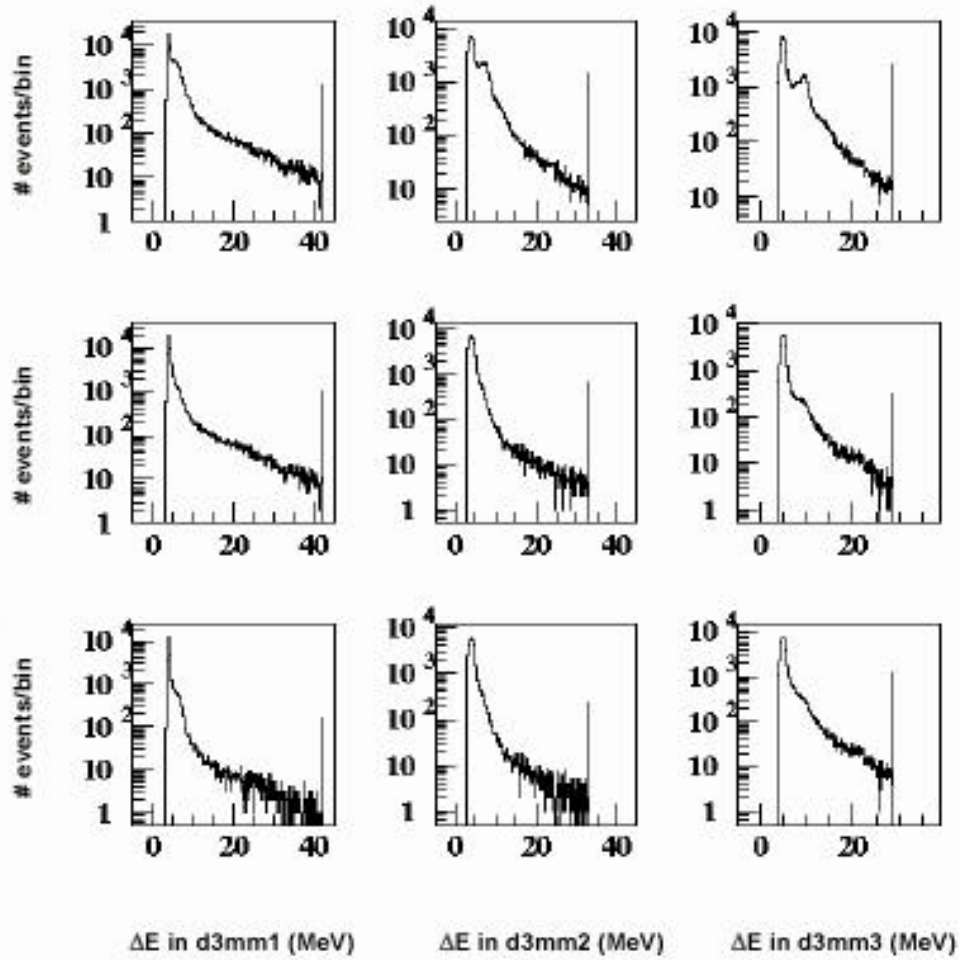


**Figure 3-12.** Histograms of  $\Delta E$  for the run in phantom slice 9 with the 155 MeV extracted beam energy. Top row: Spectra with no cuts to remove pile-up; peaks from 2-proton events are visible, especially in d3mm2 and 3. Middle row: Spectra after method (1) applied. Bottom row: Left-most histogram, d3mm1 after method (3) applied; middle and right, d3mm2 and 3 after method (1) applied.

**Table 3-8.** Fractions of Events Found in the High- $\Delta E$  Tails of the Distributions in the Three Detectors for the Runs in Slice 9 of the Phantom, the Lower Abdomen

136 MeV beam			
% of events in high- $\Delta E$ tail			
Method	d3mm1	d3mm2	d3mm3
1	9.9	7.7	10.0
2	—	3.8	6.6
3	3.4	—	3.0
4 ( $4\Delta E_p$ )	3.9	3.1	3.0
4' ( $3\Delta E_p$ )	5.9	5.6	5.4

**Table 3-9.** Average  $\Delta E$ s in the Three Detectors Using the Four Methods of Pile-Up Rejection (PUR) for the Runs in Phantom Slice 9

PUR Method	136 MeV					
	d3mm2		d3mm2		d3mm3	
	Avg $\Delta E$ (MeV)	$\delta\Delta E$ (%)	Avg $\Delta E$ (MeV)	$\delta\Delta E$ (%)	Avg $\Delta E$ (MeV)	$\delta\Delta E$ (%)
1	5.77	45	5.11	29	6.54	35
2	—	—	4.61	16	5.95	22
3	4.71	18	—	—	5.48	13
4	6.11	54	6.19	56	7.31	50
p peak	3.98	—	3.96	—	4.86	—

The single-proton peak locations are most consistent with calculations where the proton energy at d3mm1 was  $120 \pm 5$  MeV. Assuming the presence of the upstream scattering foils, the nozzle energy of 136 MeV would be reduced to 120 MeV by the  $2.7 \text{ g cm}^{-2}$  of the first plug. This is marginally consistent with the result obtained with the 250 MeV extracted energy, in that both imply a negligible amount of material in between the nozzle and d3mm1. It is possible that this region of the phantom was shielded only by thin layers of fabric (recall that thinnest parts of the suit consist of about  $0.2 \text{ g cm}^{-2}$  of material).<sup>12</sup>

With pile-up removal methods (3) and (4), which are the most restrictive, the fractions in the tails are all estimated to be between 3.0% and 3.9%; with methods (2) and (4'), the estimated fractions are in the range 3.8% to 6.6%; and with method (1), the fractions are estimated to be about 10% in d3mm1, 8% in d3mm2, and 10% in d3mm3. The fractions found in d3mm1 are generally larger than in d3mm2 or 3 for a particular method. The

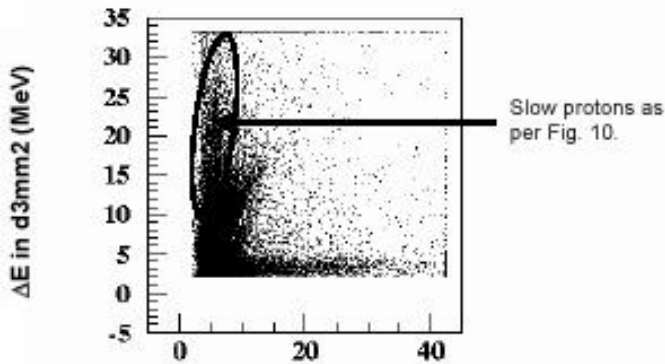


**Figure 3-13.** Scatter plot of  $\Delta E$  in d3mm2 vs.  $\Delta E$  in d3mm1 for the run with the detectors in slice 9 of the phantom and extracted beam energy of 155 MeV.

fractions with all methods except (1) are all approximately double those found in the phantom's brain; for method (1), the fractions here are about 2.5 times larger than in the brain. Since the beam energy estimate based on the single-proton  $\Delta E$  peaks shows there was less material in the path of the beam in this location than there was in the brain, there is no reason to expect an increase in the contribution of target fragments/recoils. Rather, given the proximity of slice 9 to slice 8 (center-to-center distance of about 12 cm), these results suggest that the source of the slow protons that reached the detectors when they were in slice 8 also

<sup>12</sup> The estimate of  $120 \pm 5$  MeV for the proton energy at d3mm1 also allows for the possibility that the scattering foils were not present, as per the discussion in the preceding section; if both foils were absent, the nozzle energy would have been 150 MeV and up to 5 cm of water-equivalent material (including the first plug) could have been present between the nozzle and d3mm1. While this scenario cannot be ruled out, there also is no particular reason to suspect the scattering foils were absent for this run.

produced slow protons that reached slice 9. This is consistent with the hypothesis that the slow protons were scattered into the detectors from something outside the center of the beam spot: If protons can scatter into the volume of space occupied by the detectors in slice 8, then there must be scattered trajectories that would also reach the detectors when placed in slice 9. That there are apparently fewer slow protons in slice 9 suggests that the scattering source was closer to slice 8.

Additional evidence for the presence of slow protons comes from examining the scatter plot of  $\Delta E$  in d3mm2 vs.  $\Delta E$  in d3mm1, shown in **Figure 3-13**. The upward-turning band of events indicated in the figure is similar to that seen in **Figure 3-10**. Given the presence of slow protons, we again opt to estimate the dose increase from high-LET particles using events with  $\Delta E > 23$  MeV in d3mm2. The events above 23 MeV pull the average up by 10.7%; dividing by the 4.0% increase seen in the comparable bare-beam data (i.e., accounting for p-Si reactions), we find a net dose increase of 6.4%.

### 3.4.8 Alternative Explanation of Slow Protons

We have shown evidence of low-velocity protons hitting the silicon detectors during the runs in slices 8 and 9; the energies were far below the nominal beam energies. If it can be demonstrated that there was no piece of the space suit in the beam that is thick enough to account for the observed energy losses, then another explanation is required. It is conceivable that the beam was scraping off one of the apertures in the transport line downstream of the last bending magnet. By scraping, we mean that some of the beam particles traversed more material than intended, e.g., a housing of one of the beam-monitoring detectors or the inner wall of the beam pipe itself.

As described above, the comparatively tiny beam currents required for satisfactory performance of the silicon detectors were too small for the operator to monitor the beam directly. Also, just before the runs with the detectors in the abdominal area of the phantom, beam was lost due to a power supply fault in the beam switchyard. Recovery from the fault was difficult and time-consuming, and there was not sufficient time remaining<sup>13</sup> to remove the detectors from the phantom and perform a diagnostic bare-beam run. It may be that, in recovering the beam without the usual feedback signals available, the operator was unable to steer the beam properly and some portion of it was slowed by scraping. Scraping protons would also tend to scatter much more than those that followed straight trajectories through the beam line; this could account for the highly divergent beam seen in the abdominal data, particularly the slice-8 data.

### 3.4.9 Summary of Results With Detectors in the Phantom

The results obtained in the preceding subsections are summarized in **Table 3-10**. Despite the complicated steps needed to extract the information, the results are generally consistent with our physical picture of energy deposition from protons and nuclear interaction products. We estimate that the 155 MeV extracted beam produces dose contributions from target fragments in the 2% to 10% range, and the 250 MeV extracted beam produces contributions in the 8% to 10% range. These results have large systematic uncertainties associated with them,

---

<sup>13</sup> The measurements were performed in between the end of one day's patient treatments and the beginning of the next, severely constraining the time available for these runs.

perhaps as large as 50%, but they are at least of the same order of magnitude as the dose increases measured in CR-39, and the 8%-9% estimate obtained in the phantom's brain agrees well with the 7.6% found in the CR-39 data with the same beam and detector location.

**Table 3-10:** Calculated Values of Incident Energy at d3mm1 for the Two Beam Energies and Three Locations in the Phantom

	Brain	Slice 8	Slice 9
$E_{\text{nozzle}} = 223 \text{ MeV}$	$E_{\text{d3mm1}} = 181 \pm 5$	$E_{\text{d3mm1}} = 205 \pm 5$	$E_{\text{d3mm1}} = 223 \pm 10$
$E_{\text{nozzle}} = 136 \text{ MeV}$	$E_{\text{d3mm1}} = 66 \pm 2$	$E_{\text{d3mm1}} = 105 \pm 5$	$E_{\text{d3mm1}} = 123 \pm 5$
Estimated water-equiv. material before d3mm1	9.5 cm	4.5 cm	2.7 cm
Estimated dose contribution from high-LET particles	223:8-9% 136:2-5%	223:9% 136:10%	— 136:6%
Proton Peak LET ratio, in situ/nozzle	223:1.14 $\pm$ 0.02 136:1.71 $\pm$ 0.04	223:1.05 $\pm$ 0.02 136:1.21 $\pm$ 0.04	223:1.00 $\pm$ 0.03 136: 1.07 $\pm$ 0.03

Note: (All energies are in MeV.) Third row: Water-equivalent depth estimates based on the proton peak  $\Delta E$ s; depths include the 2.7 cm of water-equivalent plastic comprising the plug in front of d3mm1. Fourth row: Estimated increase in dose due to high-LET target fragments and recoils. Bottom row: Ratios of LETs of the protons at depth to LETs at the nozzle for the 223 MeV and 136 MeV nozzle energies. The estimated dose contributions from high-LET particles are in addition to the dose increases from ionization energy loss increases along the Bragg curve.

In addition to the dose increases from high-LET secondaries, doses at depth increase due simply to the higher LET of the primary beam protons as their energy decreases. Using the calculated proton energies incident on d3mm1 in each location in the phantom, we have calculated the proton LET at depth; the ratio of that LET to the bare-beam LET (i.e., the LET of the beam as it exits the nozzle) is shown, for each location, in the bottom row of **Table 3-10**. As one would expect, the ratios are all higher for the beam with 136 MeV nozzle energy; the effect is particularly pronounced in the brain location. Because it was at the greatest depth in tissue, this location was ostensibly the most shielded; however, these results clearly show that the materials in front of the detectors cause dose increases, not just from high-LET secondaries, but also by slowing the incident protons so that their LETs (and hence doses per particle) increase significantly. In slice 8, where there was considerably less material in front of the detectors, the dose increase due to the slowing of the protons is smaller than that due to high-LET secondaries for the 223 MeV beam; the opposite is true for the 136 MeV beam in this location. In slice 9, where the shielding was minimal, the two effects are of roughly equal importance with the 136 MeV beam.

It is clear that, with protons as energetic as the ones used in this experiment, the usual relation between increased shielding and reduced dose does not apply. Materials in front of a given point in the body—whether they are the walls of a spacecraft, or a space suit, or the body's own tissue—cause the doses from such high-energy particle to increase at points deep in the body. This is a result of both of the mechanisms described above, the production of target fragments/recoils, and the increased LET of protons as they slow significantly at depth in tissue.

## 3.5 CONCLUSIONS

Deposited energy spectra have been measured with the LLUMC proton beams incident on unshielded silicon detectors and on the same detectors placed in three locations inside a human phantom that was shielded by the EMU space suit. The locations of single-proton peaks have been used to determine the incident energies at the first detector (d3mm1), and these in turn have been used to estimate the depth of water-equivalent material interposed between the nozzle and d3mm1. The data show that a considerable depth of material, about 9.5 cm of water-equivalent, was present upstream of d3mm1 in the brain location. Of this, 2.7 cm was in a plug of material immediately in front of d3mm1. Presumably, most of the rest is attributable to the phantom's skull. Less material, approximately 4.5 cm water-equivalent depth, was present when the detectors were placed in the upper abdominal position in the phantom (slice 8); again, 2.7 cm of this was in the plug in front of d3mm1. In slice 9, the data are consistent with 2.7 cm water-equivalent depth in front of d3mm1; this implies a negligible amount of material in between the nozzle and the plug in front of d3mm1.

Compared to CR-39 detectors, the silicon detectors are thick and have large volume, making them unsuitable for measuring the LET spectra of low-energy particles that do not traverse the full detector depth, or that are incident at a large angle with respect to the nominal beam axis; unfortunately, this describes many of the target fragments and recoils produced in nuclear interactions of protons with nuclei in the space suit and phantom materials. Nonetheless, because the detectors accurately record the energy deposited in them by beam protons and any target fragments or recoils that reach them, it is reasonable to use them to estimate dose. Elaborate procedures have been developed to make these estimates, accounting for the contributions expected from protons interacting in the detectors and for other complicating features in the data such as event pile-up and the slow protons seen in slice 9 and especially slice 8. The results are estimates with considerable uncertainties, but they show internal consistency and are in reasonable accord with the CR-39 measurements.

The fact that protons at these energies can produce a flux of high-LET secondary particles has important implications for possible future improvements to the shielding properties of space suits to be worn on EVAs. Adding mass to the suits would stop more of the low-energy electron and proton flux, which would have the desirable effect of reducing the dose to the skin and other shallow points in the body. However, this would also have the consequence of increasing the buildup of secondaries, thus increasing the dose at greater depth. The optimal design (i.e., the one that leads to the greatest overall reduction in risk) will have to balance these competing factors, while taking into account the detailed composition of the incident radiation field and the variations in radiation sensitivity of different organs.

## 3.6 ACKNOWLEDGMENTS

The experiments were possible only because of the substantial organizational and logistical support given by Drs. Greg Nelson, George Coutrakon, and Michael Moyers of LLU, and by Lora Benzatyan, also of LLU. The authors wish to thank them all for graciously hosting us and making their facilities available, and in particular we express our gratitude to Dr. Moyers not only for his help during the experiment but also for his continuing support as the analysis work proceeded. We thank Dr. Premkumar Saganti of JSC and Eric Benton of Eril Research for the many helpful discussions we have had with each of them. We are grateful to Dr. Frank Cucinotta of JSC for

organizing the experiments and for supporting our participation. This work was supported at Lawrence Berkeley National Laboratory (LBNL) by the Space Radiation Health Project of NASA under NASA Grant Number T5606W, through the U.S. Department of Energy under Contract No. DE-AC03076SF00098.

### 3.7 REFERENCES

1. NCRP Report No. 98, Guidance on Radiation Received in Space Activities, National Council on Radiation Protection and Measurements (1989). See especially pp. 15-24.
2. M. F. Moyers, in "Proton Therapy" in *The Modern Technology of Radiation Oncology: A Compendium for Medical Physicists and Radiation Oncologists*, ed. J. vanDyk, Wisconsin: Medical Physics Publishing, (1999) p. 823 - 869.
3. M. F. Moyers, G. A. Nelson, and P. Saganti, *Med. Phys.* 27 (6), 1405 (2000).
4. J. W. Wilson, J. Tweed, C. Zeitlin, M.-H. Y. Kim, B. Anderson, F. A. Cucinotta, J. Ware, and A. E. Persans, SAE Paper Number 01ICES-299.
5. J. D. Bowman, W. J. Swiatecki, and C. F. Tsang, Lawrence Berkeley Laboratory No. LBL-2908, 1973.
6. ICRP Publication 60, 1990 Recommendation of the International Commission on Radiological Protection, Pergamon Press (1991).
7. E. Benton, Eril Research, Inc., Report No. ERI-000501.
8. T. Doke et al., *Radiat. Meas.* 24, (1) 75 (1995).
9. E. Benton, private communication.
10. C. Zeitlin, K.A. Frankel, W. Gong, L. Heilbronn, E.J. Lampo, R. Leres, J. Miller, W. Schimmerling, *Radiat. Meas.*, 23, No. 1, 65-81 (1994).
11. C. Zeitlin, L. Heilbronn, J. Miller, L. Heilbronn, K. Frankel, W. Gong and W. Schimmerling, *Radiat. Res.* 145, 655-665 (1996).
12. C. Zeitlin, L. Heilbronn, J. Miller, S. E. Rademacher, T. Borak, T.R. Carter, K. Frankel, W. Schimmerling and C. E. Stronach, *Phys. Rev. C* 56, 388-397 (1997).
13. C. Zeitlin, L. Heilbronn, and J. Miller, *Radiat. Res.* 149, 560-569 (1998).
14. C. Zeitlin, A. Fukumura, L. Heilbronn, Y. Iwata, J. Miller, and T. Murakami, Lawrence Berkeley National Laboratory Report No. 45771 (2000), and *Phys. Rev. C* (in press).
15. S.W. Alderson, L.H. Lanzl, M. Rollins, and J. Spira. *The American Journal of Roentgenology, Radium Therapy, and Nuclear Medicine*, Vol. 87(1), 185 (1962).
16. A detailed description and specifications of the Amptek A225 chip can be found on the World Wide Web at <http://www.amptek.com/a225.html>
17. Particle Data Group, D. E. Groom et al., *European Physical Journal C* 15, 1 (2000). See Sec. 23.2 for a detailed discussion.
18. M. F. Moyers, private communication.

19. S. M. Selzer and M. J. Berger, Technical Report SP 3012, NASA, 1964.
20. W. B. Christie et al., Nucl. Instr. Meth., A225 466-476 (1987).
21. The ESTAR program was used. ESTAR was written by M. J. Berger of the National Institute of Standards and Technology, and can be found (and run interactively) on the World Wide Web at: <http://physics.nist.gov/PhysRefData/Star/Text/ESTAR.html>.
22. C. Zeitlin, A. Fukumura, L. Heilbronn, Y. Iwata, J. Miller, and T. Murakami, Lawrence Berkeley National Laboratory Report No. 47655 (2001).
23. W. R. Webber, J. C. Kish and D. A. Schrier, *Phys. Rev. C* **41**, 533 (1990).
24. J. W. Wilson, J. L. Shinn, L. W. Townsend, R. K. Tripathi, F. F. Badavi, and S. Y. Chun, *Nucl. Instr. Meth. B* **94**, 95 (1994).
25. R. K. Tripathi, J. W. Wilson, and F. A. Cucinotta, NASA TP-2000-210534.

## APPENDIX A – NUCLEAR INTERACTIONS IN SILICON

We first consider p-Si reactions in the rest frame of the proton. Preliminary data obtained by our group [23] with a 600 MeV/nucleon  $^{28}\text{Si}$  beam yield a cross section of  $374 \pm 11$  mb, in excellent agreement with the value of  $379 \pm 6$  mb reported by Webber et al. [24] at 500 MeV/nucleon. The semi-empirical nuclear cross section model NUCFRG2 [25] predicts a charge-changing cross section of 368 mb at 250 MeV/nucleon. In the rest frame of the silicon (the laboratory frame for the present experiment), a cross section of 374 mb yields a mean free path of 53 cm for protons in silicon. In a 3-mm-thick detector, therefore, 0.57% of incident protons are expected to undergo an interaction in which a silicon nucleus is broken up.

Elastic reactions are also expected to contribute to the high- $\Delta E$  tails in the detected spectra; in these reactions, the projectile scatters and the target nucleus recoils, leaving a short track in the detector. For instance, a recoiling silicon nucleus with 1 MeV/nucleon kinetic energy has a range of about 3  $\mu\text{m}$  and will deposit all 28 MeV of its total energy in the detector. At 250 MeV, the proton-proton cross section is entirely due to elastic scattering, and has a value of about 20 mb, very near its minimum. Using the empirical scaling law defined in Ref [17], the elastic scattering cross section for protons on silicon is predicted to be  $\mathbf{s}_{\text{p-Si}} = \mathbf{s}_{\text{p-p}} A_{\text{Si}}^{0.77} = 260$  mb (with  $A_{\text{Si}} = 28$ ). Added to the fragmentation cross section of 374 mb, the total cross section  $\mathbf{s}_{\text{tot}} = \mathbf{s}_{\text{inel}} + \mathbf{s}_{\text{el}} = 634$  mb. A recent calculation of  $\sigma_{\text{tot}}$  for protons on aluminum [25] predicts a value of 580 mb, in agreement with experimental data; assuming a power-law scaling in  $A_{\text{targ}}$ , this predicts  $\sigma_{\text{tot}}$  for protons on silicon of about 600 mb, within 6% of our estimate.

Using 260 mb for the elastic cross section gives a mean free path for elastic reactions of 76.8 cm, so that 0.39% of incident protons will undergo an elastic reaction with a silicon nucleus in a 3 mm depth. Combined with the 0.57% of protons predicted to cause fragmentation of a silicon nucleus, we expect 0.96% of protons to interact in a detector. The Si fragmentation cross section is expected to be weakly dependent on beam energy, and the proton-proton elastic cross section increases only slightly in going from 250 MeV to 155 MeV; therefore only a small change in the fraction of high- $\Delta E$  events is expected at the lower beam energy.



**CHAPTER 4**

**CHARACTERIZATION**

**OF THE RADIATION**

**SHIELDING PROPERTIES**

**OF U.S. AND RUSSIAN**

**EXTRAVEHICULAR ACTIVITY**

**SUITS**

E. R. Benton, E. V. Benton, and A. L. Frank  
Eril Research, Inc.,  
San Rafael, California

# CHARACTERIZATION OF THE RADIATION SHIELDING PROPERTIES OF U.S. AND RUSSIAN EXTRAVEHICULAR ACTIVITY SUITS

## ABSTRACT

Reported herein are results from the Eril Research, Inc. (ERI) participation in the JSC-sponsored study characterizing the radiation shielding properties of the two types of space suit that astronauts are wearing during the EVA on-orbit assembly of ISS. Measurements using passive detectors were carried out to assess the shielding properties of the U.S. EMU Suit and the Russian Orlan-M suit during irradiations of the suits and a tissue-equivalent phantom to monoenergetic proton and electron beams at LLUMC. During irradiations of 6 MeV electrons and 60 MeV protons, absorbed dose as a function of depth was measured using TLDs exposed behind swatches of the two suit materials and inside the two EVA helmets. Considerable reduction in electron dose was measured behind all suit materials in exposures to 6 MeV electrons. Slowing of the proton beam in the suit materials led to an increase in dose measured in exposures to 60 MeV protons. During 232 MeV proton irradiations, measurements were made with TLDs and CR-39 PNTDs at five organ locations inside a tissue-equivalent phantom, exposed both with and without the two EVA suits. The EVA helmets produce a 13% to 27% reduction in total dose and a 0% to 25% reduction in dose equivalent when compared to measurements made in the phantom head alone. Differences in dose and dose equivalent between the suit and non-suit irradiations for the lower portions of the two EVA suits tended to be smaller. Proton-induced target fragmentation was found to be a significant source of increased dose equivalent, especially within the two EVA helmets, and average quality factor inside the EMU and Orlan-M helmets was 2% to 14% greater than that measured in the bare phantom head.

## 4.1 INTRODUCTION

The on-orbit assembly of ISS requires a level of EVA unprecedented in the history of human spaceflight. The assembly of the ISS is anticipated to require over 1,000 hours of EVA spanning a five-year period—more than two and a half times more than the total EVA time accrued by all astronauts and cosmonauts to date [1]. This large amount of EVA will expose space workers to the radiation environment in LEO present on the outside of the ISS. During EVA, astronauts and cosmonauts are shielded only by the material of their suits and lack the benefit of the greater shielding provided by the mass of the station. To assess the radiation shielding effectiveness of the U.S. and Russian EVA suits, both of which will be used during ISS assembly, one suit of each type was brought to LLUMC and exposed to beams of monoenergetic protons at two energies and to a beam of monoenergetic electrons at one energy. At the behest of JSC's Space Radiation Health Project, ERI participated with a number of other investigators in characterizing the radiation shielding properties of the two EVA suits.

In the 51.56° inclination, ~400 km altitude orbit of the ISS, it is trapped protons and electrons that are of principle concern to astronaut health and safety during EVA. Trapped electrons range in energy up to ~6 MeV and are encountered while the station is at high latitudes and passing through the cusps of the trapped electron belt [2]. The spectrum of trapped protons extends from several MeV up to several hundred MeV, with a broad peak between

~150 and ~250 MeV. The trapped proton flux is greatest when the ISS is passing through the South Atlantic Anomaly (SAA), a region off the coast of Brazil where the Earth's magnetic field dips unusually low, allowing trapped protons to intersect the orbit of the ISS [2]. All but the most energetic electrons and a substantial fraction of the trapped proton flux are attenuated within the shielding represented by the outer structure of the ISS. However, during EVA, astronauts are protected only by the shielding provided by their suits, which is substantially less than that provided by the structure of the ISS. This decreased shielding permits lower-energy particles to penetrate the astronaut's body, increasing his total radiation exposure. Doses measured in the Russian Orlan suit during a 1997 EVA on the Russian *Mir* Orbital Station using the Hungarian Pille portable TLD system were 3 to 4½ times greater than that measured inside *Mir* during the same time [3].

Two types of EVA suit were tested. The EMU, manufactured for NASA by ILC Dover, is the current design used aboard the Space Shuttle and the ISS. The Orlan (Eagle)-M suit, produced by NPP Zvezda, is the current Russian EVA suit and has been previously used aboard *Mir*. An example of each suit was used in radiation exposures at LLUMC. In addition, swatches of suit material from each type of suit were used in some of the exposures. A tissue-equivalent human phantom was used to simulate an astronaut body. Detectors were exposed at specific organ sites of interest in the phantom while wearing the suits.

Radiation detectors were exposed behind portions of the suit to monoenergetic electrons of 6 MeV and to monoenergetic protons of two energies: 60 MeV and 232 MeV. The choice of electron and proton energies was dictated both by the radiation environment present outside the station in the ISS orbit and by the capabilities of the radiation facilities at LLUMC.

The objective of the ERI measurements made during both the 6 MeV electron and 60 MeV proton irradiations was to measure dose as a function of depth behind each of the two EVA suits and inside the two EVA helmets. For these measurements, stacks of TLDs were exposed perpendicular to the electron and proton beams behind swatches of EVA suit material and behind the visors of the EVA helmets. Dose as a function of TLD position in each stack was measured and TLD position was then converted to depth in water.

The objectives of the ERI measurements made during the 232 MeV proton irradiations were to:

- measure total dose, dose equivalent, and average quality factor at several specific organ sites inside the tissue-equivalent phantom both with and without the EVA suits
- assess the contribution to total dose and dose equivalent from proton-induced, high-LET target fragmentation
- assess the contribution to total dose and dose equivalent from thermal ( $\leq 0.2$  eV) and epithermal ( $0.2$  eV  $< E_n < 1$  MeV) neutrons

To meet these objectives, two types of passive radiation detector were used. CR-39 PNTD was used to measure the LET spectrum, dose, and dose equivalent from charged particles of  $LET_{\infty H_2O} \geq 5$  keV/ $\mu$ m. TLDs were used to measure absorbed dose and to assess the contribution to dose from thermal and epithermal neutrons. Measurements from the two detector types were combined to yield total dose, dose equivalent, and average quality factor, and to assess the contribution to total dose and dose equivalent from high-LET target fragments.

## 4.2 EXPERIMENT

### 4.2.1 Detectors

#### 4.2.1.1 Thermoluminescence Dosimeters

TLDs were used to measure absorbed dose in all three types of irradiation. For the 6 MeV electron and 60 MeV proton irradiations, TLD-700 ( ${}^7\text{LiF}$ ) was used. For the 232 MeV proton irradiation, two types of TLD materials, TLD-700 ( ${}^7\text{LiF}$ ) and TLD-600 ( ${}^6\text{LiF}$ ), were used. The difference in the responses of TLD-700 and TLD-600 is due to the high cross section of  ${}^6\text{Li}$  in the TLD-600 for absorption of thermal and epithermal neutrons in the  ${}^6\text{Li}(n,\alpha){}^3\text{H}$  reaction. Both TLD types measure total gamma ray/charged particle absorbed dose while the TLD-600 measures an additional dose proportional to low-energy neutron fluences present during the exposure. The sensitivity to neutrons is poor in TLD-700. The use of TLD-600 covered and uncovered by Gd foil allows thermal neutron induced response to be separated from epithermal response. Following the irradiations, the TLDs were read out using a standard Harshaw-4000 TLD reader. Each TLD was individually calibrated using ERI's  ${}^{137}\text{Cs}$   $\gamma$ -ray source.

#### 4.2.1.2 CR-39 Plastic Nuclear Track Detectors

CR-39 PNTDs were used to measure the LET spectra, dose, and dose equivalent from charged particles of  $\text{LET}_{\infty\text{H}_2\text{O}} \geq 5 \text{ keV}/\mu\text{m}$  during the 232 MeV proton irradiations. The protons produced by the LLUMC synchrotron range in energy from 50 to 250 MeV corresponding to an LET between 1.3 and 0.4  $\text{keV}/\mu\text{m}$ . Particles with LET below 5  $\text{keV}/\mu\text{m}$  do not register in CR-39. Thus, the primary protons produced by the accelerator are not recorded in the detector. The vast majority of tracks formed in the detector are from secondary particles—target fragments—produced in interactions between the primary protons and the nuclei of the stopping medium (EVA suit, tissue-equivalent phantom and the PNTD itself in this case). The LET spectrum measured in CR-39 PNTDs exposed to 232 MeV protons is primarily the result of target fragmentation.

Four layers of CR-39 PNTD were included in each passive detector stack; two layers were used to measure the LET spectrum and two layers were held in reserve should problems arise during chemical processing of the first two layers. One CR-39 PNTD was chemically processed for a short duration (36 hours) to reveal tracks from short-range, high-LET secondary particles, while the second CR-39 PNTD was processed for a longer duration (168 hours) to reveal small tracks produced by particles with LETs down to the 5  $\text{keV}/\mu\text{m}$  threshold. For both processing durations, chemical processing was carried out in a solution of 6.25  $N$  NaOH at 50°C.

Readout and analysis of the processed CR-39 layers was carried out using a semi-automated ELBEK track detector analysis system. The ELBEK system uses a standard optical microscope equipped with transmitted illumination, computer-controlled focus and  $x$ - $y$  stage. The surface of each detector was scanned and all tracks within the scanned area of the detector surface were measured. The LET spectrum for each detector was generated using an empirically determined detector response function. Separate LET spectra were generated for both the short- and long-duration etch detectors. These two spectra were then combined to produce one total LET spectrum for that particular detector stack.

Because CR-39 possesses an LET-dependent angular response, the detector stacks exposed to 232 MeV protons were irradiated at three angles. Particles of LET near the 5 keV/μm detection threshold only form tracks in CR-39 when the particles penetrate the detector at an angle near normal (90°) to the detector surface. This registration angle widens with increasing LET so that particles of LET significantly greater than the threshold will form tracks at angles much shallower than 90°. In exposures to isotropic radiation fields like that found in LEO, the angular dependence on LET is compensated for in the data analysis software. However, in accelerator-based experiments, the direction of the incident beam produces additional angular constraints. One target fragmentation component—the evaporation component—produces an isotropic distribution of particles and the angle of the incident proton beam relative to the CR-39 detector is unimportant. However, a second target fragmentation component tends to produce secondaries in the forward direction of the beam. This component mostly consists of knock-out secondaries including secondary protons, neutrons, and alpha particles. The result of the combined effects of the LET dependence on the angular sensitivity of CR-39 with the preferred forward direction of target fragmentation in the detector’s frame of reference leads to the detector possessing a larger number of low-LET target fragments when it is exposed at 90° relative to the beam than when it is exposed at shallower angles.

To compensate for this added angular constraint, the detector stacks irradiated inside the phantom were exposed at multiple angles. Each detector stack was exposed to 1/3 of the total desired dose at normal (90°), 1/3 of the dose at an angle 30° counter clockwise to normal, and 1/3 of the dose at an angle of 45° clockwise of normal. The exposures angles are illustrated in **Figure 4-1**. The exposures made to detector stacks positioned at the eye of the phantom were the exceptions. Because the primary proton beam passed through the back of the phantom head before emerging at the eye and into the detector, it was not possible to accurately align the beam at the two off-axis angles and the entire exposure was made at 90°.

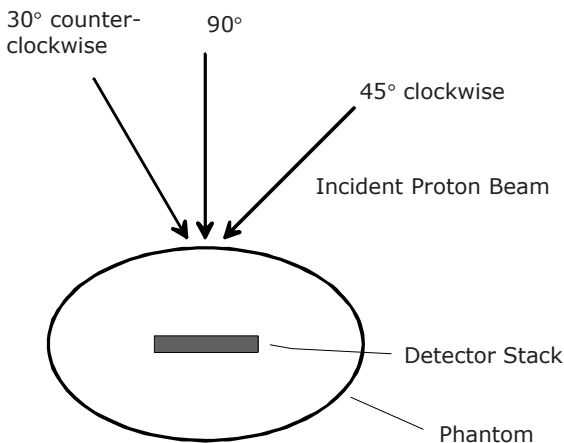


**Figure 4-1.** Due to the LET-dependent angular sensitivity of CR-39 PNTD, most of the detectors were exposed a three angles as shown above.

#### **4.2.1.3 Dose and Dose Equivalent From Combined CR-39 PNTD/TLD Measurements**

TLDs measure total absorbed dose, but have a reduced sensitivity to high-LET particles ( $LET \geq 5 \text{ keV}/\mu\text{m}$ ) [4]. Also, TLDs yield no quality factor (QF) information needed to determine dose equivalent. PNTDs measure LET spectra ( $LET > 5 \text{ keV}/\mu\text{m}$ ) from charged particles, but are insensitive to high-energy protons ( $\geq 12 \text{ MeV}$ ) where much of the dose is concentrated. Measurements from these two types of detector are combined to give total dose (corrected for high-LET particles), dose equivalent, and average quality factor.

The loss of sensitivity in the TLDs can be found by dividing the measured dose into two regions;  $LET < 5$  keV/ $\mu\text{m}$  where  $QF = 1$  and  $LET \geq 5$  keV/ $\mu\text{m}$  where  $QF > 1$ . In fact,  $QF > 1$  for  $LET > 3.5$  keV/ $\mu\text{m}$ , but the above assumption results in an insignificant error for the particle spectra in these measurements. The dose from high-LET particles can be derived from the LET spectra measured by the PNTDs. The measurement efficiency of the high-LET dose can be found from:

$$\bar{e} = \frac{\sum_{5\text{keV}/\text{mm}}^{LET_{\text{Max}}} e(LET)D(LET)}{D_{\text{PNTD}}} \quad (1)$$

where,  $e(LET)$  is the empirically derived, LET-dependent efficiency for  $^7\text{LiF}$  TLDs,  $D(LET)$  is the differential dose spectrum generated from the PNTD measurements and  $D_{\text{PNTD}}$  is the integrated dose measured by the PNTDs [4]. Total corrected dose is found from the low-LET and high-LET doses as follows:

$$D_L = D_{\text{TLD}} - \epsilon D_{\text{PNTD}}, \quad (2)$$

and

$$D_T = D_L + D_{\text{PNTD}}. \quad (3)$$

The total dose equivalent is then:

$$H_T = D_L + H_{\text{PNTD}}, \quad (4)$$

where  $H_{\text{PNTD}}$  is the integrated dose equivalent measured by the PNTDs. Average quality factor is then determined by:

$$QF = H_T/D_T. \quad (5)$$

## 4.2.2 Irradiations to 6 MeV Electrons and 60 MeV Protons

Measurements of dose as a function of depth within the two types of helmet and behind the two suit materials were made with stacks of TLD-700 ( $^7\text{LiF}$ ). The stacks were composed of approximately 20 thin (0.00914 cm) TLDs and 12 thick (0.0889 cm) TLDs. The TLDs were contained in rectangular slots milled in acrylic cylinders. A top window of 7.5- $\mu\text{m}$  Kapton (Al) foil sealed the cylinders. The TLD stack assembly is illustrated in **Figure 4-2**. The stacks were exposed to a 6-MeV electron beam from an electronic linac and to a 60-MeV proton beam from the LLUMC proton synchrotron incident through selected parts of the suits. The exposed TLDs were read out sequentially to yield a depth dose distribution inside the suit. The 6-MeV electron irradiations are summarized in **Table 4-1**, while the 60-MeV proton irradiations are summarized in **Table 4-2**. Actual doses in each table are those measured by in-line active dosimetry.

**Table 4-1.** Electron Exposures Made to Measure Dose as a Function of Tissue Depth Inside the EMU and Orlan-M Helmets and Behind Swatches of the EMU Suit and Orlan-M Suit Material

Selected Site	Suit	Particle	Energy	Actual Dose
Suit swatch	EMU	e <sup>-</sup>	6 MeV	10 cGy
Eye/Helmet	EMU	e <sup>-</sup>	6 MeV	10 cGy
Suit swatch	Orlan-M	e <sup>-</sup>	6 MeV	10 cGy
Eye/Helmet	Orlan-M	e <sup>-</sup>	6 MeV	10 cGy

**Table 4-2.** Low-Energy Proton Exposures Made to Measure Dose as a Function of Tissue Depth Inside the EMU and Orlan-M Helmets and Behind Swatches of the EMU Suit and Orlan-M Suit Material

Selected Site	Suit	Particle	Energy	Actual Dose
Suit swatch	EMU	p <sup>+</sup>	60 MeV	10.02 cGy
Eye/Helmet	EMU	p <sup>+</sup>	60 MeV	9.99 cGy
Suit swatch	Orlan-M	p <sup>+</sup>	60 MeV	10.03 cGy
Eye/Helmet	Orlan-M	p <sup>+</sup>	60 MeV	10.03 cGy

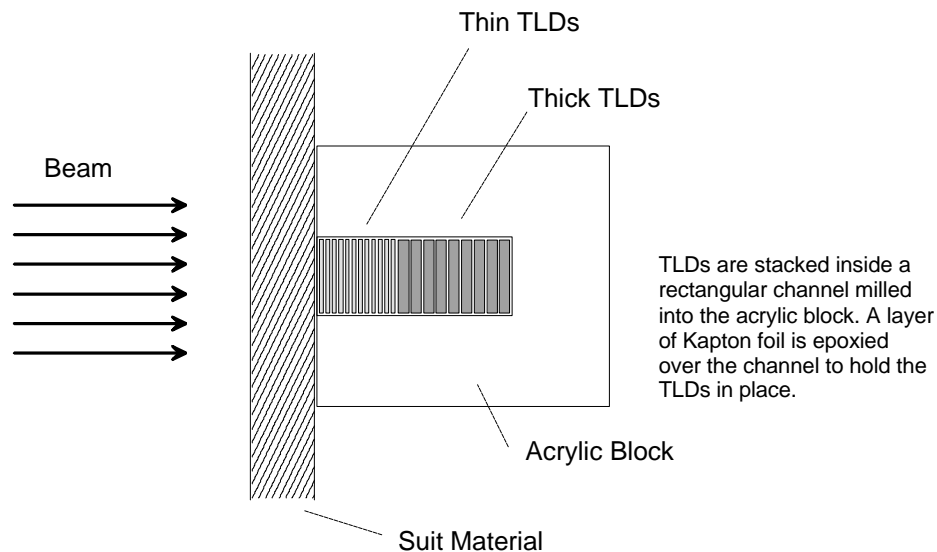


**Figure 4-2.** TLD Stack used in making dose/depth measurements behind EVA suit material and helmets exposed to 6 MeV electrons and 60 MeV protons.

### 4.2.3 Irradiations to 232 MeV Protons

A single detector stack consisting of four layers of CR-39 PNTD and an array of LiF TLDs was assembled for each irradiation. **Figure 4-3** illustrates the CR-39 PNTD/TLD stack. Each detector stack measured 4 cm × 4 cm and was ~1 cm in thickness. The four layers of CR-39, each ~600 μm in thickness, were separated by ~8 μm layers of Kimfoil polycarbonate film and a protective Lexan cover, ~250 μm in thickness, was placed at the front and back

of the four layer CR-39 stack. A  $3 \times 3$  array of TLDs was placed behind the CR-39 stack. Each TLD array consisted of five  ${}^7\text{LiF}$  TLDs, two uncovered  ${}^6\text{LiF}$  TLDs, and two  ${}^6\text{LiF}$  TLDs covered with Gd foil for the absorption of thermal neutrons. Each TLD measured  $0.3 \text{ cm} \times 0.3 \text{ cm} \times 0.09 \text{ cm}$ . The TLDs were mounted in a  $4 \text{ cm} \times 4 \text{ cm}$  acrylic holder and held in place by means of Teflon electrical tape. For cross-comparison tests, a second set of a  $3 \times 3$  array with TLDs provided by the JSC dosimetry group was also placed behind the ERI TLD array. Results from the JSC TLD exposures are not included in this report. An identifying label was affixed to each detector stack. Results from the five  ${}^7\text{LiF}$  TLDs exposed in each detector stack were averaged into a single value of dose. The 232 MeV proton irradiations are summarized in **Table 4-3**.

#### 4.2.3.1 Measurements at the Eye

Detector stacks were exposed at the location of the phantom eye in both the EMU and Orlan-M helmets, and on the bare phantom head. The stacks were attached to the left eye of the phantom head by tape as shown in **Figure 4-4**. The helmet was exposed to the proton beam from the back so that the primary protons had to pass through the back of the helmet and through the head of the phantom before reaching the detector stack as illustrated in **Figure 4-5**. This geometry was

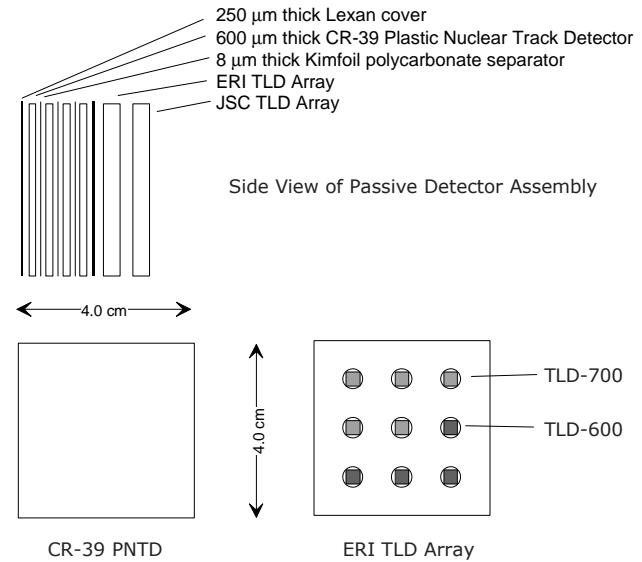


**Figure 4-3.** The CR-39 PNTD/TLD passive detector stack assembly used to measure LET spectra  $\geq 5 \text{ keV}/\mu\text{m}$ , total dose, and dose equivalent within the tissue-equivalent phantom inside of the EVA suits.



**Figure 4-4.** Detector array taped to the left eye of the phantom head in exposure configuration.

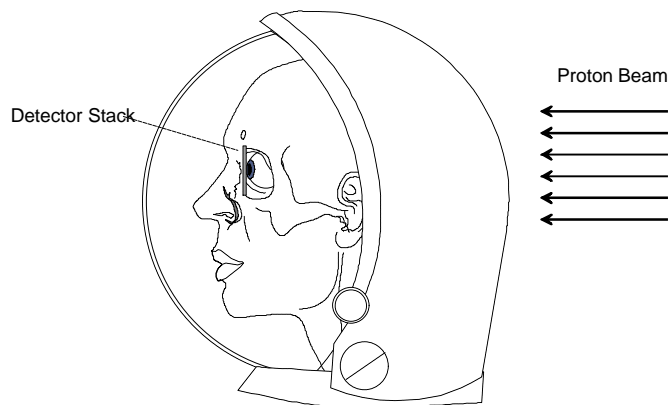


**Figure 4-5.** Geometry of the proton irradiation of the PNTD and TLD detector array positioned in front of the left eye of the phantom.

used in order to maximize the number of target fragments produced and to measure fragment fluence in the eye from protons passing through the phantom head in the helmet. **Figure 4-6** shows the EMU helmet during exposure of the detector stack at the phantom eye. Also, because of difficulty in aligning the beam in radiation gantry, so that the

primary protons would pass through the helmet and into the detector from behind, it wasn't possible to expose the detector at multiple angles and only a 90° angular alignment was used.

**Table 4-3.** High-Energy Proton (232 MeV) Exposures and Measurements at Specified Sites Within the Phantom Inside of the EMU and Orlan-M Space Suits

Stack	Organ Site	Suit	Angle	Dose (cGy)
1	eye	EMU	through back of head	10.0
2	brain	EMU	0° (normal)	3.385
			30° (ctrclkwise)	3.402
			45° (clkwise)	3.386
3	lung	EMU	0° (normal)	3.28
			30° (ctrclkwise)	3.33
			45° (clkwise)	3.37
4	stomach	EMU	0° (normal)	3.32
			30° (ctrclkwise)	3.39
			45° (clkwise)	3.35
5	thigh	EMU	0° (normal)	3.39
			30° (ctrclkwise)	3.38
			45° (clkwise)	3.37
6	eye	Orlan	through back of head	9.96
7	brain	Orlan	0° (normal)	3.58
			30° (ctrclkwise)	3.35
			45° (clkwise)	3.39
8	lung	Orlan	0° (normal)	3.35
			30° (ctrclkwise)	3.34
			45° (clkwise)	3.35
11	control		Not Exposed	n/a
B-1	eye	None	through back of head	9.83
B-2	brain	None	0° (normal)	3.39
			30° (ctrclkwise)	3.38
			45° (clkwise)	3.40
B-3	lung	None	0° (normal)	3.33
			30° (ctrclkwise)	3.40
			45° (clkwise)	3.39
B-4	stomach	None	0° (normal)	3.35
			30° (ctrclkwise)	3.42
			45° (clkwise)	3.39
B-5	thigh	None	0° (normal)	3.37
			30° (ctrclkwise)	3.41
			45° (clkwise)	3.33
B-6	control		Not Exposed	n/a

#### 4.2.3.2 Measurements in the Brain

Detector stacks were exposed to 232 MeV protons at the center of the phantom's head at the location of the brain in the EMU and Orlan-M Helmets, and in the phantom head without helmet. The region of the phantom head that corresponds to the site of the brain was removed as shown in **Figure 4-7**. A cylindrical tissue-equivalent plug was cut in half and a slot to hold the detector stack was machined into the center of the plug. The detector surface was oriented perpendicular to the bilaterally symmetric axis of the phantom head. The head with helmet was exposed from the front at three angles to a total of ~10 cGy of protons as described in section 4.2.1.2.

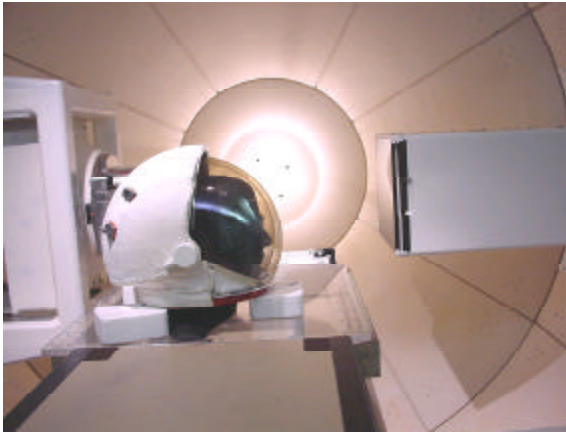


**Figure 4-6.** Proton irradiation set-up for the eye location in the EMU helmet. The beam enters the helmet from the back of the helmet.

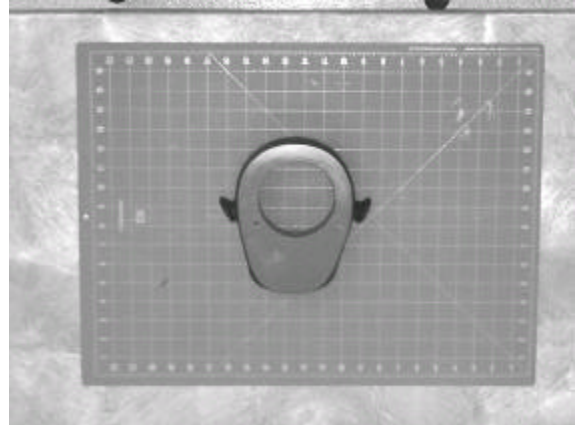


**Figure 4-7.** Horizontal cross section of the phantom head showing the opening for the cylindrical plug in which the detector stack was placed. The detector stack was oriented facing forward.

#### 4.2.3.3 Measurements in the Lung

Exposures of detector stacks at the site of the lungs were identical for the EMU and Orlan-M suits, and for the torso without suit. The exposure configuration was similar to that of the brain irradiations. The detector stack was placed inside a tissue-equivalent cylindrical plug, which was then inserted into the region of the phantom's left lung. **Figure 4-8** shows the detector stack in the tissue-equivalent plug at the site of the phantom lung. The exposure was made from the front of the suit in the case of both the EMU and Orlan-M suits. Total dose was ~10 cGy fractionated over exposures from three different angles as described in Section 4.2.1.2.

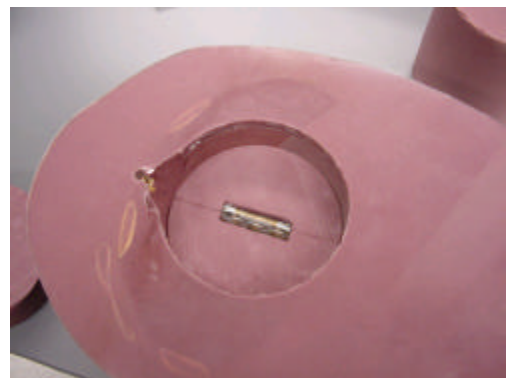


**Figure 4-8.** Detector stack as placed in the left lung of the phantom. The detector stack faced forward during the irradiation.

#### 4.2.3.4 Measurements in the Stomach

Detector stacks were exposed at the site of the phantom stomach only for the EMU suit and for the bare phantom. Since the Orlan-M suit is not modular as in the case of the EMU suit, it was not possible to irradiate detector stack in the stomach in front of the beam while inside the Orlan-M suit. In addition, the metal support attached to the Orlan-M suit to carry it on a dolly was in the way for the radiation beam trajectory.

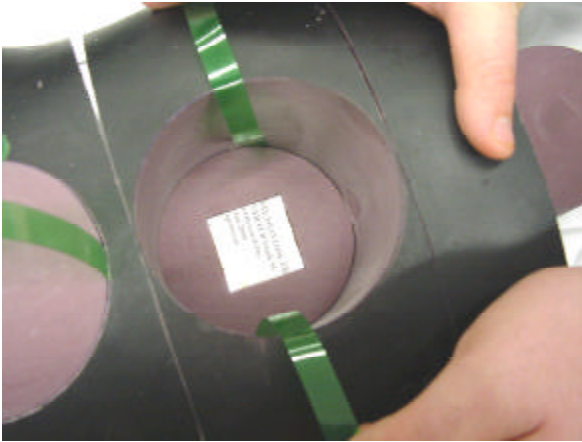


**Figure 4-9.** Detector stack placed at the back of the stomach cavity and up against the front of the spine.

At the left of the photograph the cylindrical plug at the site of the phantom abdomen can also be seen.

and the phantom torso was placed inside the EMU suit.

**Figure 4-10** shows the torso of the EMU in exposure configuration during the irradiation of the stomach detector stack. A total of ~10 cGy of 232 MeV protons was delivered in three equal exposures at 90°, 45°, and 60° relative to the plane of the detectors as explained in Section 4.2.1.2.



**Figure 4-10.** Torso portion of the EMU suit during exposure of stomach detector stack. The beam entered the suit from above.

#### 4.2.3.5 Measurements in the Thigh

Detector stacks were exposed at the site of the left thigh, directly in front of the femur of the phantom in the phantom alone and while wearing the EMU suit. As with the stomach irradiation, it was not possible to properly align the thigh detector stack with the beam while inside the Orlan-M suit and this exposure was not made. **Figure 4-11** shows the phantom thigh, detector stack, and the cylindrical plug placed in front of the detector stack during the exposures. As with most of the other exposures, the ~10 cGy dose was distributed between exposures made at three different angles.

**Figure 4-11.** A part of the phantom's right thigh, detector stack, and tissue-equivalent plug used in making irradiations of the thigh location while inside the EMU suit.



## 4.3 RESULTS AND DISCUSSION

### 4.3.1 Doses From 6 MeV Electron Irradiations

The dose/depth measurements made inside the EVA suits for the 6-MeV electron beam exposures are shown in **Figure 4-12**. The depth in water presented in **Figure 4-12** was derived from depth in LiF based on the relative ranges of electrons in the two media. Range-Energy tables show that for 6-MeV electrons, the range in water is a factor of 0.808 times the range in  ${}^7\text{LiF}$  (in units of  $\text{g}/\text{cm}^2$ ) [5].

All of the measured doses were considerably less than the incident 10 cGy, illustrating significant attenuation in the electron flux within the mass of the two helmets and the two suit swatches. The Orlan-M helmet doses were least, while doses from the EMU helmet were intermediate, indicating that the eye locations in the helmets were more heavily shielded than the other suit locations. A gradual increase in dose with depth followed by a gradual decrease with further depth is seen for all four measurements. The depth of maximum dose was  $0.34 \text{ g}/\text{cm}^2$  for the EMU helmet,  $0.46 \text{ g}/\text{cm}^2$  for EMU suit swatch, and  $0.65 \text{ g}/\text{cm}^2$  for Orlan-M suit swatch. The dose profile behind the Orlan-M helmet has a broad maximum from about  $0.24$  to  $0.65 \text{ g}/\text{cm}^2$ . The maximum was also relatively less in the Orlan-M helmet than behind the other materials, yielding a flatter dose distribution. The peaks in the EMU suit swatch and Orlan-M suit swatch may be due to the scatter of electrons off tubing used to circulate coolant within the suit.

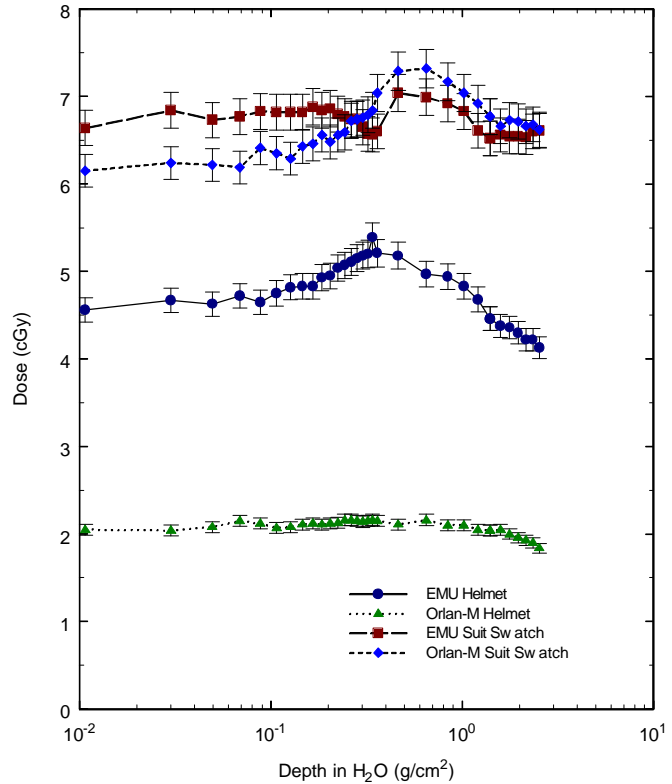


**Figure 4-12.** Dose as a function of depth in water measured using TLDs exposed behind the EMU and Orlan-M helmets and behind swatches of the EMU and Orlan-M suit material.

### 4.3.2 60 MeV Proton Irradiations

Dose/depth distributions inside the EVA helmets and behind the suit swatches for the 60 MeV proton exposures are shown in **Figure 4-13**. The depth in water presented in **Figure 4-13** was derived from depth in LiF based on the relative range of protons in LiF and  $\text{H}_2\text{O}$ . Range-Energy tables show that 60-MeV proton range in water is a factor of 0.7966 times the range in  ${}^7\text{LiF}$  (in units of  $\text{g}/\text{cm}^2$ ) [6].

All of the measured doses are higher than the corresponding incident dose, indicating that significant slowing of the proton beams occurred in passage through the suit materials. Doses immediately behind the suit vary from 11 to 14 cGy. The dose/depth profiles are characterized by gradual increases in dose through about  $1 \text{ g}/\text{cm}^2$ , then steeper

increases toward the Bragg peak maximum. Only the Orlan-M helmet profile seems to show a decrease from the Bragg peak at the last TLD location in the stack. The dose distribution at the eye/helmet location in the Orlan-M suit is (as in the electron beam irradiation) quantitatively different than that measured for the other three materials.

### 4.3.3 Results From 232 MeV Proton Irradiations

#### 4.3.3.1 Doses From 232 MeV Proton Irradiations

Results from the TLDs exposed to 232 MeV protons inside the phantom in the EMU and Orlan-M suits are presented in **Table 4-4**. The ion chamber doses reported in **Table 4-4** were made for the pristine beam before it passed through any material. The smaller doses measured by TLDs reflect attenuation of the beam as it passed through the bulk of the suit and the phantom. Differences between the doses measured by TLDs and by the beam-line ion chamber may also reflect the alignment of the detectors during the irradiations. Since the detector stack was placed inside the phantom, which itself was inside one of the suits, alignment of the detector stack relative to the beam line often had to be estimated.

Doses measured with TLD-700 show that for head exposures (eye/brain) the measured doses were considerably less than the incident doses. This was most likely due to beam attenuation. Body exposures (lung/stomach/thigh) showed that measured organ doses were only moderately lower than corresponding incident doses.

Results from the comparison of TLD-600 (6LiF) and TLD-700 (7LiF) dose measurements indicate that there was no appreciable contribution to dose from thermal and epithermal neutrons. Only in the case of the lung and stomach irradiations were the doses measured by TLD-600 significantly larger than doses measured by TLD-700. In all other cases, dose measurements from the two types of TLD agreed within experimental uncertainty. The larger doses measured in TLD-600 over TLD-700 in the lung and stomach may be due to an increase in the fluence of low energy neutrons produced by the tissue-equivalent material surrounding the detectors. In all cases, the TLD-600 dose measurements made behind Gd absorber agreed with TLD-600 measurements made with no absorber

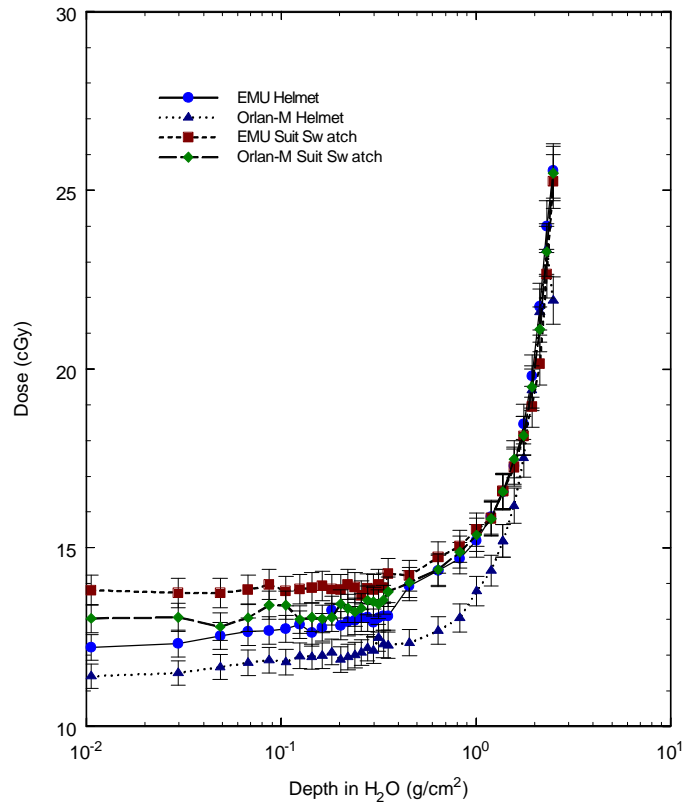


**Figure 4-13.** Dose as a function of depth in water measured using TLDs exposed to 60-MeV protons behind the EMU and Orlan-M helmets and behind swatches of the EMU and Orlan-M suit materials.

within the limits of experimental uncertainty, indicating that there was no appreciable contribution to dose from thermal neutrons.

**Table 4-4.** Absorbed Dose Measurements With TLDs (Passive Detectors) and Beam-Line Ionization Chamber Doses for 232 MeV Proton Irradiations at Selected Locations in the Phantom Inside the EMU and Orlan-M Suits

Location	Suit	Ion Chamber Dose (cGy)	TLD Absorbed Dose (cGy)		
			<sup>7</sup> LiF	<sup>6</sup> LiF	<sup>6</sup> LiF (Gd)
Eye	EMU	10.00	8.97 ± 0.27	9.23 ± 0.28	9.34 ± 0.28
Brain	EMU	10.17	8.49 ± 0.25	8.41 ± 0.25	8.80 ± 0.26
Lung	EMU	9.98	9.61 ± 0.29	10.38 ± 0.31	10.87 ± 0.33
Stomach	EMU	10.06	10.03 ± 0.30	11.47 ± 0.34	11.61 ± 0.35
Thigh	EMU	10.14	10.81 ± 0.32	10.96 ± 0.33	10.58 ± 0.32
Eye	Orlan-M	9.96	8.47 ± 0.25	8.59 ± 0.26	9.00 ± 0.27
Brain	Orlan-M	10.32	9.46 ± 0.28	n/a	n/a
Lung	Orlan-M	10.04	9.71 ± 0.29	n/a	n/a

#### 4.3.3.2 LET Spectra, Total Dose and Dose Equivalent Measurements

The integral LET fluence, dose, and dose equivalent spectra measured using CR-39 PNTDs was normalized to the incident primary proton fluence determined from dose measurements made by the in-line dosimetry ion chamber and corresponding to a total dose of ~10 cGy of 232 MeV energy beam (see **Table 4-4**). Normalization to incident proton fluence permits measurements made during separate irradiations to be directly compared. The ICRP-60 definition of quality factor was used in determining dose equivalent [7]. The error bars associated with the measurements made in the Orlan-M suit and in the bare phantom are significantly larger than those for the EMU measurements. This is a result of the smaller sample size measured in the Orlan-M and bare phantom detectors, rather than any inherent limitation in the method.

While the LET spectra  $\geq 5$  keV/ $\mu\text{m}$ , and the total dose, dose equivalent, and average quality factor measurements derived from the LET spectra, reflect the importance of high-LET target fragmentation, these measurements do not completely quantify the total target fragmentation contribution. This is due to limitations inherent in the optical microscopy method used to analyze the CR-39 PNTDs. The minimum range of the measurable target fragments are on the order of the thickness of bulk CR-39 detector removed by chemical processing. For optical microscopy analysis of CR-39 PNTD, this is  $\sim 8$   $\mu\text{m}$ . Removing less than 8  $\mu\text{m}$  of material during chemical processing results in tracks that are too small to accurately measure using optical methods. This means that target fragments of range  $< 8$   $\mu\text{m}$  are not measured and their contribution to dose, dose equivalent, and mean quality factor must be neglected.

##### 4.3.3.2.1 Eye Exposures

Integral LET fluence, dose, and dose equivalent spectra measured in detector arrays exposed in front of the phantom eye by protons passing through the back of the phantom head are shown in **Figure 4-14**. The fluence

spectra for all three detectors lie fairly close to one another at lower LET (<100 keV/μm). Differences between the Orlan-M helmet spectrum and the other two spectra in the LET region below 30 keV/μm most likely result from differences in the scanning efficiency amongst the microscopists who read out the detectors. There was a larger number of high-LET events (>200 keV/μm) measured in the EMU eye detector as compared to the other two eye detectors, which results in the dose and dose equivalent curves measured in the EMU helmet lying well above those measured for the bare phantom. These high-LET events are most likely recoil-heavy nuclei.

**Table 4-5** lists the total dose corrected for high-LET particle contribution, dose equivalent and average quality factor determined from combined CR-39 PNTD and TLD measurements. Also shown in **Table 4-5** are the dose and dose equivalents from charged particles of LET ≥5 keV/μm, assumed to be target fragments, and their relative contributions to total dose and dose equivalent. Both dose and dose equivalent are lower in the two helmets—by 22% and 27%, respectively, in dose and 14% and 25%, respectively, in dose equivalent—than for the bare phantom head, illustrating the attenuation of the beam by the shielding provided by the helmets. Furthermore, it appears that the Orlan-M helmet provides more shielding than does the EMU helmet.

**Table 4-5.** Total Dose, Dose Equivalent, and Mean Quality Factor From ~10 cGy, 232 MeV Proton Irradiations Measured Using CR-39 PNTDs and LiF TLDs at the Phantom Eye for the Bare Phantom Head, Phantom Head Inside the EMU Helmet and Phantom Head Inside the Orlan-M Helmet

Helmet	None	EMU	Orlan-M
Total Dose (cGy/proton × 10-8)	7.55 ± 0.58	5.90 ± 0.19	5.53 ± 0.42
Change in Dose due to Helmet	n/a	-22%	-27%
DoseTLD (cGy/ proton × 10-8)	7.24 ± 0.41	5.54 ± 0.17	5.28 ± 0.29
DosePNTD* (cGy/ proton × 10-8)	0.31 ± 0.02	0.37 ± 0.01	0.25 ± 0.01
Target Fragmentation Dose Contribution	4.1%	6.2%	4.6%
Total Dose Equivalent (cSv/ proton × 10-8)	10.70 ± 1.01	9.25 ± 0.29	7.99 ± 0.75
Change in Dose Equivalent due to Helmet	n/a	-14%	-25%
Dose EquivalentPNTD (cSv/ proton × 10-8)	3.42 ± 0.26	3.71 ± 0.01	2.71 ± 0.20
Target Fragmentation Dose Equivalent Contribution	32%	40%	34%
Average Quality Factor	1.41 ± 0.17	1.57 ± 0.07	1.44 ± 0.17
Change in Average Quality Factor due to Helmet	n/a	10%	2%

#### 4.3.3.2.2 Brain Exposures

Integral LET fluence, dose, and dose equivalent spectra measured in CR-39 PNTDs positioned in the center of the phantom head are shown in **Figure 4-15**. As in the eye exposures, the three fluence spectra lie fairly close to one another at lower LET (<100 keV/μm). Again, differences between the three spectra in the LET region below 30 keV/μm probably arise from differences in the scanning efficiency of individual microscopists. For LET above 100 keV/μm, both the Orlan-M and EMU spectra lie above that measured inside the bare phantom head. This difference is most notable in the dose and dose equivalent spectra.

Total dose corrected for high-LET particle contribution, dose equivalent, and average quality factor determined from combined CR-39 PNTD and TLD measurements are given in **Table 4-6**. **Table 4-6** also presents

the dose and dose equivalents from target fragments, and the relative contributions to total dose and dose equivalent from target fragments. Total dose is 21% lower in the center of the brain in the EMU helmet and 13% lower in the Orlan-M helmet than in the bare phantom head, indicating that the helmets are attenuating some of the dose. However, while the dose equivalent is 8% lower in the EMU helmet, it is nearly identical in both the Orlan-M helmet and the bare phantom. The contribution from target fragmentation to total dose at the center of the brain was 3.5% for the bare phantom head, 5.9% inside the EMU helmet, and 6.0% inside the Orlan-M helmet. The contribution of target fragments to total dose equivalent at the brain site was 33% inside the bare phantom head, 44% inside the EMU helmet, and 43% inside the Orlan-M helmet.

**Table 4-6.** Total Dose, Dose Equivalent, and Mean Quality Factor From ~10 cGy, 232 MeV Proton Irradiations Measured Using CR-39 PNTDs and LiF TLDs in the Center of the Phantom Brain for the Bare Phantom Head, Phantom Head Inside the EMU Helmet, and Phantom Head Inside the Orlan-M Helmet

Helmet	None	EMU	Orlan-M
Total Dose (cGy/proton × 10-8)	6.92 ± 0.42	5.49 ± 0.17	6.04 ± 0.19
Change in Dose due to Helmet	n/a	-21%	-13%
DoseTLD (cGy/ proton × 10-8)	6.69 ± 0.31	5.14 ± 0.16	5.68 ± 0.18
DosePNTD* (cGy/ proton × 10-8)	0.24 ± 0.01	0.32 ± 0.01	0.36 ± 0.01
Target Fragmentation Dose Contribution	3.5%	5.9%	6.0%
Total Dose Equivalent (cSv/ proton × 10-8)	9.94 ± 0.68	9.15 ± 0.28	9.99 ± 0.35
Change in Dose Equivalent due to Helmet	n/a	-8%	0.5%
Dose EquivalentPNTD (cSv/ proton × 10-8)	3.25 ± 0.17	4.01 ± 0.01	4.31 ± 0.43
Target Fragmentation Dose Equivalent Contribution	33%	44%	43%
Average Quality Factor	1.43 ± 0.13	1.66 ± 0.07	1.65 ± 0.08

The contribution of target fragments to total dose at the eye was 4.1% for the bare phantom head, 4.6% for the Orlan-M helmet, and 6.2% for the EMU helmet. Similarly, the contribution of target fragments to total dose equivalent at the eye ranged from 32% for the bare phantom and 34% for the Orlan-M helmet up to 40% for the EMU helmet. From these results, it appears that the Orlan-M helmet is not a significant source of target fragments. The EMU helmet, on the other hand, produces a sizable number of target fragments in addition to those created in the head of the phantom. This result is further borne out in the average quality factor measured for the eye exposures. Average quality factor for the bare head and the Orlan-M helmet are nearly the same at  $1.41 \pm 0.17$  and  $1.44 \pm 0.17$ , respectively. The average quality factor measured inside the EMU helmet is significantly higher at  $1.57 \pm 0.07$ . The larger number of high-LET events measured in the EMU helmet detector is principally responsible for this larger average quality factor.

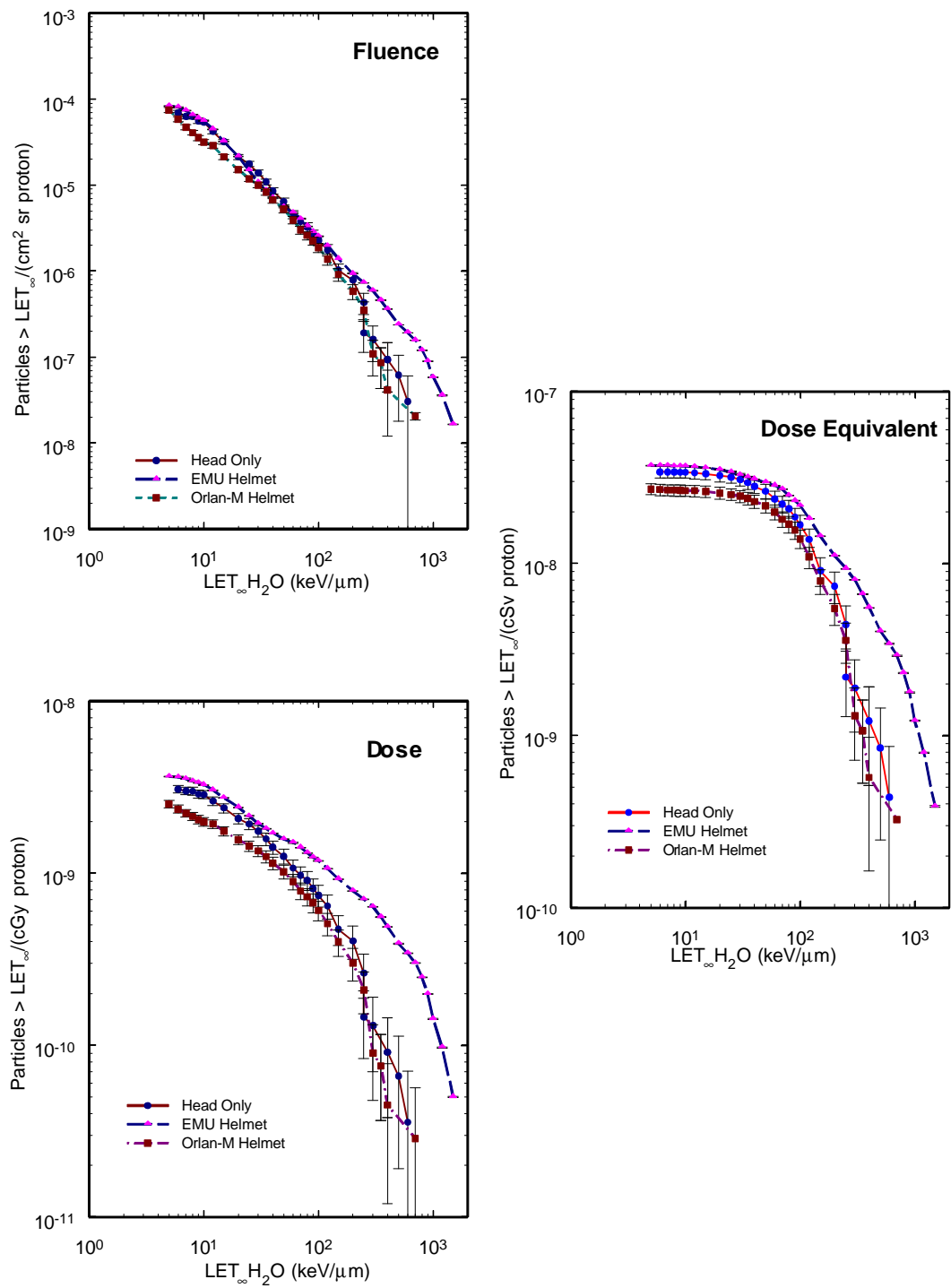


**Figure 4-14.** Integral LET Fluence, Dose and Dose Equivalent Spectra from 232 MeV proton irradiations measured using CR-39 PNTDs at the phantom eye.

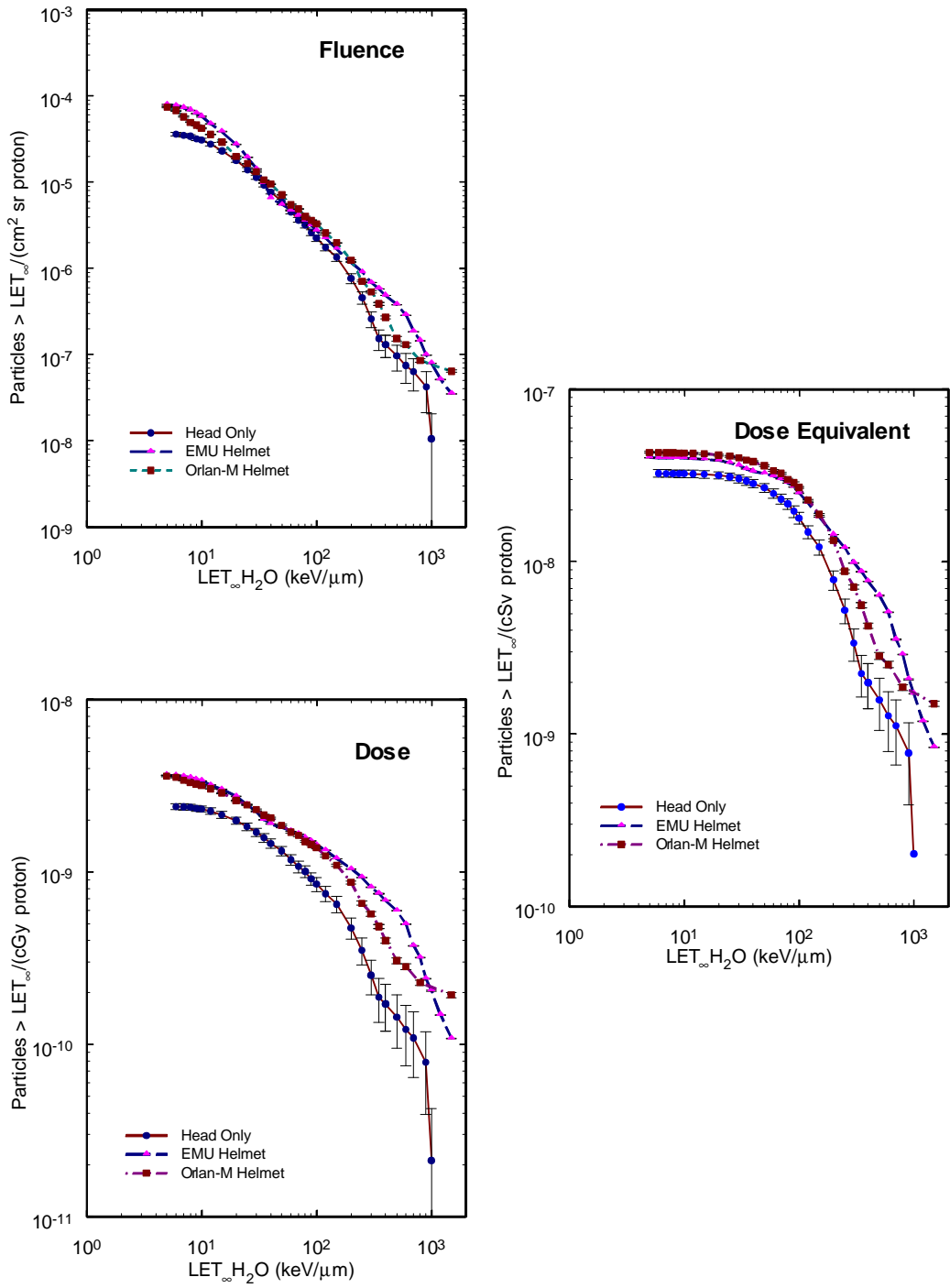


**Figure 4-15.** Integral LET Fluence, Dose and Dose Equivalent Spectra from 232 MeV proton irradiations measured using CR-39 PNTDs in the phantom brain.

Average quality factor for the bare head was  $1.43 \pm 0.13$ , in close agreement with that measured at the eye location for the bare head. Average quality factor for the EMU helmet and the Orlan-M helmet are nearly the same at  $1.66 \pm 0.07$  and  $1.65 \pm 0.08$ , respectively. Thus, both the EMU helmet and Orlan-M helmet are significant

sources of target fragments, adding to those produced in the phantom head. Unlike the eye exposures, where the proton beam passed through the back of the helmet and through the head at a single angle (see **Figure 4-5**), the brain exposures were made at three angles (**Figure 4-1**) and passed through the helmet visors.

#### 4.3.3.2.3 Lung Exposures

**Figure 4-16** shows the integral LET fluence spectra, dose spectra, and dose equivalent spectra measured at the site of the phantom lung. The LET spectra measured for the three conditions—the bare phantom torso, and the phantom inside the EMU and Orlan-M suits—are all in close agreement with one another, indicating that the suits were not a significant source of target fragments to the lung. This result is further borne out in comparisons of the total dose, dose equivalent and average quality factor. Total dose corrected for high-LET particle contribution, dose equivalent, and average quality factor determined from combined CR-39 PNTD and TLD measurements are given in **Table 4-7**, as are the dose and dose equivalents from target fragments, and the relative contributions to total dose and dose equivalent from target fragments. Both dose and dose equivalent are lower in the EMU and Orlan-M suits when compared to that measured in the lung of the bare phantom torso, illustrating the attenuation of the proton flux by the suits.

**Table 4-7.** Total Dose, Dose Equivalent, and Mean Quality Factor From ~10 cGy, 232 MeV Proton Irradiations Measured Using CR-39 PNTDs and LiF TLDs in the Phantom Lung for the Bare Phantom Torso, Phantom Torso Inside the EMU Suit and Phantom Torso Inside the Orlan-M Suit

Suit	None	EMU	Orlan-M
Total Dose (cGy/proton $\times 10^{-8}$ )	6.99 $\pm$ 0.54	6.31 $\pm$ 0.54	6.35 $\pm$ 0.51
Change in Dose due to Suit	n/a	-10%	-9%
DoseTLD (cGy/ proton $\times 10^{-8}$ )	6.63 $\pm$ 0.36	5.99 $\pm$ 0.19	6.03 $\pm$ 0.36
DosePNTD* (cGy/ proton $\times 10^{-8}$ )	0.36 $\pm$ 0.02	0.32 $\pm$ 0.01	0.35 $\pm$ 0.02
Target Fragmentation Dose Contribution	5.1%	5.0%	5.6%
Total Dose Equivalent (cSv/ proton $\times 10^{-8}$ )	10.80 $\pm$ 0.95	9.68 $\pm$ 0.30	9.30 $\pm$ 0.92
Change in Dose Equivalent due to Suit	n/a	-10%	-14%
Dose EquivalentPNTD (cSv/ proton $\times 10^{-8}$ )	4.17 $\pm$ 0.29	3.68 $\pm$ 0.01	3.28 $\pm$ 0.26
Target Fragmentation Dose Equivalent Contribution	39%	38%	35%
Average Quality Factor	1.55 $\pm$ 0.18	1.53 $\pm$ 0.07	1.47 $\pm$ 0.19
Change in Average Quality Factor due to Suit	n/a	-1%	-5%

The contribution from target fragments to total dose in the lung was 5.1% for the bare phantom torso, 5.0% inside the EMU suit, and 5.6% inside the Orlan-M suit. Similarly, the contribution from target fragments to total dose equivalent was quite close for all three measurements, with a 39% contribution for the bare phantom torso, a 38% contribution for the torso inside EMU suit, and a 35% contribution for the torso inside the Orlan-M suit. Average quality factor was 1.55  $\pm$  0.18 for the phantom torso alone, 1.53  $\pm$  0.07 for the EMU suit, and 1.47  $\pm$  0.19 for the Orlan-M suit. It appears that neither the EMU suit nor the Orlan-M suit added significantly to the target fragmentation dose and dose equivalent measured in the lung. However, it should be noted that a dummy chest unit and backpack were in used in place of the actual Display and Control Module and Life Support Unit during these

irradiations and the dummy units were probably of very different composition than the actual flight hardware. Thus, the effect of the EMU suit on dose and dose equivalent to the lung may not have been accurately measured.

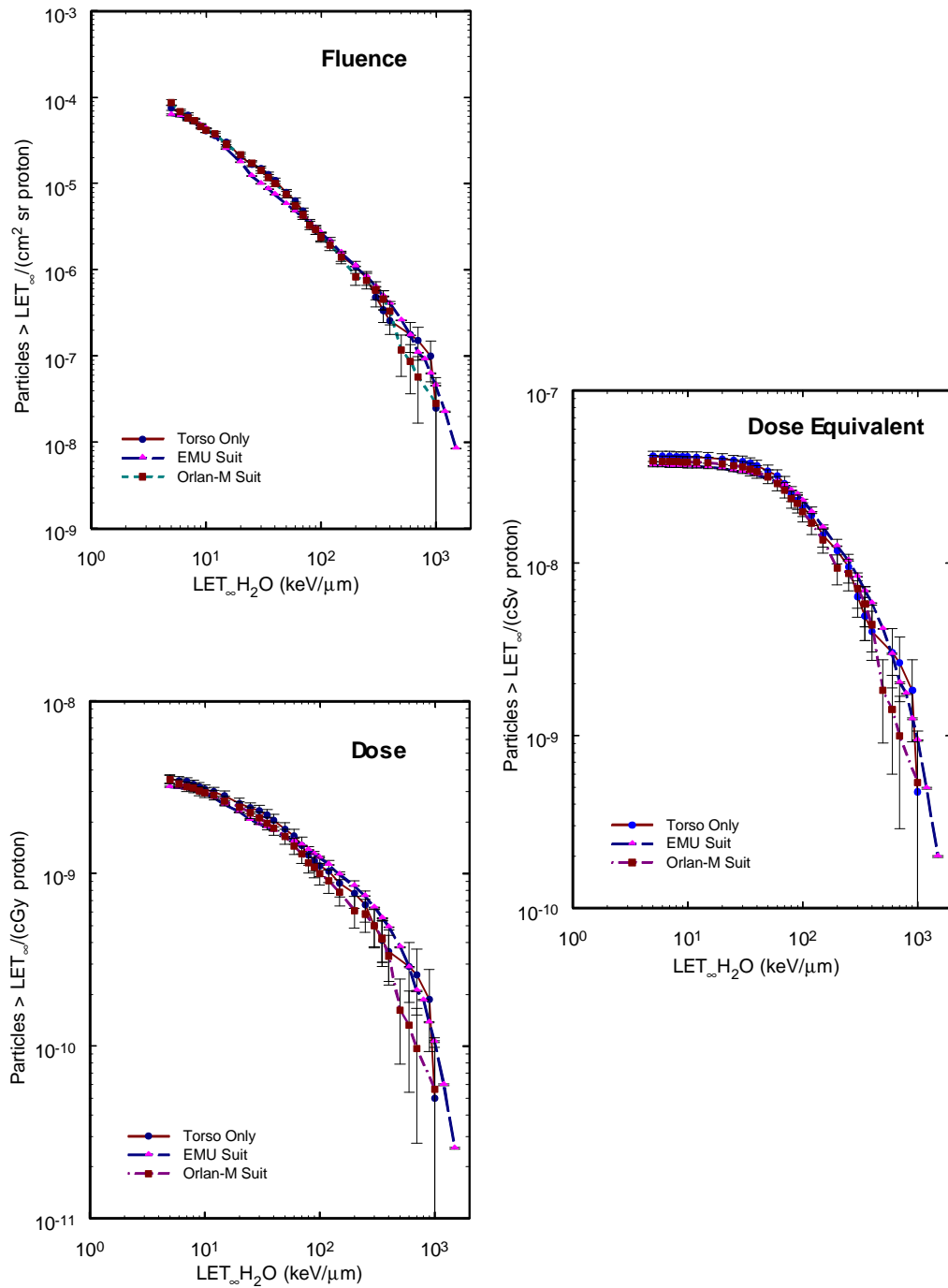


**Figure 4-16.** Integral LET Fluence, Dose and Dose Equivalent Spectra from 232 MeV proton irradiations measured using CR-39 PNTDs in the phantom lung.

#### 4.3.3.2.4 Stomach Exposures

The integral LET fluence, dose, and dose equivalent spectra measured in the stomach of the phantom for the bare phantom and the phantom with EMU suit are shown in **Figure 4-17**. As noted above, irradiations to the phantom stomach while inside the Orlan-M suit were not possible due to the single-piece construction of the Orlan-M suit and to the stand on which it was attached. The curves from measurements made with and without the EMU suit are in close agreement. The measurements made inside the EMU suit show slightly more signal from particles of LET >300 keV/μm. **Table 4-8** gives the total dose, dose equivalent, and average quality factor measurements made in the phantom stomach both with and without the EMU suit. Attenuation of the total proton flux can be seen in the smaller values of dose and dose equivalent in the EMU suit measurements. While the contribution to dose from target fragments was higher in the EMU suit—4.6% versus 3.9%—contribution from target fragments to dose equivalent was little changed by the presence of the suit—32% with the suit as compared to 31% without the suit. The average quality factor was the same for both situations: 1.40. Since the suit adds little in the way of mass in front of the stomach, it is not surprising that there should be little difference between the two sets of measurements.

**Table 4-8.** Total Dose, Dose Equivalent, and Mean Quality Factor From ~10 cGy, 232 MeV Proton Irradiations Measured Using CR-39 PNTDs and LiF TLDs in the Phantom Stomach for the Bare Phantom Torso and Phantom Torso Inside the EMU Suit

Suit	None	EMU
Total Dose (cGy/proton × 10 <sup>-8</sup> )	7.11 ± 0.64	6.55 ± 0.21
Change in Dose due to Suit	n/a	-13%
DoseTLD (cGy/ proton × 10 <sup>-8</sup> )	6.79 ± 0.42	6.27 ± 0.19
DosePNTD* (cGy/ proton × 10 <sup>-8</sup> )	0.28 ± 0.02	0.29 ± 0.01
Target Fragmentation Dose Contribution	3.9%	4.6%
Total Dose Equivalent (cSv/ proton × 10 <sup>-8</sup> )	9.93 ± 1.07	9.08 ± 0.28
Change in Dose Equivalent due to Suit	n/a	-9%
Dose EquivalentPNTD (cSv/ proton × 10 <sup>-8</sup> )	3.10 ± 0.27	2.86 ± 0.01
Target Fragmentation Dose Equivalent Contribution	31%	32%
Average Quality Factor	1.40 ± 0.20	1.40 ± 0.06
Change in Average Quality Factor due to Suit	n/a	0%

#### 4.3.3.2.5 Thigh Exposures

A similarly close agreement between measurements made with and without the EMU suit in the phantom stomach is seen in measurements made with and without the EMU suit in the phantom thigh. As with the stomach irradiations, it was not possible to expose the phantom thigh while inside the Orlan-M suit. **Figure 4-18** shows the integral LET fluence, dose, and dose equivalent spectra measured at the site of the phantom thigh for the bare phantom and for the phantom inside the EMU suit. There is very close agreement between the two measurement conditions for the thigh in all three spectra, illustrating that the EMU suit in the area of the thigh adds little in the way of shielding. This observation can also be seen in comparisons of total dose, dose equivalent, and average quality factor from the combined TLD and CR-39 PNTD measurements for the thigh, shown in **Table 4-9**. Both dose and dose equivalent are practically the same for the bare phantom thigh with and without the EMU suit. There

is a somewhat higher dose from particles of  $LET \geq 5 \text{ keV}/\mu\text{m}$  in the bare thigh versus the thigh inside the EMU suit. However, this high-LET dose does not propagate to an increased dose equivalent and the 30% contribution from target fragments to total dose equivalent is the same for both situations. Average quality factor in the bare thigh is slightly higher than that measured inside the EMU suit, reflecting some attenuation of the proton flux by the suit.

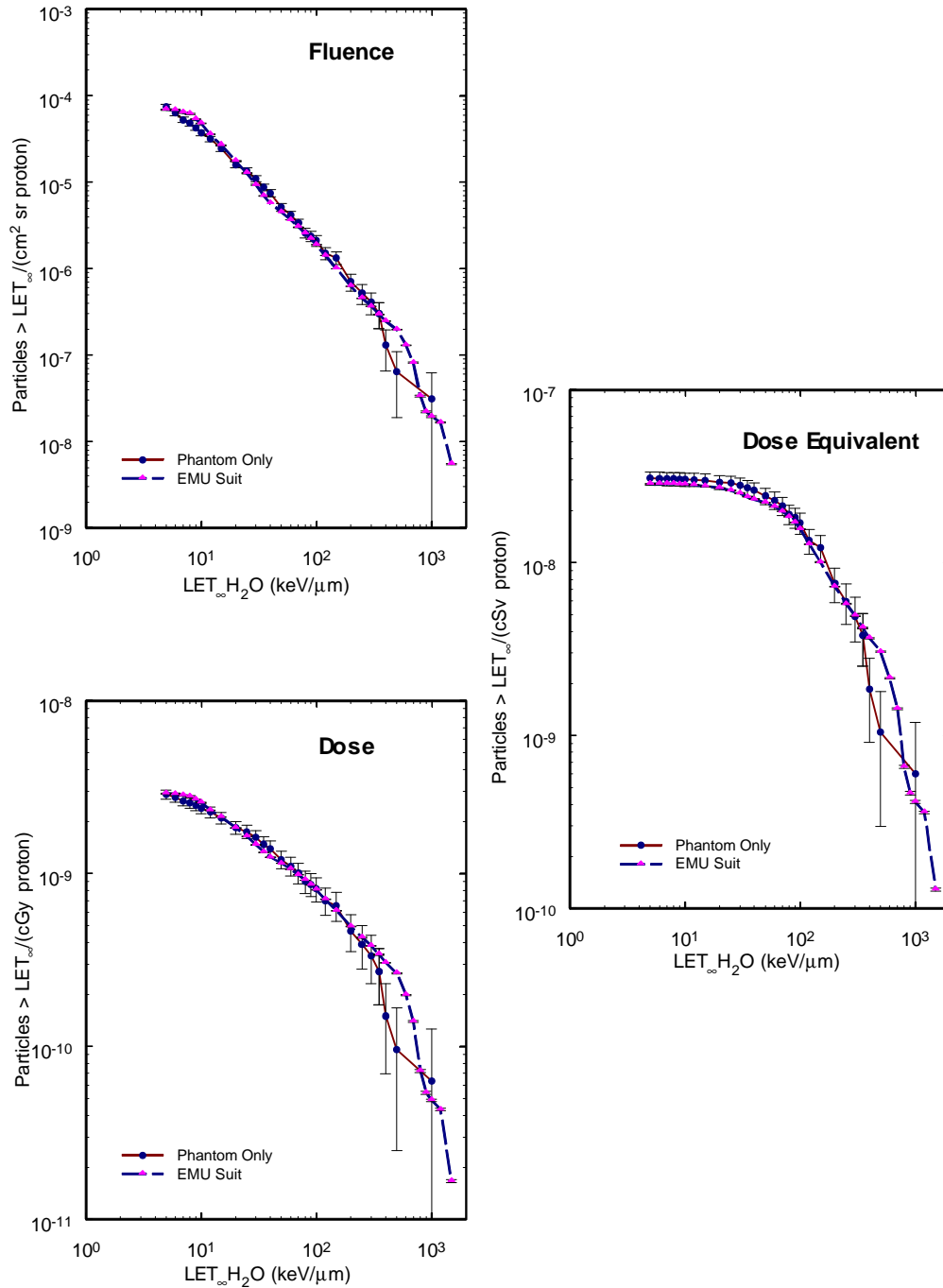


**Figure 4-17.** Integral LET Fluence, Dose and Dose Equivalent Spectra from 232 MeV proton irradiations measured using CR-39 PNTDs in the phantom stomach.

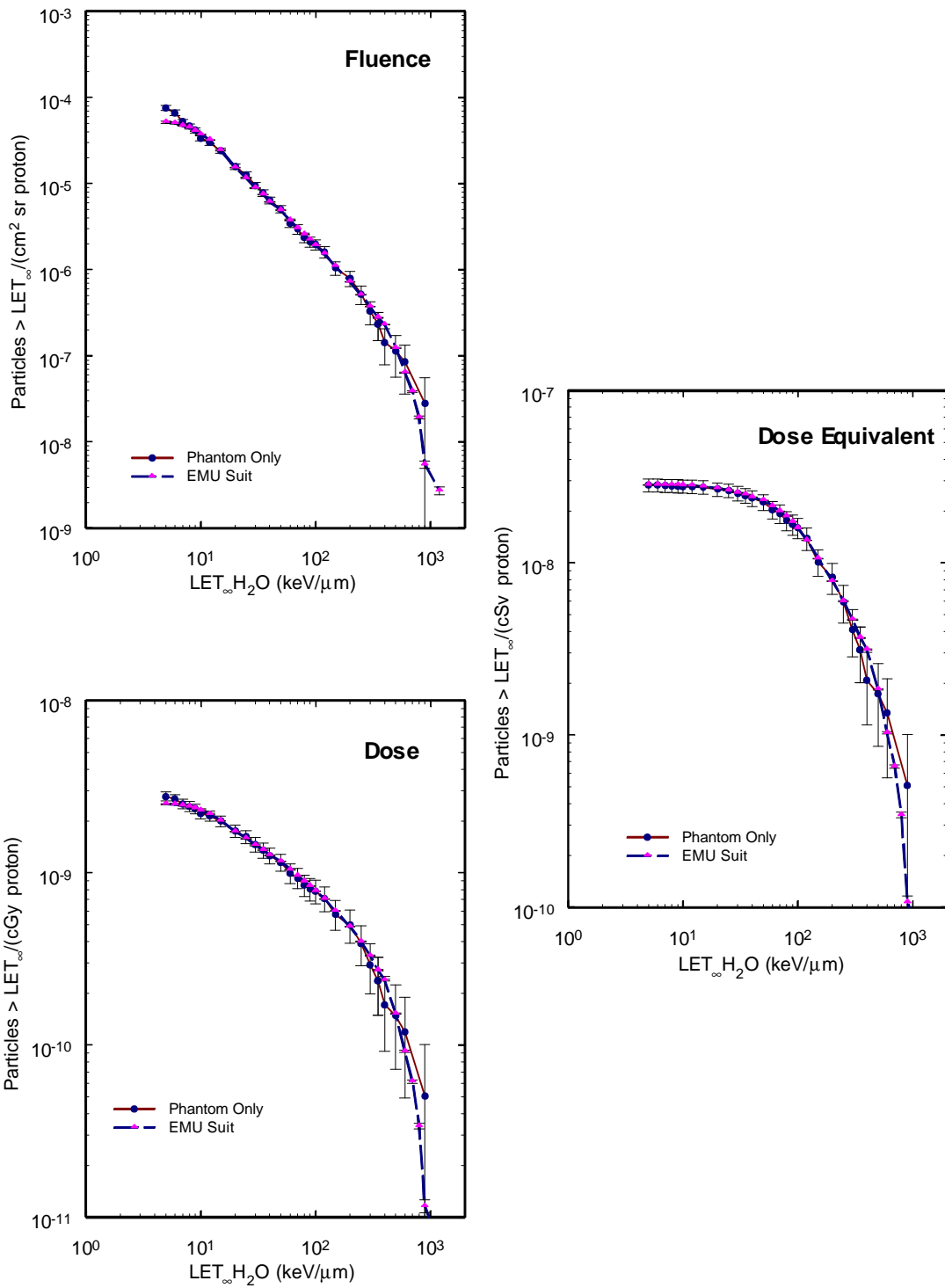


**Figure 4-18.** Integral LET Fluence, Dose and Dose Equivalent Spectra from 232 MeV proton irradiations measured using CR-39 PNTDs in the phantom thigh.

**Table 4-9.** Total Dose, Dose Equivalent, and Mean Quality Factor From ~10 cGy, 232 MeV Proton Irradiations Measured Using CR-39 PNTDs and LiF TLDs in the Phantom Thigh for the Bare Phantom Thigh and Phantom Thigh Inside the EMU Suit

Suit	None	EMU
Total Dose (cGy/proton $\times 10^{-8}$ )	6.95 $\pm$ 0.59	6.92 $\pm$ 0.22
Change in Dose due to Suit	n/a	-0.4%
DoseTLD (cGy/ proton $\times 10^{-8}$ )	6.67 $\pm$ 0.64	6.67 $\pm$ 0.21
DosePNTD* (cGy/ proton $\times 10^{-8}$ )	0.28 $\pm$ 0.02	0.25 $\pm$ 0.01
Target Fragmentation Dose Contribution	4.0%	3.7%
Total Dose Equivalent (cSv/ proton $\times 10^{-8}$ )	9.50 $\pm$ 1.00	9.51 $\pm$ 0.30
Change in Dose Equivalent due to Suit	n/a	0.1%
Dose EquivalentPNTD (cSv/ proton $\times 10^{-8}$ )	2.83 $\pm$ 0.24	2.84 $\pm$ 0.01
Target Fragmentation Dose Equivalent Contribution	30%	30%
Average Quality Factor	1.37 $\pm$ 0.19	1.34 $\pm$ 0.06
Change in Average Quality Factor due to Suit	n/a	-2%

## 4.4 CONCLUSIONS

Measurements inside the NASA EMU and Russian Orlan-M EVA helmets and behind swatches of the NASA EMU and Russian Orlan-M EVA suit materials in exposures to 6-MeV electrons and 60-MeV protons were analyzed to produce profiles of dose as a function of depth in water. The electron beam doses are reduced by as much as a factor of 5 (for the Orlan-M helmet exposure), showing the considerable attenuation of the electron flux within the mass of the suits. Further depth dose variations over 2.5 cm of water equivalent vary only a few percent. This does not fit the expectations for a monoenergetic 6-MeV beam where one would expect an initial dose buildup with depth to a broad peak, then a continuous decline to zero dose at the maximum electron range. Most likely, there was significant scattering off the coolant tubing and other surfaces within the suit materials.

The 60-MeV proton beam exposures behind the suit swatches and inside the helmets resulted in dose/depth distributions, which can be explained by an initial slowing of the beam in the suit, followed by a gradual slowing toward the Bragg peak in a 2.5 cm equivalent depth of water. Doses immediately behind the suit materials varied from 11 to 14 cGy, considerably greater than the ~10cGy incident proton dose. The dose/depth distribution for the Orlan-M helmet exposure was somewhat different from the other three, suggesting that the beam may have passed through an area composed of different material thicknesses.

The most significant results from measurements made using passive detectors to characterize the shielding effectiveness of the NASA EMU and Russian Orlan-M EVA suits were derived from the 232 MeV proton irradiations. The LET spectra  $\geq 5$  keV/ $\mu\text{m}$ , total dose, dose equivalent and average quality factor were measured at five locations (eye, brain, lung, stomach, and thigh) inside the tissue-equivalent phantom both by itself and while inside the NASA EMU and Russian Orlan-M EVA suits. Absorbed dose was measured using a combination of two types of TLD—TLD-600, sensitive to thermal and epithermal neutrons, and TLD-700, insensitive to neutrons. Results for all quantities measured, except for thermal and epithermal neutron contribution, were significantly

greater than values expected from 232 MeV protons when neglecting secondary particles. Little indication of buildup of low energy neutrons in the body (lung/stomach/thigh) was noted from the TLD-600 doses. The comparison of doses from TLD-600, covered and uncovered by Gd thermal neutron absorber foil, and TLD-700 showed no appreciable dose from thermal or epithermal neutrons.

Differences in total dose and dose equivalent between irradiations made inside the EMU and Orlan-M suits and those made with only the bare phantom are driven by three competing processes. The additional shielding represented by the suits tended to reduce both dose and dose equivalent through attenuation and scattering of the primary proton flux. The mass of the suits and the phantom body slowed the proton beam and increased the LET of the primary protons as they approached the Bragg peak. The increased LET led to increased dose and dose equivalent. Finally, proton-induced target fragmentation within the mass of the suit—most notably within the two EVA helmets—tended to increase total dose and especially dose equivalent through the production of high-LET secondaries. For the most part, the attenuation of the primary proton flux appeared to dominate over the slowing of the beam and the production of target fragment secondaries. Both the total dose and dose equivalent tended to be lower inside the two suits than in the bare phantom. There were two instances in which the dose equivalent inside the suits was higher than that in the bare phantom, but in both cases—the brain measurement inside the Orlan-M helmet and the thigh measurement inside the EMU suit—the difference between the dose equivalent measurements made with and without the suits was less than 1%.

The greatest attenuation in dose was seen inside the two EVA helmets. For proton irradiations through the back of the head, dose to the eye was 22% less inside the EMU helmet and 27% less inside the Orlan-M helmet than in the phantom head alone. Similarly, for proton irradiations through the visors, dose to the brain was 21% smaller inside the EMU helmet and 13% smaller inside the Orlan-M helmet as compared to the bare head. The reduction in dose due to the suits was more modest in measurements made in the rest of the phantom body. Doses measured in the lung inside the EMU and Orlan-M suits were 10% and 9% smaller, respectively, than the lung dose measured in the bare phantom torso. Due to the way in which the Orlan-M suit was mounted on its stand and because the Orlan-M is a single-piece suit, it was not possible to make 232 MeV proton exposures to the stomach and thigh inside the Orlan-M suit. Dose at the stomach inside the EMU suit was 13% less than in the bare phantom stomach, while the thigh dose inside the EMU suit showed less than a 1% reduction from that measured in bare phantom.

Changes in dose equivalent due to the presence of the suits were also greater in the helmets than in the lower parts of the suit. However, the changes in dose equivalent were generally smaller than the corresponding changes in total dose. Dose equivalent measured at the eye was 14% less inside the EMU helmet and 25% less inside the Orlan-M helmet than for the phantom head alone. Inside the brain, the dose equivalent was lower by 8% for the EMU helmet and actually 0.5% greater for the Orlan-M helmet as compared to the measurement made in the bare phantom head. Dose equivalent measurements made in the lung were 10% and 14% less than in the bare phantoms for the EMU suit and Orlan-M suit, respectively. Dose equivalent in the stomach while inside the EMU suit was 9% less than in the bare phantom and dose equivalent in the thigh while inside the EMU suit was practically identical to that measured in the bare phantom thigh.

Average quality factor increased when measured inside the two EVA helmets, but showed little difference with bare phantom measurements in the lower portions of the two suits. Average quality factor measured at the eye

was 10% greater in the EMU helmet and 2% greater in Orlan-M helmet when compared to that measured in the bare phantom head. Similarly, average quality factor measured in the brain was 14% greater in the EMU helmet than in the bare head and 13% greater in the Orlan-M helmet than in the bare head. For the lung measurements, average quality factor was reduced by 1% by the EMU suit and 5% by the Orlan-M suit. Average quality factor was unchanged in the stomach measurements by the shielding of the EMU suit and reduced by 2% in the thigh by the presence of the EMU suit.

As expected, both the NASA EMU and Russian Orlan-M EVA suits were found to provide some shielding from the charged particle fluxes encountered outside the ISS. This shielding is most significant in the case of low-energy protons and electrons. Previous measurements made by our laboratory on the exterior surface of *Mir* showed a three orders of magnitude reduction in both dose and dose equivalent within the first 0.2 g/cm<sup>2</sup> of Al-equivalent shielding [8]. This large decrease is due to the attenuation of low-energy protons and electrons. Note that the increased doses measured immediately behind the suit materials for the 60-MeV proton irradiations are for a single proton energy. External to the ISS in LEO, protons will occupy a broad spectrum of energies both above and below the 60-MeV protons used in this experiment. This broad energy spectrum will tend to smear out the dose distribution behind the EVA suit.

The helmets of the two EVA suits were found to reduce dose and dose equivalent from 232 MeV protons—representative of proton energy in the broad peak of the trapped proton energy spectrum encountered in the SAA. There was also a reduction in dose and dose equivalent measured in the lungs due to the shielding provided by the suits. Little effect from the EMU suit was seen in measurements made in the stomach and thigh, areas where the suit is relatively thin. While proton target fragmentation added only modestly to the total dose—between 4% and 6%—it made a significant contribution to the dose equivalent—between 30% and 40%. It should be noted that this includes not only target fragmentation produced inside the suit, but also target fragmentation from the body of the phantom.

## 4.5 REFERENCES

- [1] NASA Space Station Extravehicular Activity Web site, <http://spaceflight.nasa.gov/station/eva/index.html>
- [2] Benton, E. R. and Benton, E. V. (2001) "Space radiation dosimetry in low Earth orbit and beyond," *Nucl. Inst. & Meth. B*, **184**, Nos. 1-2, pp. 255- 294.
- [3] Deme, S., Apathy, I., Hejja, I., Lang, E., and Feher, I. (1999) "Extra dose due to extravehicular activity during the NASA-4 mission measured by an on-board TLD system," *Rad. Prot. Dos.* **85** (1-4) 121-124.
- [4] Benton, E. R., Frank, A. L., and Benton, E. V. (2000) "TLD efficiency of <sup>7</sup>LiF for doses deposited by high-LET particles," *Rad. Meas.* **32** (3) pp.211-214.
- [5] International Commission on Radiation Units and Measurements (1984) *Stopping Powers for Electrons and Positrons*, ICRU Report No. 37, ICRU, Bethesda.
- [6] International Commission on Radiation Units and Measurements (1993) *Stopping Powers and Ranges for Protons and Alpha Particles*, ICRU Report No. 49, ICRU, Bethesda.
- [7] International Commission on Radiological Protection (1991) *1990 Recommendations of the International Commission on Radiological Protection*, ICRP Report No. 60, Pergamon Press, Oxford.
- [8] Benton, E. R., Benton, E. V., and Frank, A. L. "Dosimetric measurement of the radiation environment as a function of shielding made on the exterior of the Mir orbital station," *Rad. Meas.* in press.

**CHAPTER 5**  
**A COMPARISON**  
**OF MODEL CALCULATION**  
**AND MEASUREMENT OF ABSORBED**  
**DOSE FOR PROTON IRRADIATION**

N. Zapp, E. Semones, and P. Saganti  
Lockheed-Martin  
Houston, Texas

F. Cucinotta  
NASA Johnson Space Center  
Houston, Texas

# A COMPARISON OF MODEL CALCULATION AND MEASUREMENT OF ABSORBED DOSE FOR PROTON IRRADIATION

## ABSTRACT

With the increase in the amount of time spent EVA that is necessary to complete the construction and subsequent maintenance of ISS, it will become increasingly important for ground support personnel to accurately characterize the radiation exposures incurred by EVA crewmembers. Since exposure measurements cannot be taken within the organs of interest, it is necessary to estimate these exposures by calculation. To validate the methods and tools used to develop these estimates, it is necessary to model experiments performed in a controlled environment. This work is such an effort. A human phantom was outfitted with detector equipment and then placed in American EMU and Orlan-M EVA space suits. The suited phantom was irradiated at the LLUPTF with proton beams of known energies. Absorbed dose measurements were made by the spaceflight operational dosimetrist from JSC at multiple sites in the skin, eye, brain, stomach, and small intestine locations in the phantom. These exposures are then modeled using the BRYNTRN radiation transport code developed at the NASA Langley Research Center (Wilson et al., 1989), and the CAM (computerized anatomical male) human geometry model of Billings and Yucker (1973). Comparisons of absorbed dose calculations with measurements show excellent agreement. This suggests that there is reason to be confident in the ability of both the transport code and the human body model to estimate proton exposure in ground-based laboratory experiments.

## 5.1 INTRODUCTION

The increase in radiation exposure associated with EVA operations places significant importance on the capability to accurately characterize the crew organ doses shielded by a space suit. To validate risk assessment tools for EVA space suits, we must compare the results of model calculations with data from controlled exposures. This is accomplished as a two-stage process. First, the shielding characteristics of the suit must be characterized at several locations on each suit. Different parts of the suit are composed of very different materials, providing for very different radiation shielding properties. Once the shield measurements have been taken, then controlled irradiations of specific organ locations are performed using a human phantom (Alderson et al., 1962) inside the suit to simulate the body of a crewmember on EVA. Measurements of these irradiations are compared with the results of transport code calculations, giving an indication of the validity of the measured suit shielding qualities, the physical and analytical human geometry models used to simulate the anatomy, and the transport code used to evaluate the travel of the radiation through both suit and body material.

## 5.2 METHODS

We determined EVA suit thickness by adjusting the amount of water-equivalent absorber upstream of the suit or bare-beam to obtain the 50% distal dose point for a 155 MeV proton beam, as described by Moyers et al., in Chapter 2.

First, threshold measurements are taken by placing active radiation detectors (bare ion chambers) on the inner skin of the suit at several key locations, and carefully varying the energy of the incident proton beam to determine the

minimum energy necessary for the radiation to penetrate the suit skin. These penetration energy measurements then are used to derive radiological thicknesses of the suit at these locations. Estimates of the radiological thicknesses of both space suits are developed from ion chamber measurements by the following method:

1. Bare ion chamber measurements are taken in a beam of 155 MeV protons.
2. Absorber material is placed in the beam and the chamber dose re-measured incrementally until the absorber thickness places the measurement at 50% of the Bragg peak value on the distal edge.
3. The space suit is placed into the above configuration, and the same measurement increments are performed, again until the 50% distal dose point is located.
4. The difference in these absorber thicknesses is a first-order estimate of the radiological thickness of the space suit material.

The methodology minimizes the absorber-generated error by first using the same absorber blocks for each measurement, as well as making use only of the differential range relation on the distal edge. These thicknesses provide the primary information necessary to develop shielding models of the space suit that can be used to better characterize the on-orbit exposures to EVA crewmembers. Values of the radiological thickness measured at LLU are given for reference in **Table 5-1** (Moyers et al., Chapter 2, *infra*). Further revisions (~5%) have been made to these thickness estimates since the calculations presented in this report were done, and the revised values are given in an additional column in **Table 5-1**. These values should be used in any future work.

**Table 5-1.** Water-Equivalent Shield Thicknesses of the EMU and Orlan-M as Determined by Energy Threshold Measurements With Proton Beam

Suit	Location	Number of measurement locations	Thickness (g•cm <sup>-2</sup> Water)	Revised thickness (g•cm <sup>-2</sup> Water)
EMU	Soft Layup Swatch	1	0.164	0.164
	Helmet, anterior entrance (visor in place)	1	0.435	0.404
	Helmet, anterior entrance (visor/sun visor in place)	1	0.61	0.589
	Helmet, posterior entrance	1	1.364	1.37
	Glove, dorsal <sup>a</sup>	3	0.224	0.198
	Boot, inferior <sup>b</sup>	1	1.07	1.69
	Helmet-HUT Ring	1	4.45	4.42
	HUT <sup>c</sup>	1	0.43	0.393
	Arm (Soft Area)	1	0.126	0.143
Orlan-M	Soft Layup Swatch	1	0.244	0.244
	Glove <sup>d</sup>	2	0.228	0.198
	Helmet, anterior entrance <sup>e</sup>	1	0.618	0.599
	Arm (Elbow Patch)	1	0.563	0.542
	HUT <sup>c</sup>	1	0.899	0.876

<sup>a</sup> Average of right hand, dorsal entrance, index and ring fingers

<sup>b</sup> Middle phalanx, inferior surface

<sup>c</sup> The value reported for each HUT represents a measurement at a single medial location. Both HUTs have numerous pieces of individual hardware mounted externally on the front of the torso. This shield thickness is not known to be a minimum thickness. Since the external hardware was avoided for these measurements, the given value is reasonably conservative for radiation protection purposes.

<sup>d</sup> Average of right hand dorsal entrance, middle and distal phalanx

<sup>e</sup> Average of measurements, with (0.687) and without (0.511) sun visor in place

The second step was to perform controlled irradiations of the simulated organs of a phantom in each space suit, and to compare the measured absorbed doses with model calculations. To this end, a human phantom (Alderson et al., 1962) was outfitted with passive radiation detectors at specific organ locations, and placed within the suit. The suit thicknesses reported in the fourth column of **Table 5-1** were used in this study to represent the shielding provided by the suits. The EVA crewmember mock-up was then irradiated at sufficient energy (232 MeV for the modeled exposures) to ensure penetration through the suit and into the organs of interest. Dosimeters (including those of Benton et al. *infra*) were placed at well-defined depths within the simulated body. Exposures were then modeled by calculation, and the results compared to the measurements. This comparison provides an indication of the validity of the suit shield values obtained from the threshold measurements, the human geometry model used, and the radiation transport models used to characterize exposures to EVA crewmembers.

Measurements of absorbed dose were made in the EMU-suited phantom at the eye, brain, stomach, lung, and small intestine locations. The eye, brain, and lung represent single detector assembly point measurements in both suits. In the Orlan-M, measurements of absorbed dose were made at the eye and the lung. At the stomach and small intestine locations, multiple-array measurements were taken of absorbed dose versus depth in the body. Additional measurements were taken at the lung and small intestine locations of the EMU-suited phantom. When multiple entry angles were performed, the angle of incidence was rotated about the body's vertical axis. This was done to test the expected effect of the anisotropic shielding provided by both the suit and the body on multidirectionally exposed organ absorbed dose. Each irradiation is characterized by detector location, angle of incidence as measured clockwise from phantom anterior, beam energy, and reference dose. Reference doses for normalization of subsequent model simulations were derived as follows: A reference exposure of an ion chamber under a 5-mm buildup cap was performed absent the suit and phantom for each irradiation configuration to determine the number of counts in beam control detectors per unit dose delivered to the chamber. The number of counts for a given irradiation corresponds to a reference ion chamber dose, to give a reference ion chamber measurement for each experimental irradiation. The operational radiation dosimetry personnel from JSC measured, using the same materials and analytic methods deployed on crewed NASA missions. The measured and modeled irradiation conditions and reference measurements are provided in **Table 5-2**.

**Table 5-2.** Measurement Descriptions

Suit	Organ Location	Type of Measurement	Entry Angle(s) (Degrees)	Reference Ion Chamber Exposure (cGy)
EMU	Eye	Single Point	180	10.0
	Brain	Single Point	135, 180, 210	10.17
	Lung	Single Point	315, 0.0, 30	9.98
	Stomach	Dose vs. Depth	0.0	9.95
	Small Intestine	Dose vs. Depth	0.0	9.99
	Lung	Multi-Angle	0.0, 16.9, 73, 84, 275, 286, 298, 309, 320, 343, 354	4.1 Per exposure, 46.09 Total
	Small Intestine	Multi-Angle	5.6, 16.9, 73, 84, 275, 286, 298, 309, 320, 331, 343, 354	4.2 Per exposure, 53.9 Total
Orlan-M	Eye	Point	180	9.96
	Lung	Point	0.0	9.96

Modeling the exposures for comparison was performed using the CAM model of Billings and Yucker (1973) to describe the composition and geometry of human organs. This model maps the intersection of approximately 1100 quadratic surfaces to construct approximately 2500 volumes that describe internal organs and structures. An example of two views of the CAM modeling of the human head is shown in **Figure 5-1**.

Simulations of absorbed dose measurements were performed using the BRYNTRN proton transport code developed at the NASA Langley Research Center (Wilson et al., 1989). The one-dimensional transport model uses a discrete-ordinates solution to analytically transport protons and secondary charged particles and neutrons through shield materials of arbitrary composition and thickness. For the present work, the threshold thicknesses measured at various points on both suits are used to estimate shielding provided to the measurement locations. Then, a second layer of body material is added to the calculation to model the self-shielding that the body itself provides for an internal dose point.

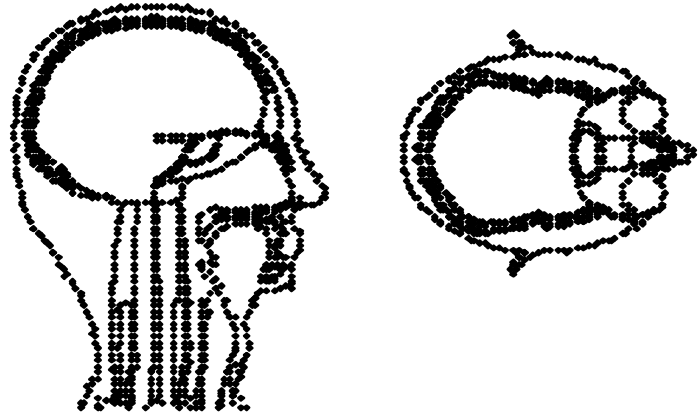


**Figure 5-1.** Example of CAM-derived surfaces that describe internal organ locations and geometries.

For this work, absorbed doses in organ tissues were simulated using two separate methods to simulate the self-shielding of the body. Initially, the actual compositions of tissues in the body are approximated by water. This is accomplished by first deriving the amount of a specified material traversed, and then range-scaled to a representative amount of a surrogate (usually water for body calculations) material. “Range scaling” is a common practice in both radiation protection and radiotherapy applications, and allows a conversion between materials to facilitate calculation. For this work, the ratio of ranges in a given body tissue and water for 155 MeV protons was used for the scaling. A second calculational approach (unpublished) is to forego scaling body materials and instead use more realistic tissue compositions and densities to construct multilayered shields at each location for each entry angle. Transport through tissues such as soft tissue, bone, bone marrow, fat, and water is modeled with BRYNTRN. This second method, implemented herein with the CAM model, provides a more realistic representation of radiation transport in the mock-up, but requires significant time for calculation.

## 5.3 RESULTS

For each irradiation, the results of the simulation are compared with measurements. Results for the point measurements, and percentage differences between measurement and calculation using the measured shield values for the suits are given in **Table 5-3**.

**Table 5-3.** Results of Measurements and Simulation of Absorbed Dose at Experimental Dose Points

Suit, Organ	In-Organ Measurement (cGy)	Calculated Exposure (Water equiv.) (cGy)	Calculated Exposure (Body Materials) (cGy)
EMU Eye	10.05	11.01 (+9.5%)	9.59 (-4.6%)
EMU Brain	10.5	10.74 (+2.3%)	10.51 (0.0%)
EMU Lung	11.5	11.73 (+2%)	11.6 (+0.8%)
EMU Lung (Multi Angle)	54.83	58.08 (+5.9%)	54.83 (0.0%)
EMU Small Intestine (Multi-Angle)	60.0	63.25 (+5.4%)	62.60 (+4.3%)
Orlan-M Eye	9.0	9.28 (+3.2%)	9.29 (+3.2%)
Orlan-M Lung	10.0	9.52 (-4.8%)	9.48 (-5.2%)

As can be seen from the table, the agreement between measurement and calculation appears excellent. This is a preliminary indication that the threshold measurements made in the suits are in fact suitable for use in developing shield models for estimating EVA crew absorbed doses.

Additional proton irradiations were performed in the EMU-suited phantom to measure dose as a function of depth in the stomach and small intestine locations. Again, the beam energy incident on the suit was 232 MeV. These results are compared with simulations in **Figure 5-2**. The thickness indicated on the abscissae includes the pathlength through the suit. Differences are expressed as a percentage of measurement (lower curves, read on the second y-axis). The largest difference between measurement and model calculation is observed for the deepest set of detectors in the stomach. Agreement is within 10% for all other detector locations. The depth-dose results at the “stomach” location in **Figure 5-2** appear to be more flat and less consistent than at the “lower intestine” location lower in the abdomen. These differences may be attributed to beam interactions with bulky metallic items on the anterior of the suit torso. As noted by Zeitlin et al. elsewhere in this publication, the most significant item that partially occluded the beam was a large metallic connector for the LCVG. The attachment ring between the HUT and the lower torso of the suit was another metallic item present in the beam upstream from the detectors in the stomach. The ring may have been positioned directly between the beam entrance and the detectors for this case. It was not possible to attach the phantom absolutely rigidly to the interior of the EMU, so that some shifting was possible. In order to ensure that the beam had sufficient overlap with the detectors, a rather large beam spot was used for this application (15×15 to 20×20 cm). The ring is a relatively thick metallic structure, while the suit around comprises predominantly softer fabric materials, and plastics, all of which have relatively low mass numbers compared with the ring. The proton beam would tend to interact in the higher-z material of the ring, which would cause scattering and produce higher-LET secondaries, and neutrons. Most high-LET secondaries would be stopped before entering the active volume of the TLD, but the neutrons would not. The net result is a portion of the incident protons being replaced by neutrons. The detector material used has a low response to neutrons, and thus may be exhibiting an artificially low response. As stated, however, it must also be allowed that the possibility exists that the beam did not have adequate overlap of the detectors due to the phantom shifting within the suit. Regardless of the exact cause of the error, overall the relative 15% error bound is still considered excellent agreement. The results in **Figure 5-2** illustrate the difficulties inherent to experimental measurement of multiple, large materials of complex shapes and constituents, and demonstrate the crucial role of this experiment to validate charged-particle transport models for risk assessment for critical organs.

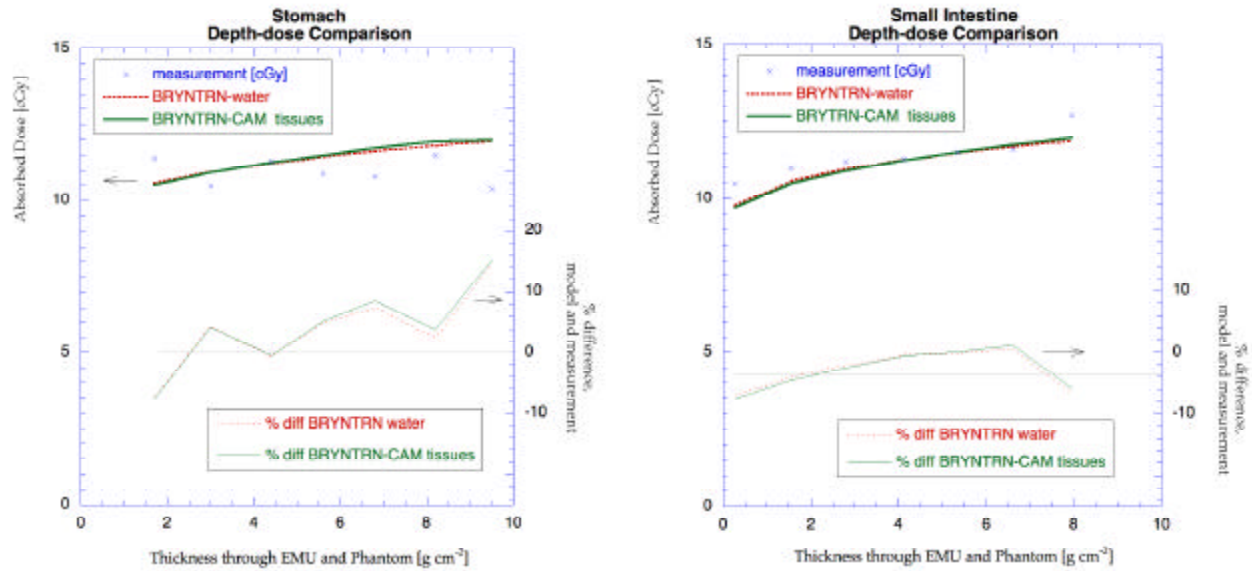


**Figure 5-2.** Comparison of measured depth-dose with BRYNTRN estimates for a water slab or in CAM-derived body tissues along a single ray.

## 5.4 CONCLUSIONS

The observed differences between dosimetry and model calculation for these exposures is bounded in every case save one (9.5 g cm<sup>2</sup> depth measurement in the stomach) by 10%. This indicates two things. First, it is a validating indication for the threshold energy (shield thickness) information measured for both suits. This means that this information is useful in developing realistic shield models of the two suits and for use in characterizing and estimating EVA crew exposures. Second, it indicates a validation of the human geometry model (CAM) used, as well as the BRYNTRN transport model used to calculate the flux of particles at depth in material.

## 5.5 REFERENCES

- Alderson, S.W., Lanzl, L.H., Rollins, M., Spira, J., 1962. An instrumented phantom system for analog computation of treatment plans. *The American Journal of Roentgenology, Radium Therapy, and Nuclear Medicine*, Vol. 87(1), p185.
- Billings, M. P., Yucker, W. R., 1973. *The computerized anatomical man (CAM) model*. Washington, DC: U.S. Government Printing Office, NASA Contractor Report No. CR-134043.
- Wilson, J. W., Townsend, L. W., Nealy, J., Chun, S. Y., Hong, B. S., Buck, W. W., Lamkin, S. L., Ganapol, B. D., Kahn, F., Cucinotta, F. A. *BRYNTRN: A baryon transport model*. Washington, DC: U.S. Government Printing Office, NASA TP-2887, 1989



# **CHAPTER 6**

## **IN VITRO STUDIES ON**

### **SPACE RADIATION-INDUCED**

#### **DELAYED GENETIC RESPONSES:**

##### **SHIELDING EFFECTS**

Munira A. Kadhim<sup>1,2</sup>, Lora M. Green<sup>1,3,4,5</sup>, Daila S. Gridley<sup>1,3</sup>, Deborah K. Murray<sup>1,5</sup>,  
DaThao Tran<sup>1,3</sup>, Debbie Pocock<sup>2</sup>, Denise Macdonald<sup>2</sup>, Melba Andres<sup>1</sup>,  
Michael F. Moyers<sup>6</sup>, Dudley T. Goodhead<sup>2</sup>, Gregory A. Nelson<sup>1</sup>,

<sup>1</sup>Loma Linda University  
Loma Linda, California

<sup>2</sup>MRC Radiation and Genome Stability Unit,  
Harwell, Didcot, Oxon,  
United Kingdom

<sup>3</sup>Loma Linda University Graduate School  
[Green, Tran, & Gridley—Department of Microbiology & Molecular Genetics,  
Green—Physiology]  
Loma Linda, California

<sup>4</sup>Loma Linda University Medical School  
Department of Rheumatology  
Loma Linda, California

<sup>5</sup>JL Pettis Memorial Veterans Medical Center  
Molecular Immunology  
Loma Linda, California

<sup>6</sup>Loma Linda University  
Department of Radiation Medicine  
Loma Linda, California

# IN VITRO STUDIES ON SPACE RADIATION-INDUCED DELAYED GENETIC RESPONSES: SHIELDING EFFECTS

## ABSTRACT

Understanding the radiation risks involved in spaceflight is of considerable importance, especially with the long-term occupation of ISS and the planned crewed exploration missions. Several independent causes may contribute to the overall risk to astronauts exposed to the complex space environment, such as exposure to GCR as well as SPEs. Protons and high-Z energetic particles comprise the GCR spectrum and may exert considerable biological effects even at low fluence. There are also considerable uncertainties associated with secondary particle effects (e.g. HZE fragments, neutrons etc.). The interaction of protons and high-LET particles with biological materials at all levels of biological organization needs to be investigated fully in order to establish a scientific basis for risk assessment. The results of these types of investigation will foster the development of appropriately directed countermeasures.

Since the early 1990s, a number of high profile studies have shown that, as well as acute effects present in cells a few divisions after irradiation, longer-term changes occur in the surviving cells leading to pronounced genomic/chromosomal instability. There are genetic components in mouse and man that determine the relative sensitivity of their cells to radiation-induced genomic instability and ultimately their cancer risk. The genomic instability phenotype may be explained as manifestations of transmissible genomic aberrations that occur at higher frequencies than would be expected from the statistics of individual particle hits to surviving cell nuclei, and may be transmitted from an irradiated cell to a non-irradiated cell by a bystander effect mechanism. However, little is known about either the underlying mechanisms or the *in vivo* consequences of such induced phenotype(s).

In this study, we compared the biological responses to proton irradiation presented to the target cells as a monoenergetic beam of particles of complex composition delivered to cells outside or inside a tissue phantom head placed in the United States EVA space suit helmet. Measurements of chromosome aberrations, apoptosis, and the induction of key proteins were made in bone marrow from CBA/CaJ and C57BL/6 mice at early and late times post exposure to radiation at 0, 0.5, 1 and 2 Gy while inside or outside of the helmet. The data showed that proton irradiation induced transmissible chromosomal/genomic instability in haematopoietic stem cells in both strains of mice under both irradiation conditions and especially at low doses. Although differences were noted between the mouse strains in the degree and kinetics of transforming growth factor- $\beta$ 1 and tumor necrosis factor- $\alpha$  secretion, there were no significant differences observed in the level of the induced instability under either radiation condition, or for both strains of mice. Consequently, when normalized to physical dose, the monoenergetic proton field present inside the helmet-protected phantom produced equivalent biological responses, when compared to unshielded cells, as measured by the induction of delayed genetic effects in *murine* haematopoietic stem cells.

## 6.1 INTRODUCTION

The assembly of ISS is expected to require 1000 hours of EVA during a period of high solar activity. Exposure to GCR and SPEs are a major health risk to humans. Protons and high Z, energetic particles comprise the GCR spectrum and may exert considerable biological effects even at low fluence. During the construction of ISS, the astronauts could be exposed to substantial levels of protons and electrons from SPEs and trapped radiation belts [Space Rad Health Vol1 (1) 2001]. To estimate the protective properties and characterize radiation transport processes they provided, the U.S. and Russian suits were irradiated with protons and electrons at LLUMC facilities in California.

Recent studies have shown that, in addition to acute effects of radiation that occur within a few cell divisions, longer-term changes occur in the surviving cells, leading to pronounced chromosomal instability (Kadhim et al., 1992; Kadhim et al., 1995; Kadhim et al., 2001). However, and perhaps more importantly, there are genetic components in mouse and man that determine the relative sensitivity of their cells to radiation-induced genomic instability and ultimately their cancer risk. Additionally, untargeted genetic lesions occur wherein the induced “mutation rate” at specific loci are higher than can be attributed to initial or direct radiation-induced DNA damage. Transmitted genetic instability may in part be due to a bystander effect mechanism. Despite many high-profile studies, little is known about either the underlying mechanisms or the in vivo consequences of such induced phenotype(s).

In this study, we conducted in vitro biological experiments using murine haematopoietic stem cells. Cytogenetic aberrations, apoptosis, and cytokine production were assessed in bone marrow cultures derived from CBA/CaJ and C57BL/6 mice harvested at early and late times post exposure to proton beam radiation while inside or outside a human tissue phantom placed inside the United States EMU.

## 6.2 MATERIALS AND METHODS

### 6.2.1 Source of Proton Radiation

Proton beam irradiations were performed using 250 MeV protons from the LLUPTF synchrotron accelerator. Protons were delivered from the accelerator in 0.3 s pulses every 2.2 s (Moyers, 1999). Calibration of the dose received by the cells was performed using an N.I.S.T.-traceable Markus<sup>TM</sup> parallel plate ionization chamber in a polystyrene phantom set to mimic the cell culture set-up. The ICRU 59 calibration method (ICRU, Report 59, 1998) was used to convert the ionization signal to dose. The dose ranged from 0 to 2 Gy delivered at a dose rate of approximately 0.35 Gy/minute.

### 6.2.2 Setup of Phantom Head and EMU Helmet

To compare the responses of cells in a relatively pure proton beam to responses under simulated conditions inside the body of an astronaut wearing space suit protection, we placed polypropylene vials of cells in 1) the entrance region of a monoenergetic beam or 2) inside a tissue phantom head covered by the U.S. EMU suit helmet. The two setups were calibrated with an Exradin model T1 thimble ionization chamber placed at the vial location that was adjusted to beam isocenter.

The unshielded configuration consisted of cells placed in polypropylene cryovials located at isocenter behind a 1-cm buildup layer of polystyrene. Delivered physical doses were: 0, 50.3 or 100.3 and 200.1 cGy. For the shielded condition, the vials of cells were placed in a row of machined holes located near the center of the head section of the phantom (average of 90 mm from the “skin” surface at the level of the orbits). The phantom was placed inside the U.S. EMU helmet with sun visor up and facing the oncoming beam. The arrangement of target cells in the phantom head within the helmet and the non-shielded set of cells are shown in the four-panel composite labeled **Figure 6-1**.

The phantom is a custom sliced model # RAN100C (ser. # 731) RANDO<sup>®</sup> Man Phantom. (The Phantom Laboratory, P.O. Box 511, Salem, NY) It is a radiologically accurate phantom representing a 50% anthropometric standard male determined from an Air Force survey renormalized to civilian populations. The material of construction is based on an isocyanate rubber whose density and effective atomic composition are based on the ICRP standard Man for muscle equivalent soft tissue. A natural human skeleton is embedded in the phantom.

### **6.2.3 Source of Haemopoietic Bone Marrow Stem Cells/In Vitro Culture Conditions**

Bone marrow stem cells from two inbred strains of mice, known to be sensitive (CBA) or resistant (C57) to high-LET type of radiation-induced delayed expression of chromosomal/genomic instability (Watson et al. 1997), were selected for use in this study. Male C57 (n =10) and CBA (n=10) mice were purchased from Jackson Laboratories (Bar Harbor, MA), housed and maintained according to specific regulations specified in our approved animal protocol in accordance with the current animal welfare act. From each strain of 10- to 12-week-old animals, we obtained femoral bone marrow cells by removal of the epiphysis and metaphysis at the proximal and distal ends of the femurs and flushing the cells out of the marrow cavity by distal insertion of a 21-gauge needle attached to a syringe containing complete medium (Alpha-MEM, supplemented with 10% fetal calf serum and 1mM glutamine).

The isolated cells were counted and two sets of single-cell suspensions were placed in 2-ml vials and irradiated at 0, 0.5, 1.0 and 2.0 Gy placed either inside the phantom and helmet, or outside the helmet. Immediately after irradiation, haemopoietic stem cell cultures were established by transferring cells to T-75 cm<sup>2</sup> flasks containing 30 ml of medium supplemented with 25% pretested horse serum, antibiotics, and pretested conditioned medium from the AF1.19T and L929 cell lines as sources of colony stimulating activity (Kadhim et al. 1992). Cells were incubated at 37°C in a fully humidified atmosphere of 5% CO<sub>2</sub> in air for a total of 7 days.

Forty-eight hours post-irradiation, 20 ml of the culture were removed from each flask to assess initial genetic damage (Kadhim *et al.* 1992). The cells were used for cytogenetic analysis, and a battery of immunocytochemical measurements [apoptosis (annexin V) and BrdU incorporation into enzymatically induced DNA cleavage] (Green *et.al.* 2001). The supernatant were stored frozen at -70°C and later tested for cytokines released into the supernatant (Gridley *et al.* 1996).

The remaining cultures received 10 ml of fresh medium, supplemented with serum and growth factors (as described above) and incubated an additional 5 days. At the end of the 7-day period (12-15 cell divisions) the

progeny of the surviving cells were assayed for delayed effects of radiation exposure by repeating the cytogenetic, immunocytochemical, and cytokine measurements.

## **6.2.4 Cytogenetic Analysis**

Coded chromosome preparations of various cell populations were made by accumulating metaphases in the presence of 0.02  $\mu\text{g/ml}$  Colcemid for 2h, followed by treatment with 0.5% (w/v) potassium chloride and fixation in methanol:acetic acid (3:1 v/v). Fixed cells were spread on slides, air dried, aged for 1 week at room temperature, and stained with Giemsa. To determine the frequency of karyotypic abnormalities, evident as induced and transmissible chromosomal instability in the progeny of surviving cells, except those samples with low mitotic index, a maximum of 100 well spread metaphases per time point and treatment condition were analyzed.

## **6.2.5 Apoptosis-DNA Damage**

### **6.2.5.1 Annexin V Binding Assay**

When cells are damaged and begin to undergo apoptosis, there is an early event wherein phosphatidylserine is displaced from the inner surface to the outer surface of the plasma membrane (Majno & Joris, 1995). This early event can be detected by the binding of annexin V. To assess the proportion of cells in the irradiated and control cultures that were in early stages of apoptosis, we used an FITC-annexin V labeling procedure (PharMingen, San Diego, CA), modified as described in Green et al. 2001. Bone marrow cells from in vitro cultures were incubated with FITC-conjugated annexin V for 45 min at room temperature. The cells were then centrifuged and washed with wash buffer, fixed in  $-20^{\circ}\text{C}$  70% ethanol for 15 min, rehydrated in PBS and counter-stained with propidium iodide (PI) and RNase for 30 min. The cells were centrifuged and washed in wash buffer before spreading onto microscope slides. The cells were protected with permafluor (Fisher Scientific) and covered with glass coverslips. The slides were dried flat in the dark and scanned on the laser scanning cytometer (CompuCyte, Cambridge, MA).

All of the cell nuclei were labeled red (PI), which allowed them to be located and counted by the laser scanning cytometer. The PI measurements were placed on the y-axis as integrated fluorescence. The x-axis was set to measure green (FITC-annexin V) integral fluorescence. The optimized protocol and display settings were confirmed visually by the microscope camera and stored for use in subsequent analysis of all cells analyzed in these experiments. The average number of cells scanned per slide was 1500+/-200.

### **6.2.5.2 DNA Damage-BrdU Incorporation**

Bone marrow in vitro cultured cells were harvested at early (48 hours) and late (7 days) times post irradiation to measure DNA strand breaks using terminal deoxynucleotidyl-transferase (TdT) mediated fluorescent (FITC)-conjugated BrdU incorporation into free 3' ends of nucleic acids. This methodology does not distinguish single from double strand breaks in the DNA molecules (Li, 1995). The procedure has been previously described in Green et al. 2001. Briefly, cells were fixed in  $-20^{\circ}\text{C}$  70% ethanol for 15 min. The fixed cells were then rehydrated in PBS for 5 min and incubated with a mixture of TdT, reaction buffer, and FITC-BrdU provided with the kit. Cells were

incubated with the DNA labeling mixture overnight at room temperature (22-24°C), washed and counter-stained for 30 min with PI/RNase, washed, and placed on microscope slides protected with permafluor.

FITC-BrdU incorporated into DNA strand breaks were quantified using the laser scanning cytometer. To measure DNA damage, scanning parameters were adjusted by signal intensity to create a contour of the PI nuclear label. To quantify the cells that were both red and green, the gating parameters were set to contour on red (PI) (y-axis) and to sum (integrate) the green fluorescence intensity (FITC-BrdU) (x-axis). Green fluorescent intensity reflected a quantitative measure of DNA damage, as exposed 3' ends, in the irradiated and control cells. Optimized protocol and display settings were stored and used for all samples in these experiments. An average of 1,000+/-200 cells were scanned per side.

## 6.2.6 Analysis for Cytokines

Quantification of *murine* tumor necrosis factor- $\alpha$  (TNF- $\alpha$ ), interleukin-1 $\beta$  (IL-1 $\beta$ ), IL-2, and granulocyte/macrophage-colony stimulating factor (GM-CSF) in bone marrow cell culture supernatants were performed using enzyme-linked immunosorbent assays (ELISA) (Quantikine™ kits, R & D Systems, Minneapolis, MN). These tests are based on the multiple antibody sandwich technique that results in a color reaction and were performed according to the manufacturer's instructions. Supernatants were first centrifuged to remove nonadherent (floating) cells or cell debris. The absorbance in each well was measured in an automated plate reader (Model Fluorite 1000, Dynex Technologies, Inc., Chantilly, VA) equipped with Revelation software version 3.0 and set at appropriate wavelength. Concentration of each cytokine in the test samples was obtained from the respective standard curve. Quantification of transforming growth factor- $\beta$ 1 (TGF- $\beta$ 1) was performed using an ELISA technique (R & D Systems), similar to those for the cytokines described above. However, before testing for TGF- $\beta$ 1, test samples, standards, and control media were activated by acidification with 1N HCl for 1 hr and subsequently neutralized with 1N NaOH to pH 7.0-7.4. Thus, this assay measured the total TGF- $\beta$ 1 (i.e., latent plus biologically active forms). Assay sensitivities were: 5.1 pg/ml (TNF- $\alpha$ ), 3 pg/ml (IL-1 $\beta$ ), 3 pg/ml (IL-2), 1 pg/ml (GM-CSF), and 7 pg/ml (TGF- $\beta$ 1). The number of viable bone marrow cells in the cultures had been determined at harvest by manual counting in the presence of trypan blue. The pg/ml of each cytokine measured was normalized to pg/10<sup>5</sup> cells.

## 6.3 RESULTS

### 6.3.1 Cytogenetic Analysis

Bone marrow stem cells from CBA and C57 mice irradiated while shielded or unshielded from proton radiation were assessed for chromosomal aberrations at early and late times post-irradiation. The early time corresponded to 1-2 cell divisions and the late to 12-15 cells division equivalents, respectively. Aberrations were detected in all cultures and at all doses whether they were placed inside or outside the shielded location. Examples of the types of aberrations typically seen in metaphase chromosome spreads are shown in **Figure 6-2**. Graphs of the total aberrations for the two strains of mice are shown in **Figure 6-3** and specifics on the types of aberrations scored are compiled in **Table 6-1**.

The CBA mouse marrow cells scored at the early time point showed that the unshielded marrow had a reduced frequency of aberration compared to the shielded cells. For the C57 early sample, there was no significant difference between the shielded or unshielded samples. Both strains showed a tendency for the cells exposed to the highest dose of radiation (2 Gy) to have a lower relative level of aberrations than either the 0.5 or 1 Gy irradiated samples (**Table 6-1, Figure 6-3**). In the late time point (12-15 population doublings) samples, the proportion of chromosomally aberrant cells from both strains of mice was highly significant compared to the non-irradiated control group (see p values in **Table 6-1**). This finding was consistent for the lower doses and under both irradiation conditions, with no apparent dose response. The expression of instability determined by chromatid type of aberrations was declining in the 2 Gy proton-irradiated groups under both conditions, the level however remained elevated relative to the control cell levels (p values are in **Table 6-1**).

### 6.3.2 Apoptosis-DNA Damage

The sum of annexin V binding (early apoptosis) and BrdU incorporation (late apoptosis) was used to reflect the total level of cell death occurring in the bone marrow cultures at the two selected harvest times. The values for these two assays are listed in **Table 6-2**. Generally, the strand break assay (BrdU) yielded higher levels for all samples than did the binding of annexin V. Thus, the majority of cells undergoing radiation-induced cell death were in the later stages of apoptosis/necrosis at the early harvest, which was reflected by DNA fragmentation. At the early harvest post-irradiation, the highest level of apoptosis occurred in the CBA cultures at 1 Gy, whereas the C57 cultures had their highest level of apoptosis occurring at 0.5 Gy. There was no radiation dose response in either the shielded or unshielded cells, but the samples that were shielded had a generally higher level of total apoptosis (**Table 6-2, Figure 6-4**).

The apoptotic measurements taken from the cultures harvested at the late time point lacked a dose response similar to that seen in the early harvested cultures. However, the major difference between the early and late harvests were the dose at which the peak cell damage occurred. The highest level of apoptosis occurred in the CBA cultures at 0.5 Gy, whereas the C57 cultures had their highest level of apoptosis occurring at 1 Gy. The CBA late harvest, like the early harvest, had generally higher levels of apoptosis occurring in the shielded cultures. C57 mouse marrow had higher levels of apoptosis occurring, but there was no significant difference between shielded or unshielded samples ( $p > 0.5$ ) (**Table 6-2, Figure 6-4**).

### 6.3.3 Cytokine Production/Release in Irradiated and Control Culture Supernatants

The supernatant harvested from the early and late, shielded and non-shielded cultures were tested for various cytokines; the only significant production was for TGF- $\beta$ 1 and TNF- $\alpha$  (**Table 6-3**). TGF- $\beta$ 1 concentrations increased dramatically in supernatants of cells from both strains of mice compared to non-irradiated cultures under certain conditions. With CBA cells, the greatest increase in TGF- $\beta$ 1 was at 7 days after a shielded dose of 0.5 Gy (23-fold higher than 0 Gy), whereas the peak level in C57 cells occurred at 48 hr after the unshielded dose of 1 Gy (16.5-fold higher than 0 Gy) (**Figure 6-5**). Changes in TNF- $\alpha$  expression were also observed (**Table 6-3, Figure 6-6**), but to a much lesser degree than with TGF- $\beta$ 1. With CBA cells, the greatest increase was at 7 days following a dose of 0.5 Gy

(2.0-fold higher than 0 Gy); the highest levels in supernatants from C57 cells occurred at 7 days after a 2-Gy shielded dose of radiation (3.6-fold higher than 0 Gy). IL-1, IL-2, and GM-CSF were below detectable levels in supernatants from non-irradiated controls, as well as those from irradiated cells, regardless of shielding (data not shown).

## 6.4 DISCUSSION

The cytogenetic investigations demonstrate that proton irradiation can induce transmissible chromosomal/genomic instability in hematopoietic stem cells in both strains of mice under both irradiation conditions, especially at low doses. Previous studies found that the CBA mice were sensitive to the induction of genomic instability in response to high-LET radiation, whereas the C57 mice were relatively resistant (Watson et al. 1997). The major cytogenetic aberrations (chromatid breaks, chromosome fragments) were consistent with the transmission of chromosomal instability. Moreover, the frequency of induced instability was considerably greater than the frequency of induced mutations at specific loci which are characterized by a higher ratio of chromatid to chromosome-type aberrations (Kadhim et al. 1992). In this study, at the times measured, we have demonstrated cytogenetic abnormalities, and detected significant apoptosis in the progeny of stem cell cultures from both strains of mice and under both conditions post-irradiation. There was an inverse relationship between aberrations and apoptosis; this was especially so for the C57 mouse bone marrow cultures (see **Tables 6-1** and **6-2**). These findings have significant implications, in that instability induced per irradiated cell(s) was higher than the number of initial cells at risk, and appears to be exaggerated at the lower doses under both radiation conditions. In one-half of the samples, there was a trend wherein the increased level of TGF- $\beta$ ?measured was coincident with the increased level of cytogenetic aberrations.

The selection of cytokines for assay was based on evidence that they are radiation-inducible, associated with malignant transformation, and/or are important regulators of hematopoiesis (Fortunel et al. 2000; Hallahan 1996). Studies with cytotoxic drugs that affect primarily proliferating cells have demonstrated that TGF- $\beta$  plays a protective role in the bone marrow by inhibiting stem/progenitor cell cycling, an effect that is later reversible (Bottinger et al. 1997). In the present study, the peak level of TGF- $\beta$ 1 produced by irradiated CBA cells was approximately 3.5-fold higher than that produced by irradiated C57 cells (**Table 6-3**). It is tempting to speculate that the high TGF- $\beta$ 1 produced by the CBA strain may have protected progenitors in which subtle radiation-induced mutations existed (e.g. inactivation of a gene involved in growth regulation), but were not detectable by the methods used. Indeed, it has been proposed that genomic instability and mutations leading to defects in TGF- $\beta$  signaling may work in concert to accelerate tumor progression in multistage carcinogenesis (Glick et al. 1999). If this is proven true, it may account at least partly for the high susceptibility of CBA/Ca mice to radiation-induced acute myeloid leukemia. Our observation of somewhat lower levels of apoptosis in the CBA cultures, suggesting that these cells are less prone to die as a result of irradiation compared to C57 cells, is consistent with this premise. However, the well-documented transforming potential of TGF- $\beta$ 1 and the variable responses of different bone marrow cell populations to the factor should also be considered.

TNF- $\alpha$  is a cytokine that can induce oxygen radical production, DNA damage, and apoptosis (Gupta et al. 1992; Rath & Aggarwal 1999), and has, like TGF- $\beta$ , been associated with genetic instability (Rosselli et al, 1994). Studies also indicate that TNF- $\alpha$  can augment the effects of radiation on a variety of cell types (Griley 1996;

Hallahan 1996). The presented data show that peak TNF- $\alpha$  levels occurred at late harvest for both strains of mice, but no consistent patterns or correlations with the other measurements were identified.

In conclusion, the present study has demonstrated the induction of transmissible chromosome/genomic instability in *murine* haematopoietic stem cells after proton irradiation whether shielded or unshielded, that were most pronounced at the lower doses implemented. Consistent with previous observations, the frequency of induced instability in the present study was considerably greater than the frequency of conventional chromosome aberrations or gene mutations, which persisted as a result of the direct effect of ionizing radiation. The absence of significant differences in the level of instability between the shielded and unshielded radiation conditions suggest that at equal physical dose there was no quantitative difference in the biological response between the complex radiation environment produced by shielding components and the relatively pure proton beam. The differences in TGF- $\beta$ 1 and, to a much lesser extent, TNF- $\alpha$  expression between the two strains of mice warrant further investigation regarding the role that these cytokines may play in radiation-induced leukemogenesis.

## 6.5 ACKNOWLEDGMENTS

The authors wish to thank Steven Rightnar for his help with these experiments. These studies were supported by a NASA Cooperative Research Agreement # NCC9-79 with contributions from the Chan Shun International Foundation.

## 6.6 REFERENCES

- Alderson S.W., Lanzl L.H., Rollins M., Spira J., 1962. An Instrumented Phantom System for Analog Computation of Treatment Plans. *The American Journal of Roentgenology, Radium Therapy, and Nuclear Medicine*; 87, p185.
- Bottinger E.P., Letterio J.J., Roberts A.B., 1997. Biology of TGF- $\beta$  knockout and transgenic mouse models. *Kidney Int*; 51, 1355-1360.
- Fortunel N.O., Hatzfeld A., Hatzfeld J.A., 2000. Transforming growth factor- $\beta$ : pleiotropic role in the regulation of hematopoiesis. *Blood*; 96; 2022-2036.
- Geng Y., Hellstrand K., Wennmalm A., Hansson., 1996. Apoptotic death of human leukemic cells induced by vascular cells expressing nitric oxide synthetase in response to  $\gamma$ -interferon and tumor necrosis factor- $\alpha$ . *Cancer Res*; 56, 866-874.
- Glick A., Popescu N., Alexander V., Ueno H., Bottinger E., Yuspa S.H., 1999. Defects in transforming growth factor-beta signaling cooperate with a ras oncogene to cause rapid aneuploidy and malignant transformation of mouse keratinocytes. *Proc Natl Acad Sci USA*; 96, 14949-14954.
- Green L.M., Murray D.K., Tran D.T., Bant A.M., Kazarians G., Moyers M.F., Nelson, G.A., 2001. Response of thyroid follicular cells to gamma versus proton irradiation: I. Initial characterization of DNA damage, micronuclei formation, apoptosis, survival and cell cycle phase redistribution. *Radiat. Res*; 155, 32-42.
- Green L.M., Lazarus J.P., LaBue M., Shah M.M., 1995. Deficient cell-cell communication in a spontaneous *murine* model of autoimmune thyroiditis. *Endocrinol*, 136, 3611-3618.

- Gridley, D.S., 1996. The role of cytokines in radiation therapy for cancer (Review). *Cancer J.* 9:236-242, 1996.
- Gridley D.S., Slater J.D., Yonemoto L., Miller D.W., Rossi C., Archambeau J.O., Slater J.M., 1996. Pilot study of cytokine profiles in prostate cancer patients undergoing proton radiotherapy. *Int J Oncol*; 8, 175-181.
- Gupta J.W., Kubin M., Hartman L., Cassatella M., Trinchieri G., 1992. Induction of expression of genes encoding components of the respiratory burst oxidase during differentiation of human myeloid cell lines induced by tumor necrosis factor and g-interferon. *Cancer Res*; 52, 2530-2537.
- Hallahan D.E., 1996. Radiation-mediated gene expression in the pathogenesis of the clinical radiation response. *Sem Radiat Oncol*; 6, 250-267.
- International Commission on Radiation Units and Measurements, Clinical proton dosimetry part 1: Beam production, beam delivery and measurement of absorbed dose, 1998. (Maryland: *ICRU*, Report 59.
- Kadhim M.A., Macdonald D.A., Goodhead D.T., Lorimore S.A., Marsden S.J., Wright E.G., 1992. Transmission of chromosomal instability after plutonium  $\alpha$ -particle irradiation. *Nature* 355:738-740.
- Kadhim M.A., Lorimore S.A., Townsend K.M.S., Goodhead D.T., Buckle V.J., Marsden S.J., Wright E.G., 1995. Radiation-induced genomic instability: delayed cytogenetic aberrations and apoptosis in primary human bone marrow cells. *Int. J. Radiat. Biol.*; 67, 287-293.
- Kadhim M.A., Marsden S.J., Wright E.G., 1998. Radiation-induced chromosomal instability in human fibroblasts: temporal effects and the influence of radiation quality. *Int. J. Radiat. Biol*; 78, 143-148.
- Li F., Traganos M., Melamed R., Darzynkiewicz Z., 1995. Single step procedure for labeling DNA Strand breaks with fluorescein- or BODIPY-conjugated deoxynucleotides. Detection of apoptosis and bromodeoxyuridine incorporation. *Cytometry*; 20, 172-180.
- Majno G., Joris I., 1995. Apoptosis, oncosis and necrosis. An overview of cell death. *Am. J. Pathol.*; 46, 3-15.
- Moyers M.F., 1999. "Proton Therapy" in *The Modern Technology of Radiation Oncology: A Compendium for Medical Physicists and Radiation Oncologists* (J. VanDyk, Ed.). Pp 823-869. Wisconsin: Medical Physics Publishing.
- Rath P.C., Aggarwal B.B., 1999. TNF-induced signaling in apoptosis. *J Clin Immunol*; 19, 350-364.
- Space Radiation Health Project web site: <http://srhp.jsc.nasa.gov>.
- Rosselli F, Sanceau J, Gluckman E, Wietzerbin J, Moustacchi E., 1994. Abnormal lymphokine production: a novel feature of the genetic disease Fanconi anemia. II. In vitro and in vivo spontaneous overproduction of tumor necrosis factor alpha. *Blood* 83(5),1216-25.
- Watson G.E., Lorimore S.A., Clutton S.M., Kadhim M.A., Wright E.G., 1997. Genetic factors influencing alpha-particle-induced chromosomal instability. *Int J Radiat Biol*; 71, 497-503.

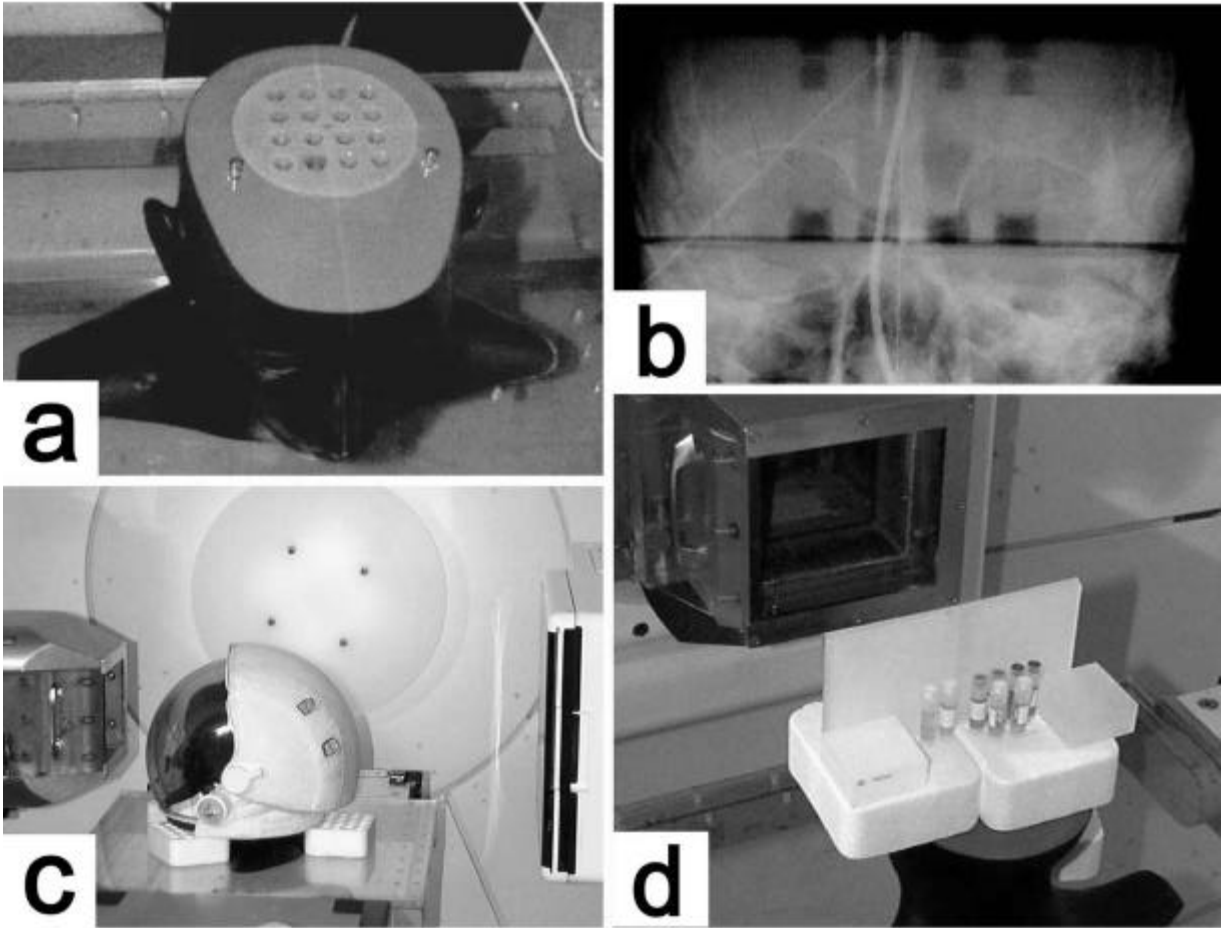


**Figure 6-1.** Proton Irradiation Set-up for Biological Experiment in U.S. EMU Helmet. The four-panel composite depicts the arrangement of the target cells used in these experiments. The half-phantom head is shown in panel a, and an x-ray of the cell alignment is shown in panel b. The full set-up of cells in the phantom head plus helmet placed in front of the proton beam nozzle are shown in panel c, and the non-shielded cells in position for proton beam irradiation are shown in panel d (with a 1cm buildup layer of polystyrene).

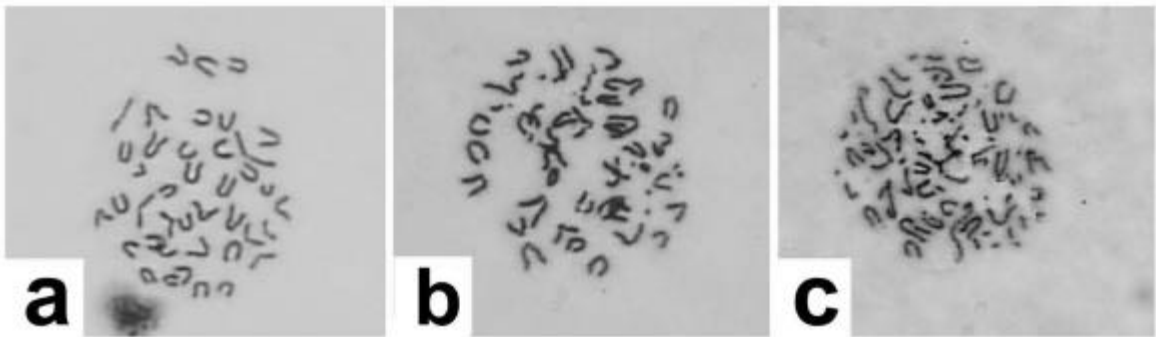


**Figure 6-2.** Metaphase Chromosome Spreads from Mouse Bone Marrow Stem Cells. Cytogenetic aberrations in bone marrow cultures were assessed from chromosome spreads like those depicted in this three-panel composite. Panel a depicts a typical chromosome spread from a normal *murine* cell with no obvious aberrations. Panel b shows moderate damage with two sets of double minutes and a translocation. Panel c is an example of significant damage with multiple small fragments of chromosomes, and double minutes. Specific details on the aberrations scored in these experiments can be found in Table 6.1.

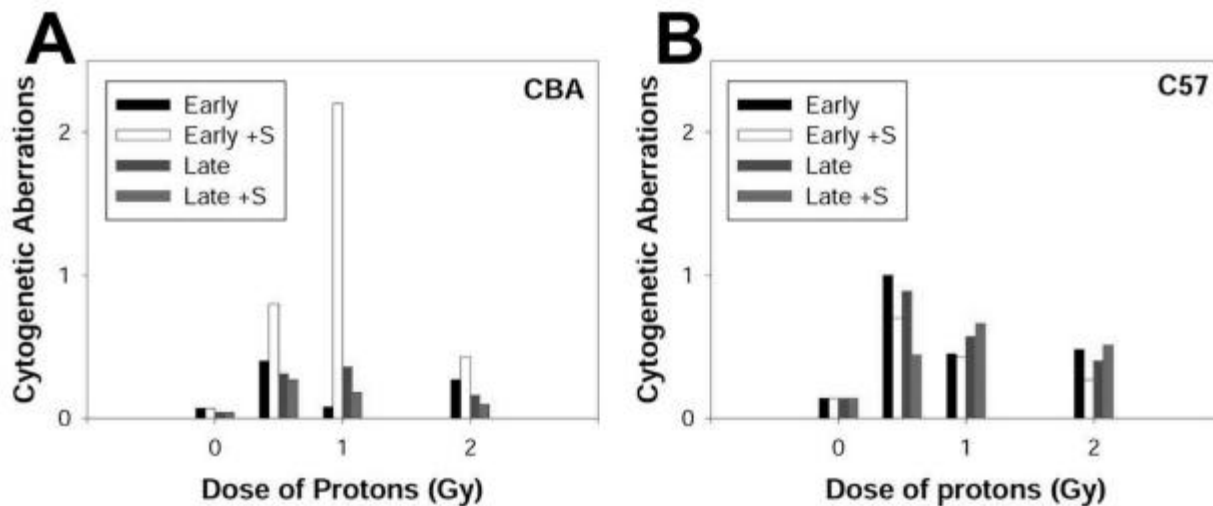


**Figure 6-3.** Cytogenetic Aberrations in Bone Marrow Stem Cell Cultures Exposed to Proton Radiation While Shielded or not Shielded by the U.S. EMU Helmet and Rando Phantom Head. Panel A shows the results of cytogenetic aberrations scored in cultures established from CBA mouse bone marrow. Panel B shows the aberrations detected in the C57 mouse bone marrow cultures. In general, C57 marrow cells had higher levels of aberrations at all doses and conditions tested. The specific details obtained from the metaphase chromosome spread analyses are compiled in Table 6-1.

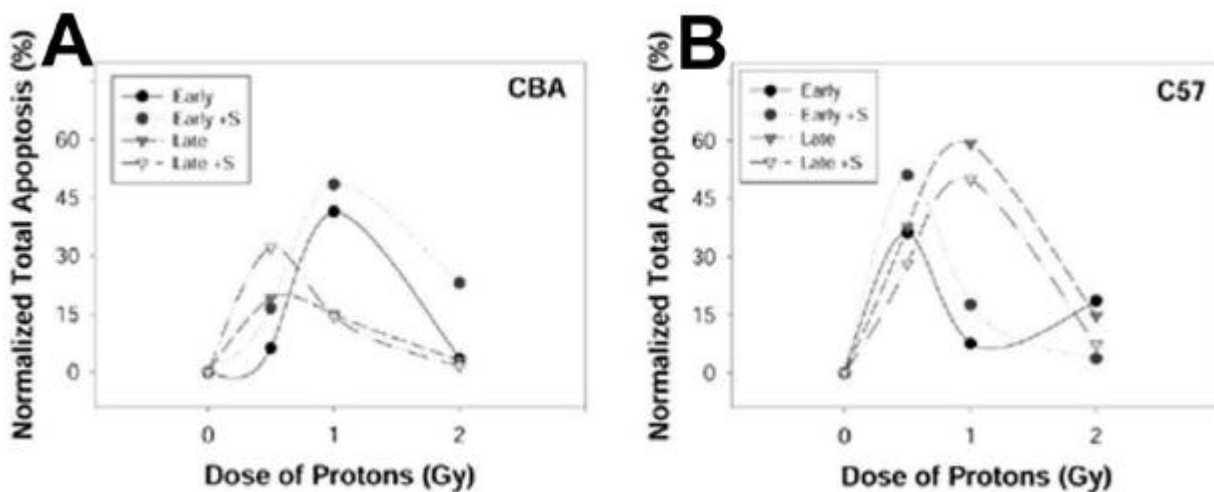


**Figure 6-4.** Apoptosis in Bone Marrow Stem Cell Cultures Exposed to Proton Radiation While Inside or Outside the Phantom Head and Helmet. The sum of annexin V binding (early apoptosis) and BrdU incorporation (late apoptosis) were used to determine total apoptosis in the bone marrow cultures. Panel A shows CBA mouse marrow cells and Panel B shows the results for C57 mouse marrow. The C57 mouse cells were generally more apoptotic than the CBA marrow cells. The peak level of apoptosis was seen at 0.5 and 1Gy, with the 2Gy dose point being depressed for both strains. The breakdown of % of annexin V (early apoptosis) and BrdU-incorporation (late apoptosis) per dose of radiation and time are shown in Table 6-2.

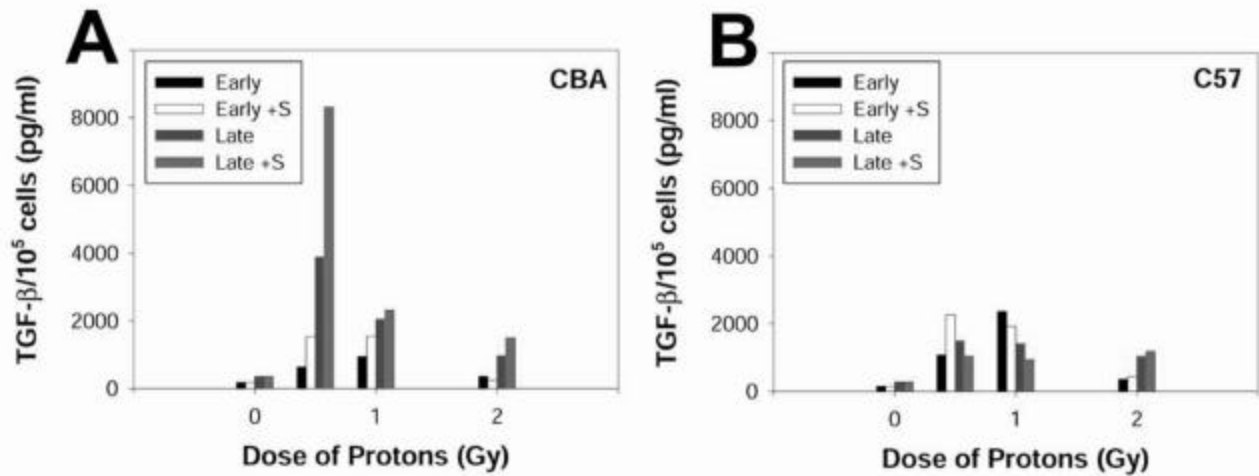


**Figure 6-5.** TGF- $\beta$ 1 in Bone Marrow Cell Supernatants. The concentration (pg/ml) of the cytokine in each supernatant was determined by ELISA and then normalized to  $10^5$  viable cells present at the time of harvest. The values represent the summation of the active and latent forms of the factor. The control level from the kit was 287.3 pg/ml and the assay sensitivity was  $\pm 7$  pg/ml.

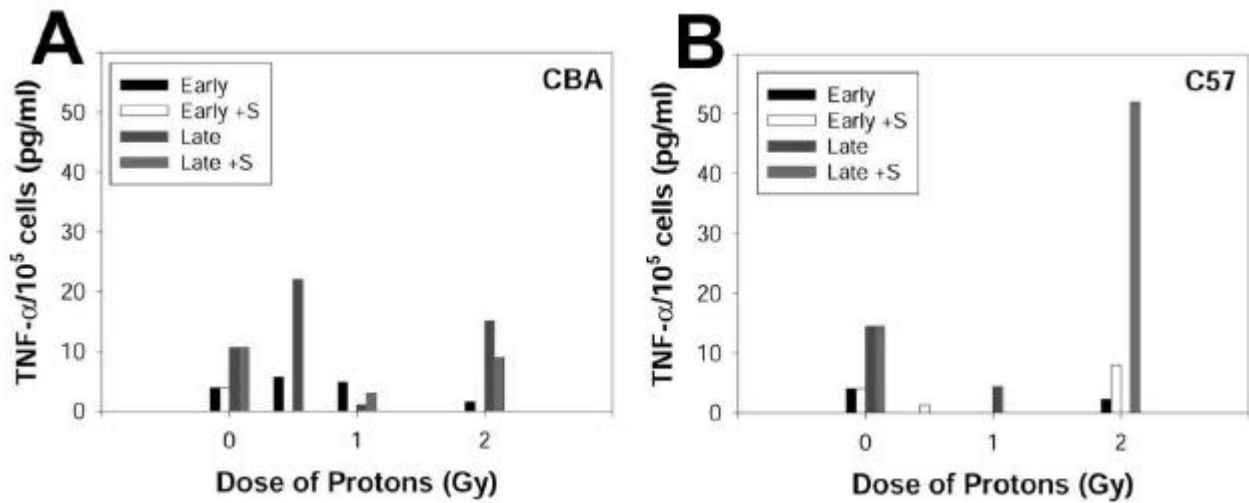


**Figure 6-6.** TNF- $\alpha$  in Bone Marrow Cell Supernatants. The concentration (pg/ml) of the cytokine in each supernatant was determined by ELISA and then normalized to  $10^5$  viable cells present at the time of harvest. The control level from the kit was 94.1 pg/ml and the assay sensitivity was  $\pm 5.1$  pg/ml.

**Table 6-1. Cytogenetic Aberrations**

	Dose <sup>a</sup>	#scored	Type of Aberration <sup>b</sup>							Total <sup>c</sup>	% Ab <sup>d</sup>
			B	Ring	DM	Transl	Chrt Aber	Iso Cht			
<b>CBA</b>											
Early <sup>e</sup>	0	100	0	0	0	0	7	0	7.0	7	
Harvest	0.5	15	0	0	0	0	6	0	6.0	40 <sup>**</sup>	
	1	12	0	0	0	0	1	0	1.0	8	
	2	100	1	1	1	1	22	1	27.0	27 <sup>***</sup>	
Early +S <sup>f</sup>	0.5	5	0	1	1	0	2	0	4.0	80 <sup>**</sup>	
Harvest	1	12	0	1	0	0	24	1	26.0	220 <sup>***</sup>	
	2	100	0	4	2	0	36	1	43.0	43 <sup>***</sup>	
Late <sup>g</sup>	0	100	0	0	0	0	4	0	4.0	4	
Harvest	0.5	93	0	1	2	0	23	3	29.0	31 <sup>***</sup>	
	1	100	0	3	0	0	30	3	36.0	36 <sup>***</sup>	
	2	100	0	2	0	1	11	2	16.0	16 <sup>**</sup>	
Late +S	0.5	100	0	3	1	0	20	3	27.0	27 <sup>***</sup>	
Harvest	1	55	0	2	0	0	7	1	10.0	18 <sup>**</sup>	
	2	100	0	1	0	0	9	0	10.0	10	
<b>C57</b>											
Early	0	100	1	0	0	0	13	0	14.0	14	
Harvest	0.5	53	10	3	0	1(di)	38	1	53.0	100 <sup>***</sup>	
	1	64	1	0	4	0	19	5	29.0	45 <sup>***</sup>	
	2	100	0	2	22	0	21	3	48.0	48 <sup>***</sup>	
Early +S	0.5	42	6	2	1	0	20	0	29.0	69 <sup>***</sup>	
Harvest	1	75	2	4	2	1	21	1	32.0	43 <sup>***</sup>	
	2	100	0	0	6	0	21	0	27.0	27 <sup>***</sup>	
Late	0	100	1	0	0	0	13	0	14.0	14	
Harvest	0.5	100	0	3	4	0	76	6	89.0	89 <sup>***</sup>	
	1	100	2	4	2	0	46	3	57.0	57 <sup>***</sup>	
	2	100	2	11	2	0	24	1	40.0	40 <sup>***</sup>	
Late +S	0.5	100	2	6	2	0	31	3	44.0	44 <sup>***</sup>	
Harvest	1	100	1	5	11	0	46	3	66.0	66 <sup>***</sup>	
	2	100	3	5	3	1	39	0	51.0	51 <sup>***</sup>	

a= Dose of 250MeV proton beam radiation delivered to the cells.

b= Type of aberrations, including: breaks (B); rings; translocations and chromatid/chromosome.

c= Total aberrations scored.

d= Percentage of aberrations scored.

e= Early refers to cultures that were maintained for 1-2 cell divisions (48hrs).

f= S, represents samples that were irradiated while shielded by the helmet and phantom head.

g= Late refers to cultures that were maintained for 12-15 cell divisions (7 days).

\*P<0.05, \*\*P<0.01; \*\*\*P<0.001 compared to 0 Gy

**Table 6-2.** Apoptosis Measured by Annexin V and BrdU Incorporation

	Dose <sup>a</sup>	Early Apoptotic Events % Annexin V Binding	Late Apoptotic Events BrdU-Incorporation	Total (%) <sup>b</sup> Apoptosis
<b>CBA</b>				
Early <sup>c</sup>	0	0.0	0.0	0.0
Harvest	0.5	0.0	6.2	6.2
	1	15.4	26.0	41.4
	2	1.0	3.4	4.4
Early +S <sup>d</sup>	0.5	0.0	16.6	16.6
Harvest	1	19.4	29.1	48.5
	2	0.0	23.0	23.0
Late <sup>e</sup>	0	0.0	0.0	0.0
Harvest	0.5	9.6	9.5	19.1
	1	7.7	7.4	15.1
	2	0.0	3.0	3.0
Late +S	0.5	18.3	13.9	32.2
Harvest	1	5.9	8.6	14.5
	2	1.5	0.0	1.5
<b>C57</b>				
Early	0	0.0	0.0	0.0
Harvest	0.5	3.5	32.7	36.2
	1	7.6	0.0	7.6
	2	15.5	3.2	18.7
Early +S	0.5	2.1	49.0	51.1
Harvest	1	0.0	17.7	17.7
	2	0.5	3.2	3.7
Late	0	0.0	0.0	0.0
Harvest	0.5	11.5	26.2	37.7
	1	9.0	50.2	59.2
	2	11.7	3.9	14.7
Late +S	0.5	11.4	16.8	28.2
Harvest	1	11.0	39.7	50.0
	2	5.0	2.3	7.3

a= Dose of 250MeV proton radiation (Gy).

b= Total apoptosis expressed as the sum of annexin V & BrdU displayed as % of the cells scored.

c= Early- refers to cultures maintained for 1-2 cell divisions (48hrs).

d= S, represents samples that were irradiated while shielded by the helmet and phantom.

e= Late- refers to cultures maintained for 12-15 cell divisions (7 days).

**Table 6-3.** Cytokine Production/Release in Irradiated & Control Culture Supernatants

	Dose <sup>a</sup>	TGF- $\beta$ <sup>b</sup> pg/ml/ 10 <sup>5</sup> Cells	TNF- $\alpha$ <sup>c</sup> pg/ml/ 10 <sup>5</sup> Cells
CBA			
Early <sup>d</sup>	0	180.9	3.8
Harvest	0.5	633.3	5.7
	1	944.0	4.8
	2	363.9	1.6
Early +Se	0.5	1,530.6	0.0
Harvest	1	1,549.9	0.0
	2	241.6	0.0
Late <sup>f</sup>	0	356.6	10.6
Harvest	0.5	3,884.6	21.6
	1	2,050.4	0.2
	2	954.4	15.0
Late +S	0.5	8,307.0	0.0
Harvest	1	2,316.7	2.9
	2	1,498.3	8.5
C57			
Early	0	143.2	3.7
Harvest	0.5	1,066.7	0.0
	1	2,363.2	0.0
	2	357.0	2.3
Early +S	0.5	2,254.1	1.3
Harvest	1	1,928.5	0.0
	2	436.1	7.7
Late	0	277.1	14.6
Harvest	0.5	1,483.6	0.0
	1	1,413.4	4.4
	2	1,036.0	NT*
Late +S	0.5	1,035.6	0.0
Harvest	1	938.1	0.0
	2	1,177.8	52.2

a= Dose of 250MeV proton radiation (Gy).

b= Total TGF- $\beta$  (pg/ml) in supernatant adjusted per 10<sup>5</sup> cells (assay sensitivity 7pg/ml)

c= Total TNF- $\alpha$  (pg/ml) in supernatant adjusted per 10<sup>5</sup> cells (assay sensitivity 5.1pg/ml)

d= Early- refers to cultures maintained for 1-2 cell divisions (48hrs).

e= S, represents samples that were irradiated while shielded by the helmet and phantom.

f= Late- refers to cultures maintained for 12-15 cell divisions (7 days).

Note: IL-1 $\beta$ , IL-2 and GM-CSF were not detected in these supernatants; NT: not tested.

# **CHAPTER 7**

## **RADIATION DOSE**

### **FROM REENTRANT ELECTRONS**

(previously published,  
Radiation Measurements 2001 June 33(3):369-72)

G.D. Badhwar, T.E. Cleghorn  
NASA Johnson Space Center  
Houston, Texas

J. Watts  
NASA Marshall Space Flight Center  
Huntsville, Alabama

# RADIATION DOSE FROM REENTRANT ELECTRONS

## ABSTRACT

In estimating the crew exposures during an EVA, the contribution of reentrant electrons has always been neglected. Although the flux of these electrons is small compared to the flux of trapped electrons, their energy spectrum extends to several GeV compared to about 7 MeV for trapped electrons. This is also true of splash electrons. Using the measured reentrant electron energy spectra, it is shown that the dose contribution of these electrons to the blood forming organs (BFO) is more than 10 times greater than that from the trapped electrons. The calculations also show that the dose-depth response is a very slowly changing function of depth, and thus adding reasonable amounts of additional shielding would not significantly lower the dose to BFO.

## INTRODUCTION

The astronaut exposures from trapped protons and electrons have traditionally been estimated using the AP8 and AE8 models (Sawyer and Vette, 1976, Heyndrickx, 1999). However, the contribution of reentrant and splash electrons has always been neglected. The reentrant electrons are the decay products of nuclear interactions in the upper atmosphere of GCR particles, which are trapped in the Earth's magnetic field, spiral along field lines, and reenter, in a downward direction in the opposite hemisphere, but at similar latitudes. The reentrant electrons are distinguished from *splash albedo* electrons, which are upward moving secondary electrons.

In this note, the dose to BFO from reentrant electrons has, for the first time, been calculated. It is compared to the dose from the trapped electrons for a typical ISS orbit of  $51.65^\circ \times 400$  km.

## RESULTS

**Figure 7-1** is plot of the AE8 estimated electron differential energy spectra and reentrant electron energy spectrum. The reentrant electron spectrum was obtained from measurements of Barwick et al. (1998) made during May 1994 (the value of deceleration potential that describe the level of solar modulation,  $\phi$ , was estimated from the Climax neutron monitor rates, to be 640 MV) using the High-Energy Antimatter Telescope (HEAT). The reentrant flux is higher beyond  $\sim 8$  MeV compared to that from the trapped component, assuming that the angular distribution of both components is isotropic. In thinly shielded locations, the dose contribution of trapped electrons would clearly be dominant. **Table 7-1** gives the estimated EVA exposures using the AE8-MIN model. The calculations were done using a Computerized Anatomical Model (Billings and Yucker, 1973) and electron transport program SheilDose2 (Seltzer 1988, Berger and Wang 1988). Data acquired by the Radiation Environment Monitor (REM) instrument mounted on the outside of the Mir core module (Buhler et al., 1996) shows that the AE8-MIN model over-predicts the electron dose by a factor of three and the AE8-MAX model over-predicts the dose by a factor of  $\sim 8$ . Data acquired onboard the CRESS satellite during solar maximum (Gussenhovan et al., 1991) also shows that the AE8-MAX model over- predicts the dose by nearly a factor of  $\sim 8$ . Thus, the actual BFO dose rate from trapped electrons is probably less than  $0.23 \text{ mrad day}^{-1}$ .

As is clear from **Table 7-1**, there is very large attenuation of the trapped electron dose due to their soft electron spectrum going inward from skin to BFO. The reentrant spectrum however is hard. An approximate idea of the dose contributed by these electrons can be obtained by integrating the reentrant flux with the stopping power (<http://physics.nist.gov/PhysRefData/Star/Text/contents.html>). This is the dose rate at zero depth and is 2.56 mrad/day. Because of the hardness of this spectrum, the dose rate would be a slowly decreasing function of depth and thus it is expected that the BFO dose contribution would be higher than that estimated from just trapped electrons. A number of electron transport codes have been developed to study the propagation of high-energy electrons (Nelson et al., 1985, GEANT 3, 1994) that take into account pair production. The dose was calculated by two methods. **Figure 7-2** gives the dose rate-depth dependence. The curves identified as rad dose (tissue) were calculated by using GEANT3 version 123-radiation transport code. The electrons, positrons, and photons were transported and their energy deposition in a thin tissue detector (assumed to be 0.001 cm thick) was tabulated. When the energy dropped below 100 keV, the kinetic energy of the particle was deposited and the particle terminated. The energy deposition was then converted to absorbed dose in rads. The results are given in **Figure 7-2** as a function of aluminum shielding thickness and show that the dose rate barely drops as the thickness increases from 0.5 to 20 g/cm<sup>2</sup>. The curves in **Figure 7-3** marked as rem dose (in tissue) were also calculated using fluxes from GEANT3 and energy dependent flux to dose conversion factors for each particle type (Iwai et al., 1998), which yielded a dose in rems rather than rads. The factors used are for the maximum dose equivalent generated in a 30 cm slab of tissue, which should yield a moderate overestimate of dose. The factors were augmented at energies below 10 MeV for photons (Swanson et al., 1979). These results also show that the dose rate is a very shallow function of shielding depth and thus integrating them over the BFO shielding distribution has little effect. Using GEANT3 one gets a BFO dose equivalent rate of 4 mrem/day compared to 6 mrem/day using dose conversion factors. If the angular distribution were not isotropic, as is most certainly the case, these values would decrease somewhat. There is, however, the splash electron flux, which is nearly equal to that from reentrant electrons (Barwick et al., 1998). It is also worth noting that the measurements of Barwick et al. were not made near the solar minimum ( $\phi = 640$  MV) and as such represent a lower limit to flux for a solar minimum time period ( $\phi \approx 470$  MV). Thus the true combined solar minimum reentrant and splash electron fluxes is thus shown to be more than 10 times larger than the contributions from trapped electrons.

The nearly flat response of the dose rate with depth shows that augmenting the space suit by increasing the volume of the cooling garment or adding water through other means would not lower the BFO dose from electrons significantly.

## CONCLUSIONS

Reentrant and splash electrons have never before been considered in estimating crew exposures during EVAs. It is shown that the contribution of reentrant electrons is more than 10 times greater than the contribution of trapped electron BFO dose. Including the splash electron contribution only increases the ratio. The dose decreases very slowly with increasing shielding and thus adding reasonable amounts of material to the space suit would not lead to a significant reduction to the BFO dose rate.

# ACKNOWLEDGEMENT

We thank William Atwell, Boeing Inc., Houston, Texas for help and discussions and Dr. Tony Armstrong, SAIC, for bringing the Swanson et al. reference to our attention.

**Table 7-1.** Trapped Belt Electron Absorbed Dose Rate

Organ	Skin (Arms & Legs)	BFO	EYE
Additional Space Suit Shielding (g cm <sup>-2</sup> )	0.154	0.490	0.490
Dose rate (mrad/day)	1493	0.70	75

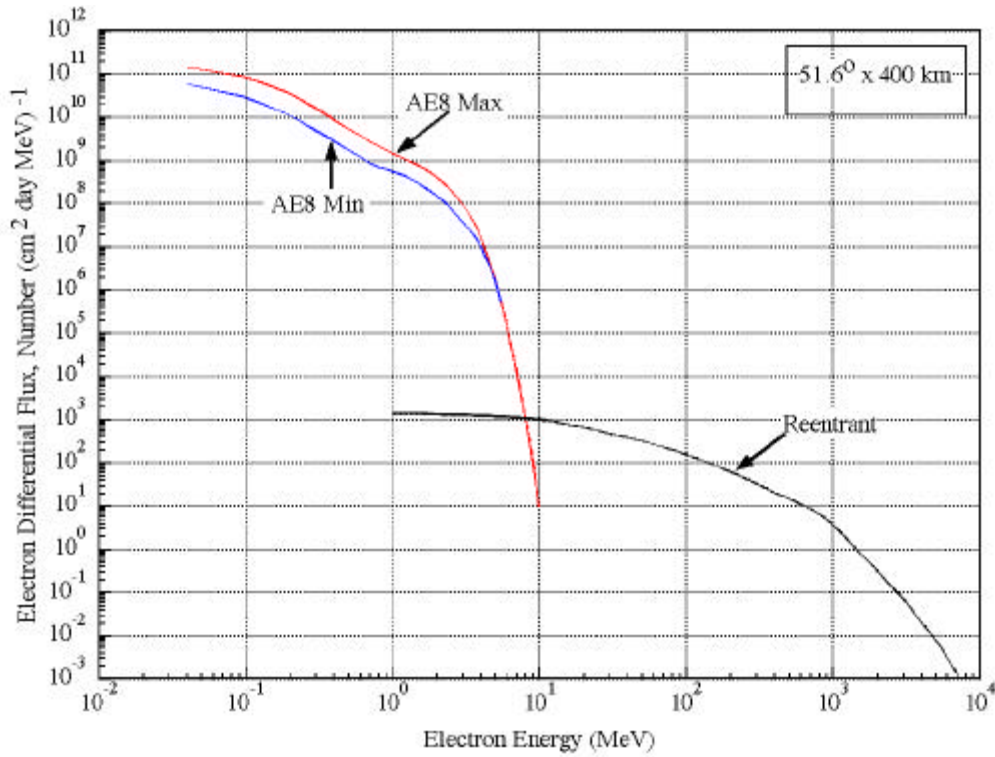


**Figure 7-1:** Plot of trapped and reentrant electron differential energy spectra.

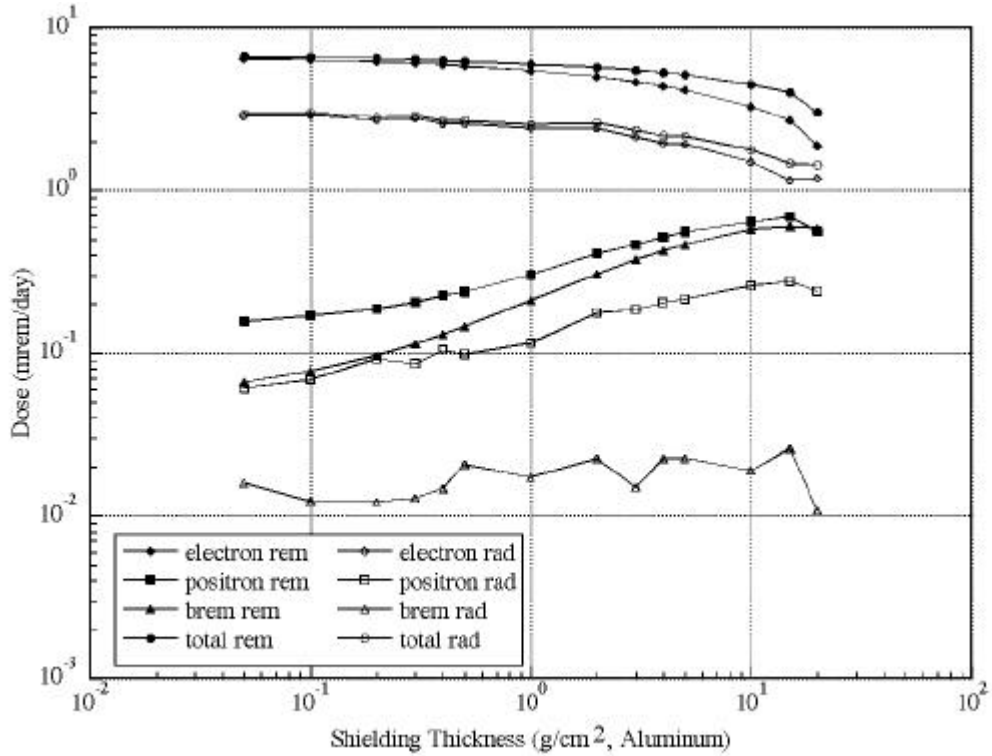


**Figure 7-2:** Plot of absorbed dose and dose equivalent rate from electrons, positrons, and photons using the fluxes from GEANT3 and the fluence to dose conversion factors.

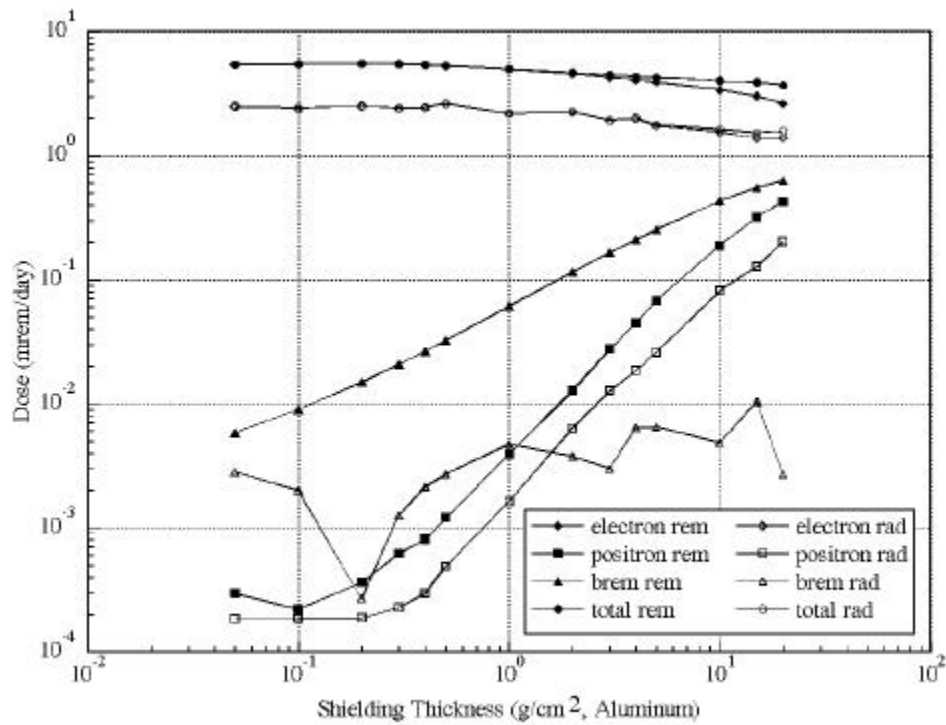


**Figure 7-3:** Plot of the absorbed dose from electrons, positrons, and bremsstrahlung using the GEANT3 transport code.

## REFERENCES

- Barwick, S.W., Beatty, J.J., Bower, C.R., Chaput, C.J., Coutu, S., de Nolfo, G.A., DuVernois, M.A., Ficenec, D., Knapp, J., Lowder, D.M., McKee, S., Miller, D., Musser, J.A., Schneider, E., Swordy, S.P., Tarle', G., Tomasch, A.D., and Torbert, E. 1998, Cosmic ray reentrant electron albedo: High-Energy Antimatter Telescope balloon measurements from Fort Sumner, New Mexico, *J. Geophys. Res.* 103, 4817-4823.
- Berger, M.J. and Wang, R.1998: in "Monte Carlo Transport of Electrons and Photons"; T.M. Jenkins, W.R. Nelson and A. Rindi (Eds.), Plenum Press, 21-56.
- Berger, M.J. 1998: in "Monte Carlo Transport of Electrons and Photons"; T.M. Jenkins, W.R. Nelson and A. Rindi (Eds.), Plenum Press, 57-80.
- Billings, M.P. and Yucker, W.R. 1973, Summary final report. The computerized anatomical man (CAM) model, Report MDC-G4655, McDonnell Douglas Company, Huntington Beach, CA (September 1973).
- Buhler, P., Desorgher, L., Zehnder, A., Daly, E., and Adams, L. 1996, Observations of the Low Earth Orbit Radiation Environment From Mir, *Rad. Meas.* 26, 917-921.
- GEANT 3, 1994: Detector Description and Simulation Tool, Application Software Group, Computing and Networks Division, CERN, Geneva, Switzerland.
- Gussenhovan, M.S., Mullen E.G., Brautigam, D.H., Holeman E., Jordon C., Hanser F., and Dichter B. 1991, Preliminary comparison of dose measurements on CRRES to NASA model predictions. *IEEE Trans. Nucl. Sci.* 39, 1655-1662.
- Heyndrickx, D. 1999, SPENVIS Space ENVironment Information System <http://www.spervis.oma.be/>
- Iwai, Satoshihi et al. 1998, Overview of Fluence to Dose Equivalent Conversion Coefficients for High-Energy Radiation-Calculational Methods and Results of Effective Dose Equivalent and Effective Dose Per Unit Particle Fluence", Proc. Shielding Aspects of Accelerators, Targets, and Irradiation Facilities (SATIF-3), OECD Nuclear Energy Agency.
- Nelson, W.R., Hirayama, H., and Rogers, D.W.O 1985, "The EGS4 Code System"; Report SLAC-265.
- Sawyer, D.M. and Vette, J.I. 1976, AE-8 Trapped Electron Environment for Solar Maximum and Solar Minimum, NSSDC/WDC-A-R&S 76-06, National Science Data Center, Goddard Space Flight Center, Greenbelt, Maryland.
- Seltzer, S.M. 1988: in "Monte Carlo Transport of Electrons and Photons"; T.M. Jenkins, W.R. Nelson and A. Rindi (Eds.), Plenum Press, 21-56.
- Swanson, W.P. 1979, "Radiological Safety Aspects of the Operation of Electron Linear Accelerators", Technical report Series No. 188, International Atomic Energy Agency, Vienna.
- Vette, J.I. 1991, "The AE-8 Trapped Electron Model Environment" NSSDC/WDC-A-R&S9-24, National Science Data Center, Goddard Space Flight Center, Greenbelt. Maryland.

# **CHAPTER 8**

## **SHUTTLE SPACE SUIT: FABRIC/LCVG MODEL VALIDATION**

(previously published)

J.W. Wilson  
NASA Langley Research Center  
Hampton, Virginia

J. Tweed  
Old Dominion University  
Norfolk, Virginia

C. Zeitlin  
DOE Lawrence Berkeley National Laboratory  
Berkeley, California

M.-H. Y. Kim  
College of William and Mary  
Williamsburg, Virginia

B.M. Anderson  
George Washington University  
Hampton, Virginia

F.A. Cucinotta  
NASA Johnson Space Center  
Houston, Texas

J. Ware, A.E. Persans  
ILC Dover  
Frederica, Delaware

## **ABSTRACT**

A detailed space suit computational model is being developed at the Langley Research Center for radiation exposure evaluation studies. The details of the construction of the space suit are critical to estimation of exposures and assessing the risk to the astronaut on EVA. Past evaluations of space suit shielding properties assumed the basic fabric layup (Thermal Micrometeoroid Garment, fabric restraints, and pressure envelope) and LCVG could be homogenized as a single layer overestimating the protective properties over 60 percent of the fabric area. The present space suit model represents the inhomogeneous distributions of LCVG materials (mainly the water filled cooling tubes). An experimental test is performed using a 34-MeV proton beam and high-resolution detectors to compare with model-predicted transmission factors. Some suggestions are made on possible improved construction methods to improve the space suit's protection properties.

## **INTRODUCTION**

The construction of ISS requires 1500 hours of EVA during construction and 400 hours per year in operations and maintenance. The orbit at 51.6 degrees inclination is in a highly variable radiation environment driven by solar activity. SPEs will enter this region, especially during an associated geomagnetic storm. The geomagnetic storm conditions also increase the trapped electron environment by up to four orders of magnitude; this electron enhancement can persist for several days. Although safety demands that such events be avoided if possible, work activity may not allow the astronaut to seek shelter in a timely fashion and the transmission properties of the basic suit are critical to astronaut safety. These exposures will add to the usual quiet-time exposures to trapped protons and electrons and galactic cosmic rays experienced by the astronaut.

The driving factor in this study is the need for an adequate space suit model for the estimation of exposures for mission planning and evaluation of safety during radiation field disturbance. Although there are several issues related to the protective properties of the space suit, we will address herein only the least shielded portions of the suit, which provides the basic protection of a large fraction of the body surface. In particular, the basic fabric portion of the suit mainly gives protection to the skin from the least penetrating radiation components. Other critical space suit issues will be addressed in subsequent studies. In addition, an improved understanding of the basic transmission properties of the space suit fabric components, which is a complex layup of materials, will provide a guide to improving the basic fabric design. Other critical space suit components will be addressed in subsequent studies.

It is customary in estimating the fabric transmission properties to assume the basic fabric layup is a homogenized whole of the associated materials [1,2]. In the present document, we will analyze this assumption in detail and perform experimental tests of this assumption using low-energy proton beams.

## **COMPUTATIONAL MODEL**

The types and energy distributions of particles transmitted through a shield material require the solution to the Boltzmann transport equation with appropriate boundary conditions related to the external space radiation

environment. The relevant transport equation [3] for the flux density  $f_j(x, W, E)$  of type  $j$  particles moving in direction  $W$  with energy  $E$  is given as

$$W \cdot \tilde{N} f_j(x, W, E) = \int \delta s_{jk}(W, W', E, E') f_k(x, W', E') dW' dE' - s_j(E) f_j(x, W, E) \quad (1)$$

where  $s_j(E)$  is the media macroscopic cross section for removal of  $j$  particles of energy  $E$ ,  $s_{jk}(W, W', E, E')$  are the media macroscopic cross sections for various atomic and nuclear processes adding  $j$  particles of energy  $E$  in direction  $W$  including spontaneous disintegration. In general, there are hundreds of particle fields  $f_j(x, W, E)$  with several thousand cross-coupling terms  $s_{jk}(W, W', E, E')$  through the integral in equation (1). The total cross section  $s_j(E)$  with the medium for each particle type of energy  $E$  may be expanded as

$$s_j(E) = s_{j,at}(E) + s_{j,el}(E) + s_{j,r}(E) \quad (2)$$

where the first term refers to collision with atomic electrons, the second term is for elastic nuclear scattering, and the third term describes nuclear reactive processes and is ordered as  $1:10^{-5}:10^{-8}$ . This ordering allows flexibility in expanding solutions to the Boltzmann equation as a sequence of physical perturbative approximations. The atomic interactions are treated using energy moments in which the leading term is the usual continuous slowing down approximation. Special problems arise in the perturbation approach for neutrons for which the nuclear elastic process appears as the first-order perturbation and has been the recent focus of research [4,5].

Important to low-energy proton penetration are the atomic processes. Traditionally we have used the first energy moment to describe the energy loss in atomic processes and the resulting range-energy relations. More recently, the second energy moment has been added as related to range straggling [6] with added improvements resulting to the evaluations shown in **Figure 8-1**. Shown in the figure is the second moment presented as the full width at half maximum (FWHM) of the resultant energy distribution about the first energy moment seen at a depth  $x$  in aluminum for 49.1 MeV protons where  $R_0$  is the mean range. Excellent agreement is found for the second energy moment in comparison with the experiments of Tschalar and Macabee [7].

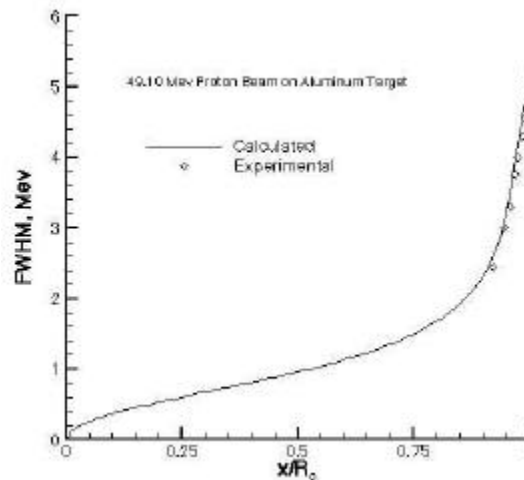


**Figure 8-1.** FWHM of 49.1 MeV protons in an aluminum target.

## SPACE SUIT FABRIC MODEL

The Shuttle space suit is manufactured by ILC Dover for use in the space program. The basic components are shown in **Figure 8-2**. Not shown in the figure is the life support system held mainly in a backpack attached to the HUT. We are mainly concerned herein with the Arm assembly and Lower Torso Assembly (LTA) consisting mainly of fabric and the LCVG consisting of fabric and the water filled cooling tubes. The basic layout of the fabric and LCVG are shown in **Figure 8-3**.

The most easily penetrated portion of the space suit is covered only by the fabric (Arm Assembly and LTA) and the LCVG. This is of greatest importance when the environment contains low energy particles with limited penetration power. Most environmental components contain such particles, and these are often the most intense component. They are only of concern for tissues which are poorly shielded and not of concern within a space vehicle assembly such as the Shuttle or ISS or for organs deep within the body. The basal layer of the skin is somewhat sensitive to radiation and therefore of concern in a lightly shielded space suit in an intense and low-energy environment.

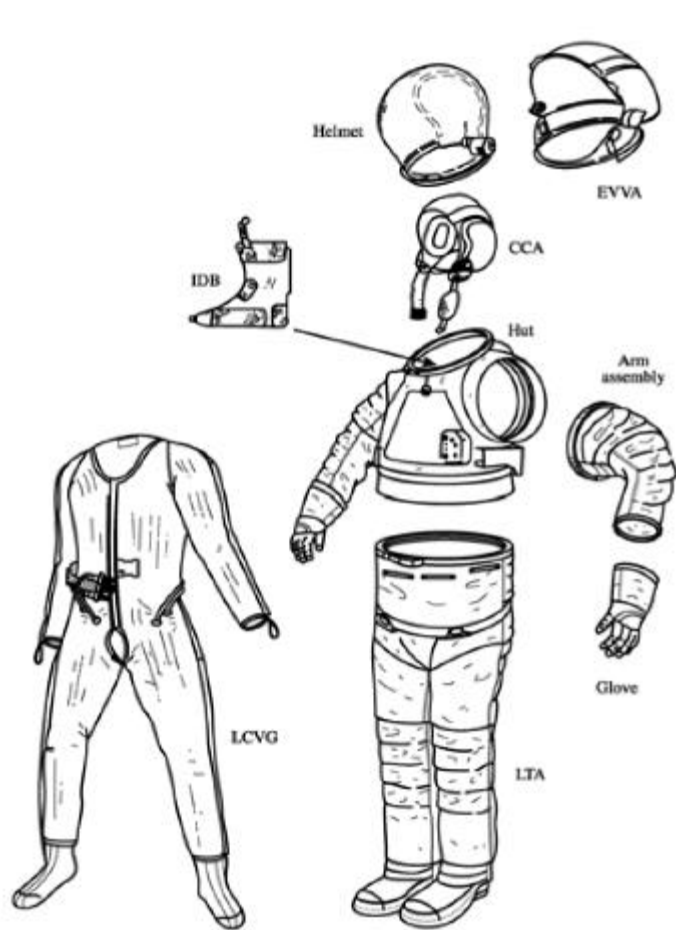


**Figure 8-2.** Basic components of the Shuttle space suit.

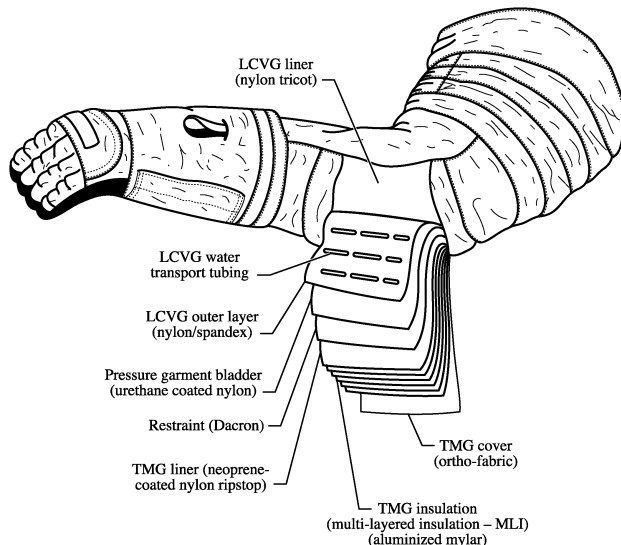


**Figure 8-3.** Cross section of material layup.

The material layup for the fabric including the inner LCVG is given in **Table 8-1**. The outer fabric layer, the Thermal Micrometeoroid Garment (TMG), is composed of the OrthoFabric, five layers of Reinforced Aluminized Mylar for thermal insulation and Neoprene Coated Nylon Ripstop. Below the TMG is the Dacron® pressure restraint. This is followed by the Urethane Coated Nylon (pressure bladder) and the LCVG of a multifilament Nylon/Spandex knit which contains the ethylvinyl-acetate tubes filled with water.

**Table 8-1.** Material Layup of the Space Suit Fabric and Water Filled Tube [1,8]

Material	Areal density, g/cm <sup>2</sup>
Orthofabric-Teflon/Nomex/Kevlar	0.049
Reinforced Aluminized Mylar	0.014
Neoprene Coated Ripstop	0.028
Dacron® Polyester	0.021
Urethane Coated nylon Ripstop	0.014
Nylon/Spandex/water/ethylvinylacetate	0.154

In past calculations [1], the materials in **Table 8-1** were described by equivalent amounts of aluminum by scaling with the ratio of range of a 50 MeV proton in aluminum to the range in the specific material and calculations made for penetration in the equivalent aluminum. There are three concerns with this approach: the equivalent aluminum scale factor depends on the proton energy yet the assumed equivalency at 50 MeV is not accurate for minimum penetration particles; the water filled tubes cover only 40 percent of the surface area and the homogenization with the Spandex over-estimates the protection properties of the fabric (with homogenized tube) over 60 percent of the area; and, many components of the fabric layup are inhomogeneous structures and may not be well represented by an average areal density.

The surest way to represent the actual fabric/tube transmission properties is to remove these defects by representing the water filled tube geometry specifically, transporting through actual material layers as opposed to assuming equivalent aluminum, and performing penetration test to test models of the inhomogeneities within the remaining fabric. These tasks are performed in the present study and the fabric transmission properties are represented as an analytical model with good agreement with low-energy proton transmission testing. The improved understanding of the fabric transmission properties will allow redesign considerations to improve the space suit radiation safety. The basic penetration test is shown schematically in **Figure 8-4**. The test is in principle quite simple; a low-energy proton beam is incident from the left on a swatch of the space suit and water filled tubes as shown. The arrangement of the experimental setup is shown in **Figure 8-5** as used in the present testing. A reasonably uniform beam of approximately 34.5 MeV protons enters the Lexan collimator from the left and is monitored by a 3mm thick silicon detector (d3mm1). The transmitted spectrum through d3mm1 was measured in a “target out” test. The monitored beam passes through the target station and analyzed by a set of position sensitive detectors (PSD1X&Y) with total remaining energy detected by the 5-mm silicon detector (d5mm1).

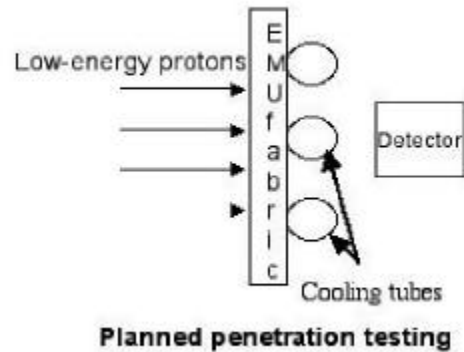


**Figure 8-4.** Basic experimental set up.

The test is in principle quite simple; a low-energy proton beam is incident from the left on a swatch of the space suit and water filled tubes as shown. The arrangement of the experimental setup is shown in **Figure 8-5** as used in the present testing. A reasonably uniform beam of approximately 34.5 MeV protons enters the Lexan collimator from the left and is monitored by a 3mm thick silicon detector (d3mm1). The transmitted spectrum through d3mm1 was measured in a “target out” test. The monitored beam passes through the target station and analyzed by a set of position sensitive detectors (PSD1X&Y) with total remaining energy detected by the 5-mm silicon detector (d5mm1).

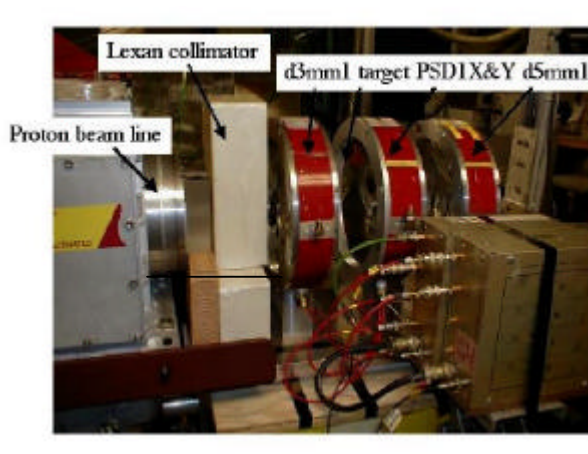


**Figure 8-5.** Proton beamline used at the LBNL 88” cyclotron.

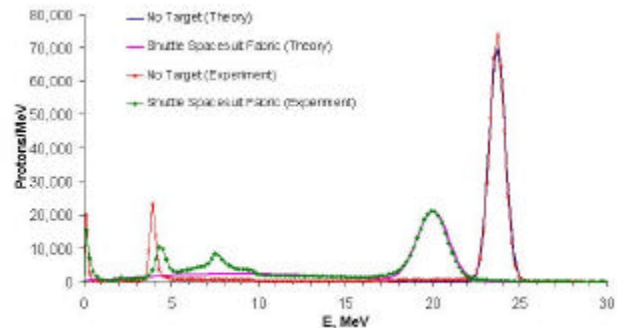


**Figure 8-6.** Experimental and analysis results.

## RESULTS AND IMPLICATIONS

The beam was first analyzed without the target in place with results (no target) appearing as the near normal distribution of particles at the far right in **Figure 8-6**. The computational model was fit to the beam parameters before the d3mm1 and found to be of 34.54 MeV with a standard deviation of 0.27 MeV resulting in the  $23.68 \pm 0.46$  MeV beam incident on the target shown in the figure. The additional broadening of the energy spectrum is due to

straggling in the d3mm1 monitor. The results of the analysis are shown in comparison to the experimental estimate of the beam properties at the target. There is an added spectral feature near 4 MeV in the experimental data believed to be due to multiple scattering effects in the collimator.

The beam transmitted through the target is shown also in the figure. The spectral feature at  $19.94 \pm 0.967$  MeV results from the transmission through the fabric without a tube in the proton path. The increased width of this peak relative to the beam before the target results from straggling effects in the fabric and the non-uniformity of some of the fabric components. The fabric is best fit as a normal distribution of material of mean thickness of  $0.161 \pm 0.03$  g cm<sup>-2</sup> of material. The mean areal density of the fabric (without the cooling tubes) is measured to be  $0.185$  g cm<sup>-2</sup>. The height of the transmitted peak is critically dependent on the size of the tube (tube diameter is 4 mm) and tube spacing (1 per centimeter). In the model, the water filled tube was assumed to be a homogeneous mixture of appropriate mass of water and ethylvinylacetate. The experiment indicates that the improved penetration properties of the water may be apparent in the data as the experimental transmitted spectral feature near 7 MeV may be due to water in the tube. Hence, some added detail for the model is required.

## **FUTURE ACTIVITY**

The next step in the analysis will be to model the tube to better understand the lowest energy transmission of this complex system. Additional experiments will be performed to better understand the source of the non-uniformity of the fabric components. This will be accomplished by noting that the penetration properties of the fabric components are near that of polycarbonate. The nonuniform elements (e.g., spandex) will be modeled by an equivalent sheet of uniform polycarbonate and the transmitted spectrum will be determined and analyzed. This should provide a reasonable model of the space suit fabric and cooling tubes for use in estimating astronaut exposures. Finally it would be desirable to study the electron transmission characteristics for which the basic physical description of the fabric should be similar. An appropriate electron beam for experimental testing is being investigated.

Secondly, upon complete understanding of the current space suit transmission properties we can improve estimates of the astronaut exposures in space activity [9]. In addition, this understanding of the performance of the fabric layup elements and experimental testing procedures will allow evaluation of alternative space suit designs.

The next least protected critical organ is the lens of the eyes. They are protected mainly by the helmet components. Plans for testing the helmet component transmission properties are in progress.

## **CONCLUSION**

Considerable progress was made in understanding the basic transmission properties of the space suit fabric as it is now used in the space program. Additional detail is required to adequately model the proton transmission properties of the LCGV cooling tubes. It is desirable to also study the electron transmission properties to insure that a consistent picture of the space suit fabric is obtained. The basic fabric model as outlined is being integrated into a space suit model for estimates of astronaut exposures during future missions.

## REFERENCES

1. Kosmos J.J., Nachtwey D.S., Hardy A. JSC/CTSD-SS-241, 1-24-1989.
2. Wilson J. W. et al. NASA CP 3360, 1997.
3. Wilson, J. W. et al., Transport Methods and Interactions for Space Radiations. NASA Reference Publication, RP-1257, 1991
4. Heinbockel, J. H. et al. An Improved Neutron Transport Algorithm for Space Radiation. NASA TP-2000-209865, 2000.
5. Cloudsley, M. S. et al., A comparison of the multigroup and collocation methods for solving the low energy neutron Boltzmann equation. To be published Cana. J. Phys. 78: 45-56, 2000.
6. Wilson J.W., Tai H.A. NASA 2000-209864, 2000.
7. Tschalar C., Maccabee, H. D. Phys. Rev. B 1: 2863-2869, 1970.
8. Ross A.J. et al. NASA CP 3360, 1997.
9. Anderson B. M. et al. SAE 01ICES-147, 2001.

## CONTACT

The communicating author email address is:

John.W.Wilson@LaRC.NASA.GOV

# **CHAPTER 9**

## **PRELIMINARY SHUTTLE SPACE SUIT SHIELDING MODEL**

Brooke M. Anderson  
George Washington University  
Hampton, Virginia

J. E. Nealy  
Old Dominion University  
Norfolk, Virginia

G.D. Qualls, P.J. Staritz, J.W. Wilson  
NASA Langley Research Center  
Hampton, Virginia

M.-H. Y. Kim  
College of William and Mary  
Williamsburg, Virginia

F. A. Cucinotta  
NASA Johnson Space Center  
Houston, Texas

W. Atwell  
The Boeing Co.  
Houston, Texas

G. De Angelis  
NASA Langley Research Center  
Hampton, Virginia  
& Istituto Superiore di Sanita'  
Rome, Italy

J. Ware, A. E. Persans  
ILC Dover  
Frederica, Delaware

# PRELIMINARY SHUTTLE SPACE SUIT SHIELDING MODEL

## 9.1 INTRODUCTION

A detailed space suit computational model is being developed at the Langley Research Center for exposure evaluation studies. The details of the construction of the space suit are critical to an estimate of exposures and for assessing the risk to the astronaut during EVA. Fine detail of the basic fabric structure, helmet, and backpack is required to assure a valid evaluation. The exposure fields within the computerized anatomical male (CAM) and female (CAF) are evaluated at 155 and 160 points, respectively, to determine the dose fluctuations within critical organs. Exposure evaluations for ambient environments will be given and potential implications for geomagnetic storm conditions discussed.

It has been stated that ISS will require up to 1500 hours of EVA during its construction and 400 hours of EVA per year in operations and maintenance. The 51.6° inclination of the ISS orbit provides a highly variable radiation environment driven by solar activity. SPEs will adversely impact the radiation environment in this region, especially in the case of an associated geomagnetic storm, during which the region of influence is expanded during the storm main phase [1]. The geomagnetic storm conditions also increase the strength of the trapped electron environment by up to four orders of magnitude; this electron enhancement can persist for several days. Even under quiet field conditions, the distribution of dose within the body is vastly different than that experienced within ISS and dose gradients near the body surface are important to the evaluation of effective dose as related to cancer and cataract risks. This gradient is related to the material make-up of the space suit about critical body organs and enhancements of the electron environment during times of geomagnetic activity.

There are two space suits in current usage within the space program: EMU [2] and Orlan-M Space Suit [3,4]. The Shuttle space suit components are discussed elsewhere [2,5,6] and serve as a guide to development of the current model. The present model is somewhat simplified in details which are considered to be second order in their effects on exposures. A more systematic approach is ongoing on a part-by-part basis with the most important ones in terms of exposure contributions being addressed first with detailed studies of the relatively thin space suit fabric as the first example [7]. Additional studies to validate the model of the head coverings (bubble, helmet, visors...) will be undertaken in the near future. The purpose of this paper is to present the details of the model as it is now and to examine its impact on estimates of astronaut health risks. In this respect, the nonuniform distribution of mass of the space suit provides increased shielding in some directions and some organs. These effects can be most important in terms of health risks [8] and especially critical to evaluation of potential early radiation effects [9].

## 9.2 SPACE SUIT DESCRIPTION

The basic space suit assembly is shown in **Figure 9-1**. The LCVG fits close to the body and is constructed of Spandex, Nylon net, and ethylvinylacetate tubing filled with circulating water. The areal density of the Spandex/Nylon net is 0.076 g/cm<sup>2</sup> and the 4-mm o.d. tube is 0.078 g/cm (including water); they are inserted in the Spandex at the rate of 1 tube per centimeter (**Figure 9-2**). The usual approximation of the LCVG material is

0.154 g/cm<sup>2</sup> as used by Kosmo et al. [5]. The inadequacy of this approximation is thoroughly discussed in [7]. The communications carrier assembly is currently not represented in the model. The helmet with its internal vent deflector is constructed of polycarbonate, as is the protective visor of the EVVA. The remaining visors are constructed of polysulfone. The assembly has an inner Teflon liner and is covered by an Orthofabric for mechanical protection, aluminized Mylar for thermal insulation, and Dacron. The material list is given in **Table 9-1**.

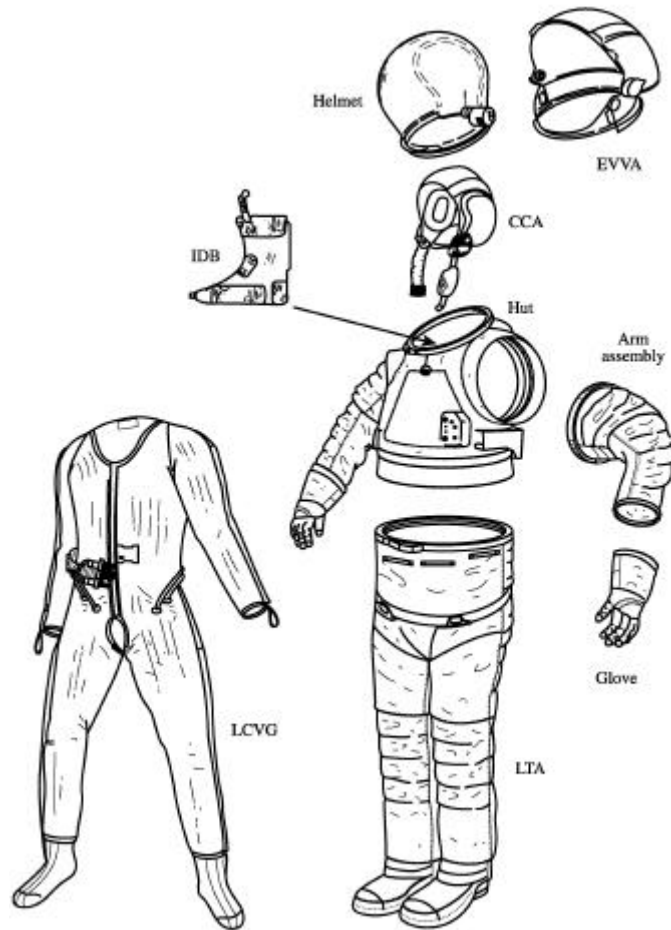


**Figure 9-1.** Basic components of the Shuttle space suit.

**Table 9-1.** Material Layups of Helmet and Extravehicular Visor Assembly

Layer	Material	Areal Density, g/cm <sup>2</sup>
Outer layer	Orthofabric-Teflon/Nomex/Kevlar	0.049
Insulation	Aluminized Mylar- 5 plys	0.014
Spacer	Dacron fiber- 5 plys	0.011
Inner liner	Teflon	0.028
Extravehicular visor assembly shell	Polycarbonate	0.381
Sun visor	Polysulfone	0.190
Eye shade	Polysulfone	0.190
Protective visor	Polycarbonate	0.182
Helmet	Polycarbonate	0.182

The remainder of the suit consists of the HUT, the arm assemblies including gloves, and the LTA. The HUT main body is constructed of Fiberglas and covered outside with Orthofabric, aluminized Mylar, and Neoprene-coated Nylon ripstop. Under the HUT is the LCVG next to the astronaut body. The material layup in the HUT region of the suit is given in **Table 9-2**. The arm assemblies and LTA are made of fabric and water-filled cooling tubes. The fabric layups are shown in **Figure 9-2** and described in **Table 9-3** and [6]. The fabrics of the arm assembly and LTA, gloves, and boots are given a simplified representation in the present model. For example, there is additional fabric in locations where bending occurs to allow flexibility. These will be modeled later in the next level of detail.

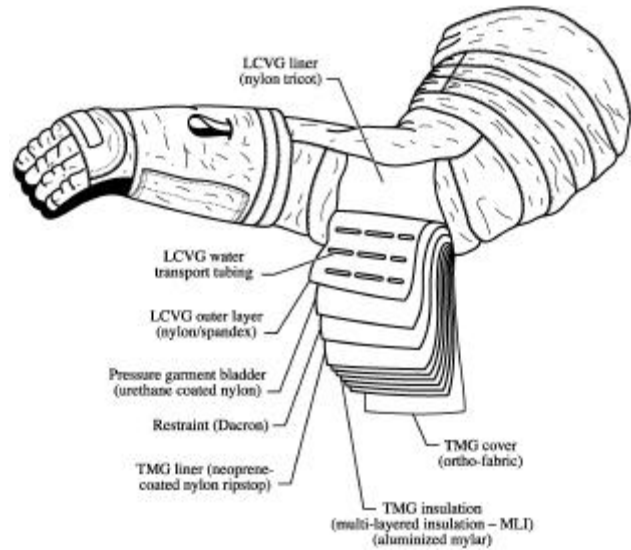


**Figure 9-2.** Cross section of material layup.

**Table 9-2.** Material Layups of the Hard Upper Torso

Layer	Material	Areal density, g/cm <sup>2</sup>
Outer layer	Orthofabric-Teflon/Nomex/Kevlar	0.049
Insulation	Aluminized Mylar- 5 plys	0.014
Inner liner	Neoprene coated Nylon ripstop	0.028
Hard shell	Fiberglas	0.354
LCVG	Spandex/water/ethylvinylacetate	0.154

**Table 9-3.** Material Layup of the Space Suit Fabric and Water-Filled Tube [2,7]

Material	Areal density, g/cm <sup>2</sup>
Orthofabric-Teflon/Nomex/Kevlar	0.049
Reinforced aluminized Mylar	0.014
Neoprene coated ripstop	0.028
Dacron® Polyester	0.021
Urethane Coated Nylon	0.014
Nylon/Spandex/water/ethylvinylacetate	0.154

An important component of the space suit shield model is the portable life support system (PLSS) shown in **Figure 9-3**. Not shown in the figure are the secondary oxygen tanks that attach to the lower section of the PLSS. Approximate estimates of material mass of various subsystems and overall dimensions are given in **Table 9-4**. As seen in the table, a major fraction of the mass of the extravehicular maneuvering unit (EMU) is associated with the backpack and is expected to be important in providing protection to internal organs.

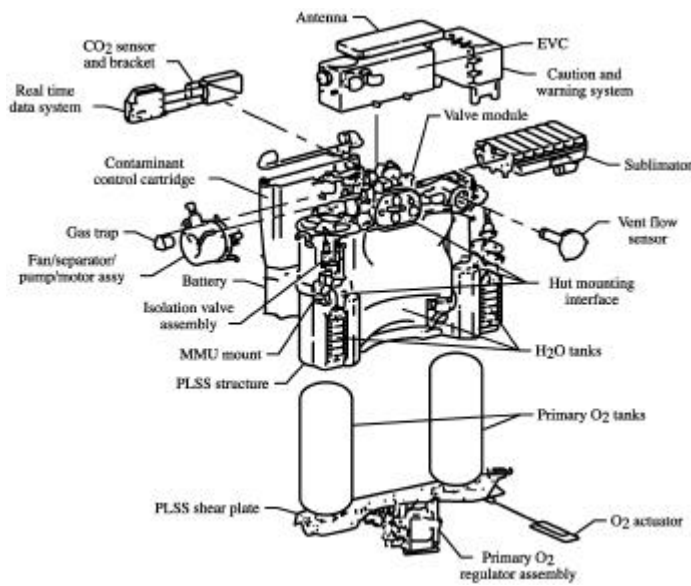


**Figure 9-3.** EMU portable life support system.

The geometric arrangement of materials in **Tables 9-1 to 9-4** will then provide a preliminary model of the space suit. Although the description is somewhat simplified, this is the most complete shielding model to date. This is an important step in understanding the expected exposures in ISS operations and will be useful in mission planning.

### 9.3 SPACE SUIT MODEL

The preliminary space suit model is implemented using the CAD geometry package of IDEAS<sup>2</sup> software. The geometry is simplified but represents the location of major massive components and the distribution of fabric and other components about an astronaut within the suit cavity. The CAD derived model is shown in **Figure 9-4**.

**Table 9-4.** Approximate Material and Dimensions of Portable Life Support System

Subsystem	Materials	Mass, kg	Dimensions, inch (h,w,d)
O <sub>2</sub> Ventilating Circuit:			
Regulators, vessels, fans...	Fe, Cr, Ni, Cu...	14.4	
LiOH assembly	LiOH, Fe	6.4	
H <sub>2</sub> O transport:			
Pump, valves, sensors	Fe, Cu	6.5	
Liquid	H <sub>2</sub> O	4.5	
Electrical system:			
Electronics	Si, O, Cu...	15.1	
Battery	ZnAgO	4.5	
O <sub>2</sub> purge system:			
Bottles	Fe, O	8.6	
Regulator	Fe	4.2	
<b>Total</b>		<b>65.2</b>	<b>25 × 23 × 7</b>

In the model, it is assumed that the Spandex/Nylon net of the LCVG are part of the suit fabric and that the ethylvinylacetate tubes filled with water are lying on the skin surface except for the head, hands, and feet. In testing, it is found that the fabric of **Table 9-3** (less the water-filled tube) presents a distribution [7] of material along a given path that is random according to

$$p(t) = \exp[-(t-t_o)^2/(2\mathbf{s}^2)]/(2\mathbf{ps}^2)^{1/2} \quad (1)$$

where the mean thickness  $t_o$  is 0.161 g/cm<sup>2</sup> and  $\mathbf{s}$  is 0.03 g/cm<sup>2</sup>. It is assumed that each ray through the fabric is scaled according the distribution (1). In the CAD model the fabric is of fixed thickness  $t_{min}$  but rays passing through the surface in direction  $W$  see thickness along the slant height  $t_m(W)$  and needs relation to the fabric distribution (1). The ray thickness is then taken as a random variable in which

$$t_{ray}(W) = t(\mathbf{k})t_m(W)/t_{min} \quad (2)$$

where  $\mathbf{k}$  is a uniform random number on the interval {0,1} and

$$t(\mathbf{k}) = t_o + 2^{1/2} \mathbf{s} \operatorname{erf}^{-1}(2\mathbf{k}-1) \quad (3)$$

where  $\operatorname{erf}^{-1}$  is the inverse error function and a different random number  $\mathbf{k}$  is taken for each ray direction. The scaling in equation (2) represents the nonuniformity in the fabric observed in transmission testing [7].

The water-filled tubes are likewise complicated in their representation within the CAD model. The tubes are located in parallel arrays separated by 1 cm [7]. Since the tubes are held on the skin of the astronaut (represented by the CAM or CAF models) and an arbitrary point in the astronaut's body at which the exposure is to be evaluated can be considered randomly, then the problem is to find the probability that the rays passing through the dose point in fact passed through a section of a water-filled tube. The tubes are mainly important to the skin points located near a tube. Points remote from any tube (e.g., deep in the body) are little affected. Since the tubes are parallel and 1 cm apart, then each point will only consider the two nearest tubes. This is accomplished as follows.

The nearest tube to the dose point will lie near the ray of minimum distance to the surface of the skin. This ray direction  $W_{min}$  is found by searching over the body thickness function  $t_b(W)$  for the smallest value. At that point on the surface with minimum thickness to the dose point, we place two tubes on opposite sides, one located at a distance  $x(\mathbf{k})$  given as

$$x(\mathbf{k}) = 0.5 \mathbf{k} (\text{cm}) \quad (4)$$

where the second tube is at a distance  $1 - x(\mathbf{k})$  and  $\mathbf{k}$  is a uniformly distributed random number on the interval {0,1} as before. However, whereas each direction  $W$  has a separate  $\mathbf{k}$  in equation (2), there is only one  $\mathbf{k}$  for each dose point in equation (4). For a given  $x(\mathbf{k})$  and direction  $W$ , we require the chord through either of the two tubes. To calculate this chord, we require solving the appropriate geometry. The first step is to define a coordinate system. Since  $W_{min}$  is assumed normal to the local surface, then any unit vector  $\mathbf{b}$  such that  $\mathbf{b} \cdot W_{min} = 0$  is tangent to the local



**Figure 9-4.** CAD model in faceted representation.

surface. We will use an arbitrary tangent vector to define the direction to the tube and a unit vector  $g$  parallel to the tube axis for the calculations. We take

$$\mathbf{b} \cdot \mathbf{W}_{min} = \mathbf{b}_1 \mathbf{a}_1 + \mathbf{b}_2 \mathbf{a}_2 + \mathbf{b}_3 \mathbf{a}_3 = 0 \quad (5)$$

which we solve by finding  $\mathbf{a}_{lm} = \min\{\mathbf{a}_l\}$  and set  $\mathbf{b}_{lm} = 0$ . The remaining  $\mathbf{b}_l$  can be solved with the requirement of normalization to unity. The vector parallel to the tube is given as

$$\mathbf{g} = \mathbf{b} \cdot \mathbf{W}_{min} \quad (6)$$

The point on the tube axis located at  $x(\mathbf{k})$  along the surface nearest the dose point as defined above is

$$\mathbf{x}_{tube} = t(\mathbf{W}_{min}) \mathbf{W}_{min} + x(\mathbf{k}) \mathbf{b} \quad (7)$$

An arbitrary point on the tube axis is given as

$$\mathbf{x}(s) = \mathbf{x}_{tube} + s \mathbf{g} \quad (8)$$

where  $s$  is the distance along the tube measured from the point on the tube nearest the dose point. We need the nearest point to the tube axis along an arbitrary direction  $W$  to evaluate the chord for that ray. This is accomplished by finding the minimum of the distance  $D$  as

$$D^2 = \text{Min}_{s,v} \{ [\mathbf{x}(s) - v \mathbf{W}]^2 \} \quad (9)$$

The solution can be written as

$$D^2 = [t(\mathbf{W}_{min}) - v \mathbf{w}_1]^2 + [x(\mathbf{k}) - v \mathbf{w}_2]^2 \quad (10)$$

where

$$v = [t(\mathbf{W}_{min}) \mathbf{w}_1 + x(\mathbf{k}) \mathbf{w}_2] / [\mathbf{w}_1^2 + \mathbf{w}_2^2] \quad (11)$$

The chord is, for  $D$  less than the tube radius  $r_o$ , given as

$$C = 2 [r_o^2 - D^2]^{1/2} \quad (12)$$

and has value zero for values of  $D$  greater than  $r_o$ . The material the ray must penetrate to reach the astronaut within the suit is the chord so that the total shielding is

$$t_{ray}(\mathbf{W}) = t(\mathbf{k}) t_m(\mathbf{W}) / t_{min} + C \quad (13)$$

Note, even if an intersection of the tube at  $x(\mathbf{k})$  is not found the calculation is to be repeated by replacing  $x(\mathbf{k})$  with  $x(\mathbf{k}) - 1$  for the second tube of the nearest pair. The chord of the next nearest pair is evaluated by replacing the  $x(\mathbf{k})$  by  $x(\mathbf{k}) + 1$  and then by  $x(\mathbf{k}) - 2$ . The appropriate value(s) of  $C$  is (are) used (summed) in equation (13).

The CAD model of the space suit is used to generate shielding distributions about the dose points chosen in the CAM and CAF models and will be modified according to the above analysis to represent the materials about the dose points.

## 9.4 HUMAN GEOMETRY MODEL

The CAM model was first developed by Kase [10] in 1970. Numerous errors were discovered in the combinatorial geometry, and Billings and Yucker [11] corrected the geometrical representation in 1973 using a QUAD geometry modeling technique [12] where geometrical regions and surfaces are used to represent the 50<sup>th</sup> percentile U.S. Air Force male. The model is very detailed, comprising some 1100 unique geometric surfaces and approximately 2400 solid regions. The internal body geometry, such as critical body organs, voids, bone, and bone marrow, are explicitly modeled with the proper chemical composition and density. A supporting program called CAMERA was developed to perform analyses on the model, which include ray tracing to generate shielding distributions for any point in and on the CAM model. CAMERA also has the capability to generate cross-sectional views of the coordinate (dose) point of interest.

With the increase of females being assigned to fly on Shuttle missions, Yucker and Huston [13] developed the CAF model. Using the existing CAM model, they “removed” the male organs and “replaced” them with the appropriate female organs (breast, uterus, and ovaries). Since the average female is approximately 92% the size of the average male, the CAF was scaled accordingly.

Since astronauts come in all sizes, Yucker [15] developed a three-dimensional scaling capability, and Atwell [16,17] later refined and made several corrections to the CAF model. The CAM and CAF models have been used extensively to compute astronaut body organ exposures for the Space Shuttle and ISS programs.

## 9.5 ENVIRONMENTAL MODELS

The environments of concern are the LEO environment of ISS and the deep space (beyond the geomagnetic field) environment. They differ on account of the geomagnetic field. Although the GCRs are part of the over all exposure, only the trapped radiations during quiet geomagnetic periods will be considered in LEO and the SPEs in deep space.

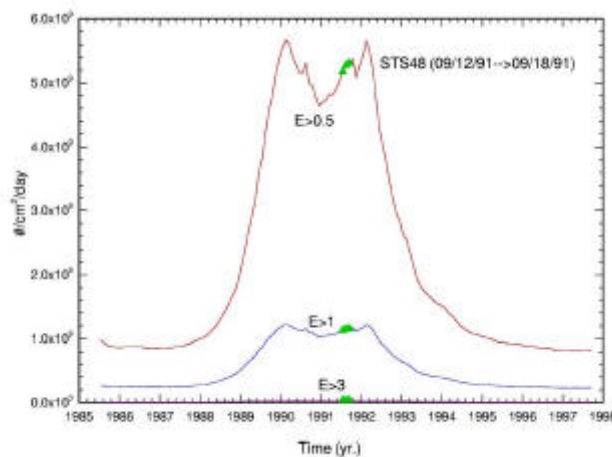


Figure 9-5. STS-48 electron environment.

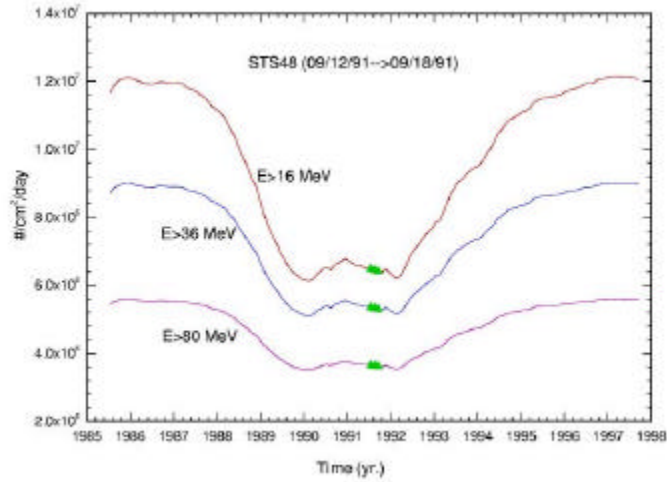


Figure 9-6. STS-48 proton environment.

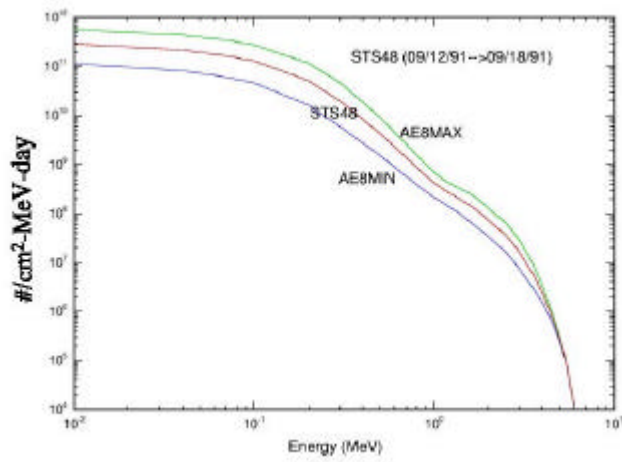


Figure 9-7. STS-48 electron environment compared to AE8 model.

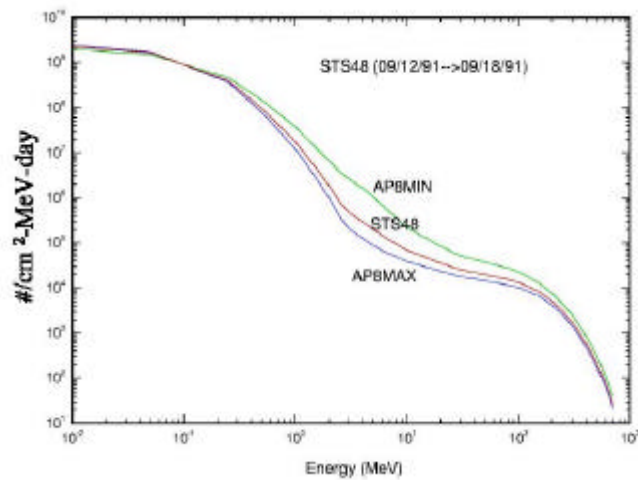
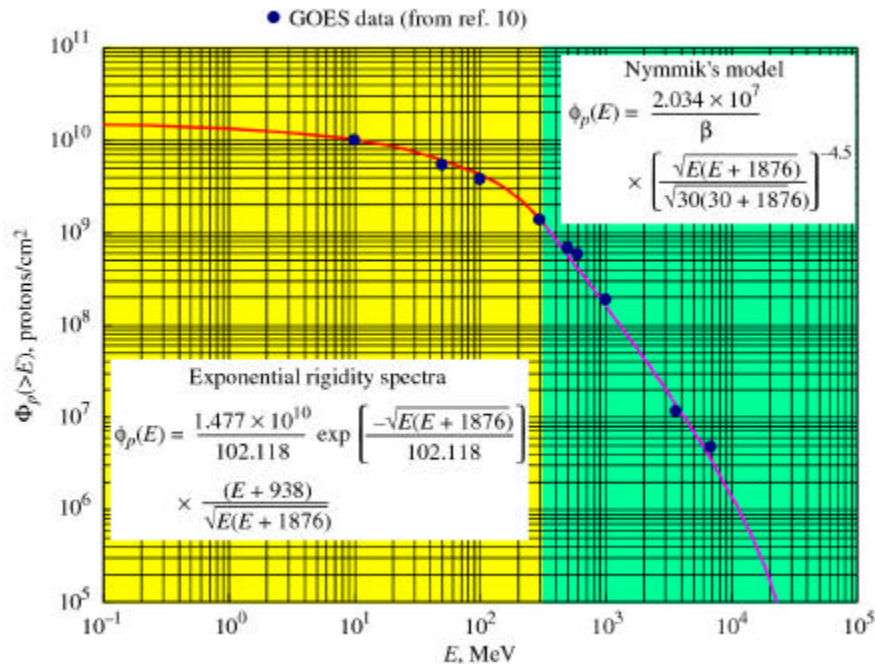


Figure 9-8. STS-48 proton environment compared to AP8 model.

Even during geomagnetic quiet times, the particle fields are variable over the solar cycle. The time-dependent fields are shown relative to the Sept. 1991 flight environment of STS-48 at 313 nmi and 57° in **Figures 9-5 and 9-6** as evaluated by a recently derived model [17]. The model utilizes the environmental maps of AE8 and AP8 with superimposed solar cycle variations related to particle source and loss terms. The STS-48 spectra during Sept. 1991 are compared to the base models at solar maximum and minimum in **Figures 9-7 and 9-8**. The GCR background will be ignored in the present calculation. The solar energetic particles are deflected in the geomagnetic field and will be ignored in the present study, although they can be an important contribution especially during geomagnetic storms [1]. Even more common and troubling are large geomagnetic disturbances and the associated increase in the trapped electron environment by three or four orders of magnitude lasting for several days.

SPEs in deep space operations are of great concern, since a lethal exposure can be received over a several-hour period [18] and the resultant biological response will be serious. This is especially true in a space suit, where only minimal protection is available [18]. The largest observed high-energy event is that of Feb. 23, 1956, with the second-largest such event being an order-of-magnitude smaller, occurring on Sept. 29, 1989. The Feb. 23, 1956, event was only observed on the ground, and the spectrum at low energies is most uncertain. It has been suggested that the Sept. 29, 1989, event where detailed measurements exists should be scaled by perhaps a factor of 10 and used as the event appropriate for design. Studies have shown that such an event would provide a considerable health risk to the astronaut although an overly simplified space suit model was used [19]. The fluence spectra of the Sept. 29, 1989, event [19] are shown in **Figures 9-9 and 9-10**.



**Figure 9-9.** Sept. 29, 1989, solar proton spectrum.

The low-level GCR exposures appear as background and will be ignored in the present study. The present emphasis is on the short-term exposures, although the background from the trapped particles in LEO during

geomagnetic quiet times is evaluated to estimate the dose during large electron population variations under disturbed geomagnetic conditions.

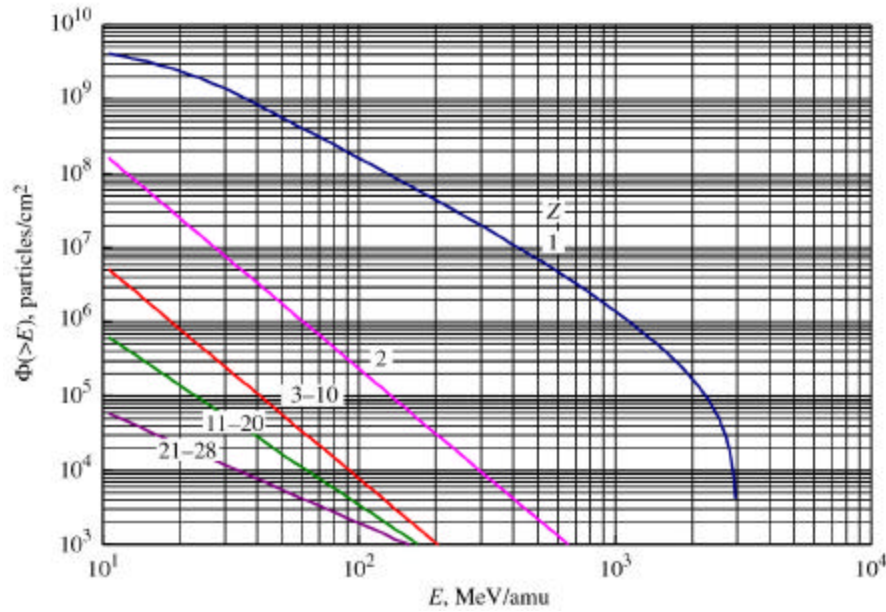


Figure 9-10. Sept. 29, 1989, solar heavy ion spectra.

## 9.6 COMPUTATIONAL PROCEDURES

The types and energy distributions of particles transmitted through a shield material require the solution to the Boltzmann transport equation with appropriate boundary conditions related to the external space radiation environment. The relevant transport equation [20] for the flux density  $f_j(x, W, E)$  of type  $j$  particles moving in direction  $W$  with energy  $E$  is given as

$$W \cdot \tilde{N} f_j(x, W, E) = \int \hat{\sigma}_{jk}(W, W', E, E') f_k(x, W', E') dW' dE' - s_j(E) f_j(x, W, E) \quad (14)$$

where  $s_j(E)$  is the media macroscopic cross section for removal of  $j$  particles of energy  $E$ ,  $\hat{\sigma}_{jk}(W, W', E, E')$  are the media macroscopic cross sections for various atomic and nuclear processes adding  $j$  particles of energy  $E$  in direction  $W$  including spontaneous disintegration. In general, there are hundreds of particle fields  $f_j(x, W, E)$  with several thousand cross-coupling terms  $\hat{\sigma}_{jk}(W, W', E, E')$  through the integral in equation (14). The total cross section  $s_j(E)$  with the medium for each particle type of energy  $E$  may be expanded as

$$s_j(E) = s_{j,at}(E) + s_{j,el}(E) + s_{j,r}(E) \quad (15)$$

where the first term refers to collision with atomic electrons, the second term is for elastic nuclear scattering, and the third term describes nuclear reactive processes and is ordered as  $1:10^{-5}:10^{-8}$ . This ordering allows flexibility in expanding solutions to the Boltzmann equation as a sequence of physical perturbative approximations. The atomic interactions are treated using energy moments in which the leading term is the usual continuous slowing down approximation. Special problems arise in the perturbation approach for neutrons for which the nuclear elastic process appears as the first-order perturbation and has been the recent focus of research [21].

The electrons have negligible nuclear reaction cross sections and are dominated by atomic and elastic processes. The basic electron transport is treated by invoking the “continuous-slowing-down-approximation” range, where the usual “continuous-slowing-down-approximation” range has been modified parametrically to account for shortened path length due to multiple scattering. The practical ranges and corresponding range-energy relations are derived from the parameterizations of Tabata et al. [22]. For an electron of initial energy,  $E$ , its residual energy,  $W$ , after going distance,  $t$ , in an attenuating medium may be found by solving the equation

$$R(W) = R(E) - t \quad (16)$$

for  $W$  when the practical range  $R(W) > 0$ . Effects of energy fluctuations are incorporated using the energy dissipation formulation of Kobetich and Katz [23,24], in which actual energy dissipation,  $G$ , is expressed in terms of a transmission function,  $\mathbf{h}$ , as

$$G = d(\mathbf{h}W)/dt \quad (17)$$

The parameterizations for  $R$  and  $\mathbf{h}$  have been based on numerous electron beam experiments for energy ranges and material elements applicable to space radiation calculations.

The dose at distance  $t$  for electron differential flux  $\mathbf{f}_e$  may then be expressed in terms of the initial and final energy spectra [25]

$$D(t) = \int \mathbf{d}G(E,t) \mathbf{f}_e(E) dE = \int \mathbf{d}S(W) \mathbf{f}_e(W) dW \quad (18)$$

where  $S$  is stopping power. In conformance with the “continuous-slowing-down-approximation” range, the emerging electron spectrum may then be expressed in terms of the initial spectrum as [25]

$$\mathbf{f}_e(W) = \mathbf{f}_e(E) G(E) S(E) / [S(W)]^2 \quad (19)$$

In passing through condensed matter, the decelerating electrons give rise to energetic photons (bremsstrahlung), which also contribute to the total energy deposition. The photon production may be expressed in terms of a differential cross section,  $\mathbf{s}(W, E')$ , which represents a probability that an electron of energy  $W$  produces a photon of energy  $E'$  in its interaction with an atom of the material. These cross sections are generally complicated functions of  $W$ ,  $E'$ , and material composition. They have been extensively tabulated by Seltzer and Berger [26] for wide energy ranges and most elements of the periodic chart. The effective production cross sections for a given material are determined in the present calculations by appropriate spline interpolations of the Berger-Seltzer tabulations.

The photon source term,  $\mathbf{V}$ , at distance  $x$  and energy  $E'$  may be calculated from the electron spectrum as

$$\mathbf{V}(x, E') = \int \mathbf{d}\mathbf{f}_e^{W(x)} \mathbf{f}_e \mathbf{s}(W, E') dW \quad (20)$$

The photons are also being attenuated in accordance with an extinction coefficient,  $\mathbf{m}$  and the photon differential spectrum,  $\mathbf{f}_p(E')$ , at distance  $t$  may be found using the transfer equation

$$\mathbf{f}_p(E') = \int \mathbf{d}\mathbf{V}(x, E') e^{-\mathbf{m}(t-x)} dx \quad (21)$$

and the subsequent energy deposition as

$$D_p(t) = \int \mathbf{d}\mathbf{m} E' \mathbf{f}_p(E') dE' \quad (22)$$

where  $m_i$  is an absorption coefficient for photon energy loss resulting in ionizing energy deposition (generally less than the total extinction coefficient,  $m$ ). The present code formulation assumes all photons generated propagate in the direction of electron motion.

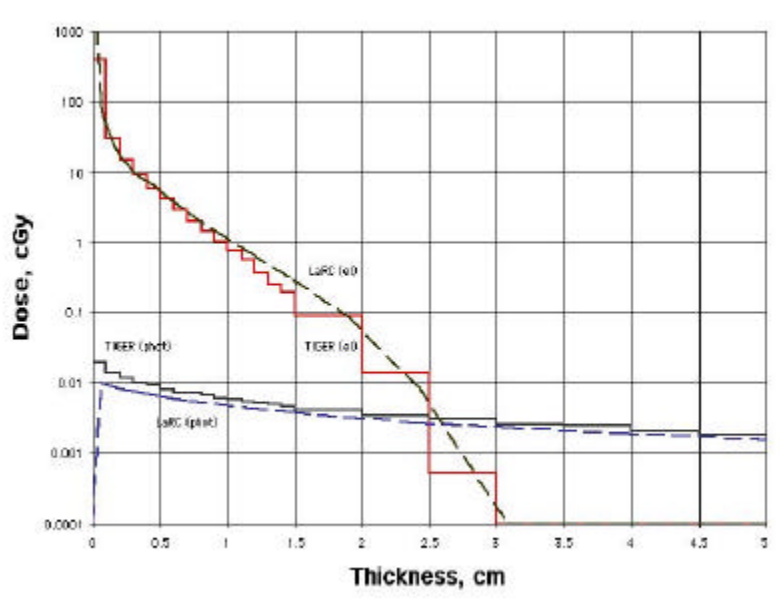


Figure 9-11. STS-63 electron generated dose in a water shield of the present model and TIGERP.

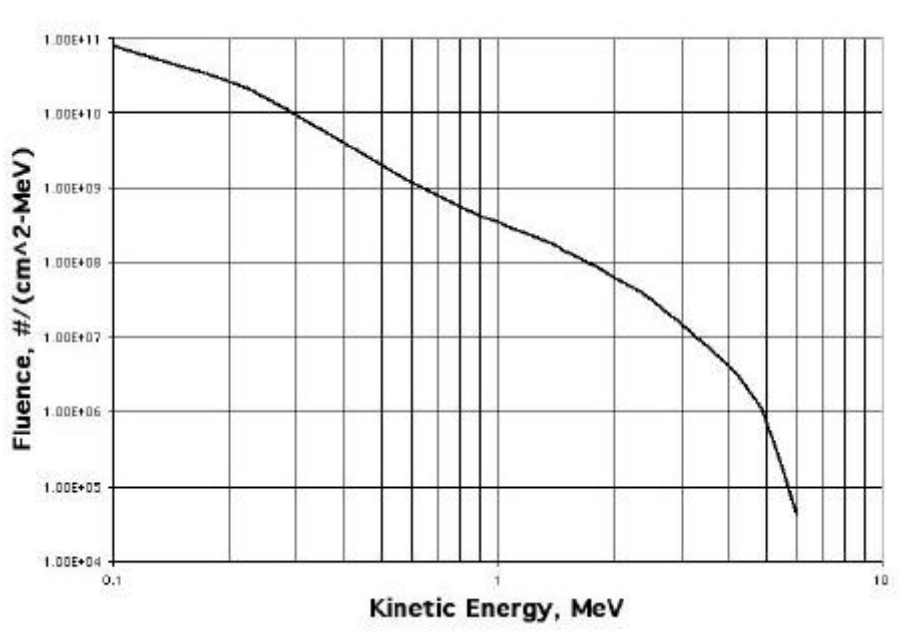


Figure 9-12. Ten-day electron fluence for STS-63.

This simple procedure is of recent vintage, and validation and benchmarking continue at the present time. Calculations for benchmark comparisons made thus far indicate that accuracy has not been substantially degraded at the expense of computational speed. An example of a comparison calculation is given in **Figure 9-11** for the electron fluence spectrum shown in **Figure 9-12** appropriate to the STS-63 10-day mission at 213 nmi (392 km) at

51.6° inclination and is propagated at normal incidence through a semi-infinite water slab. The Monte Carlo code TIGERP [27] was used to validate the computation and the very favorable comparison is evident.

## 9.7 RESULTS

The dose at a location within the astronaut's body depends on the surrounding space suit materials and body tissues. The space suit material's distributions are evaluated along 1922 ray directions associated with a fixed solid angle ( $\Delta\Omega = 4\pi/1922$ ) as discussed elsewhere [29]. Various three-dimensional visualization techniques are useful in understanding these distributions. For example, the projected rays through the space suit materials about a location in the sternum are shown in **Figure 9-13**. The potential role of the EMU lights and camera, the backpack, and the display control module are clearly evident.

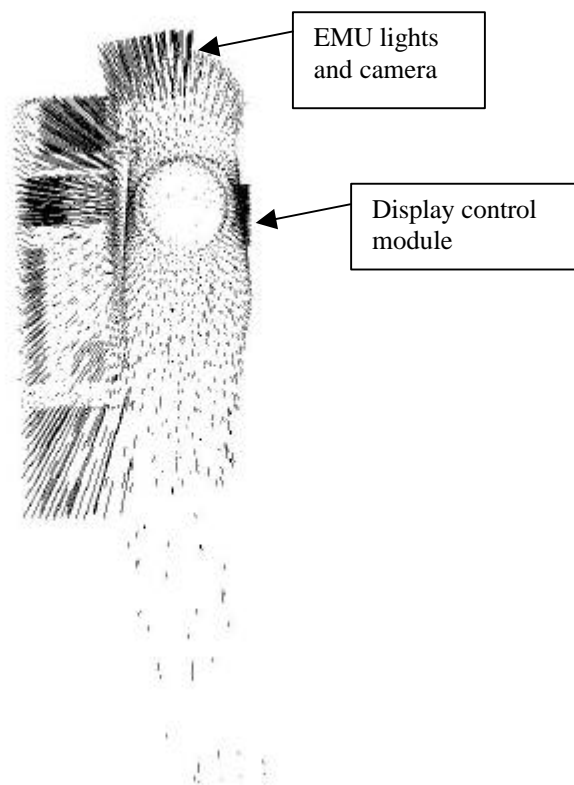


**Figure 9-13.** Projected space suit material crossings along 1922 ray directions.

Another visualization device is shown in **Figure 9-14** where the gray scale (normally color is used) displays the relative shielding about the dose point. For online analysis, the spherical shape in **Figure 9-14** is rotated to fully examine the total solid angle. The power of such analysis techniques is further discussed by Qualls and Boykins [28] and provides a basic tool for design analysis and optimization.

The environments of concern are the LEO environment of ISS and the deep space environment. They differ on account of the geomagnetic field. Although the GCR are part of the overall exposure, only the trapped radiations during quiet geomagnetic periods will be considered herein.

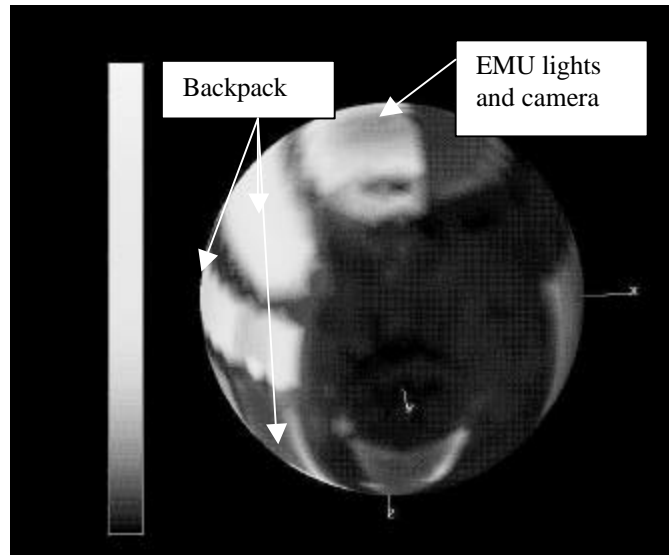


**Figure 9-14.** Visualization of the space suit shield materials distribution about a point in the sternum.

LEO OPERATIONS – The trapped environment near solar maximum is shown in **Figures 9-5** through **9-8** for this high inclination and relatively high altitude orbit. The attenuation of that environment is shown in **Figures 9-15** and **9-16** for low penetration depths. One can see from the figures that the doses can be quite high for low penetration depths and reduce quickly with increasing depth. The basal layer of the skin lies about 1 mm below the surface and the additional  $0.28 \text{ g/cm}^2$  of fabric used in prior calculations would result in about 6 cGy per day from electrons neglecting self-shielding. The present estimate of the mean fabric penetration is  $0.161 \text{ g/cm}^2$  with resultant exposures on the order of 14 cGy/day, or more than a factor of two higher than results for the prior model. The relative difference between the two fabric models will remain, although self-shielding will lower the total dose considerably. Although the protons likewise attenuate quickly at low penetration depths, the resultant exposure is not as large as that for electrons.

The dose incurred during a six-hour exposure for geomagnetic quiet times near solar maximum is not to be expected to a serious limiting factor. However, geomagnetic storms are observed during solar active years to increase the electron environment, over a period of approximately an hour or less, by three or four orders of magnitude greater than the quiet time levels shown in **Figures 9-5** and **9-15**. Even a modest amount of time in such an environment can lead to serious exposures, especially to the skin. The thresholds for the early radiation responses (deterministic effects as opposed to the stochastic effects such as cancer induction) are very narrow and a factor of two in exposure is extremely important to radiation health outcome [18,29].

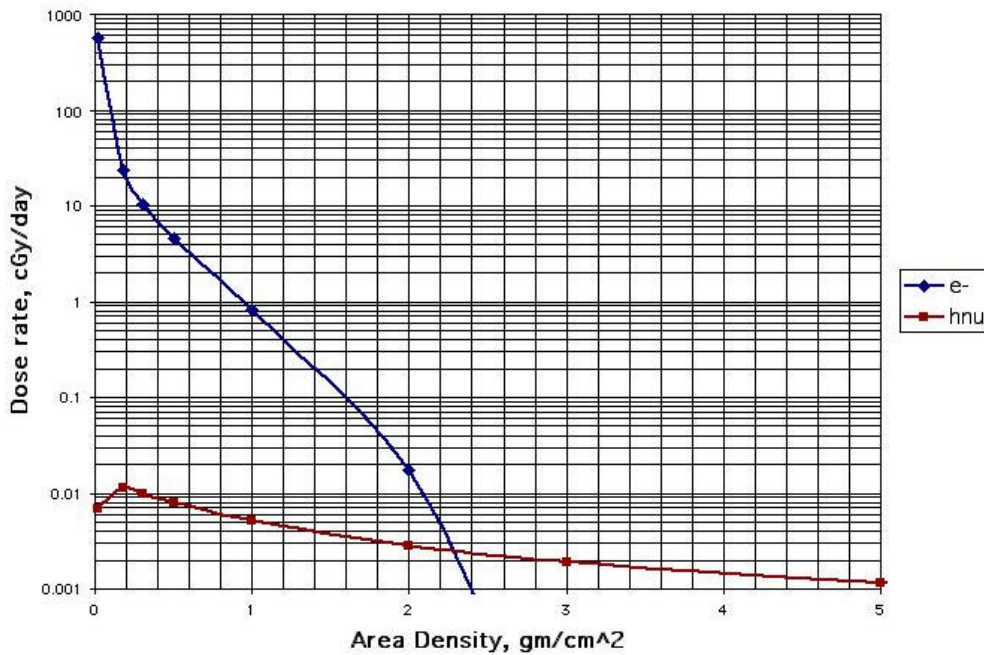


**Figure 9-15.** STS-48 electron and photon (h?) dose as a function of fabric thickness.

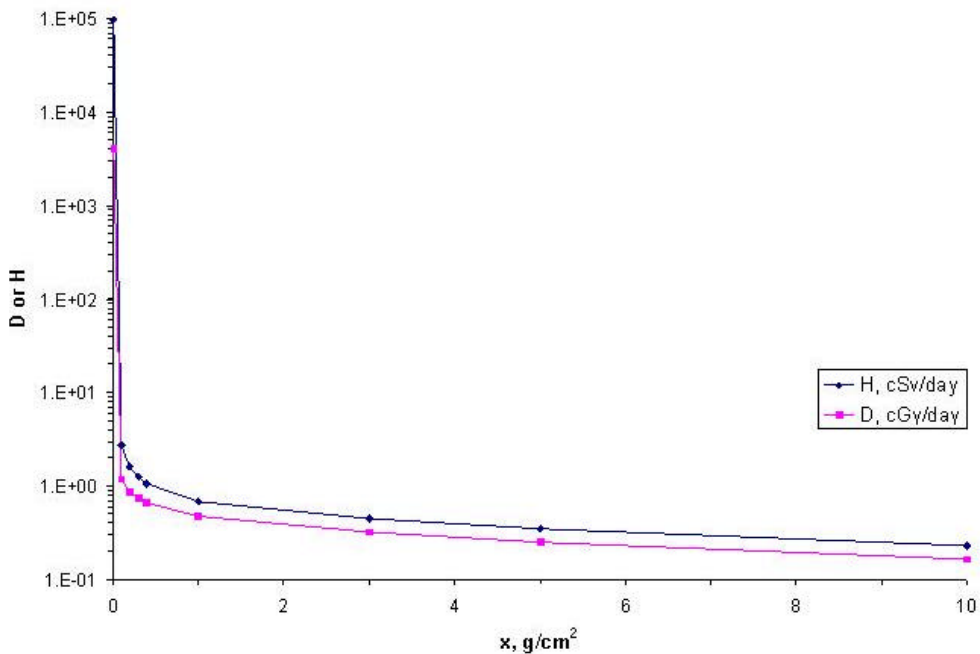


**Figure 9-16.** STS-48 proton daily dose and dose equivalent as a function of fabric thickness.

DEEP SPACE OPERATIONS – There are two issues in deep space exposures: the rates of cancer induction from GCRs and concern for a SPE. SPEs are of potentially grave concern in space exploration where astronauts will spend periods in poorly protected regions as the space suit. The August 4, 1972, SPE is the worst-case event for which some details of the low-energy proton spectrum was measured and used to analyze their importance to

astronaut health [18]. The single largest ground-level event observed is the February 23, 1956, event but little is known of the low-energy spectrum. The second largest ground-level event observed is that of September 29, 1989, and good details on the spectral properties [19] are available as shown in **Figures 9-9** and **9-10**. The importance of the September 29, 1989, event, which we evaluate herein, is that ten times the September 29, 1989, event is a proxy for the February 23, 1956, event.

The dose and dose equivalent in tissue from various components within a spherical shell of space suit fabric material is shown in **Figures 9-17** and **9-18**, with the totals in **Figure 9-19**. The dose is dominated by the proton fluence over most shielding thicknesses. The dose equivalent from helium ions gives an important contribution for thicknesses on the order of the space suit fabric. The heavier ions are always unimportant to the exposure.

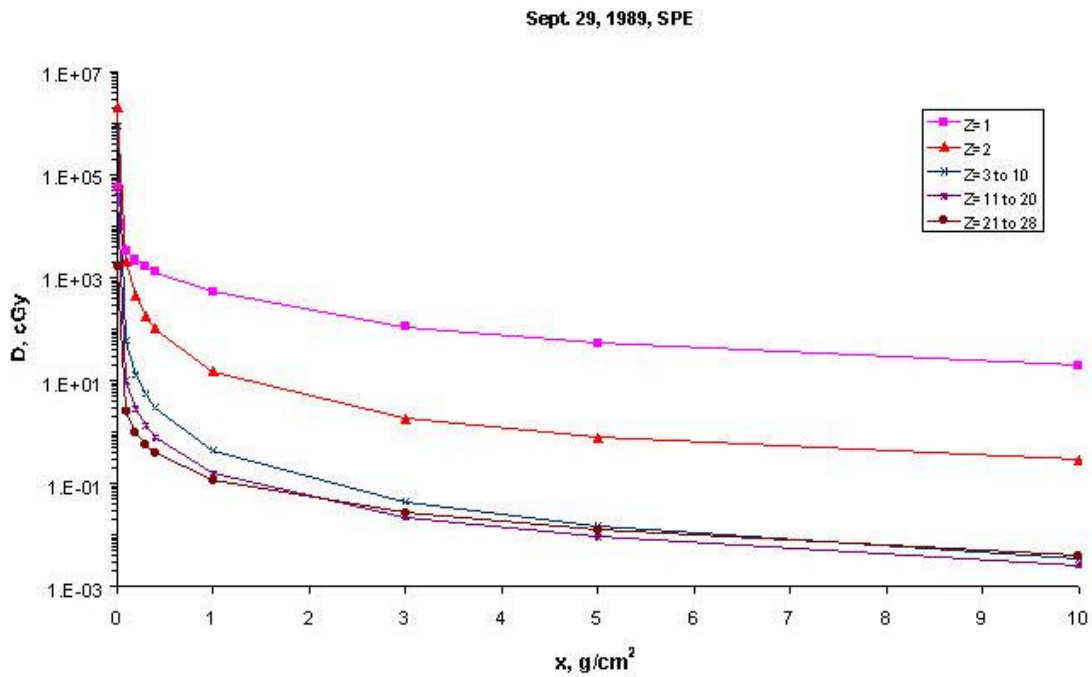


**Figure 9-17.** Dose within a fabric shield during the September 29, 1989, SPE.

It is clear from the results in **Figure 9-19** that very high skin exposures can be expected for this event. However, even modest amounts of additional shielding in the thermal micrometeoroid garment are expected to have important effects in reducing the exposures. Still, some caution in redesign is warranted since mobility and comfort to the astronaut is a key issue in space operations.

There is a slow but significant decline in dose and dose equivalent with larger shield thickness, indicating some advantage is to be gained by the more massive components of the suit and the self-shielding of critical tissues of the astronaut’s body. These will be evaluated in terms of the CAM/CAF geometry and the present space suit model.

Sept. 29, 1989, SPE

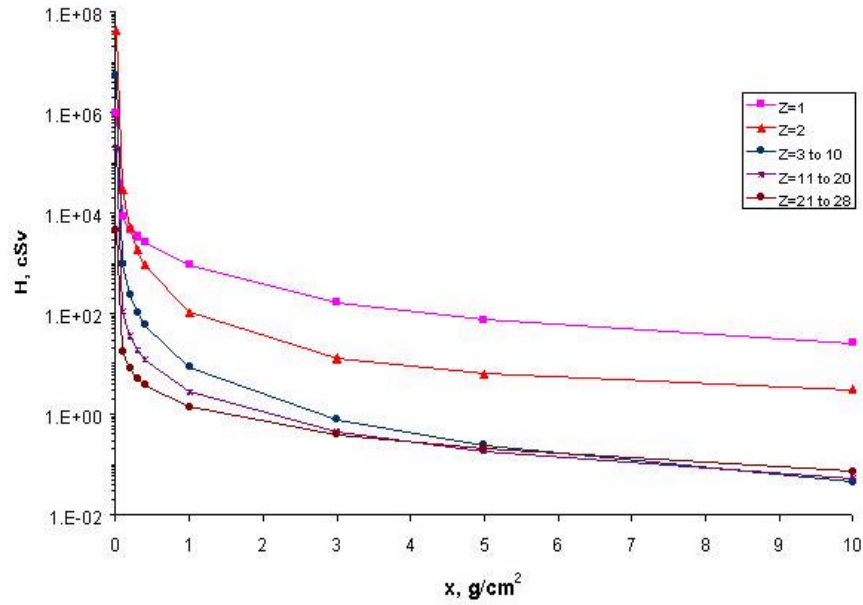


Figure 9-18. Dose equivalent within a fabric shield during the September 29, 1989, SPE.

Sept. 29, 1989, SPE

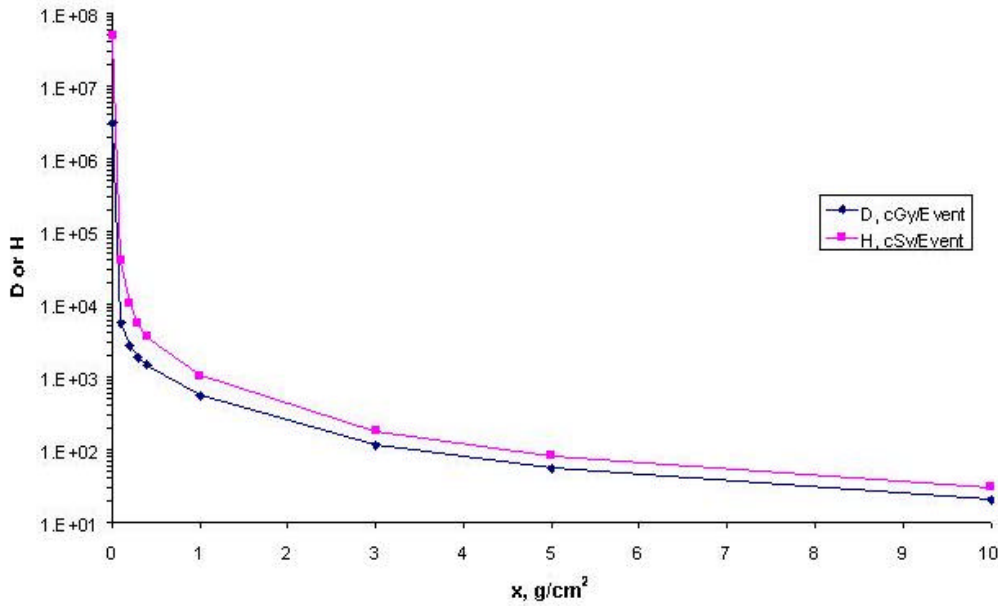


Figure 9-19. Total dose and dose equivalent within a fabric shield during the September 29, 1989, SPE.

## 9.8 CONCLUSION

It is clear from the present analysis and results that the space suit has some important features that will have some benefit for reducing the astronaut health risks under the extreme exposure conditions in space. Even so, some

weaknesses in the space suit design are already clear. Mainly, attention has presently been given to the space suit fabric (thermal micrometeoroid garment/LCVC) that is less effective in protecting the skin from exposure than previously assumed and could be greatly improved. It is clear that only modest additions to the fabric elements will have a large payoff in protection. What still needs addressed is the remaining more massive elements within the space suit and their effects on specific organ tissue exposures. This will be more fully addressed in the near future.

## 9.9 REFERENCES

1. Nealy, J.E. et al. *Adv. Space Res.* 17(2): 117-120, 1996.
2. Kozloski L.D., *US Space Gear: Outfitting the Astronaut*, Smithsonian Institution Press, Washington DC, 1994.
3. Severin G.I., *Acta Astronautica* 32(1): 15-23, 1994.
4. Abramov I.P., *Acta Astronautica* 36(1): 1-12, 1995.
5. Kosmo J.J., Nachtwey D.S., Hardy A. *JSC/CTSD-SS-241*, 1-24-1989.
6. Ross A.J. et al. *NASA CP 3360*, 1997.
7. Wilson, J.W. *SAE 01ICES-299*, 2001.
8. Wilson, J.W. *Health Phys.* 28:812-813, 1975.
9. Wilson, J.W. et al. *NASA TP-3668*, 1997.
10. Kase, Paul G., "Computerized Anatomical Model Man," Report AFWL-TR-69-161, Air Force Weapons Laboratory, Kirtland Air Force Base, NM, January 1970.
11. Billings, M.P., and W.R. Yucker, "Summary Final Report. The Computerized Anatomical Man (CAM) Model," Report MDC G4655, McDonnell Douglas Astronautics Company, Huntington Beach, CA, September 1973.
12. Jordan, T.M., "QUAD, A Computer Subroutine for Ray Tracing in Quadric Surface Geometries," Douglas Report SM-46333, 1964.
13. Yucker, W.R., and S.L. Huston, "Computerized Anatomical Female. Final Report," Report MDC H 6107, McDonnell Douglas Corporation, Huntington Beach, CA, September 1990.
14. Yucker, W.R., "Computerized Anatomical Female Body Self-Shielding Distributions," Report MDC 92H0749, McDonnell Douglas Corporation, Huntington Beach, CA, March 1992.
15. Atwell, W., "Anatomical Models for Space Radiation Applications: An Overview;" Invited paper (F2.4-M.1.06) presented at the Committee on Space Research (COSPAR), Washington, DC, August 28 - September 5, 1992.
16. Atwell, W., A. C. Hardy, and L. Peterson, "Organ Radiation Doses and Lifetime Risk of Excess Cancer for Several Space Shuttle Missions," Invited paper # F2.4-001, Committee on Space Research (COSPAR), Hamburg, Germany, July 11-21, 1994.
17. Wilson, J.W. et al. *NASA/TP-1999-209369*, 1999.

18. Wilson, J.W. et al. Radiat. Measurement 30: 361-382; 1999.
19. Kim, H.-Y. M. et al. NASA TP/1999-209320, 1999.
20. Wilson, J. W. et al., *Transport Methods and Interactions for Space Radiations*. NASA Reference Publication, RP-1257, 1991.
21. Cloudsley, M. S. et al., Cana. J. Phys. 78: 45-56, 2000.
22. Tabata, T., et al., Nucl. Inst. & Meth. 103: 85-91, 1972.
23. Kobetich, E. J. and Katz, R., Nucl. Inst. & Meth. 71: 226-230, 1969.
24. Kobetich, E. J. and Katz, R., Phys. Rev. 170(2): 391-396, 1968.
25. Cucinotta, F.A.; Katz, R.; and Wilson, J.W.: Radial Distributions of Electron Spectra From High-Energy Ions. Radiat. Environ. Biophysics 37, 259-265, 1998
26. Seltzer, S. M. and Berger, M. J., Nucl. Inst. & Meth. B12: 95, 1985.
27. Halbleib, J. A. and Morel, J. E., Nucl. Sci. Eng., 70: 219, 1979.
28. Qualls, G.D. and Boykins, R., Space Radiation Shielding Analysis by CAD Techniques. NASA CP 3360, pp. 365-382; 1997.
29. NCRP, Guidance on Radiation Received in Space Activity, NCRP Report No. 98, 1989.

## **CONTACT**

b.m.anderson@larc.nasa.gov

# **CHAPTER 10**

## **RADIATION EXPOSURE ANALYSIS**

### **FOR ISS: THE FEMALE ASTRONAUT**

#### **IN EVA**

(previously published)

Brooke M. Anderson, John W. Wilson  
NASA Langley Research Center

William Atwell  
The Boeing Company

Craig P. Hugger  
Swales Aerospace

John E. Nealy  
Old Dominion University

Copyright © 2001 Society of Automotive Engineers, Inc.

# RADIATION EXPOSURE ANALYSIS FOR ISS: THE FEMALE ASTRONAUT IN EVA

## ABSTRACT

Special exposure limit recommendations have been designated by the NCRP for U.S. astronauts in LEO operations. These have been established from consideration of a 3% lifetime excess risk of cancer mortality for a 10-yr. active career. The most recent recommendations of the NCRP have incorporated modified procedures for evaluating exposures with accompanying adjustments in career limits. Of special importance are the limit specifications for female exposures, which are approximately 40% less than those for males. Furthermore, radiosensitive organs unique to females require additional attention.

## INTRODUCTION

For EVA at altitudes maintained by ISS, observations have shown that a large exposure rate results from passage through the region of the SAA and near the magnetic poles [1]. All of these radiations show a high degree of directionality allowing a shadow cast by the large ISS structure. Thus the process of estimating potential dosimetric exposures for such scenarios involves special complexities. Recent efforts in this area at NASA-Langley have included development of generalized deterministic electron/proton transport codes [2], [3], sophisticated CAD models of the U.S. space suit [4] and the current ISS configuration (8A), and an algorithm to describe the directional flux in the SAA [5]. The present subject work utilizes these procedures in conjunction with the NASA Computerized Anatomical Female (CAF) model [6] to examine potential exposures to female astronauts in the event of performing EVA in the SAA region. It is conceivable that unfavorable orientation during EVA could significantly impact accrued exposure and result in an abbreviated active career. It is found that there is a “shaded” side of the ISS, dependent on direction of traverse through the region that may provide sheltering to the extent that potential exposures may be reduced to practically insignificant levels.

## SCENARIO AND MODEL-DERIVED ENVIRONMENT

### Orbital Tracks and Fluxes

The exposure scenario has been chosen to represent an EVA extending through three orbital periods (approximately 4.5 hours) for the nominal ISS parameters of 400 km altitude and 51.6 ° inclination. The consecutive orbits have been selected so that each of the orbital paths includes transit through a portion of the SAA while going from south to north. Under quiescent conditions (i.e., no solar flares or magnetic storms) this scenario should represent a case approaching maximum exposure to be expected during an EVA operation. The orbit generator provided by the SPENVIS [7] interactive website was used to obtain the orbital ground track data as well as the omni-directional energetic particle fluxes along the paths traversed. Portions of the orbital paths of interest in the southern hemisphere are shown in **Figure 10-1** along with the contours of geomagnetic field intensity, where the field minimum near the coastal regions of Brazil and Argentina is outlined.

In order to simulate the directionality of the charged particle flux, the local 3-D components of the magnetic field must be known; these have been obtained for the present study from the NASA NSSDC website [8] where the IGRF Geomagnetic Field Model has been invoked for projected July 2003 conditions.

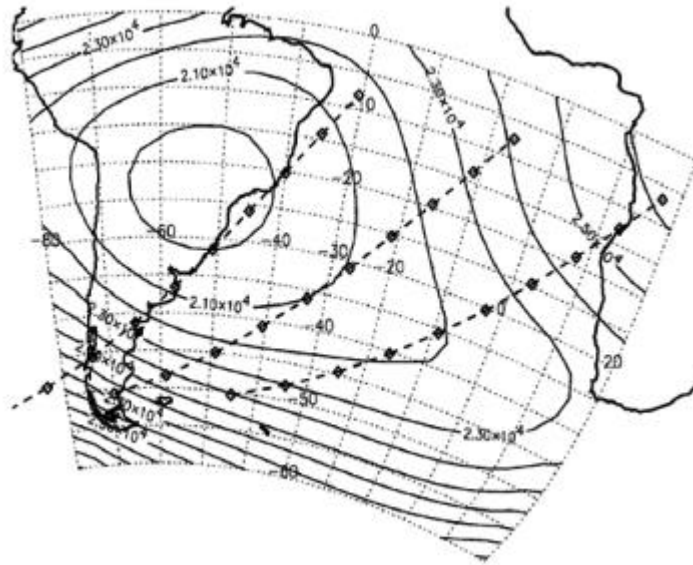


**Figure 10-1.** Orbital paths traversing area of SAA near South America with superimposed geomagnetic field contours indicative of high radiation exposure area. (Field strength units are nT.)

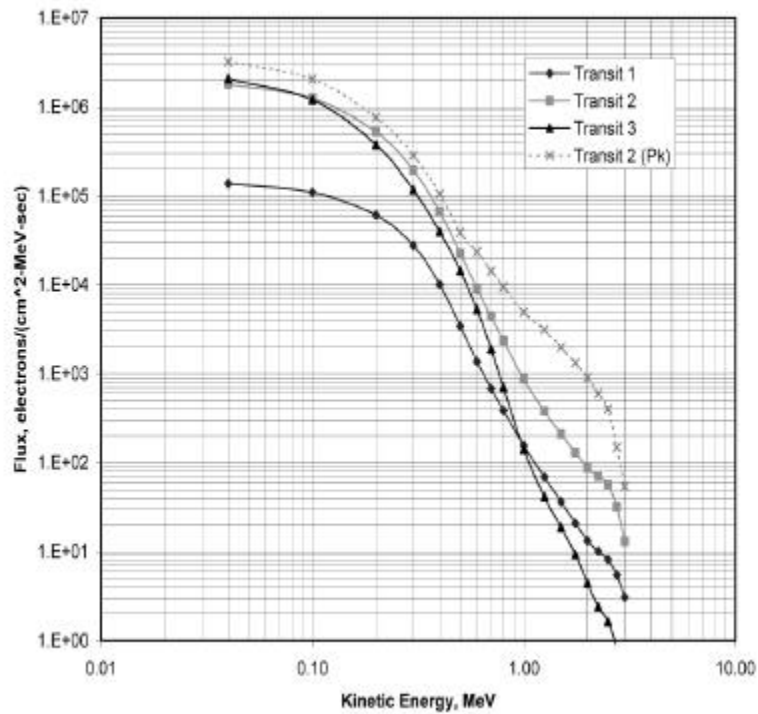


**Figure 10-2.** Orbit-averaged differential electron fluxes for present scenario along with spectrum for peak flux near center of SAA.

The assumption has been made that the total dose for an orbit is incurred during the relatively brief transit through the SAA. The single orbit-averaged fluxes for electrons and protons for each transit was also obtained from the SPENVIS calculation, and are plotted in **Figures 10-2** and **10-3**. The protons, while much less numerous than the electrons, attain much greater kinetic energies and are correspondingly much more penetrating.

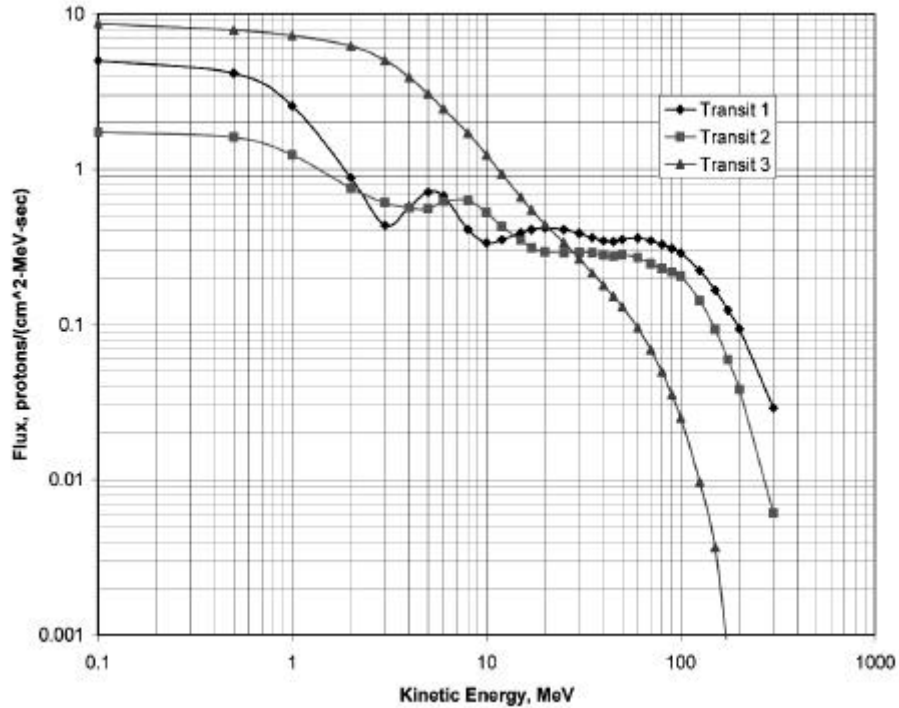


**Figure 10-3.** Orbit-averaged proton fluxes for present scenario.

## Flux Directionality

The particle spectra of **Figures 10-2** and **10-3** refer to omni-directional fluxes. In order to characterize the directional (vectorial) nature of the flux it is necessary to examine the charged particle interaction with the local geomagnetic field components. Heckman and Nakano [9] give a clear description of the theoretical basis along with critical assumptions and approximations of directional flux properties in the SAA region. Computational models have been developed for analyzing the effects of directionality [10], [11]. The theoretical formulation ultimately results in a distribution function for the ratio of directional flux to the omni-directional flux,  $J/J_{4\pi}$ , in terms of the angles specifying direction. This function, in the nomenclature of Kern [11], may be written in terms of the local magnetic field vector,  $B$ ; altitude,  $H$ ; ionospheric scale height,  $h_s$ ; and the pitch and azimuth angles ( $\theta$  and  $\lambda$ , respectively); as:

$$\frac{J}{J_{4p}} = F_N \exp\left[\frac{-(p/2 - q)^2}{2s_q^2}\right] \exp\left[\frac{r_g \cos I \cos \lambda}{h_s}\right]$$

where  $I$  is the magnetic dip angle and  $r_g$  is the gyroradius, given by

$$r_g = \frac{\sin q \sqrt{E^2 + 2m_0 E}}{30 |\vec{B}|}$$

with the particle kinetic energy, E, in MeV and magnetic field strength, B, in gauss;  $m_0$  is the rest mass energy. The standard deviation of pitch angle is given by

$$s_q = \sqrt{\frac{h_s}{K \sin I}}, \text{ where } K = \frac{4(R_E + H)}{3 \sin I (2 + \cos^2 I)},$$

with  $R_E$  representing the Earth radius.  $F_N$  is a normalization factor parameterized by Kern [11] as:

$$\text{where } x = \frac{r_g \cos I}{h_s \sin q}.$$

During passage through the SAA, it is found that the particle flux is prominent only over a relatively narrow latitude-longitude region. Consequently, the present analysis is constrained to the conditions for each path that correspond to peak particle flux as determined from the SPENVIS [7] calculations. The accompanying magnetic field components have been specified according to the NSSDC IGRF model [8], and are given in **Table 10-1**.

**Table 10-1.** Magnetic Field (nT) at Peak Flux Conditions

	Location	B-North	B-East	B-Down
Path I	44.56S, 24.7W	11631	-3692	-18840
Path II	40.84S, 40.6W	13557	-3362	-16352
Path III	36.63S, 57.4W	16073	-1504	-13252

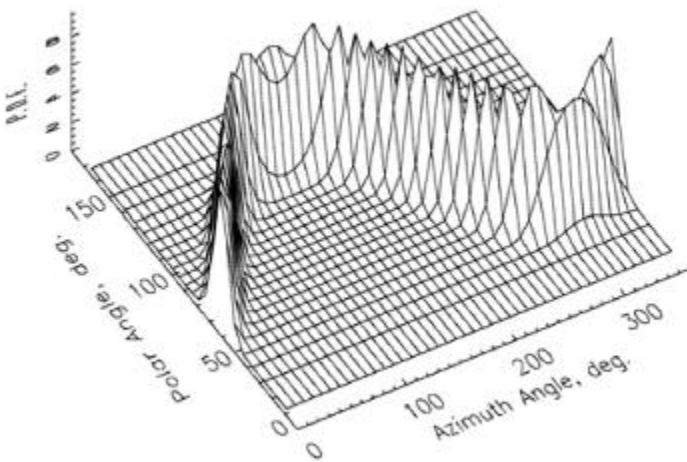


**Figure 10-4.** 2 MeV electron directional distribution function in terms of vehicle orientation angles.

To illustrate the qualitative features of the directional distribution function, sample surface plots of its magnitude in the spherical angular coordinate space (polar and azimuth angles) of the vehicle (ISS at  $51.6^\circ$  inclination) are given for electrons and protons in Path II of the scenario. **Figure 10-4** depicts the surface map of the distribution function for 2 MeV electrons, and **Figure 10-5** shows the function for 100 MeV protons. The general energy dependence of the distribution function is relatively weak for particle energies of importance in LEO. It should be noted that the distributions shown represent an instantaneous, as opposed to an orbit- averaged, calculation.

One may also note a more pronounced preferred direction of incident proton flux from the general westerly angles (200 to 300 deg.) that is not observed for the electron flux. This may be attributed to the difference in rest mass, and hence gyroradii of the two particle types.

## CONFIGURATION CAD SOLID MODELS

### ISS 8-A Configuration

The primary components of the ISS 8A Configuration are the U.S. Lab module, the U.S. Node 1, the U.S. Airlock, the three U.S. Pressurized Mating Adaptors (PMA), the Russian Functional Cargo Block (FGB), the Russian Service Module (SM), the Russian Docking Compartment and truss structures. A simplified model of this configuration along with the location of the target points is illustrated in **Figure 10-6**. The primary shielding for astronauts in the space station is the micrometeoroid debris shielding and the pressure vessel. Many components of the space station also include a protective bumper over the pressure vessel. The cargo within the primary modules will also provide additional shielding for astronauts within the space station. In this analysis it is assumed that these components are primarily made up of aluminum. More information on the space station model may be found in Hugger, et al [12].

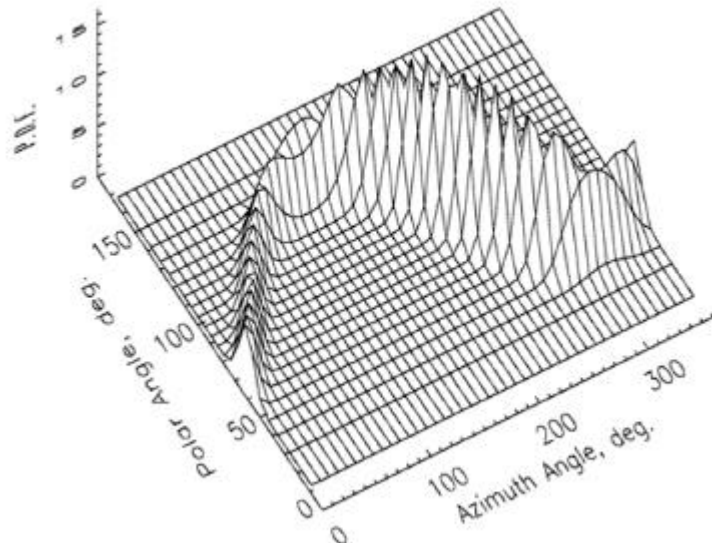


**Figure 10-5.** 100 MeV proton directional distribution function in terms of vehicle orientation angles.

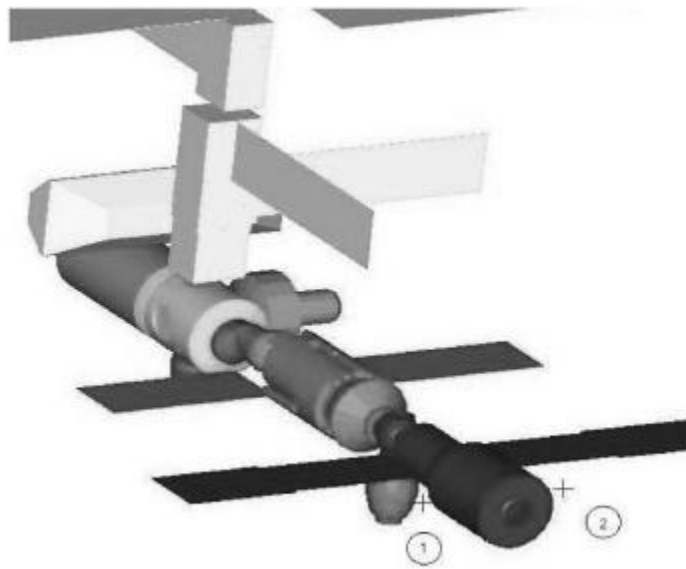


**Figure 10-6.** Location of target points outside the ISS.

Resultant thickness distributions for the ISS as seen from the chosen EVA points are shown in **Figure 10-7**. These points are taken to be alongside the module and 1 meter away from the outer wall. At these locations, the distributions indicate that only about  $\frac{1}{4}$  of the  $4\pi$  solid angle is subtended by the ISS structure, with the remainder open to the free space environment. Also, the symmetry of the configuration with respect to the target points shows that the “shadowing” of the two points is practically identical.

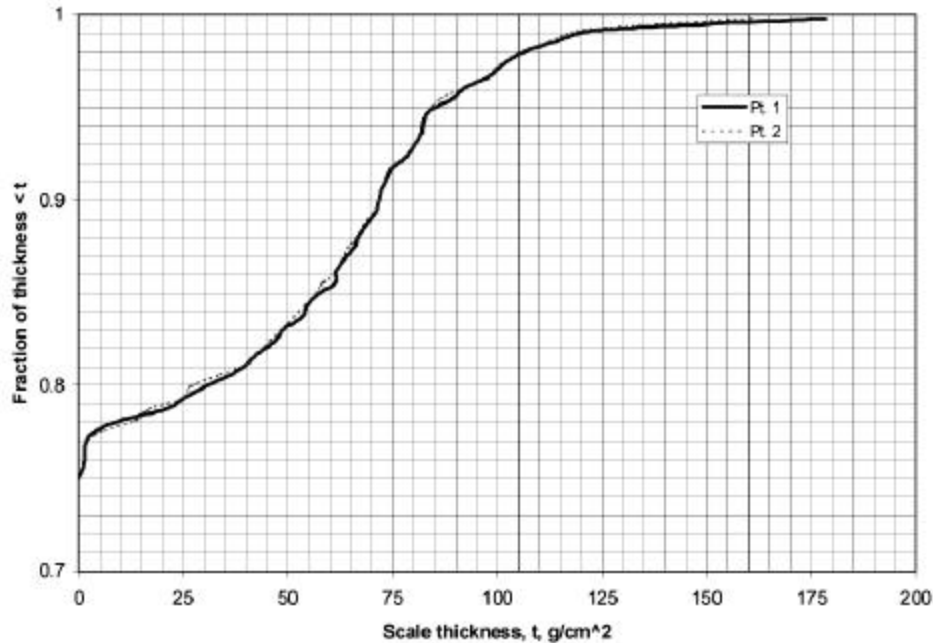


**Figure 10-7.** Thickness distributions for the ISS as seen from the EVA target points outside the Service Module.

## ***Shuttle Space Suit***

Principal components of the Shuttle space suit are the HUT, arm assemblies, Lower Torso Assembly (LTA), extravehicular gloves, and helmet. The PLSS is attached to the back of the suit, the LCVG is under the pressure suit and against the astronaut’s body, and the EVVA goes over the helmet. The major components are shown in **Figure 10-8**; a more complete description may be found in Anderson, et al [13]. The HUT is constructed of fiberglass and covered outside with orthofabric, aluminized Mylar, and neoprene-coated nylon ripstop. The LTA and arm assemblies, including the LCVG, consist of orthofabric, aluminized Mylar, neoprene-coated ripstop, polyester, urethane-coated nylon, and water-filled cooling tubes. The extra-vehicular gloves are similar but do not include the cooling tubes. Due to the sensitivity of the eyes the EVVA consists of numerous visors that have been constructed to provide maximum eye protection. These are constructed primarily of polycarbonate or polysulfone. The PLSS (or “backpack”) consists of the primary oxygen system, oxygen ventilation system, liquid transport system, water feed circuit, secondary oxygen pack (SOP), EMU radio, caution and warning system, Contaminant Control Cartridge (CCC), EMU electrical system, EMU battery, and the Display and Control Module (DCM) located on the front of the HUT. The overall dimensions of the PLSS unit are 23 x 25 x 7 inches.

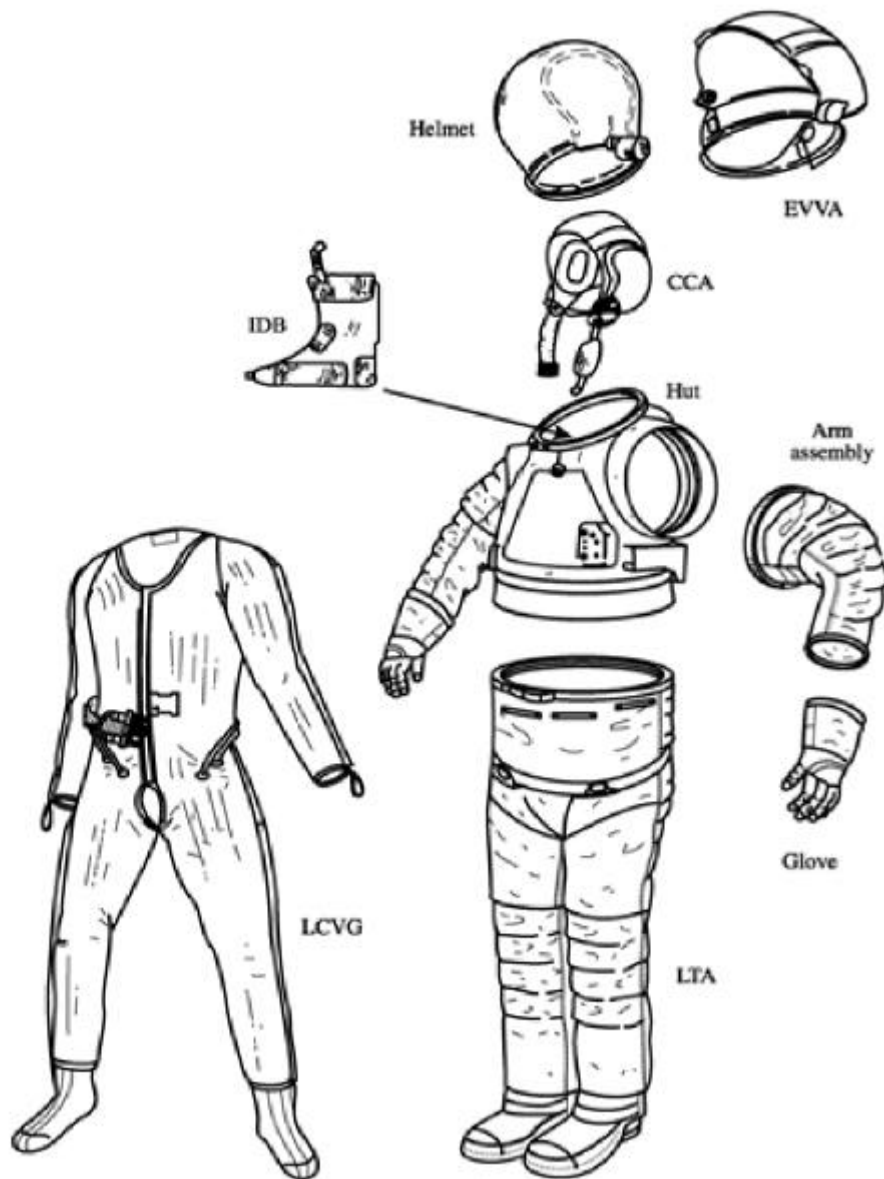


**Figure 10-8.** Basic components of the Shuttle space suit.

In modeling the suit the commercial CAD software package I-DEAS was used. The modeling effort was focused on simplicity while keeping an accurate representation of those components that contribute most to radiation shielding, e.g., the visors and the PLSS. Special attention was given to ensuring that solid angles subtended by the modeled elements were compatible with those of the true suit. Depictions of the CAD solid-modeled main suit and PLSS are given in **Figures 10-9** and **10-10**, respectively.

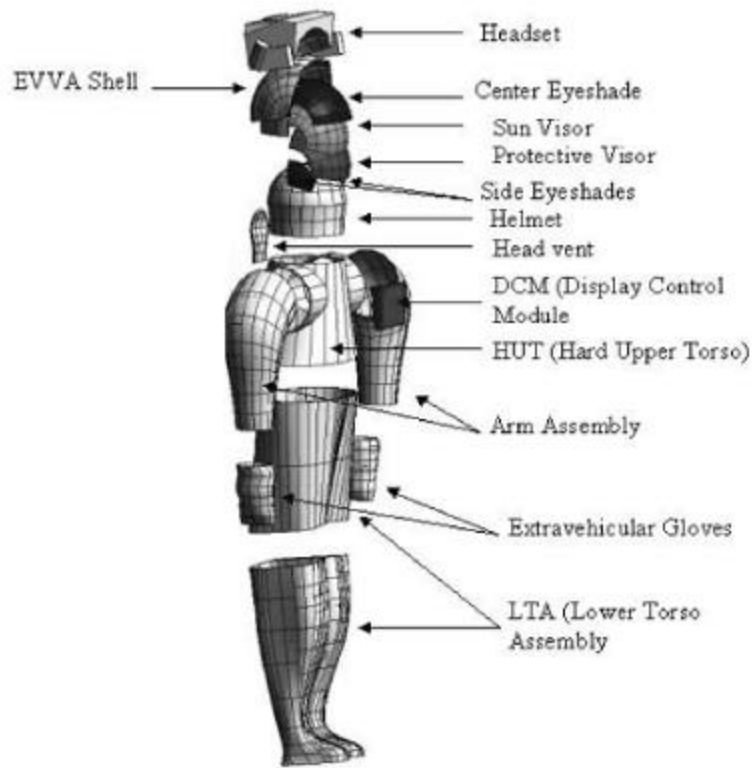


Figure 10-9. Exploded view of CAD-modeled components of main suit.

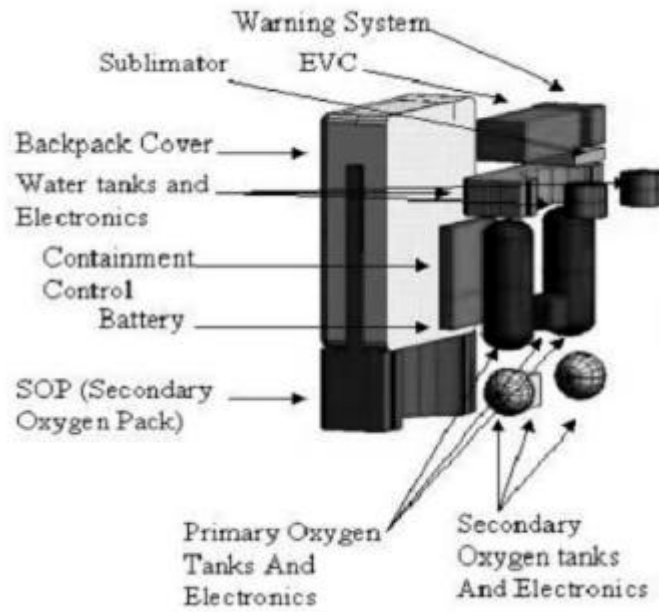
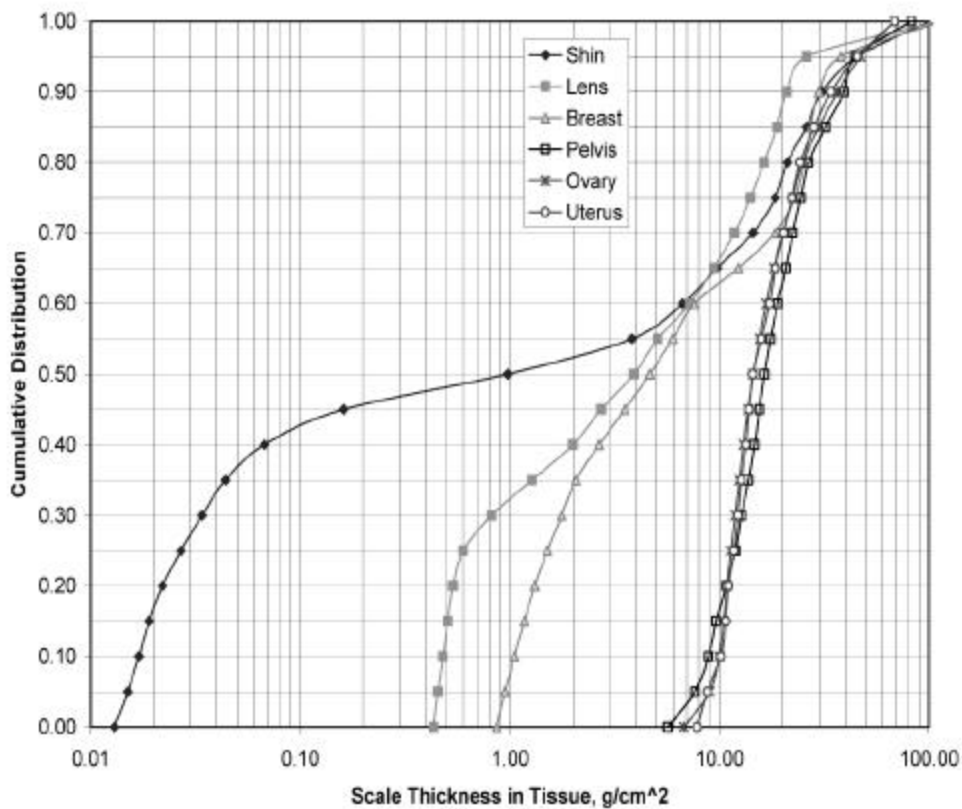


Figure 10-10. Exploded view of CAD-modeled PLSS space suit backpack.

## HUMAN GEOMETRY MODEL

With an increasing number of females being assigned to fly on Shuttle missions, Yucker and Huston [6] developed the Computerized Anatomical Female (CAF) model to help determine the astronaut's exposures for the Shuttle and ISS programs. They used the existing CAM model that was first developed by Kase [14]. The CAM model is very detailed, comprising approximately 1100 unique geometric surfaces and about 2400 solid regions. The internal body geometry critical body organs, voids, bone, and bone marrow are explicitly modeled with the proper chemical composition and density. The CAF model was constructed by "removing" the male organs and adding the appropriate female organs (breast, uterus, and ovaries). Since the average female is approximately 92% of the size of the average male, the CAF was scaled accordingly. A special algorithm has been used to map the directional distribution of matter (scaled thickness) about selected target points within the CAF model. The coordinate system chosen has origin at the top of the head with positive z toward the feet, positive x outward from the chest, and positive y through the right shoulder. The directional grid is based on the corresponding spherical coordinates and for the present calculations consists of 44 evenly distributed azimuth angles and 22 polar angles chosen so that the interstitial solid angles are constant. Six particular body points have been chosen for analysis: a skin point on the right shin, an ocular lens point, a BFO point in the pelvic region, along with the exclusively female organ points at the breast, ovary, and uterus locations. The normalized ordered distributions of thicknesses for each of the CAF target points are shown in **Figure 10-11**.



**Figure 10-11.** Thickness distributions for selected CAF target points.

## Transport of Energetic Trapped Particles

Evaluation of the desired dosimetric quantities at a target location requires knowledge of the energy spectra of the various particle types involved. These spectra are strongly influenced by the interactions and general attenuation of the particles as they pass through the material surrounding the target point. Analytical calculations of the transport of the trapped protons and electrons are performed by solving some form of the basic Boltzmann transport equation. Fortunately, high-energy particle transport can usually be well described using greatly simplified forms of the transport equation. Due to the wide differences in mass and kinetic energy of the two types of trapped particles, different codes are used for the respective transport calculations. For the electrons, a code of recent vintage developed by Nealy et al. [2] has been implemented. This formulation may be described as a “quasi-CSDA (Continuous Slowing Down Approximation)” application, with the prominent aspects of multiple scattering and energy fluctuations inherent in electron transport described with parameterizations based on laboratory beam measurements. The well-established Langley heavy ion code HZETRN [3] has been used to characterize the proton transport. A significant feature of the proton transport is the production of secondary neutrons and charged target fragments that augment the radiation field. Detailed descriptions of the algorithmic formulation and associated databases for the two codes may be found in the noted references.

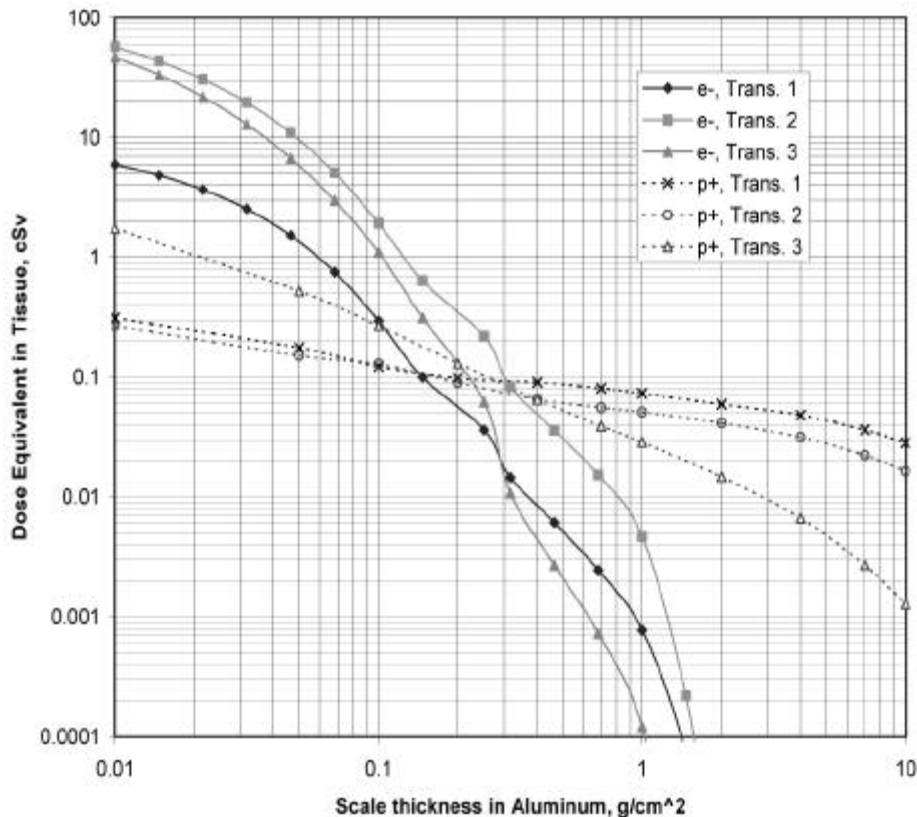


**Figure 10-12.** Sample dose-vs-depth functions for SAA trapped spectra in aluminum shield.

Evaluation of the dosimetric quantities at a given target location in the human body for an EVA astronaut requires calculation of the transport environment particles through the pertinent portions of the spacecraft structure, followed by the EMU configuration, and finally through the surrounding body tissue. Many transport calculations

are involved in such an assessment, have been performed for a variety of the constituent materials for each of the SAA transit spectra. Results of sample transport calculations for aluminum are shown in **Figure 10-12** in which the dose equivalent in tissue is given as a function of thickness traversed for both protons and electrons. The more penetrating nature of the protons is readily apparent. For the EVA scenario, the electron exposure is significant only for small thicknesses ( $< \sim 0.2 \text{ g/cm}^2$ ), typical of material amounts in thinner portions of the space suit.

## RESULTS

The several parameters selected for investigation of the female astronaut EVA in LEO have led to a fairly large number (several hundred) of dosimetric evaluations. In addition to six specific target organs included for three successive transits through the SAA, there are three types of radiation, options for inclusion or exclusion of magnetic field influences (directional properties) of the external charged particle field, and port and starboard spatial locations of the EVA being performed. Astronaut orientation with respect to the spacecraft has also been examined in terms of rotations facing toward and away from the space station structure. The solar maximum scenario has been chosen primarily in order to examine the role of the greatly enhanced fluxes of electrons that occur in peak solar activity along with the shielding provided by the EMU.

Initial consideration is given to the second transit through the SAA region, where the higher energy electrons are approximately 10 times more numerous than for the other passes (see **Figures 10-1** and **10-2**). Values of the calculated doses for each target organ point are presented in **Table 10-1** for the vector flux incident on the astronaut facing away from and toward the ISS module. **Table 10-2** gives the results for the same situation as **Table 10-1**, but with the external (free space) fluxes assumed to be isotropic with respect to direction. It is immediately obvious in these tables that the proton contribution dominates the total exposures, whereas the impact of electrons and photons is essentially negligible (except for skin points where absence of body self-shielding becomes a factor). Another discernible feature are the relatively small differences in the dose values for vector vs. isotropic fluxes. However, the cited results are for integration over all solid angles and do not imply that large variations in the directional properties (steradian) of the radiation field are not present. On the other hand, substantial differences are observed for the different astronaut orientations, especially for the organs situated near the body surface.

A summary of the dose calculations for the combined three transits and for both of the EVA points is given in **Tables 10-3** and **10-4**. Comparisons of the totals for point 1 (port side) with those of **Tables 10-1** and **10-2** for the second pass indicates that most of the electron and photon dose is incurred during this transit. This is not generally the case for the proton exposures; proton fluxes of moderate energy ( $\sim 20\text{-}30 \text{ MeV}$ ) (see **Figure 10-3**) are of comparable magnitude for all transits, and translate directly to significant contributions to the more exposed target points during the first and third transits.

The effect of incorporating the directional redistribution due to magnetic forcing ('vector flux') is most readily apparent by comparing the proton doses of points 1 and 2 for the EVA subject facing outward. According to the scenario, radiation intensity for protons should be reduced for directions generally facing magnetic east (starboard, point 2). This is particularly notable for the skin, breast, and ovary target points. The magnetic effect is markedly diminished when the subject is facing the structure and frontal target points are better shielded by the

EMU backpack, the generally enhanced body self-shielding, and the ISS structure itself. The port vs. starboard values show much greater similarity for the isotropic (omni-directional) fluxes. At the time of this writing, no published results of direct measurements under comparable conditions have been available to the authors for comparison purposes. However, an extensive database of U.S. Space Shuttle (STS) measurements exists [15], and measured dose rates for approximate ISS conditions range from ~.1 to ~.5 mSv/day of which ~50 % may be attributed to trapped particle exposures in the SAA region. When consideration is given to the adverse exposure conditions for the present simulation, the calculations appear to be entirely reasonable.

**Table 10-1.** Dose Values for Vector Flux

Incident on Target Point 1 for Transit 2

Facing away from ISS

	electrons	photons	protons
BFO 17	0.00000	0.00006	0.072
breast	0.00000	0.00027	0.160
lens	0.00400	0.00057	0.223
ovary	0.00000	0.00004	0.043
skin	0.13340	0.00203	0.380
uterus	0.00000	0.00005	0.583

Facing toward ISS

	electrons	photons	protons
BFO 17	0.00000	0.00003	0.025
breast	0.00000	0.00018	0.075
lens	0.00000	0.00033	0.109
ovary	0.00000	0.00004	0.048
skin	0.06740	0.00102	0.132
uterus	0.00000	0.00004	0.039

**Table 10-3.** Total Dose Values for All Three Transits Through SAA for Point 1

Facing away from ISS

VECTOR FLUX

	electrons	photons	protons
BFO 17	0.00000	0.00012	0.222
breast	0.00000	0.00057	0.442
lens	0.004	0.00117	0.624
ovary	0.00000	0.00009	0.148
skin	0.17000	0.00409	1.196
uterus	0.00000	0.00006	0.1872

OMNI-DIRECTIONAL

	electrons	photons	protons
BFO 17	0.00000	0.00012	0.142
breast	0.00000	0.00057	0.347
lens	0.0007	0.00117	0.457
ovary	0.00000	0.00009	.0125
skin	0.3987	0.000409	0.846
uterus	0.00000	0.00006	0.131

**Table 10-2.** Dose Values for Omni-Directional Flux

Incident on Target Point 1 for Transit 2

	electrons	photons	protons
skin	0.0659	0.00206	0.449
uterus	0.00000	0.00005	0.039

Facing toward ISS

	electrons	photons	protons
BFO 17	0.00000	0.00003	0.028
breast	0.00000	0.00018	0.085
lens	0.00006	0.00033	0.109
ovary	0.00000	0.00004	0.030
skin	0.0479	0.00102	0.167
uterus	0.00000	0.00004	0.029

	electrons	photons	protons
BFO 17	0.00000	0.00006	0.072
breast	0.00000	0.00027	0.160
lens	0.00400	0.00057	0.223
ovary	0.00000	0.00004	0.043
skin	0.13340	0.00203	0.380
uterus	0.00000	0.00005	0.583

	electrons	photons	protons
skin	0.0659	0.00206	0.449
uterus	0.00000	0.00007	0.115

OMNI-DIRECTIONAL

	electrons	photons	protons
BFO 17	0.00000	0.00007	0.100
breast	0.00000	0.00037	0.248
lens	0.00007	0.00068	0.317
ovary	0.00000	0.00006	.108
skin	0.0594	0.00206	1.230
uterus	0.00000	0.00007	0.773

Facing away from ISS

VECTOR FLUX

	electrons	photons	protons
BFO 17	0.00000	0.00012	0.222
breast	0.00000	0.00057	0.442
lens	0.004	0.00117	0.624
ovary	0.00000	0.00009	0.148

In further perspective, dose incurred as a result of full diagnostic X-ray examination for pelvis, breast, and urethra are on the order of .5 mSv [16] and on the basis of conventional dosimetry, the space walks presently simulated would result in exposures comparable to a typical X-ray examination and would not be considered to be especially hazardous.

**Table 10-4. Total Dose Values for All Three Transits Through SAA for Point 2**

Facing away from ISS VECTOR FLUX			
	electrons	photons	protons
BFO 17	0.00000	0.00012	0.121
breast	0.00000	0.00056	0.268
lens	0.00000	0.00118	0.358
ovary	0.00000	0.00009	0.110
skin	0.2913	0.00389	0.652
uterus	0.00000	0.00010	0.112
OMNI-DIRECTIONAL			
	electrons	photons	protons
BFO 17	0.00000	0.00012	0.141
breast	0.00000	0.00056	0.348
lens	0.00000	0.00018	.0461
ovary	0.00000	0.00009	0.120
skin	0.1663	0.00389	0.815
uterus	0.00000	0.00010	0.129
Facing toward the ISS VECTOR FLUX			
	electrons	photons	protons
BFO 17	0.00000	0.00007	0.089
breast	0.00000	0.00037	0.217
lens	0.00005	0.00066	0.275
ovary	0.00000	0.00007	0.093
skin	0.0475	0.00223	0.455
uterus	0.00000	0.00007	0.096
OMNI-DIRECTIONAL			
	electrons	photons	protons
BFO 17	0.00000	0.00007	0.100
breast	0.00000	0.00037	0.246
lens	0.00007	0.00066	0.311
ovary	0.00000	0.00007	0.107
skin	0.0709	0.00223	0.533
uterus	0.00000	0.00007	0.104

## SUMMARY AND CONCLUSIONS

The somewhat detailed and complex study described in preceding sections has yielded some results that were anticipated and others that were unexpected. From the expected results one may conclude that:

- Doses encountered during relatively brief times in EVA in the SAA region should be generally comparable to observed daily dose rates in LEO, since a substantial part of the dose incurred over an orbital period passing through the region relates to the time spent in the SAA.
- The known proximity of the magnetic mirror point to the orbital altitude in the SAA should result in substantial effects due to directional redistribution of particle fluxes.
- Exposures due to bremsstrahlung are essentially negligible. Inferences from results not anticipated beforehand include:
- The EMU effectively eliminates dose from electrons even in the high-flux solar maximum situation for ISS orbital conditions. (Certain skin areas are predicted to incur some electron dose, but values remain far below levels that would induce erythema.)
- Even in conditions for which electron flux is greatly enhanced and protons relatively subdued (solar max.), the dose levels are dominated by protons for all target points chosen.
- A complementary analysis for solar minimum conditions would be a logical continuation of this work. It should also be noted that much of the computational procedure and analysis has been performed in a somewhat piecemeal fashion, and the amount of bookkeeping required involved an inordinate expenditure of time. These separate procedures are currently in the process of being combined and linked at NASA-Langley, so that future studies that involve case multiplicity caused by changing environment, orientation, and temporal and spatial location may be effectively automated.

## REFERENCES

1. Atwell, W.: "Anisotropic Trapped Proton Effects on the International Space Station". Paper No. 2001- 01-2328 in Proc. 31st International Conf. On Environmental Systems (ICES), Orlando, FL, July 9- 12,2001.
2. Nealy, J. E., Anderson, B. M., Cucinotta, F. A., Wilson, J. W., Katz, R., and Chang, C. K.: "Transport of Space Environment Electrons: A Simplified Rapid-Analysis Computational Procedure". NASA TP-2002-211448, Mar. 2002.
3. Wilson, J. W., Badavi, F. F., Cucinotta, F. A., Shinn, J. L., Badhwar, G. D., Silberberg, R., Tsao, C. H., Townsend, L. W., and Tripathi, R. K.: "HZETRN: Description of a Free-Space Ion and Nucleon Transport and Shielding Computer Program". NASA TP 3495, May 1995.
4. Anderson, B. M., Nealy, J. E., Wilson, J. W., and Simonsen, L. C.: "CAD Model of Astronaut Exposures during EVA: Nominal and Extreme Scenarios". Paper No. 2002-01-2458, Proc. Of 32nd International Conf. On Environmental Systems, San Antonio, TX, July 15-18, 2002.

5. Nealy, J. E., Anderson, B. M., Wilson, J. W., and Qualls, G. D.: "High-Speed Computational Applications for Space Radiation Shielding Analysis". Proc., Space Technology & Applications International Forum, ed. M. El-Genk, Albuquerque, NM, Feb. 2-6, 2003.
6. Yucker, W. R. and Huston, S. L.: "Computerized Anatomical Female. Final Report". Report MDC H6107. McDonnell Douglas Corporation, Huntington Beach, CA, Sept. 1990.
7. SPENVIS (website): SPace ENVironment Information System (URL: <http://www.spennis.oma.be/spennis/>). June 2000.
8. NSSDC (website): National Space Science Data Center (URL: <http://nssdc.gsfc.nasa.gov>), Version 3.3, Dec. 1998. 9. Heckman, H. H. and Nakano, G. H.: "Low-Altitude Trapped Protons during Solar Minimum Period, 1962-1966". J. Geophys. Res.-Space Physics, v74, no. 14, pp. 3575-3590, July 1969.
10. Watts, J. W., Parnell, T. A., and Heckmann, H. H.: "Approximate Angular Distribution and Spectra for Geomagnetically Trapped Protons in Low Earth Orbit". AIP Conference Proceedings on High Energy Radiation in Space, eds. Rester, A. C. and Trombka, J. I., pp. 75-85, Sanibel I., FL, 1989.
11. Kern, J. W.: "A Note on Vector Flux Models for Radiation Dose Calculations". Radiation Meas., v23, no. 1, pp. 75-85, 1994.
12. Hugger, Craig P., Qualls, Garry D., Wilson, John W., Cucinotta, Frank A., Shavers, Mark R., and Zapp, Neal, "ISS as a Platform for Environmental Model Evaluation". Proc., Space technology & Applications International Forum, ed. M. El-Genk, Albuquerque, NM, Feb.2-6, 2003
13. Anderson, B. M., Nealy, J. E., Kim, M-H., Qualls, G. D., and Wilson, J. W.: "Analysis of a Radiation Model of the Shuttle Space Suit". NASA Technical Publication, control number L-18235 (in press)
14. Kase, P. G.: "Computerized Anatomical Model Man". Report AFWL-TR-69-161, Air Force Weapons Laboratory, Kirtland AFB, NM, Jan. 1970.
15. Badhwar, G. D.: "Radiation Dose Rates in Space Shuttle as a Function of Atmospheric Density". Radiation Meas., v30, pp.401-414, 1999.
16. Paic, G.: "Ionizing Radiation: Protection and Dosimetry". CRC Press, ISBN 0-8493-6713-1, 1988.

# **CHAPTER 11**

## **RISK OF SKIN CANCER FROM SPACE RADIATION**

Francis A. Cucinotta<sup>1</sup>, Myung-Hee Y. Kim<sup>1,2</sup>,  
Kerry A. George<sup>1,2</sup>, and Honglu Wu<sup>1</sup>

<sup>1</sup>NASA Johnson Space Center  
Houston, Texas

<sup>2</sup>Wyle Labs  
Houston, Texas

# RISK OF SKIN CANCER FROM SPACE RADIATION

## ABSTRACT

We review the methods for estimating the probability of increased incidence of skin cancers from space radiation exposure, and describe some of the individual factors that may contribute to risk projection models, including skin pigment, and synergistic effects of combined ionizing and UV exposure. The steep dose gradients from trapped electrons, protons, and heavy ions radiation during EVA and limitations in EVA dosimetry are important factors for projecting skin cancer risk of astronauts. We estimate that the probability of increased skin cancer risk varies more than 10-fold for individual astronauts and that the risk of skin cancer could exceed 1% for future lunar base operations for astronauts with light skin color and hair. Limitations in physical dosimetry in estimating the distribution of dose at the skin suggest that new biodosimetry methods be developed for responding to accidental overexposure of the skin during future space missions.

## INTRODUCTION

In this report, we summarize issues important for estimating skin cancer risks on space missions. NASA's career dose limits set an upper level of acceptable fatal cancer to an increased risk of 3%. Risk assessment models are used to describe gender- and age-dependent dose to risk conversion factors. Short-term limits for protection of the skin, lens, and BFOs (NCRP, 2000) are levied to prevent the occurrence of acute health effects such as skin ulceration, moist and dry desquamation, and erythema. The threshold doses for skin damage and corresponding dose limits (1.5 Gy-Eq in 30 days and 3.0 Gy-Eq in 1-year) are such that it is difficult to find a mission scenario for LEO where these limits would be exceeded. For exploration missions to the moon or Mars, such possibilities exist if effective shielding and operational warning systems are not in place. The scientific basis for the deterministic dose limits are well established, originating in fairly extensive human data for skin reactions following exposures to both low- and high-LET radiation (NCRP, 2000). There is also a risk of late effects from ionizing radiation exposure of the skin, namely carcinogenesis. Because cancer risks projections for protons and heavy ions are highly uncertain (Cucinotta *et al.*, 2001) and individual factors play a prominent role in the incidence of skin cancers, the inclusion of such factors in risk assessment approaches is warranted.

## BIOLOGICAL FACTORS IN SKIN CARCINOGENESIS

There are three major types of skin cancers: melanoma, basal cell carcinoma (BCC), and squamous cell carcinoma (SCC). The incidence of skin cancer has risen dramatically in the 20<sup>th</sup> century due to increased UV exposures from changes in clothing and other lifestyle factors. Melanoma is the most serious of the skin cancers; about 37,000 new cases of melanoma are reported annually in the U.S. (Kamb and Herlyn, 1998). Early detection is effective for assuring high cure rates with 5-year survival rates above 85% for these cases. However, if untreated, advanced stages of melanoma can metastasize and lead to fatalities with common secondary sites of brain, bone, lung, and liver. BCC and SCC are the more prevalent skin cancers and, in fact, are the most common of all cancers in the U.S. with about 750,000 cases of BCC and about 150,000 of SCC reported annually (Rees, 1998). However,

BCC is largely noninvasive with less than 1 in 4,000 cases undergoing metastasis. Metastasis rates for SCC are about 1 in 100 cases; however, fatalities are much smaller than for melanoma. Under-reporting or lack of histological confirmation of skin cancers, especially BCC and SCC, is a common problem and leads to uncertainties in estimates of UV or ionizing radiation risks. Tumor registers typically only track melanoma because of these problems.

Melanomas originate from the pigment-producing (melanin) melanocyte cells in the skin. The number density of melanocytes does not vary with skin color; rather the amount of melanin pigment is reduced in dark skin (Kamb and Herlyn, 1998). Melanocytes develop from progenitor cells in the central nervous system, reside at the interface between the epidermal and dermal layers of the skin, and form aggressive tumors when fully transformed. Genetic damage to melanocytes are causative of melanomas with disruption of the restriction point early in the cell cycle through mutations in cell cycle inhibitors such as the p16 protein, cyclin-dependent kinases, and the pRb protein, a key factor in their formation. Loss of heterozygosity and point mutations, efficiently produced by UV radiation, are common steps in tumor formation.

The more prevalent BCC and SCC originate in the keratinocyte cells of the skin. Point mutations in tumor suppressor genes, efficiently produced by UV exposure, are a common factor in BCC. However, aneuploidy is rare and BCCs are typically diploid. In contrast, the more aggressive SCC shows aneuploidy in a majority of the cases (Rees, 1998). For both BCC and SCC, point mutations in the p53 gene are a common event, with loss of heterozygosity of the p53 locus occurring frequently for SCC. Differences in the types of DNA damage produced by UV and ionizing radiation will be consequential in the probabilities for the induction of these specific skin cancer types. Genetic disorders account for less than 1% of skin cancers, however skin color plays a major role, with over a 10-fold difference increase in incidence for those with fair complexion and red or blonde hair compared to those with dark skin and dark hair.

## **RADIATION EPIDEMIOLOGY OF SKIN CANCERS**

Two-epidemiology studies that can be used to form the basis of skin cancer risk estimates are the lifespan study of about Japanese 85,000 survivors of the atomic bombs (Preston *et al.*, 1994), and the study of 2,226 persons treated in childhood with 100 kVp X-rays to the scalp for treatment of tinea capitis (Shore *et al.*, 1984). In these studies, evidence for an association between ionizing radiation and BCC is quite strong, modest for SCC, and nonexistent for melanoma. For estimating skin cancer risks to astronauts, the differences in susceptibility of the Japanese, the role of UV exposures, and the different molecular lesions produced by high-LET radiation in space are important factors that lead to uncertainties in skin cancer risk from space radiation.

In the tinea capitis study, doses at the scalp ranged from 3.3 to 6.0 Gy, however significant doses were received in other areas, including 0.1 to 0.5 Gy to the face and neck, where many excess cancers were observed. No skin cancers were observed in the subset of black patients in this study. For white patients, a linear dose response is observed with an apparent synergistic effect from combined UV and X-ray exposure with  $3.3 \times 10^{-5}$  cases per  $\text{cm}^2$  per PY-Gy in areas exposed to UV and X-rays, and  $0.71 \times 10^{-5}$  cases per  $\text{cm}^2$  per PY-Gy in areas exposed to X-rays alone. This indicates about a fivefold enhancement due to synergistic effects with UV exposure.

In the Japanese study, fits to dose response data using a linear, linear-quadratic, or spline fit could not be distinguished (Thompson *et al.*, 1994). For the linear-fit an excess relative risk (ERR) of 1.0 per Sv with 95% confidence intervals of [0.41, 1.89] are found (Thompson *et al.*, 1994), which is one of the highest for all solid tumors found in this study. The ERR is found to decrease with age at exposure, but little dependence on attained age and gender were found. The average latency time for low-LET X-rays and gamma rays is on the order of 20 years.

Further, breakdown of skin cancer risk based on skin pigment is not possible based on existing epidemiology data. However, it is reasonable to assume that the UV interaction observed with X-rays would be influenced by skin pigmentation, such that skin cancer risk is dependent on skin color as well as area of the skin irradiated. Recently, studies of increased skin cancer risk have been reported amongst pilots (Hammar *et al.*, 2002). It is unclear if this increase is due to a synergistic effect between UV and atmospheric radiation, or if other factors such as the effects of altered circadian rhythms on melatonin regulation are involved. Another factor unique to spaceflight is the differences in UV exposure in space. Outside the Earth's atmosphere, all three UV components are present (UVA, UVB, and UVC). The risk of skin cancer from this spectrum, atypical to that on Earth, combined with the space radiation environment has not been studied.

Burns *et al.* (1994) studied radiation-induced skin tumors with high-LET radiation, using a rat model. In these studies, electrons are used as a low-LET radiation. A linear-quadratic model or threshold model best fits the data for electrons and a linear response is found for heavy ions. For electrons, a dose-rate reduction is observed following split dose experiments, however, a dose enhancement is observed for tumors induced by high-LET argon ions. Because the low-dose response for electrons is difficult to quantify, estimates of relative biological effectiveness factors for heavy ions are highly uncertain, with values as low as 10 or higher than 100 possible, which are dependent on the method used to extrapolate the electron response data to low doses and dose-rates. The use of radiation quality factors to estimate skin cancer risks is intermediate between such reductions of the rat skin tumor data for heavy ions.

## ESTIMATES OF SKIN CANCER RISK FOR SPACE MISSIONS

For transferring of cancer risks across populations, one can use multiplicative risk, additive risk, or mixture models. The NCRP risk model for solid cancer used by NASA (NCRP, 2002) uses a mixture model based on averaging the multiplicative and additive risk models in transferring risk coefficients from the Japanese to the U.S. population. Thompson *et al.* (1994) has noted that the multiplicative model may be preferred for skin cancers, such that an additive or mixture model would underestimate the risk for whites with fair skin and hair in the U.S. Skin cancer rates vary substantially based on race, ethnicity, and UV exposure. Age-adjusted-rates for the incidence of melanoma in whites living in Hawaii and Connecticut are  $45.6 \times 10^5$  and  $21.6 \times 10^5$ , respectively, and for blacks living in these same states  $0.42 \times 10^5$  and  $1.31 \times 10^5$ , respectively. In the additive risk model, the ERR expressed as an induction rate per Sv,  $\alpha$ , and the baseline rate in the Japanese population,  $B_{Japan}$ , is used to directly estimate the ERR in the US population as,

$$ERR_{additive} = \alpha B_{Japan} \quad (1)$$

In the multiplicative model, the ERR is estimated using the induction coefficient for the Japanese population times the baseline rate in the U.S.,  $B_{US}$

$$ERR_{multiplicative} = aB_{US} \quad (2)$$

and the NCRP preferred model is to average the results of Equation (1) and (2) (NCRP, 2000). In the limit of  $B_{US}/B_{Japan} \gg 1$ , it can be shown that the mixture model underestimates the multiplicative model by twofold. Since the multiplicative model is preferred for skin cancer excess incidence (Thompson *et al.* (1994)), we assume a twofold increase for the average U.S. white population over the incidence rates provided by the NCRP (NCRP, 2000). Based on other studies noted by Thompson *et al.* (1994), we estimate at least a further twofold increase for U.S. whites of fair skin and hair color. Also, we assume a fivefold increase in risk for skin areas with high UV exposure and that such areas cover about 10% of the skin area. In **Table 11-1**, we show risk estimates for the excess incidence of non-melanoma skin cancer per  $cm^2$  per Gy using the multiplicative model and the more conservative estimates for males with fair skin and hair at regions receiving combined UV and space radiation. For this estimate, we assume the surface area of the skin of  $2 m^2$  appropriate for the 50% percentile height and weight male.

The range of doses to be experienced on space missions varies substantially with the mission parameters. For nominal EVAs in LEO, skin doses of 0.1 mSv can be expected. Doses of 1 to 10 mSv are possible following frequent geomagnetic storms due to enhancement of the electron belts. Doses during the largest SPEs in LEO could reach as high as 100 mSv inside the spacecraft and could exceed dose limits on EVAs. Mission doses on ISS can exceed 200 mSv near solar minimum. For an 8-hour EVA on the surface of the Moon, doses exceeding 1,000 mSv are possible (Kim *et al.*, 1999). Note that, although the occurrence of more than a few large SPEs (>4) per solar cycle is highly unlikely, small to medium SPEs occur with a frequency of several per month at the peak of the solar cycle (Shea and Smart, 1990). The cumulative effect of such frequent SPEs could substantially increase skin doses to astronauts working at future lunar bases. Using the estimates of **Table 11-1**, one would expect that astronauts with high susceptibility would have skin cancer risks exceeding 1%. The results of **Table 11-1** can be used with transport codes and computerized anatomical geometry models to estimate the distribution of skin cancer risks for specific space missions.

**Table 11-1.** Estimates of Percent Excess Non-Melanoma Skin Cancer Risk for Low-Dose Rate Exposure of 1,000 mSv Delivered in Less Than 1 Year for Whites of Differential Skin Pigmentation With or Without UV Exposure\*

Age, y	Whole body averages for excess risk per Sv		Partial skin averages for excess risk per Sv per $cm^2$	
	Average U.S. White	U.S. White, fair skin & hair	U.S. White, fair skin & hair (no UV exposure)	U.S. White, fair skin & hair (synergistic UV exposure)
25	0.96	1.92	$0.69 \times 10^{-4}$	$3.46 \times 10^{-4}$
35	0.72	1.54	0.54	2.77
45	0.16	0.32	0.11	0.58
55	0.1	0.2	0.07	0.36

\*Assumes total skin surface area of  $20,000 cm^2$

A persistent problem for EVA is the limitations in EVA dosimetry, including its ability to detect steep dose gradients at the less shielded skin areas, such as the arms, hands, and face. Skin doses for soft proton or electron

spectra could vary more than fivefold at various locations of the skin. Since these least-shielded areas also receive the highest UV exposures, they will have an appreciable probability for skin cancer risk. Biodosimetry (George *et al.*, 2001) provides an alternative approach to estimate radiation exposure in accidental situations. Biodosimetry using cytogenetic methods could be used to validate a high exposure, however methods for performing these assays on skin plugs would need to be developed and the development of protocols to observe base damage or other biomarkers of skin cancer precursor would also be useful. For individuals of light skin color, biodosimetry methods should be pursued in order to improve the understanding of risk estimates, and to ensure adequate preparation for emergency responses to adverse radiation situations.

## REFERENCES

- Burns, F. J., Yin, Y., Garte, S. J., and Hosselete, S., Estimation of Risk Based on Multiple Events in Radiation Carcinogenesis of Rat Skin. *Adv. Space Res.* **14**, 507-519, 1994.
- Cucinotta, F. A., Schimmerling, W., Wilson, J. W., Peterson, L. E., Badhwar, G. D., Saganti, P., and Dicello, J. F., Space Radiation Cancer Risks and Uncertainties for Mars Missions. *Radiat. Res.* **156**, 682-688, 2001.
- George, K., Wu, H., Durante, M., Willingham, V., and Cucinotta, F. A., Chromosome Aberrations in Blood Lymphocytes of Astronauts after Space Flight. *Radiat. Res.* **156**, 731-738, 2001.
- Hammar, N., Linnarsjö, A., Alfredsson, L., Dammström, B., Johansson, M. and Eliasch, H., Cancer Incidence in Airline and Military Pilots in Sweden 1961-1996. *Aviat. Space Environ. Med.* **73**, 2-7, 2002.
- Kamb, A., and Herlyn, M., Malignant Melanoma. In: *The Genetic Basis of Human Cancer*. Ed. B. Vogelstein and K.W. Kinzler, McGraw-Hill Co., pp. 507-518, 1998.
- Kim, M. Y., Wilson, J. W., Cucinotta, F. A., Simonson, L. C., Badavi, F. F., Atwell, W., and Miller, J., Contribution of High-Charge and Energy (HZE) Ions During Solar Particle Event of September 29, 1989. NASA TP-1999-20930.
- NCRP, National Council on Radiation Protection and Measurements. Radiation protection guidance for activities in low-earth orbit. NCRP Report No. 132. Bethesda, MD: NCRP, 2000.
- Rees, J. L., Skin Cancer (Gorlin's Syndrome). In: *The Genetic Basis of Human Cancer*. Ed. B. Vogelstein and K. W. Kinzler, McGraw-Hill Co., pp. 527-536, 1998.
- Shore, R. E., Albert, M., Reed, N., Harley, N., and Pasternack, B. S., Skin Cancer Incidence Among Children Irradiated for Ringworm of the Scalp. *Radiat. Res.* **100**, 192-204, 1984.
- Shea, M. A., and Smart, D. F., A Summary of Major Solar Proton Events. *Solar Phys.* **127**, 297-320, 1990.
- Thompson, D. E., Mabuchi, K., Ron, E., Soda, M., Tokunaga, M., Ochikubo, S., Sugimoto, S., Takayoshi, I., Terasaki, M., Izumi, S., Preston, D. L., Cancer Incidence in Atomic-Bomb Survivors Part II: Solid Tumors, 1958-1987. *Radiat. Res.* **137**, S17-S67, 1994.

# **CHAPTER 12**

## **SUMMARY AND RECOMMENDATIONS**

### **FOR FUTURE WORK**

Francis A. Cucinotta<sup>1</sup>, Mark R. Shavers<sup>1</sup>, Premkumar B. Saganti<sup>2</sup>, and Jack Miller<sup>3</sup>

<sup>1</sup>NASA Johnson Space Center  
Houston, Texas

<sup>2</sup>Prairie View A&M University  
Prairie View, Texas

<sup>3</sup>Lawrence Berkeley National Laboratory  
Berkeley, California

## SUMMARY AND RECOMMENDATIONS FOR FUTURE WORK

The safety of astronauts is the primary concern of all space missions. Space radiation has been identified as a major concern for ISS, and minimizing radiation risks during EVA is a principle component of NASA's radiation protection program. The space suit plays a critical role in shielding astronauts from EVA radiation exposures. In cooperation with the JSC Extravehicular Activity Project Office, and the Space Radiation Health Project Office, the NASA EMU and RSA Orlan space suits were taken to the LLUPTF for a series of measurements with proton and electron beams to simulate exposures during EVA operations. Additional tests with material layouts of the EMU suit sleeve were made in collaboration with NASA LaRC at the LBNL 88-inch cyclotron and at the Brookhaven National Laboratory Alternating Gradient Synchrotron. Participants in the activity were scientists from the JSC Space Radiation Health Project Office, LLU, LBNL, ERIL Research, Inc., and the LaRC Radiation Shielding Design and Analysis Group.

**The objectives** of the measurements and analyses were to determine the radiation transmission properties of NASA's EMU and the Russian Orlan-M suit assemblies. Measurements focused on electrons and protons with energy sufficient to penetrate the EMU or Orlan suit and reach the skin, eyes, blood-forming organs, stomach, lung, and brain. A second set of tests considered the transmission properties of a relativistic iron and proton beams on a sample layout of the EMU. Tests used a human phantom to estimate organ doses and consider the effects of high-Z materials in the EMU or Orlan suit assembly and helmet and the dose contributions from target fragments, including secondary neutrons. Data collected were used to validate models that predict EVA organ doses in real time and improve accuracy of astronaut career exposure histories. Specific objectives included:

- Determine the minimal electron and proton penetration (threshold) energies at several locations on the EMU and Orlan-M suit assemblies.
- Using a human phantom, measure the dose, dose equivalent, and LET spectra at the skin, eyes, blood-forming organ, and other organs for several electron and proton energies.
- Measure transmission properties of a relativistic iron beam at tissue depths using a sample layout of the EMU.
- Compare the results of the measurements to the NASA Space Radiation Transport Code (HZETRN/BRYTRN) and CAM model.
- Develop data and knowledge for considering new approaches for design of EVA suits for LEO or Lunar/Mars missions.

**Background:** Astronauts are exposed during spaceflight to trapped protons and electrons and GCR, which consist of high-energy protons and heavy ions. During EVAs, astronauts may experience enhanced doses to the skin and eyes from low-energy protons and electrons in Earth's trapped radiation belts (including the SAA) that do not penetrate inside the spacecraft. Severe solar weather conditions can produce dose enhancements due to the possible occurrence of SPEs or disturbed Earth magnetic field conditions leading to transitory enhancements of the trapped belts. Analysis of the characteristic spectra of electron and proton environments suggest that a critical factor in managing EVA safety is the ability to determine the minimal penetration energies of electrons and protons at critical locations on the EMU or Orlan suit. Skin responses to radiation include erythema, epilation, and desquamation [1].

Different anatomical skin sites vary in sensitivity with decreased order of responsiveness as follows: 1) anterior aspect of neck, antecubital, and popliteal areas, 2) anterior surfaces of extremities, chest, and abdomen, 3) face, 4) back and posterior surfaces of extremities, 5) nape of neck, 6) scalp, palms and soles. Due to variation of skin shielding within the EMU and Orlan suit assemblies and the range of sensitivities of different regions of the skin, it is important to determine the shielding properties at different skin locations as well as internal organs. In addition, the risk of skin cancer, especially basal cell carcinoma, is increased by electron and proton exposures. The lens of the eye is radiosensitive and receives minimal shielding protection during EVAs and the risk of cataractogenesis is a concern during spaceflight [2]. For the deep-seated tissues, only penetrating high-energy particles are of concern and the shielding provided by EVA suits plays only a minor role, except for the backpack and helmet.

Operational planning of EVA timing to minimize passes in the SAA, regions of high geomagnetic latitudes where solar protons can enter the orbit, and the trapped electron horns will remain the principle method to reduce EVA exposures to astronauts. However, limitations in the current EVA dosimetry, especially for electrons, and the value to the EVA safety that would result from eliminating radiation threats through optimization of space suit shielding suggests that a comprehensive evaluation of the current ISS space suits be performed. Dosimetry issues for ISS include the absence of an electron dosimeter [3] and deficiencies in high-LET crew dosimetry, including the measurements of secondary neutrons and target fragments. The latter is being corrected based on the recommendations from the JSC Radiation Health Officer, including integrating CR-39 into the crew dosimeter. The relative effective dose (tissue weighted organ dose equivalent) for EVA compared to IVA from GCR are similar, however the EVA dose will have a higher contribution from heavy ions and a smaller contribution from secondary neutrons.

**Recommendations:** A series of conclusions and recommendations for future work were generated from the studies conducted as reported in this volume:

1. The thicknesses of U.S. and Russian EVA suits at various locations were determined using a CT scanner, electron beam, and proton beam. The threshold energies for penetration by electron and proton beams were evaluated (Moyers *et al.*, Chapter 2). Typical threshold energies ranged from 0.5 to 1.2 MeV for electrons, and 12 to 25 MeV for protons at the arms, legs, and torso with higher values for the helmet (>3 MeV for electrons and >40 MeV for protons) and backpack (>7 MeV for electrons and >70 MeV for protons). There was no clear indication that the EMU or Orlan were superior for threshold energy comparisons as differential values are found at different locations. It is recommended that the better resolving power, reduced scatter, and variable distance snout argue for the proton thickness measurements to be used to calculate the electron threshold energies as well as the proton threshold energies.

2. The non-uniformity of the suit fabric was identified as an important issue near the soft tissues of the skin, however this was tested for the EMU only. Additional experiments are recommended to better understand the source of the non-uniformity of the fabric components, and to collect data for an Orlan swatch. It is recommended (Wilson *et al.*, Chapter 8) that the non-uniform elements (e.g., spandex) be modeled by an equivalent sheet of uniform polycarbonate and the transmitted spectrum determined and analyzed. This should provide a reasonable model of the space suit fabric and cooling tubes for use in estimating astronaut exposures from differential radiation components.

3. Considerable progress was made in understanding the basic transmission properties of the space suit fabric currently used in the space program. Additional detail is required to adequately model the proton transmission properties of the LCVG cooling tubes where non-uniformity was identified as a critical issue for low-energy electrons and proton exposures during EVA. The basic fabric model was integrated into a CAD space suit model developed by LaRC and made available to the Space Radiation Health Project Office at JSC for supporting estimates of astronaut exposures during ISS missions. Further analysis is recommended to fully understand the energy transmission of this complex system.

4. Measurements by Benton *et al.* (Chapter 4) and Zeitlin *et al.* (Chapter 3) of total dose, dose equivalent, or LET spectra inside the EMU and Orlan-M suits and those made with only the bare phantom using TLDs and CR-39 or solid-state detectors demonstrate the important role of target fragmentation in increasing the average quality factor (and dose equivalent) from high-energy protons. The additional shielding represented by the suits tended to reduce both dose and dose equivalent through attenuation and scattering of the primary proton flux for the proton energies considered in the experiments. However, theoretical models are needed to extend the observations to the complete spectrum of protons present during EVA. Many detailed comparisons at specific tissue locations are provided by Benton *et al.* and indicate some variation between the shielding properties of the EMU and Orlan, however the results are differential for the tissues considered and there is no clear reason to favor one suit over the other based on these comparisons. Target fragmentation plays a dominant role in the energy deposition and biological risk from high-energy protons and it is recommended that materials with low-Z atomic constituents be considered in the design of future EVA suits, including helmets.

5. The observed differences between proton measurements and the BRYNTRN/CAM model calculation was generally less than 10% for high-energy proton exposures, indicating that the threshold energy (shield thickness) information measured for the EMU and Orlan suits is adequate for protons above 100 MeV (Zapp *et al.*, Chapter 5). The comparisons provide a useful validation of the human geometry model (CAM) and the BRYNTRN transport model [4] used to calculate the flux of particles at depth in material for the geometries used in these experiments. Further comparisons to LET spectral measurements are recommended.

6. The data and analysis reported herein, including the EMU computer model, should be used as a basis for optimizing designs of new space suits for lunar surface EVA where low-energy protons from frequent SPEs are a concern. Based on these results, we recommend that alternative LCVGs or space suit materials be considered.

7. Consideration should be given to adding a thin layer of material to the dorsal side of the gloves; this might result in a substantial reduction of dose to the fingers from low-energy electrons (Moyers *et al.*, Chapter 2).

8. The shadow shielding from the ISS and the EVA workstation/toolbox and SAFER (simplified aid for EVA rescue unit) plays an important role in reducing EVA exposures. The CAD models of the ISS and EMU developed by LaRC (Anderson *et al.*, Chapter, 9) are important tools for EVA assessments and should be integrated for operational planning for space missions.

In addition, we recommend that a dedicated capability be developed at the NASA Space Radiation Laboratory at Brookhaven National Lab and at LLU to test and design spaceflight components including space suits, localized shielding components, and flight dosimetry. NASA should support such a capability as retrofit shielding

for the ISS is developed and as new technological capabilities in radiation protection for lunar or Mars missions move onto more of our horizons.

## REFERENCES

1. National Council on Radiation Protection and Measurements, Recommendations of Dose Limits for Low Earth Orbit. NCRP Report 132, Bethesda MD, 2000.
2. Cucinotta, F. A., F. Manuel, J. Jones, G. Izsard, J. Murray, B. Djojonegoro and M. Wear, 2001. Space radiation and cataracts in astronauts. *Radiat. Res.* **156**: 460-466.
3. National Research Council. Radiation and the International Space Station: Recommendations to reduce risk. National Academy Press: Washington, D.C., 2000.
4. Wilson, J. W., Townsend, L. W., Schimmerling, W., Khandelwal, G. S., Khan, F., Nealy, J. E., Cucinotta, F. A., Simonsen, L. C., and Norbury, J. W., Transport methods and interactions for space radiations, RP1257, NASA, Washington D.C. 1991.

REPORT DOCUMENTATION PAGE			Form Approved OMB No. 0704-0188	
Public reporting burden for this collection of information is estimated to average 1 hour per response, including the time for reviewing instructions, searching existing data sources, gathering and maintaining the data needed, and completing and reviewing the collection of information. Send comments regarding this burden estimate or any other aspect of this collection of information, including suggestions for reducing this burden, to Washington Headquarters Services, Directorate for Information Operations and Reports, 1215 Jefferson Davis Highway, Suite 1204, Arlington, VA 22202-4302, and to the Office of Management and Budget, Paperwork Reduction Project (0704-0188), Washington, DC 20503.				
1. AGENCY USE ONLY (Leave Blank)	2. REPORT DATE December 2003	3. REPORT TYPE AND DATES COVERED NASA Technical Paper		
4. TITLE AND SUBTITLE Radiation Protection Studies of International Space Station Extravehicular Activity Space Suits			5. FUNDING NUMBERS	
6. AUTHOR(S) Francis A. Cucinotta, Mark R. Shavers, Premkumar B. Saganti*, Jack Miller**, Editors				
7. PERFORMING ORGANIZATION NAME(S) AND ADDRESS(ES) Lyndon B. Johnson Space Center Houston, Texas 77058			8. PERFORMING ORGANIZATION REPORT NUMBERS S-904	
9. SPONSORING/MONITORING AGENCY NAME(S) AND ADDRESS(ES) National Aeronautics and Space Administration Washington, DC 20546-0001			10. SPONSORING/MONITORING AGENCY REPORT NUMBER TP-2003-212051	
11. SUPPLEMENTARY NOTES *Prairie View A&M University, Prairie View, Texas **Lawrence Berkeley National Laboratory, Berkeley, California				
12a. DISTRIBUTION/AVAILABILITY STATEMENT Unclassified/Unlimited Available from the NASA Center for AeroSpace Information (CASI) 7121 Standard Hanover, MD 21076-1320			12b. DISTRIBUTION CODE	
13. ABSTRACT (Maximum 200 words) This publication describes recent investigations that evaluate radiation shielding characteristics of NASA's and the Russian Space Agency's space suits. The Introduction describes the suits and presents goals of several experiments performed with them. The first chapter provides background information about the dynamic radiation environment experienced at ISS and summarizes radiation health and protection requirements for activities in low Earth orbit. Supporting studies report the development and application of a computer model of the EMU space suit and the difficulty of shielding EVA crewmembers from high-energy reentrant electrons, a previously unevaluated component of the space radiation environment. Chapters 2 through 6 describe experiments that evaluate the space suits' radiation shielding characteristics. Chapter 7 describes a study of the potential radiological health impact on EVA crewmembers of two virtually unexamined environmental sources of high-energy electrons - reentrant trapped electrons and atmospheric albedo or "splash" electrons. The radiological consequences of those sources have not been evaluated previously and, under closer scrutiny. A detailed computational model of the shielding distribution provided by components of the NASA astronauts' EMU is being developed for exposure evaluation studies. The model is introduced in Chapters 8 and 9 and used in Chapter 10 to investigate how trapped particle anisotropy impacts female organ doses during EVA. Chapter 11 presents a review of issues related to estimating skin cancer risk from space radiation. The final chapter contains conclusions about the protective qualities of the suit brought to light from these studies, as well as recommendations for future operational radiation protection				
14. SUBJECT TERMS radiation, shielding, space suit, electrons, space radiation, anisotropy, radiation damage, radiation protection, albedo, EMU, low Earth orbit			15. NUMBER OF PAGES 196	16. PRICE CODE
17. SECURITY CLASSIFICATION OF REPORT Unclassified	18. SECURITY CLASSIFICATION OF THIS PAGE Unclassified	19. SECURITY CLASSIFICATION OF ABSTRACT Unclassified	20. LIMITATION OF ABSTRACT Unlimited	



---